

Geology and geochronology of the Nyl River floodplain sediments, Limpopo Province, South Africa

Debra Colarossi

A Dissertation submitted to the Faculty of Science, University of the Witwatersrand, Johannesburg, in fulfilment of the requirements for the Degree of Master of Science in Geology.

Johannesburg 2013

Declaration

I declare that this dissertation is my own, unaided work. It is being submitted for the Degree of Master of Science in the University of the Witwatersrand, Johannesburg. It has not been submitted before for any degree or examination in any other University.

Signed: _____

Date: _____

Abstract

The Nyl River floodplain, located in the Limpopo Province, is one of the few active sedimentary basins that exist within the South African interior, providing a unique opportunity to study the effect of climate change on fluvial systems. Progradation of tributary fans into the Nyl/Mogalakwena River has raised the surface by 30 m and forced the course of the river westwards towards the Waterberg. Periods of progradation deposited thick sequences of coarse-grained sediments with sand- to gravel-sized mean grain sizes and coarsely-skewed populations in the distal reaches of the tributary fans. These periods were interspersed with periods of relative non-deposition, when active sedimentation on the fan ceased and shallow lakes (or vleis) developed in the trunk river, resulting in deposition of fine-grained, organic-rich, floodplain sediment layers with silt-sized mean grain sizes and finely-skewed distributions in the extreme outer reaches of the tributary fan. The alternating progradational sequences and non-deposition events produced interlayered floodplain and fan deposits in the furthest reaches of the tributary fans along the banks of the Nyl/Mogalakwena River.

Incised river cuts within the Rooisloot tributary fan were dated using OSL and ^{14}C techniques. For OSL samples, the SAR protocol was used to measure the equivalent dose and the burial dose was determined using the CAM and MAM. Emission counting methods, including TSAC, GM-beta counting and HRGS were used to determine the dose-rate. The OSL ages ranged from 99 years to 3884 years, constraining the sampled deposits within the late Holocene. Although the ^{14}C ages agreed with this range, carbon contamination of the samples resulted in inverted and overestimated ages. Based on stratigraphic relationships the non-deposition events have been dated at approximately 750–800 years ago, 600 years ago, 475 years BP and 100–150 years ago and two major periods of aggradation at ~ 800–1000 years ago and ~ 500–700 years ago. The rate of aggradation (0.29 cm/year) calculated implies that the entire 30 m deposit could have been deposited in 9 000 years. However, an independent study by McCarthy *et al.* (2011) proved that tributary sedimentation began prior to 220 ka. Therefore, in order to deposit 30 m of sediment over 220 ka, either the mid – late Quaternary sedimentation rate was lower than the recent past (Late Holocene) or the system periodically undergoes extensive erosion in order to flush the accumulated sediment from the tributary fan system.

Acknowledgements

This project would not have been possible without the assistance of numerous people. First and foremost I would like to thank my supervisors. Prof. Terence McCarthy for providing the opportunity to work on this project and sending me to Aberystwyth University in Wales to learn just how complicated OSL dating can be. Also Mrs Mary Evans for always making herself available to answer my random questions over the last two years, even when she was busy with her own PhD work.

To Matt Kitching, Charldrin Bailey, David Lekota and George Susino for their assistance in the field with sample collection. The lightning fast fieldwork required during 2011 would not have been possible without you.

The time I spent at the Aberystwyth Luminescence Research Laboratory was probably the most productive 6 months over the last two years. My sincerest thanks to Prof. Geoff Duller and Dr Helen Roberts who hosted me while at the ALRL, your guidance was most appreciated and it was an honour to have the opportunity to learn from you for the brief time that I was in Wales. To Dr Stephen Tooth who organised the trip to Wales and did everything but put me on the plane in Johannesburg, thank you for organising the best opportunity I have had to date. Special thanks to Hollie Wynne, Melissa Jackson, Rachel Smedley and Rosie Stirling for your patience when answering my questions and helping me when I couldn't figure out what I was doing (and for fixing my dosimetry calculation in five minutes after I had been staring at it for two days).

This project was funded by the University of the Witwatersrand Postgraduate Merit Award, the National Research Foundation Innovation Award for postgraduate studies, the Geological Society of South Africa (GSSA) Research Education and Investment funding, the Carnegie Foundation Large Research Grant Award through Mrs Mary Evans and Prof. Terence McCarthy.

CONTENTS	PAGE
DECLARATION	ii
ABSTRACT	iii
ACKNOWLEDGEMENTS	iv
TABLE OF CONTENTS	v
LIST OF FIGURES	ix
LIST OF TABLES	xiii
ABBREVIATIONS AND ACRONYMS	xv
 CHAPTER 1 – INTRODUCTION	 1
1.1. Introduction	1
1.2. Location of the Nyl/Mogalakwena River floodplain	3
1.3. Regional geology and geomorphology	3
1.4. The depositional environment	6
1.4.1. Existing depositional model for the Nyl/Mogalakwena River floodplain	10
1.5. Research aim	12
1.6. Overview of research techniques	13
1.7. Summary	14
1.8. Dissertation preview	15
 CHAPTER 2 – GEOMORPHOLOGY AND STRATIGRAPHY	 17
2.1. Introduction	17
2.2. Alluvial fans	17
2.2.1. Classification of alluvial fans	17
2.2.2. Description of the tributary alluvial fans	18
2.3. Geomorphological investigation - Methodology and techniques	22
2.3.1. Sampling strategy	22
2.3.2. Profile stratigraphy	22
2.3.3. Grain size and sorting analysis	25
2.3.4. GRADISTAT calculations	26
2.4. Geomorphological Investigation - Results	28
2.4.1. Stratigraphic comparison of the profiles across the tributary fan	28
2.4.2. Statistical analysis of grain size data	34
2.5. Discussion	38
2.5.1. Characteristics of tributary fan and floodplain sediments	39
2.5.2. Particle sorting versus mean grain size	40
2.5.3. Transport history of sediments	42
2.5.4. Stratigraphic comparison	43
2.6. Summary	44
 CHAPTER 3 – GEOCHRONOLOGY: RADIOCARBON AND OPTICALLY STIMULATED LUMINESCENCE DATING	 46
3.1. Introduction	46
3.2. Radiocarbon dating	47

3.2.1. Measurement of radiocarbon concentrations	48
3.2.2. Reporting and calibrating ^{14}C ages	48
3.2.3. Age limit of ^{14}C dating	48
3.3. Luminescence dating	49
3.3.1. Optically Stimulated Luminescence	50
3.4. Basic concepts of OSL dating	51
3.4.1. The luminescence signal	51
3.4.2. Minerals used for optical dating	52
3.5. Measuring the equivalent dose (D_e)	53
3.5.1. The Single Aliquot Regenerative Dose (SAR) protocol	53
3.5.2. Sensitivity change of quartz during the SAR protocol	54
3.5.3. Preliminary tests for the SAR protocol	55
3.5.4. Single-grain techniques	58
3.6. Statistical analysis methods for determination of the true burial dose (D_b)	58
3.6.1. The common age model	60
3.6.2. The central age model (CAM)	60
3.6.3. The minimum age model (MAM)	60
3.6.4. The finite mixture model (FMM)	61
3.7. Calculating the environmental dose-rate (D_r)	62
3.7.1. Internal dose-rate	62
3.7.2. External dose-rate	63
3.7.2.1. Alpha particle contribution	64
3.7.2.2. Beta particle and gamma ray contribution	65
3.7.2.3. Cosmic ray contribution	65
3.7.2.4. Water content corrections	67
3.7.3. Disequilibrium in the decay chain	67
3.8. Suitability for OSL and ^{14}C dating for the Nyl/Mogalakwena River and Rooisloot sediments	70
3.8.1. Previous dating studies undertaken on the Nyl/Mogalakwena River floodplain	71
3.9. Summary	71

CHAPTER 4 – EQUIVALENT DOSE (D_e) DETERMINATION 73

4.1. Introduction	73
4.2. Sampling strategy	73
4.3. Sample preparation	75
4.3.1. Removal of carbonates	75
4.3.2. Removal of organics	76
4.3.3. Dry sieving	76
4.3.4. Extraction of quartz grains	76
4.3.5. Disc preparation	77
4.4. Instrumentation	79
4.4.1. Calibration of the beta sources	80
4.5. Optical stimulation	80
4.5.1. Single aliquot stimulation	81
4.5.2. Single-grain stimulation	81
4.5.3. Optical filters	82
4.6. Measurement of the luminescence signal	82
4.6.1. Preliminary tests for the SAR protocol	82
4.6.1.1. The preheat and dose recovery tests	83

4.6.1.2.	Sensitivity change in the Nyl/Mogalakwena River and Rooisloot quartz	84
4.6.1.3.	Recycling ratio and recuperation ratio tests	86
4.6.2.	Single aliquot measurements	86
4.6.3.	Single-grain measurements	87
4.7.	Calculation of D_e values	87
4.7.1.	Single aliquot D_e measurements	87
4.7.1.1.	Calculation of the D_b from single aliquot measurements	88
4.7.2.	Single-grain D_e measurements	92
4.7.2.1.	Calculation of D_b from single-grain measurements	93
4.8.	Summary	94

CHAPTER 5 –THE ENVIRONMENTAL DOSE-RATE (D_r) 96

5.1.	Introduction	96
5.2.	Thick Source Alpha Counting (TSAC)	96
5.2.1.	Sample Preparation	97
5.2.2.	Pairs Counting to Determine the U and Th Concentration	98
5.2.3.	Assessing Radon Escape Using TSAC	98
5.3.	GM-Beta Counting	99
5.3.1.	Sample Preparation	99
5.3.2.	Calculation of the Beta Dose-Rate	100
5.4.	High Resolution Gamma Spectrometry (HRGS)	100
5.4.1.	Sample Preparation	101
5.4.2.	Isotope Concentrations	101
5.5.	Equilibrium in the Decay Chain of the Nyl/Mogalakwena River and Rooisloot Samples	102
5.6.	Derivation of the Environmental Dose-Rate	105
5.6.1.	Combining TSAC with GM-Beta Counting	105
5.6.2.	Attenuation of the Beta Dose-Rate	106
5.6.3.	Water Content Correction	106
5.6.4.	Determining the Dose-Rate from HRGS	107
5.7.	Comparison of Data Obtained from Different Methods of Dose-Rate Determination	107
5.8.	Summary	109

CHAPTER 6 – AGE AND ENVIRONMENTAL RECONSTRUCTION OF THE NYL/MOGALAKWENA RIVER FLOODPLAIN 111

6.1.	Introduction	111
6.2.	Calculated OSL and ^{14}C ages	111
6.3.	Reliability of the OSL and ^{14}C ages	111
6.3.1.	OSL ages	111
6.3.1.1.	Partial bleaching in the Nyl/Mogalakwena River and Rooisloot samples	114
6.3.1.2.	Comparison of D_e distributions and OSL ages	115
6.3.2.	Radiocarbon ages	116
6.3.3.	Comparison of OSL and ^{14}C ages	117
6.3.3.1.	Comparison of ages in Profiles A and B	118
6.3.3.2.	Comparison of ages in Profiles C and D	118
6.3.3.3.	Age comparison across the sample area	119

6.4.	Environmental Reconstruction of the Nyl/Mogalakwena River floodplain	119
6.4.1	Stratigraphy	120
6.4.2	Depositional environment	121
6.4.3	Sedimentation and established climatic events during the Holocene	125
6.4.3.1	Timing of the floodplain deposits	125
6.4.3.2	Periods of aggradation	128
6.5	Summary	130
CHAPTER 7 – CONCLUSIONS		132
7.1.	Summary of findings	132
7.2.	Future research directions	134
8	REFERENCES	136

APPENDICES

APPENDIX A: Grain Size Distributions

APPENDIX B: Lasergranulometry of Clay-Rich Sediments

APPENDIX C: Calibration of Beta Sources

APPENDIX D: Calculating the Environmental Dose-Rate from Thick Source Alpha Counting and GM-Beta Counting

APPENDIX E: Calculating the Environmental Dose-Rate from High-Resolution Gamma Spectroscopy (HRGS)

APPENDIX F: Radiocarbon Dating Report

List of Figures

Figure 1.1:	Global temperature variations over the last 5.3 Ma relative to the peak Holocene temperature; data based on ocean core records (Hansen and Sato, 2011).	1
Figure 1.2:	(a) The location and geological setting of the Nyl-Mogalakwena River floodplain and (b) the catchment area for the Nyl River (McCarthy <i>et al.</i> , 2012).	4
Figure 1.3:	Google Earth image showing the location of the Nyl River in relation to the nearest town, Mokopane.	7
Figure 1.4:	Google Earth image showing the location of the Rooisloot tributary fan in relation to the alluvial fan complex deposited by the tributaries arising to the east of the Nyl/Mogalakwena River.	8
Figure 1.5:	Schematic diagram illustrating the association of the Rooisloot tributary fan as it progrades onto the Nyl/Mogalakwena floodplain (McCarthy <i>et al.</i> , 2012).	12
Figure 2.1:	Basic alluvial fan morphology based on topographic relationships (Harvey, 2011).	18
Figure 2.2:	Map of the geomorphological features of the tributary fan located at the confluence of the Nyl/Mogalakwena River with the Rooisloot River.	19
Figure 2.3:	Google Earth image of a section of the Rooisloot tributary alluvial fan illustrating the sample locations.	20
Figure 2.4:	The actively prograding section of the Rooisloot tributary fan.	21
Figure 2.5a:	Annotated photographs of the individual sample locations. Profiles A and B (NVA and NVB respectively) are located along the banks of the Nyl/Mogalakwena River.	23
Figure 2.5b:	Annotated photographs of the individual sample locations. Profiles C and D (NVC and NVD respectively) are located within a tributary fan environment along the Rooisloot.	24
Figure 2.6:	Grain roundness classification (modified after Sand Forum International, 2009) originally determined by Powers (1953).	25

Figure 2.7:	(a) Stratigraphic correlation between the Nyl/Mogalakwena River and Rooisloot profiles based on field descriptions, (b) schematic representation for the Nyl River floodplain showing the profile line for (c) the surface profile of the Rooisloot alluvial fan.	29
Figure 2.8:	Cumulative frequency curves for each horizontal layer sampled and dry-sieved for (a) Profile A, (b) Profile B, (c) Profile C and (d) Profile D.	35
Figure 2.9:	Cumulative frequency curves for each horizontal layer sampled and analysed using laser granulometry for Profile A and Profile B.	35
Figure 2.10a:	Comparison between the mean grain size and sorting (standard deviation) within each Profile for the samples identified as tributary fan sediments.	41
Figure 2.10b:	Comparison between the mean grain size and sorting (standard deviation) within each Profile for the samples identified as floodplain sediments.	41
Figure 3.1:	Schematic representation of the event dated by luminescence dating.	49
Figure 3.2:	Energy-level diagram depicting the three stages of the luminescence process.	52
Figure 3.3:	Graph showing the sensitivity change in a sample of South African quartz from Kosi Bay.	55
Figure 3.4:	The preheat plateau identified from a preheat test.	56
Figure 3.5:	Schematic representation of the distribution of D_e values in the various age models: a) the common age model, b) the central age model, c) the minimum age model and d) the finite mixture model.	62
Figure 3.6:	Natural radiation travelling through soil.	64
Figure 3.7:	Decay chains for the parent isotopes (a) ^{232}Th , (b) ^{238}U and (c) ^{235}U .	66
Figure 3.8:	Parameters for determination of the cosmic dose-rate as a function of altitude and geomagnetic latitude.	67
Figure 4.1:	Stratigraphic location of samples collected for OSL and ^{14}C dating.	74

Figure 4.2:	Schematic representation of a sample tube used to collect the OSL sample in the field.	76
Figure 4.3:	Examples of prepared aliquots: (a) small multiple-grain, (b) medium multiple-grain, (c) large multiple-grain and (d) single-grain aliquots.	78
Figure 4.4:	OSL decay curves for various stimulation wavelengths (Duller and Bøtter-Jensen, 1996).	82
Figure 4.5:	(a) Emission spectrum of the blue LEDs and the transmission curves for the Hoya U-340 detection filter and the Schott GG-420 green long-pass filter. (b) The Hoya U-340 is the detection filter fitted below the photomultiplier tube (PMT) and the Schott GG-420 the cut-off filter fitted in front of the blue LED clusters.	83
Figure 4.6:	Plot of preheat temperature against D_e for sample NVA6.	84
Figure 4.7:	Dose-response curve plotted from the dose-recovery test for sample NVA6 with a preheat of 160 °C.	85
Figure 4.8:	Plot of cycle number versus T_x/T_n showing the sensitivity change of the Nyl River quartz from sample NVA6 during the SAR sequence.	85
Figure 4.9a:	Radial plots of single aliquot D_e values.	90
Figure 4.10:	The a) probability density plot and b) radial plot for sample NVC2.	92
Figure 4.11:	Proportion of single grains emitting light in sample NVB10 and NVC2.	93
Figure 4.12:	Radial plots of single grain D_e values.	94
Figure 5.1:	Sketch of the container used for TSAC.	97
Figure 5.2:	Idealised sketch of TSAC sample on a ZnS screen.	97
Figure 5.3:	Schematic diagram of the GM-25-5 beta counter.	99
Figure 5.4:	Direct comparison of derived environmental dose-rates (D_r) obtained using HRGS and a combination of TSAC with GM-beta counting.	109
Figure 6.1:	Stratigraphic location of the OSL and ^{14}C ages.	113

Figure 6.2:	Graph showing the correlation between quartz OSL ages and those of independent age controls from various depositional settings.	118
Figure 6.3:	a) Composite stratigraphy of the A and B profiles along the banks of the Nyl/Mogalakwena River showing interspersed depositional sequences and non-depositional events and b) a cross-section showing the depositional setting responsible for the interlayered floodplain and tributary fan deposits.	122
Figure 6.4:	Historical images of the Nyl/Mogalakwena River floodplain taken in a) July 2004 during a dry season and b) June 2009 during a wet season.	124
Figure 6.5:	Graph depicting changes in air temperature determined from $\delta^{18}\text{O}$ variability from the NORTHGRIP ice core spanning the Holocene Epoch.	126
Figure 6.6:	Approximate ages of the depositional sequences and non-depositional events identified in Profile A-B and the periods of aggradation in Profile C and Profile D.	127

List of Tables

Table 2.1:	Scales for sorting, skewness and kurtosis as calculated by GRADISTAT.	27
Table 2.2(a):	Detailed sedimentology for Profile A along the banks of the Nyl/Mogalakwena River.	30
Table 2.2(b):	Detailed sedimentology for Profile B along the banks of the Nyl/Mogalakwena River.	31
Table 2.2(c):	Detailed sedimentology for Profile C located within the Rooisloot tributary fan.	32
Table 2.2(d):	Detailed sedimentology for Profile D located within the Rooisloot tributary fan.	33
Table 2.3(a):	GRADISTAT statistical data for the floodplain depositional environment (Profile A and B)	36
Table 2.3(b):	GRADISTAT statistical data for the tributary fan depositional environment (Profile C and D)	37
Table 3.1:	Generalised SAR sequence for quartz using blue LEDs for stimulation.	54
Table 4.1:	Samples measured at Aberystwyth University and the University of the Witwatersrand	75
Table 4.2:	Specifications of the Risø readers used in this research project	79
Table 4.3:	The SAR sequence used on the Nyl/Mogalakwena River And Rooisloot quartz	86
Table 4.4:	Overdispersion (σ_b) and true burial dose (D_b) data calculated from single aliquot measurements using the CAM and MAM	91
Table 4.5:	Overdispersion (σ_b) and true burial dose (D_b) data calculated from single-grain measurements by the CAM and MAM.	93
Table 4.6:	Final D_e measurements used to calculate OSL ages (Chapter 6)	95
Table 5.1:	Site data and dosimetry obtained using TSAC and GM-beta counting	103
Table 5.2:	Site data and dosimetry obtained using HRGS.	104

Table 5.3:	Correction factors for attenuation and the effects of HF etching on the beta dose-rate for the grain size 180 – 212 μm	106
Table 5.4:	Final corrected environmental dose-rates and ratios obtained from HRGS and a combination of TSAC with GM-beta counting (TSAC+B).	108
Table 5.5:	Final D_f measurements used to calculate OSL ages (Chapter 6)	110
Table 6.1:	OSL ages calculated for the Nyl/Mogalakwena River and Rooisloot samples	112
Table 6.2:	^{14}C ages as determined by the Radiocarbon Dating Laboratory at Lund University, Sweden.	114

Abbreviations and Acronyms

AAS	atomic absorption spectrometry
Ac	actinium
ALRL	Aberystwyth Luminescence Research Laboratory
α	alpha
a	annum (1 a = 365.25 days)
AMS	accelerator mass spectrometry
asl	above sea level
β	beta
Bi	bismuth
BIC	Bayesian Information Criterion
C	carbon
^{14}C	radiocarbon
CaCO_3	calcite
CAM	central age model
CC	corrected counts
Cl	chlorine
CO_2	carbon dioxide
D_e	equivalent dose
D_b	true burial dose
D_r	dose-rate
D_T	test dose
DRT	dose recovery test
eV	electron volt (1 eV = 1.602×10^{-19} J)
FGS	field gamma spectrometry

FMM	finite mixture model
γ	gamma
g	gram
Gy	Gray (1 Gy = 1 J/kg)
HCl	hydrochloric acid
HF	hydrofluoric acid
H ₂ O ₂	hydrogen peroxide
HPGe	high purity germanium crystal
HRGS	high resolution gamma spectrometry
hg	hectogram (1 hg = 100 g)
ICP-MS	inductively coupled plasma mass spectrometry
IR	infra-red
IRSL	infra-red stimulated luminescence
$t_{1/2}$	half-life
ICS	International Commission on Stratigraphy
K	potassium
ka	kiloannum (1 ka = 1,000 a)
keV	kilo electron volt (1000 keV = 1 MeV)
km	kilometre (1 km = 1,000 m)
K ₄ P ₂ O ₇	potassium pyrophosphate
LED	light emitting diode
L _x	luminescence signal from regeneration dose
m	meter
Ma	megaannum (1 Ma = 1,000,000 a)
MAM	minimum age model
MgO	magnesium oxide
ml	millilitre

mm	millimetre
N	nitrogen
NAA	neutron activation analysis
NaI(Tl)	sodium iodide doped with thallium
OSL	Optically Stimulated Luminescence
σ_B	overdispersion
ρ	density
Pb	lead
Po	polonium
‰	parts per thousand ($= 10^{-3}$)
%	percentage
pMC	percentage modern carbon
ϕ	phi
PMT	photomultiplier tube
ppm	parts per million (10,000 ppm = 1 %)
Ra	radium
Rb	rubidium
Rn	radon
s	second (60 s = 1 min)
SAAD	Single Aliquot Additive Dose
SAR	Single Aliquot Regenerative Dose
SPT	sodium polytungstate
Sr	strontium
Th	thorium
Tl	thallium
TL	Thermoluminescence
TSAC	Thick Source Alpha Counting

T _x	luminescence signal resulting from test dose
U	uranium
μm	micrometer (1,000 μm = 1 mm)
XRF	x-ray fluorescence
Y	yttrium
years BP	years before present
years (cal) BP	calibrated years before present
ZnS	zinc sulphide

Chapter 1:

Introduction

1.1. Introduction

The climate has varied throughout Earth's history as evidenced by existing global reconstructions such as the change in global temperatures (Figure 1.1), the variation of CO₂ concentrations and the fluctuation of sea surface temperatures. Global climate reconstructions are produced through the compilation of smaller-scale local reconstructions, for example mapping the distribution of rock types such as coal, laterites, calcretes and tillites to identify specific climate belts. Due to the short time-span relevant to Earth history for which climate records exist, environmental reconstructions are determined using various proxy records, such as ice cores, deep sea sediments, microbial life *e.g.* diatoms, foraminifera and corals, pollen records and tree rings. Proxy data provide an indirect measure of past climates and environments (Lowe and Walker, 1997) and in conjunction with a precise, high-resolution geochronology can produce environmental reconstructions which can be used to model global climate changes.

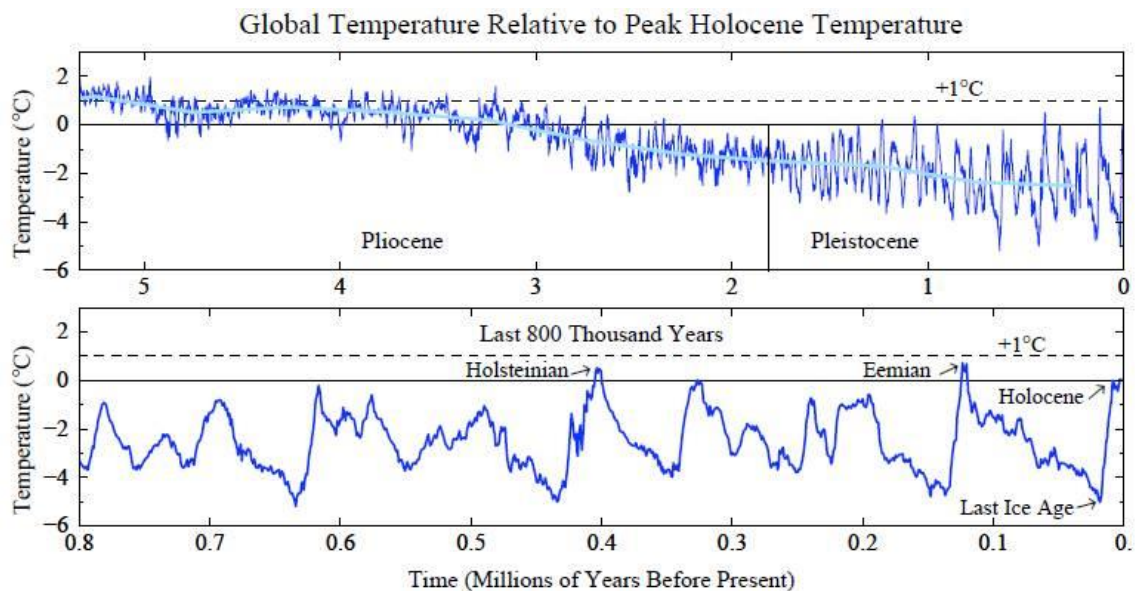


Figure 1.1: Global temperature variations over the last 5.3 Ma relative to the peak Holocene temperature; data based on ocean core records (Hansen and Sato, 2011).

By far the majority of palaeoclimatic reconstructions have been undertaken in the northern hemisphere, thus the record for the southern hemisphere is more fragmented and not well dated. Williams *et al.* (1993) maintain that the southern hemisphere record, despite its comparatively fragmentary nature, shows that the chronology of the last glacial stage in both hemispheres is very similar and the ice growth in the southern hemisphere reflects control by the same instability of global climate that the northern hemisphere does. Recently an increased number of studies have been conducted in order to obtain a more complete geochronology and palaeo-environmental history for the southern hemisphere, such as the analysis of the isotope records contained within the Vostok ice cores from Antarctica (Petit *et al.*, 1999); fission track dating of a tephra layer to date the associated interbedded glacial deposits in the Rio Grande Valley, Argentina (Espizua *et al.*, 2002) and the reconstruction of the precipitation history of tropical South America over the last 25 000 years from sediment cores from Lake Titicaca on the border of Peru and Bolivia (Baker *et al.*, 2001).

Limited environmental reconstructions have been completed within South Africa, these include OSL dating of dune sands in Blombos Cave (Jacobs *et al.*, 2003a,b) and the Kalahari (Chase, 2009); analysis of the Wonderkrater pollen sequence (Scott and Thackeray, 1987; Scott, 1999; Scott *et al.*, 2003); creation of the moisture index from the Tswaing crater infill sediments (Partridge *et al.*, 1997); speleothem records from Crevice Cave at Pinnacle Point (Bar-Matthews *et al.*, 2010) and Cold Air Cave in Makapansgat Valley (Holmgren *et al.*, 1999, 2003); and the $\delta^{18}\text{O}$ record from marine sediment cores collected off the coast of Kwazulu Natal (Prell *et al.*, 1979). Of particular interest to this research project is the luminescence dating of colluvium at St Paul's Mission, Kwazulu Natal, which represents the first use of the infra-red stimulated luminescence (IRSL) technique on colluvial sediments (Wintle *et al.*, 1995; Botha, 1996). The St Paul's Mission study used IRSL in conjunction with radiocarbon (^{14}C) dating, palynology studies and stable carbon-isotope data to reconstruct the deposition of colluvium and formation of gullies over the last 135 000 years. The current research project is similar to the St Paul's Mission research and will investigate fluvially deposited sediments within the Nyl/Mogalakwena River floodplain and examine the

depositional history of the layers in the context of existing proxy records. This project will therefore contribute to the reconstruction of the palaeo-environmental conditions in the interior of South Africa during the Quaternary.

Notable climatic events which occurred during the Quaternary include the Holocene climatic optimum ~ 7–3 ka, the Medieval Warm Period (MWP) from 900–1300 AD and the Little Ice Age (LIA) from 1300–1800 AD (Anderson *et al.*, 2007; Walker, 2005; Holmgren *et al.*, 1999; Lowe and Walker, 1997). The LIA has been identified in the southern hemisphere record in tree rings across numerous sites (Thackeray, 1996; Dunwiddie and Le Marche, 1980), foraminifera from sediment cores off the west coast of Namibia (Johnson, 1988), stable isotope series from the Cango Cave (Talma and Vogel, 1992) and the Cold Air Cave (Holmgren *et al.*, 1999) and changing water levels in Lakes Malawi and Chilwa (Crossley *et al.*, 1983). Alternatively, the MWP has not been recorded as extensively as the LIA because the MWP was highly variable and not as extensive (Tyson *et al.*, 2000). However, the MWP is evident in the coastal mollusc isotope record (Cohen and Tyson, 1995) and speleothems and tufa formations in interior southern Africa (Holmgren *et al.*, 1999; Brook *et al.*, 1997).

1.2. Location of the Nyl/Mogalakwena River Floodplain

The research site is located north of Mokopane (Potgietersrus) near the village of Maroteng in Limpopo Province, South Africa (24°08'24.38"S and 28°55'19.87"E; Figure 1.2). It is bordered by the Waterberg range to the west and northwest (rising to 1700 m asl) and the Masodi and Maroteng townships to the east. The Springbok Flats lie to the south ~1000 m asl (McCarthy *et al.*, 2010; 2011). The Nyl/Mogalakwena River meanders through the area and is joined by its tributaries, including the Rooisloot from the east.

1.3. Regional Geology and Geomorphology

The immediate area around the Nyl/Mogalakwena River lies within a downwarped basin composed of rocks from the Pretoria Group and the Rooiberg felsites of the Bushveld Complex, in addition to the Waterberg Group in the extreme west (Figure 1.2a) (South

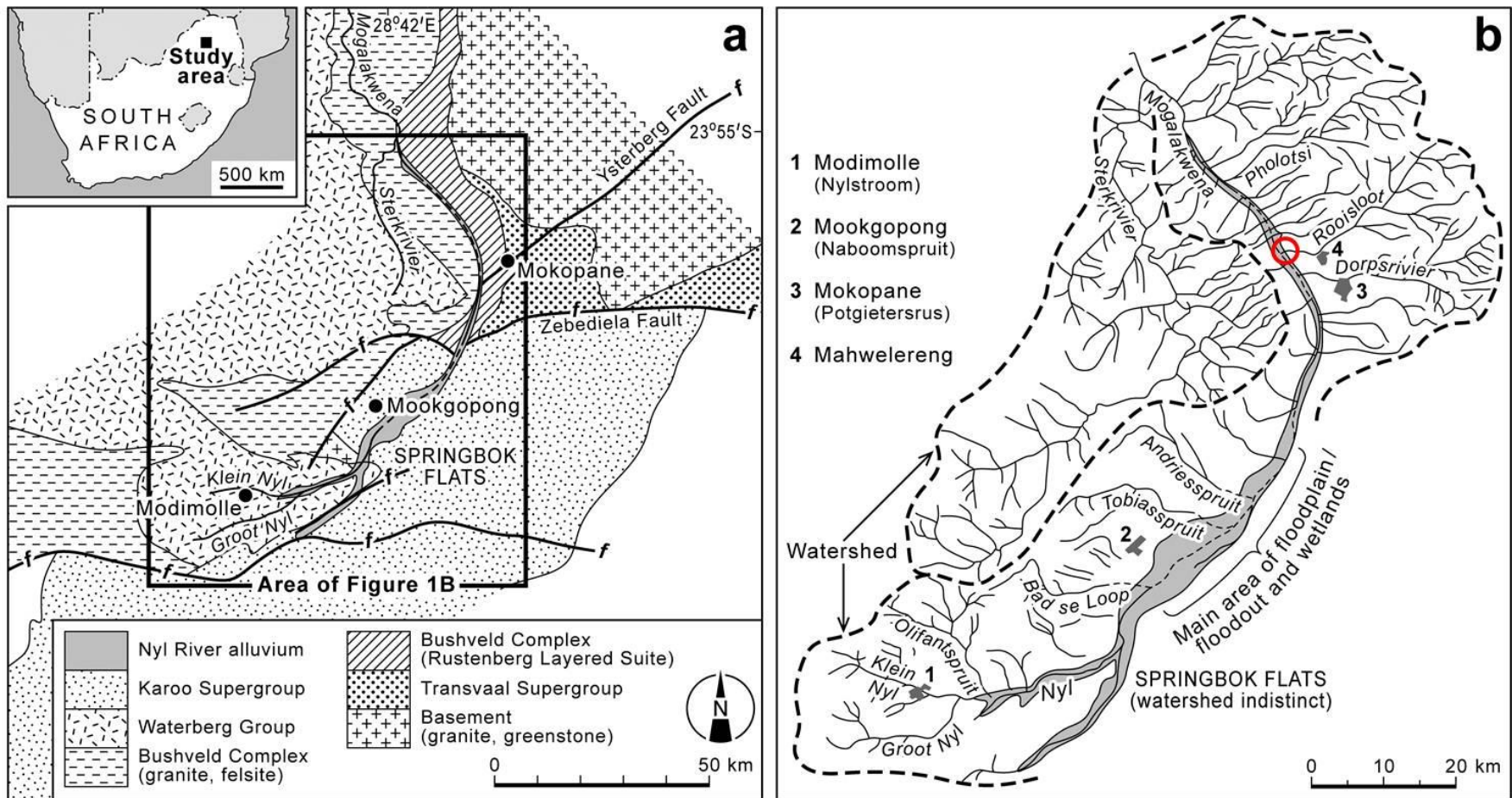


Figure 1.2: (a) The location and geological setting of the Nyl/Mogalakwena River floodplain and (b) the catchment area for the Nyl/Mogalakwena River (McCarthy *et al.*, 2011). The confluence of the Nyl/Mogalakwena River and the Rooisloot is marked by the red circle.

African Geological Survey, 1978; Frost, 1987). The basin is host to the younger Karoo Supergroup rocks which have been folded into two elongate flexures separated by a NE-SW trending anticline, composed of Karoo sandstones whilst the flexures are filled with amygdaloidal basalts that have been reduced to the fairly level plains of the Springbok Flats (Frost, 1987). The location of the Karoo Supergroup sedimentary rocks against the Bushveld Complex mafic rocks has been ascribed to movement along the Zebediela fault by McCarthy *et al.* (2011).

The currently accepted model for the landscape formation of southern Africa, specifically the modified version of King's (1962) polycyclic model as put forward by Partridge and Maud (1987), categorises the Waterberg Plateau as corresponding to the African surface and the Springbok Flats and Nyl/Mogalakwena River valley to the Post-African I surface. Therefore substantial erosion occurred in the area prior to the deposition of the tributary fan system.

The source area for the Groot Nyl and Klein Nyl Rivers is in the Waterberg. The Nyl River originates at the confluence of the Groot Nyl and Klein Nyl Rivers (Figure 1.2) and flows roughly north-eastward across the Karoo sandstones and basalts of the Springbok Flats, which features extensive floodplains and a broad channel due to the very gentle gradients. Further downstream (northwards) the channel disappears to be replaced by a floodout (a low-gradient, unchannelled floodplain) ~ 7 km wide which merges with the floodplains and forms the Nyl River floodplain wetland. The Nylsvley Nature Reserve is located in this region (Figure 1.2b). The Nyl River floodplain wetland is located in a semi-arid climate (McCarthy *et al.*, 2011). The present annual rainfall in the area varies between 250–1100 mm with a mean annual rainfall of 630 mm and an annual potential evaporation of 2400 mm which produces a net water deficit on the floodplain (McCarthy *et al.*, 2010).

Water flows through the floodout primarily as sheetflow during the rainy season, which deposits thin clay layers that effectively seal the floodplain surface, preventing groundwater recharge and prolonging inundation. A broad, shallow, defined channel

appears north of the Zebediela fault, underlain by the Rustenberg Layered Suite (the mafic rocks of the Bushveld Igneous Province), due to the convergence of flood waters by bedrock outcrop and a steepening gradient (Tooth *et al.*, 2002; McCarthy *et al.*, 2011). Here the Nyl River becomes the Mogalakwena River. The catchment area on the eastern side of the Nyl/Mogalakwena River is more extensive than on the western side (Figure 1.2b). Tributaries to the west arise in the Waterberg composed of Bushveld Complex lithologies and Waterberg sandstones, whilst tributaries to the east, including the Rooisloot, arise in the Maribashoek and Buffelshoek Mountains composed of Transvaal Supergroup rocks (McCarthy *et al.*, 2011). The Nyl/Mogalakwena River catchment feeds into the Limpopo River ~ 250 km downstream of the study site (Morgan, 1996; Tooth *et al.*, 2002).

The geology, hydrology and ecology of the Nyl/Mogalakwena River floodplain have all been documented previously (see Frost, 1987; Higgins and Rogers, 1993; Higgins *et al.*, 1996; Morgan, 1996). However Tooth *et al.* (2002) provided the first geomorphological analysis of the floodplain. They identified the downstream decrease of river channels, described the characteristic floodplain islands, and concluded that the surface and groundwater hydrology of the floodplain is influenced by the stratigraphy and sedimentology of the alluvial fill. McCarthy *et al.* (2011) suggest that the origin of the Nyl/Mogalakwena River floodplain wetland is due to progradation of tributary fans across the Nyl/Mogalakwena River (Figure 1.3), thereby creating accommodation space (the space available for potential sediment accumulation) upstream. An increase in accommodation space results in sediment accumulation upstream of the tributary fan. Furthermore, they propose that fan formation may be the result of climate change, specifically aridification. The existing model for the depositional environment was proposed by McCarthy *et al.* (2011).

1.4 The Depositional Environment

Limited work has been done on the geomorphology and sedimentation of the Nyl/Mogalakwena River floodplain (see Tooth *et al.* (2002), Rowberry *et al.* (2011) and McCarthy *et al.* (2011)). The longitudinal profile for the Nyl/Mogalakwena River

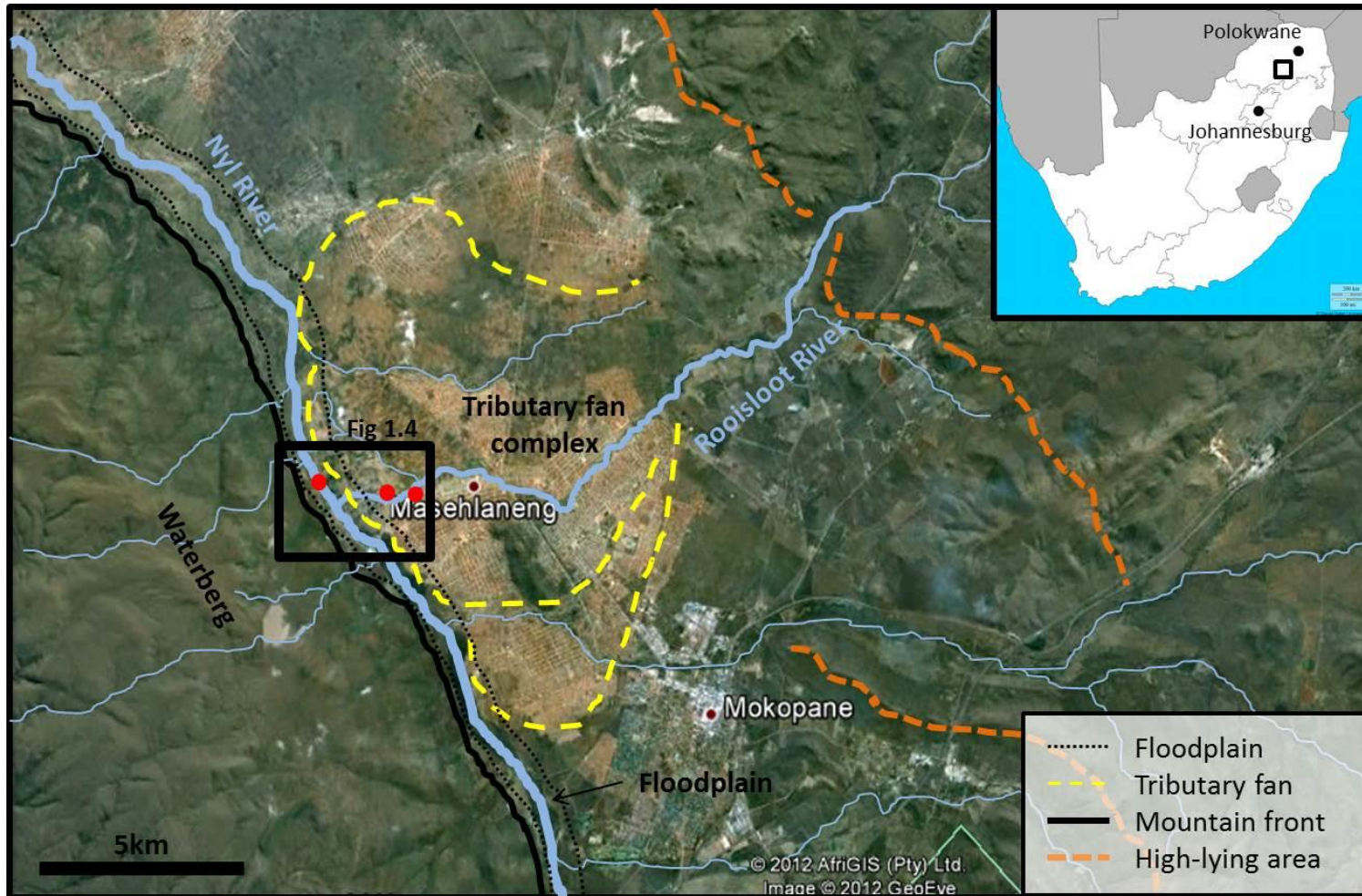


Figure 1.3: Google Earth image showing the location of the Nyl/Mogalakwena River in relation to the nearest town, Mokopane. The Waterberg range extends along the west, the mountain front is denoted by the solid line, with the high-lying area to the east denoted by the dashed line. The extent of the Nyl/Mogalakwena River floodplain and the tributary fan complex (prograding towards the mountains) are outlined.

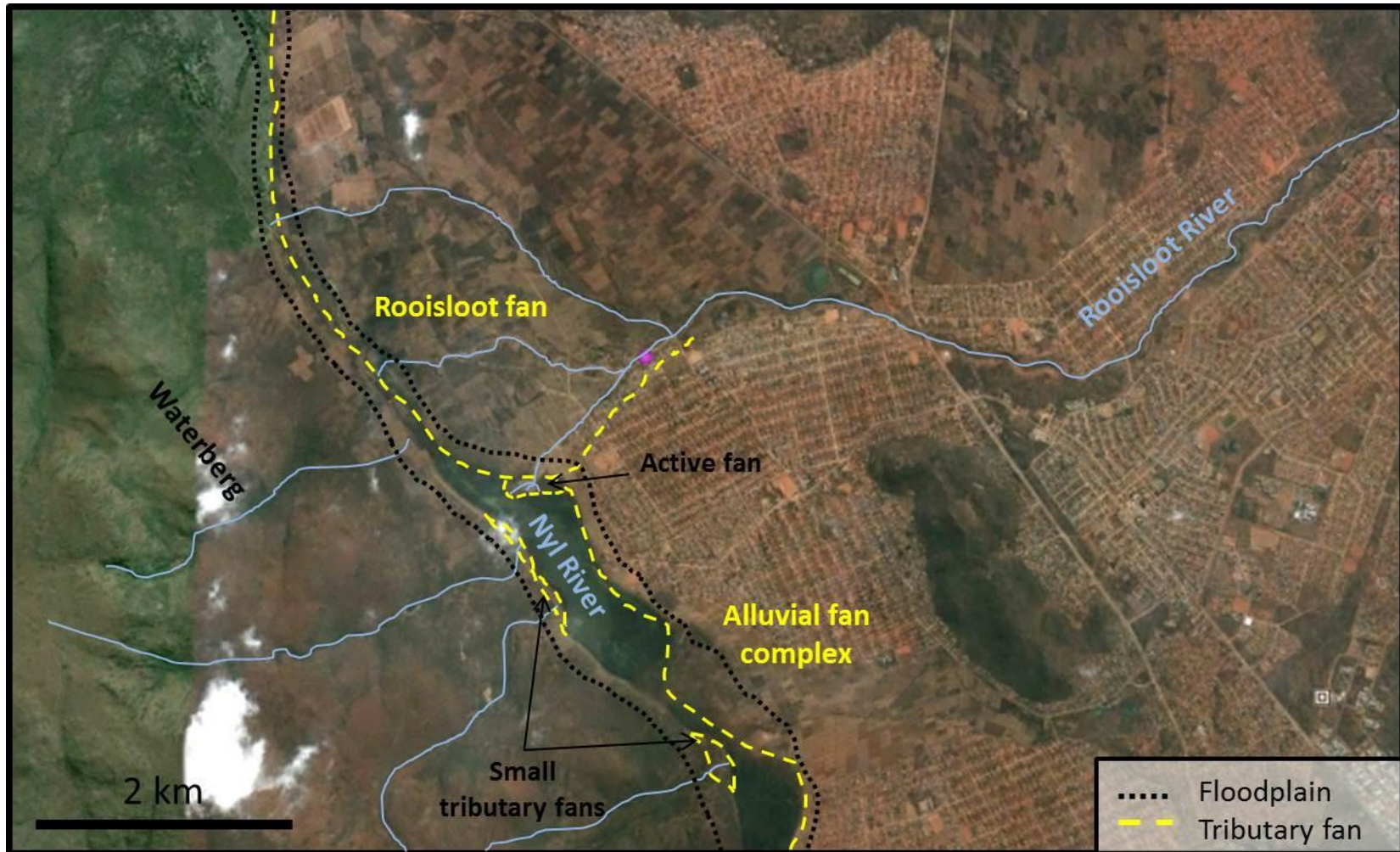


Figure 1.4: Google Earth image showing the location of the Rooisloot tributary fan in relation to the fan complex deposited by the tributaries arising to the east of the Nyl/Mogalakwena River. The tributary fans deposited by the tributaries arising to the west are much smaller in comparison to those deposited by the tributaries arising in the east.

compiled by McCarthy *et al.* (2011) shows a change in slope near the confluence of the Nyl/Mogalakwena River and the Rooisloot, where the characteristic low-gradient section of the floodplain wetland with a discontinuous or poorly-defined channel changes to a steeper gradient and more continuous, incised channel. There is no correlation between the gradient change and the underlying geology based on the lack of corresponding faults or lithology change. This lack of correlation combined with the detailed channel analysis by Tooth *et al.* (2002) prompted McCarthy *et al.* (2011) to suggest that the Nyl/Mogalakwena River was once a bedrock river where transport capacity outpaced the sediment supply.

The major tributaries also show differences in their morphology and sedimentology. The southern tributaries (such as the Andriesspruit) are long, shallow rivers that change downstream to undefined channels that flood out, depositing mud and silt onto the Nyl/Mogalakwena River floodplain; whilst the major tributaries to the north of the study reach (Dorpsrivier, Rooisloot and Pholotsi) are short and steep with defined channels that bifurcate into multiple channels and deposit coarse grained sediment into the Nyl/Mogalakwena River (McCarthy *et al.*, 2011). All tributaries terminate as tributary fans on the Nyl/Mogalakwena River floodplain (Figure 1.4). However the northern tributaries do this on a much larger scale thereby forming shallow lakes (known locally as “vleis”) within the trunk river (McCarthy *et al.*, 2011).

Rowberry *et al.* (2011) analysed the spatial and temporal patterns of flooding within the floodplain wetland and identified two distinct phases. The first phase, characterised by the ponding of water on the wetland surface, was ascribed to the presence of impermeable clay layers within the floodplain and the second phase featured water input from adjacent tributaries to the north (*e.g.* Andriesspruit and Tobiasspruit) and southwest (*e.g.* Klein Nyl and Groot Nyl).

The progradation of tributary fans across the Nyl/Mogalakwena River has resulted in the course of the Nyl/Mogalakwena River shifting westwards towards the foot of the Waterberg, the river bed being raised ~ 30 m and deposition of sedimentary deposits (up

to a thickness of 30 m) located along the eastern bank of the Nyl/Mogalakwena River (McCarthy *et al.*, 2011; see Figure 1.5).

1.4.1 Existing depositional model for the Nyl/Mogalakwena River floodplain

The existing model for deposition along the Nyl/Mogalakwena River was proposed by McCarthy *et al.* (2011). They found that the gradient change in the longitudinal stream profile was not bedrock-controlled as it occurred in an alluvial reach of the river, and yet the bedrock underlying the floodplain alluvium appears to be conformable with the exposed bedrock further downstream in the Mogalakwena River. Based on the conformable bedrock and the general erosional nature of the local landscape, they concluded that the Nyl/Mogalakwena River was once a bedrock river but then the flow transport capacity was outpaced by the sediment supply, causing the change into an alluvial river.

Once the sediment supply from the tributaries exceeded the transport capacity of the Nyl/Mogalakwena River, which could have been brought about by a pronounced climate change in the area such as aridification, active sediment accumulation would have occurred (McCarthy *et al.*, 2011). Aridification would decrease vegetation cover, which in turn would allow periods of heavy rainfall to generate large amounts of sediment-laden runoff, resulting in fan formation and progradation at the trunk-tributary confluences. Furthermore, McCarthy *et al.* (2011) propose that the prograding tributary fans obstructed the rivers' axial flow resulting in the creation of accommodation space upstream and inducing sedimentation which resulted in the widening of the floodplain and the formation of wetlands. The presence of interfingering fan sediments with floodplain sediments (Figure 1.5) confirms that sedimentation and progradation of the tributary fans has not been continuous. Exposures in the deeply incised Rooisloot tributary fan reveal periods where the fans prograded into the Nyl/Mogalakwena River depositing coarse grained tributary-derived sediments interspersed with erosional periods and floodplain sedimentation of fine grained silts and muds.

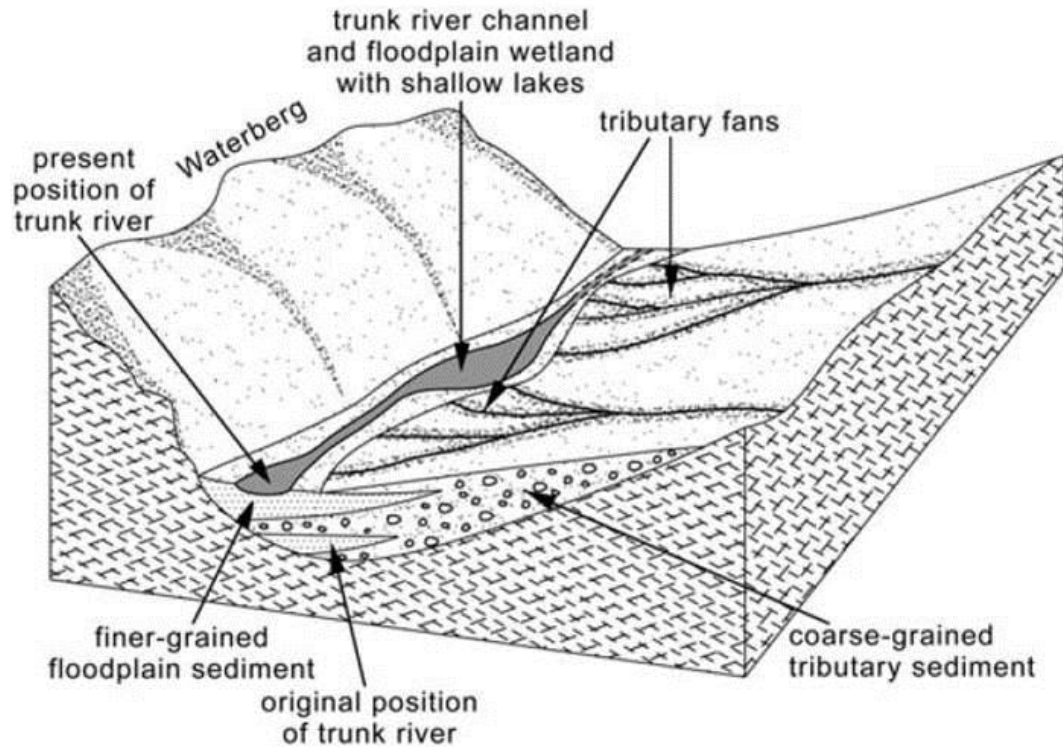


Figure 1.5: Schematic diagram illustrating the association of the tributary fans as they prograde onto the Nyl/Mogalakwena floodplain, thereby producing aggradation and forcing the Nyl/Mogalakwena River westwards toward the Waterberg (McCarthy *et al.*, 2011).

Typically, alluvial fans with thick depositional sequences are located along the edge of sedimentary basins and along faulted mountain fronts (Harvey, 2011). Numerous boreholes have been sunk in the general area of the Nyl/Mogalakwena River in an effort to obtain groundwater, and the characteristics of the sediments were described by Porszasz (1971, 1973, 1978). McCarthy *et al.* (2011) summarized the stratigraphy as weathered basalt overlain by up to 35 m of sediment and Tooth *et al.* (2002) described sediments consisting of basal gravelly sand fining upwards into fine sand, silt and clay near the floodplain surface. Complementary information is available from boreholes drilled along the Nyl/Mogalakwena River between the Rooisloot and Pholotsi confluences (see Figure 1.2b) and by natural exposures in the deeply incised Rooisloot tributary fan. The Rooisloot exposures sampled by McCarthy *et al.* (2011) represent two distinct sedimentary units; a lower red unit of gravelly, coarse sand cemented and

stained by hematite which lies unconformably on the mafic rocks of the Bushveld Complex and an upper yellow unit of unconsolidated coarse sand with cross-beds and laterally impersistent, intercalated gravel beds. The exposures sampled in this research project comprise the upper 4 m of the ~ 30 m thick sedimentary succession and therefore represent only the latest stage of Rooisloot deposition.

This research project aims to extend the work undertaken by Tooth *et al.* (2002) and McCarthy *et al.* (2011) on the Nyl/Mogalakwena River floodplain by analysing the stratigraphy and determining a detailed geochronology for the deposits exposed in head cuts at the confluence of the Nyl/Mogalakwena River and the Rooisloot. These data will be used to assess the validity of the depositional model for the floodplain as published by McCarthy *et al.* (2011). Several techniques will be used to achieve this goal, including detailed site descriptions, stratigraphic logging, grain size and distribution analysis and comprehensive optically stimulated luminescence (OSL) and radiocarbon dating.

1.5 Research Aim

The aim of this research project is to determine the validity of the existing depositional model for the Nyl/Mogalakwena River floodplain by producing a palaeo-environmental reconstruction for the Nyl/Mogalakwena River area. The reconstruction will be achieved through:

- 1) the completion of a detailed stratigraphic analysis of several sample sites representative of the tributary fan deposition environment;
- 2) the determination of a detailed geochronology of the Nyl/Mogalakwena River floodplain at the confluence of the Rooisloot with the Nyl/Mogalakwena River utilising OSL and radiocarbon dating techniques;
- 3) the examination of the evolution of the floodplain in terms of changing environmental conditions; and
- 4) the attempted correlation of the stratigraphy to recognized climatic events during the Quaternary.

This research project required the use of several techniques for the acquisition of data.

1.6 Overview of Research Techniques

A variety of techniques/methods were applied to create a clear picture of the present environment in order to produce a detailed palaeo-environmental reconstruction, including regional mapping using satellite imagery, detailed site descriptions, stratigraphic logging, grain size and sorting analyses, laser granulometry for fine-grained sediments and comprehensive dating using OSL dating in conjunction with radiocarbon dating, the latter being used as an independent age control.

In order to complete the *detailed site descriptions and stratigraphy* four profiles were selected for detailed analysis, two on the Nyl/Mogalakwena River (see Figure 2.3; Profiles A and B) representative of the floodplain depositional environment and two on the Rooisloot (see Figure 2.3; Profiles C and D) representative of the tributary fan depositional environment. Individual sedimentary layers were identified at each profile and described in terms of their colour, grain size, root traces, textures, contacts and reaction to a 10% solution of HCl as per the methodology of Retallack (2001). The detailed descriptions of each sedimentary layer in conjunction with the stratigraphic relationships were used to correlate the sample sites stratigraphically.

Every sedimentary layer identified at each of the four profiles was sampled for a detailed *grain size and sorting analysis*, whereby samples were dried in an oven and sieved to determine the spread of grain sizes of a representative sample. This method was not suitable for fine-grained samples; therefore these samples were prepared and submitted for *laser granulometry*, which utilises laser beam diffraction of grains suspended in a solution to determine the spread of grain sizes.

The *detailed geochronology* was completed using two separate techniques, OSL dating and radiocarbon dating. *Luminescence dating* utilises the emission of light from a natural material upon stimulation. When light is used to stimulate the material, the resultant luminescence signal, produced by the liberation of trapped radiation stored as electrons in defects in the crystal lattice structure known as *traps* (Duller, 2008a), is termed optically stimulated luminescence (OSL). Natural materials that act as

dosimeters, such as quartz and feldspar, record the amount of radiation they have been exposed to (mainly due to the radioactive decay of uranium (U), thorium (Th) and potassium (K) isotopes in the surrounding environment), thereby making them the best materials available for OSL dating.

Radiocarbon (^{14}C) is one of three carbon isotopes, and whilst ^{12}C and ^{13}C are stable, ^{14}C is unstable undergoing radioactive decay through beta-emission to form ^{14}N , with a half-life of 5730 years (Godwin, 1962; Walker, 2005). The half-life of ^{14}C determines the upper age limit obtainable through radiocarbon dating, as the limit of measurement is 8 half-lives which marks the upper age limit as $\sim 45\,000$ years (Walker, 2005). The *radiocarbon dating* method measures the residual ^{14}C remaining in a sample relative to a modern standard, either through beta-counting or accelerator mass spectrometry (AMS), the latter being the preferred method due to the smaller sample size required and faster and more efficient processing time.

In each profile, several layers were selected for sampling and geochronological determination by either OSL or radiocarbon dating, the former generally using sand-sized grains of fluvial origin and the latter using organic material incorporated in silt- and mud sized grains of floodplain origin.

1.7 Summary

Quaternary reconstructions are necessary to extend the palaeo-environmental record for the southern hemisphere to a comparative level with the northern hemisphere, which has been reconstructed in much greater detail. To this end, the Nyl/Mogalakwena River floodplain in Limpopo Province, located in one of the few basins in the interior of South Africa undergoing active sedimentation, was chosen for a reconstruction. It appears that the sedimentation and erosion cycles within the basin may be driven by climate change and thus may be linked to some of the notable climatic events that occurred during the Quaternary Period, such as the Medieval Warm Period and the Little Ice Age.

The geomorphic development of the Nyl/Mogalakwena River floodplain was outlined by McCarthy *et al.* (2011). They propose that tributary fans prograde into the Nyl/Mogalakwena River from the east thereby depositing thick, coarse-grained sedimentary layers and obstructing the axial flow of the river. This process creates sufficient accommodation space upstream for the widening of floodplains and the formation of wetlands to occur. Alternating periods of fan progradation and the deposition of sediments in shallow lakes, result in the interlayering of coarse-grained, fan sediments with fine-grained, floodplain sediments as observed in the incised river cuts within the Rooisloot tributary fan. Furthermore, sedimentation is not continuous and the depositional periods are interspersed with periods of erosion during which the fan is incised by channelized flow. This research aims to test the validity of this depositional model.

A variety of techniques were used in this research project, including detailed site descriptions, grain size analyses and stratigraphic correlations to interpret the sedimentary environments and infer the palaeo-environmental conditions. A detailed geochronology was completed using the OSL dating technique, with radiocarbon dating being chosen as an independent age control due to the reported compatibility of these two techniques (Rittenour, 2008; Murray and Olley, 2002).

1.8 Dissertation preview

Chapter 1 contains the project introduction and details regarding the location and physical characteristics of the Nyl/Mogalakwena River floodplain. The underlying geology, geomorphology and drainage are outlined in some detail and the analytical techniques covering the detailed stratigraphy, site descriptions, grain size analysis and geochronology used are included.

Chapter 2 contains a review of the depositional environment and the geological data accumulated for the sites, including a detailed stratigraphy and grain size analysis.

The geochronology is covered in Chapters 3 through 5 with an in-depth review of the OSL and radiocarbon dating techniques and the suitability of each technique to dating sediments from the Rooisloot and the Nyl/Mogalakwena River being provided in Chapter 3. OSL dating formed a significant part of this research project therefore a detailed discussion on the determination of the equivalent dose values is covered in Chapter 4. The dosimetry required for the technique using emission counting methods (thick source alpha counting, GM-beta counting and high-resolution gamma spectrometry) is included in Chapter 5.

The finalised OSL and ^{14}C dates for the Nyl/Mogalakwena River and Rooisloot sediments are presented at the beginning of Chapter 6. These are followed by a comparison of the collected data, considering the validity of the geochronology and relating the geological data to the geochronological data obtained from this research study. Finally, individual depositional events are associated with notable climatic events which occurred during the Quaternary.

Chapter 7 summarises the findings of this study and outlines possible future research directions.

Supplementary data is appended.

Chapter 2:

Geomorphology and Stratigraphy

2.1 Introduction

The Nyl/Mogalakwena River floodplain, located in the Limpopo Province, is an area of active sedimentation, believed to have formed due to back-ponding caused by the progradation of tributary fans across the Nyl/Mogalakwena River (McCarthy *et al.*, 2011). This chapter will focus on the fluvial sediments overlying the bedrock as discussed in Chapter 1.

2.2 Alluvial fans

Alluvial fans are depositional features commonly ascribed to arid- and semi-arid mountainous regions. However a more accurate description incorporates areas of high-relief where an abundant sediment supply is readily available; these conditions are commonly found at the base of mountain ranges in regions with sporadic and intense rainfall events (Blair and McPherson, 1994; De Chant *et al.*, 1999; Oguchi *et al.*, 2001; Boggs, 2006; Harvey, 2011). Deposition of alluvial fans is ascribed to the reduction of the flow velocity of the river due to the loss of confinement as the river exits a confined channel in a mountainous area and spreads out across a flat plain. All alluvial fans are characterised by common features, such as a steep depositional slope, a generally conical shape, concave upwards long profile, convex upwards cross profile and are typically composed of poorly sorted clastic sediments with a large proportion of gravel size particles (Blair and McPherson, 1994; Moreno and Romero-Segura, 1997; De Chant *et al.*, 1999; Boggs, 2006; Harvey, 2011).

2.2.1 Classification of alluvial fans

Alluvial fans can be classified based on their locational and topographic characteristics. The topographic classification scheme (Figure 2.1) is of particular relevance to the Nyl/Mogalakwena River floodplain. The simplest type of alluvial fans are mountain front fans fed by a single (Figure 2.1a) or multiple (Figure 2.1b) streams, with the latter case occurring commonly where fan sediments have backfilled into the mountain catchment (Harvey, 2011). Alternatively, at a tributary junction (Figure 2.1c) a fan may form where a steep confined tributary stream joins a

lower gradient main valley (Harvey, 2011). Alluvial fans can also be defined based on the dominant depositional processes at work on the fan, either debris-flow or stream-flow dominant (Blair and McPherson, 1994; Boggs, 2006). Debris-flow deposits are poorly sorted, lack sedimentary structures, are relatively impermeable due to their high proportion of muddy matrix, may contain boulders and typically have a steep surface with little vegetation (Blair and McPherson, 1994; Boggs, 2006). Alternatively, stream-flow deposits are characterized by sheetflood (a broad expanse of unconfined, sediment-laden runoff) and incised channel flow (runoff through channels that have been incised into the alluvial fan) (Blair and McPherson, 1994; Boggs, 2006). In light of the above classification systems the Rooisloot fan located on the Nyl/Mogalakwena River floodplain (Figure 2.2) can be best described as a tributary-junction fan (or tributary fan using the terminology of McCarthy *et al.* (2011)) possibly with multiple source streams and dominated by stream-flow depositional processes.

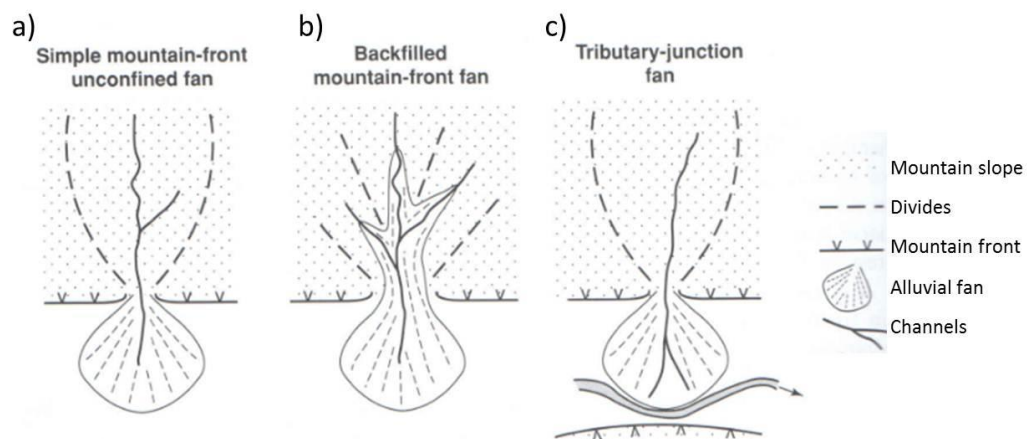


Figure 2.1: Basic alluvial fan morphology based on topographic relationships (Harvey, 2011).

2.2.2 Description of the tributary fans

A tributary fan complex is visible along the eastern bank of the Nyl/Mogalakwena River (Figure 2.2 and orthophoto 2428BB 14 in end packet), deposited by tributaries arising in the eastern catchment. The Dorpsrivier fan is immediately upstream (south) and the Pholotsi fan downstream (north) of the Rooisloot fan. The tributaries are well-defined channels that bifurcate into distinct distributary channels which terminate in tributary fans along the east bank of the Nyl/Mogalakwena River. Three

distributaries can be identified in the Rooisloot tributary fan; the abandoned channel in the north, the central channel which has been heavily mined for sand and the current channel in the south (labelled x, y and z respectively, Figure 2.2 and orthophoto 2428BB 14). The sampling sites are located along the central (y) distributary channel (Figure 2.3).

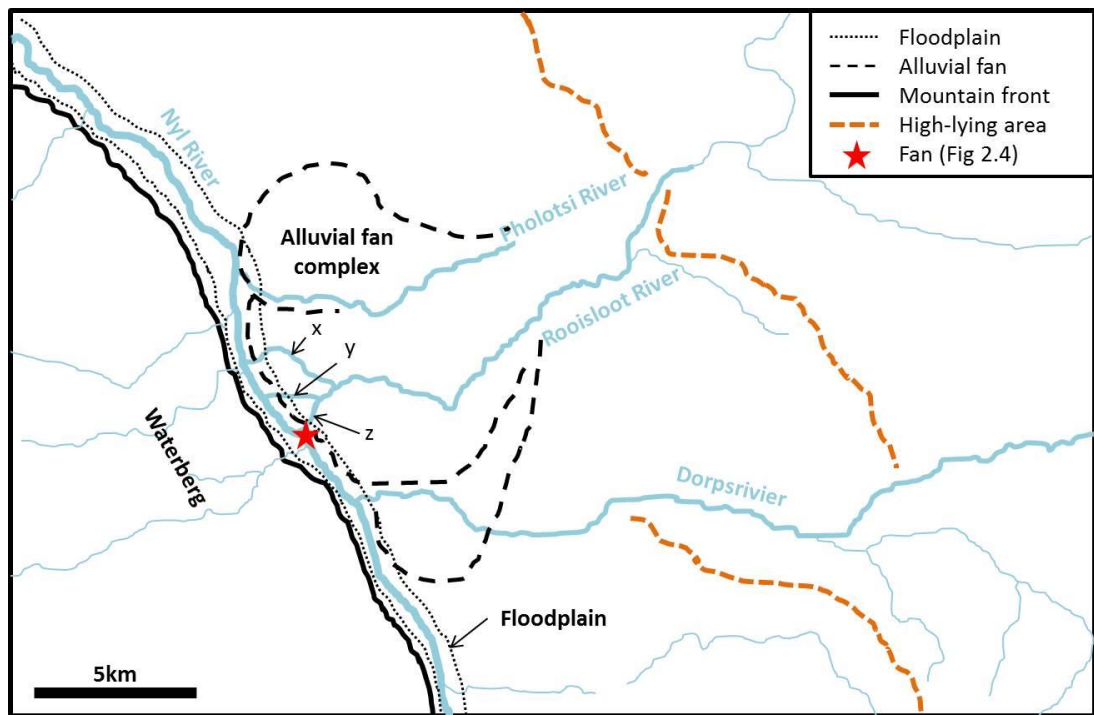


Figure 2.2: Map of the geomorphological features of the tributary fan located at the confluence of the Nyl/Mogalakwena River with the Rooisloot. Three distributaries (x, y and z) are identifiable within the Rooisloot tributary fan.

Several tributary fans have prograded into the Nyl/Mogalakwena River and extend across the river to the opposite (western) bank, such as the fans formed by the Dorpsrivier tributary and the abandoned (x) Rooisloot distributary (see orthophoto 2428BB 14 in end packet). The progradation of these tributary fans has restricted flow in the Nyl/Mogalakwena River and resulted in the formation of shallow lakes. This process can be seen on a smaller scale at the termination of the current distributary of the Rooisloot (Figure 2.4). Here a single channel bifurcates into several distributaries that are actively prograding into the trunk river. A fan lobe has formed at the current distributary (labelled “z”, Figure 2.2) and has extended into the river within the last decade. Eventually this fan lobe will prograde across the

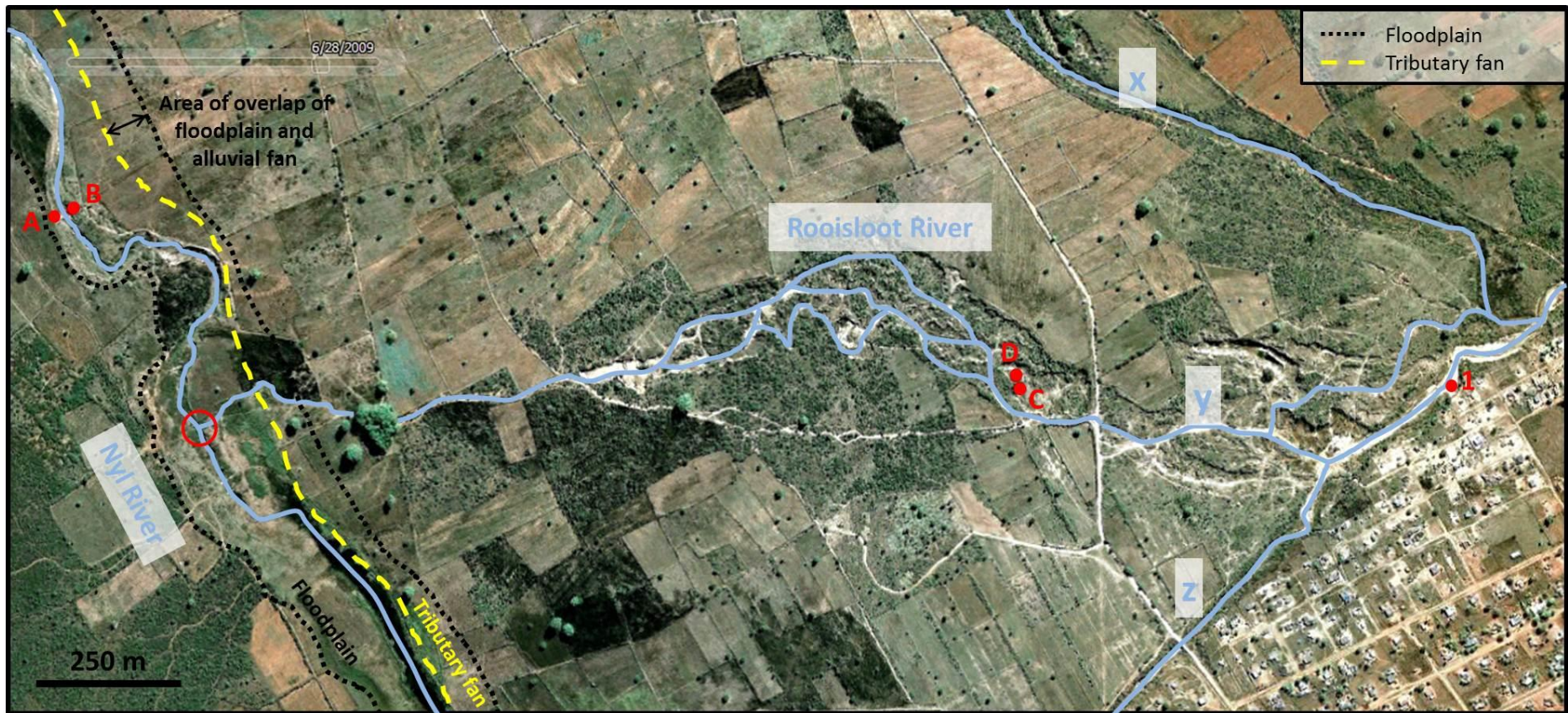


Figure 2.3: Google Earth image of a section of the Rooisloot tributary fan illustrating the sample locations; Profiles A and B are located along the Nyl/Mogalakwena River downstream of the confluence (red circle) with the Rooisloot, whilst Profiles C and D are located within the tributary fan deposit along the Rooisloot. The location marked “1” represents the sample site of independent work undertaken by McCarthy *et al.* (2011). The letters (x, y and z) denote the three distributaries of the Rooisloot.



Figure 2.4: The actively prograding section of the Rooisloot tributary fan. The fan is located along the current distributary (see “z” on Figure 2.2 and orthophoto 2428BB 14 in end packet) and has formed over the last decade. All three images show the same area with the same scale.

Nyl/Mogalakwena River, further restricting the flow within the trunk river and creating more accommodation space upstream.

There is a marked difference in the gradient on either side of the Nyl/Mogalakwena River. The Waterberg is located to the west and a steep gradient is apparent. Alternatively, to the east of the river the gentle gradient of the Rooisloot fan surface is observable (see orthophoto 2428BB 14). The fan surface has been incised by channelised flow, which has exposed the sedimentary package in vertical faces. The faces display horizontal layering of sediments with varying colours, grain sizes and textures, in particular thin, black, fine-grained layers interlayered with thick, brown-orange, sandy layers are observable (Figure 2.5).

2.3 Geomorphological Investigation - Methods and Techniques

2.3.1 Sampling Strategy

Four sites within the area of the confluence of the Nyl/Mogalakwena River with the Rooisloot (Figure 2.3) were sampled for this research project. Faces were chosen along the incised river banks and samples collected from the centre of each horizontal layer within each vertical profile (see Figure 2.5). Two profiles (referred to as Profiles A and B) located ~34 m apart on opposite banks of the Nyl/Mogalakwena River are representative of the floodplain environment, and two profiles (referred to as Profiles C and D) located ~ 20 m apart within the Rooisloot-incised tributary fan are representative of the fan environment.

2.3.2 Profile Stratigraphy

A detailed stratigraphy was recorded in the field by measuring the thickness of each layer and the contacts between each layer and describing the sediments following the methodology of Retallack (2001) which considers grain size, grain roundness, colour, contacts, thickness and reaction to a 10 % solution of hydrochloric acid (HCl). Colour was recorded using a Munsell colour chart and roundness was examined using a hand-lens and ranked according to Powers (1953) grain roundness and sphericity chart (Figure 2.6).

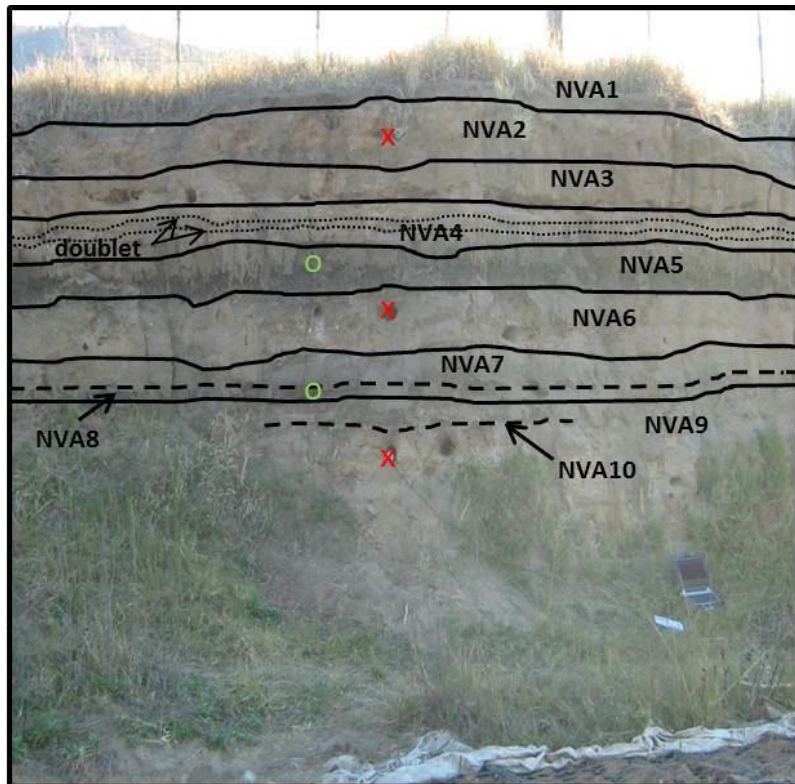


Figure 2.5: a) Annotated photographs of the individual sample locations. Profiles A and B (NVA and NVB respectively) are located along the banks of the Nyl/Mogalakwena River. The “doublet” refers to two parallel, very thin black horizons located within a single horizontal layer and is significant only in terms of the stratigraphic correlation. Crosses mark the location of the OSL sample collection points and circles the ¹⁴C sample collection points.

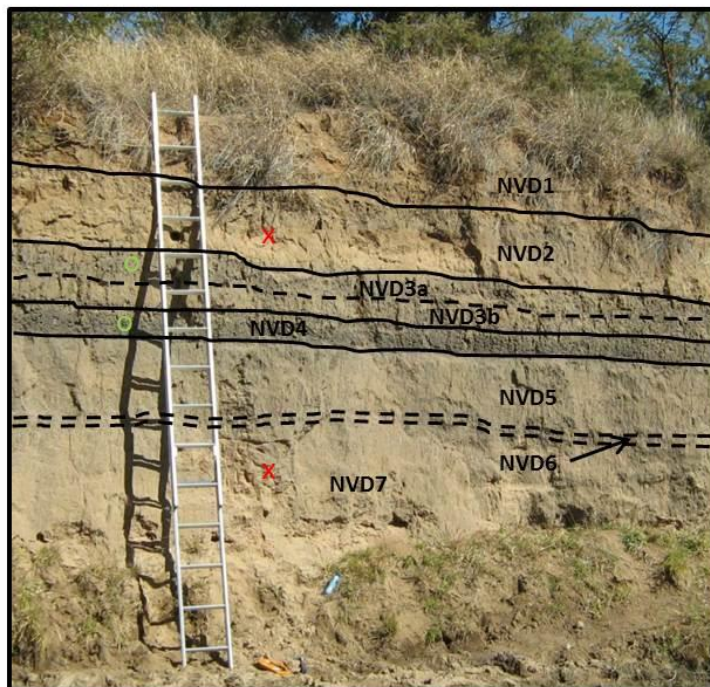
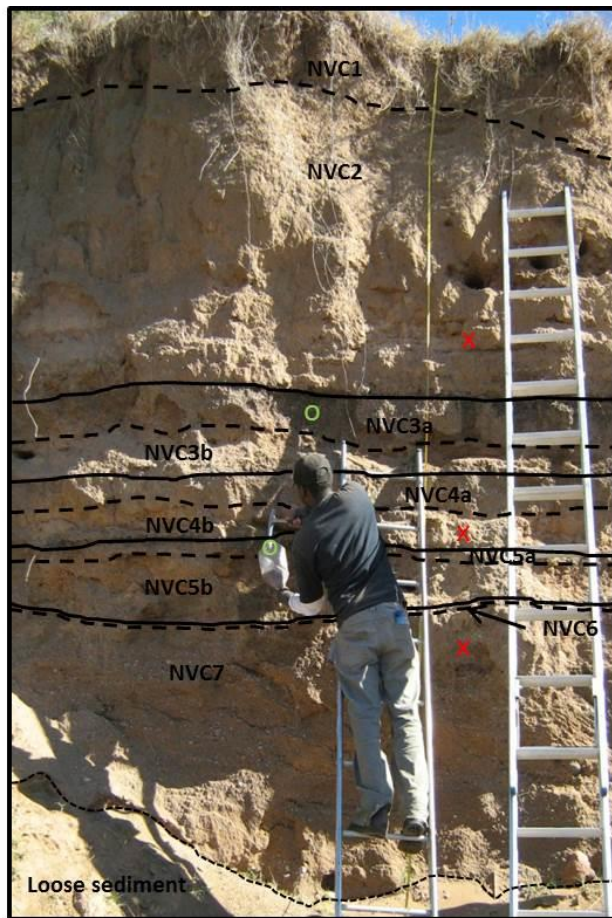


Figure 2.5: b) Annotated photographs of the individual sample locations. Profiles C and D (NVC and NVD respectively) are located within a tributary fan environment along the Roosiloot. Crosses mark the location of the OSL sample collection points and circles the ^{14}C sample collection points.

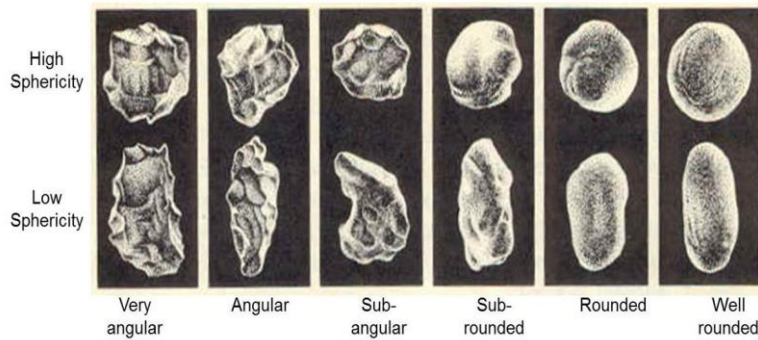


Figure 2.6: Grain roundness classification (modified after Sand Forum International, 2009) originally determined by Powers (1953).

2.3.3 Grain Size and Sorting Analysis

Grain size is a fundamental property of sediment particles which affects their entrainment, transport and deposition and therefore provides information on sediment provenance, transport history and depositional conditions. The statistical analysis of data obtained from grain size analysis will be used to comment on the transport time and depositional conditions. Several techniques are available for the determination of a sample's grain size distribution and all involve dividing the sample into size fractions and constructing the distribution based on the weight or volume percentage of sediment in each fraction (Blott and Pye, 2001). A total of 39 samples were collected from the four profiles for grain size analysis.

A sample was collected from the centre of each horizontal layer present in the four selected profiles and a quantitative analysis of the sediment grain size and sorting was completed in the Sedimentology Laboratory at the University of the Witwatersrand. The preferred method for the grain size analysis was the measurement of dry-sieved sediments, which required approximately 200 g of the sampled sediment from each layer to be dried in the oven and then sieved on the mechanical shaker for 15 min. A set of thirteen sieves (4000, 2800, 2000, 1400, 1000, 710, 500, 355, 250, 180, 125, 90 and 63 μm mesh sizes) was used. All organic material was removed from the samples prior to sieving and the sample retained in each sieve was weighed and the results plotted as cumulative frequency distributions (see Figure 2.8) in preparation for a statistical analysis. However, eight samples proved to be fine-grained and could not be dried in the oven without severe clumping

which made dry sieving impossible. As an alternative, these samples were submitted for laser granulometry.

Analysis of the fine-grained samples on the laser granulometer was completed at the Chemical Engineering department at the University of the Witwatersrand. Approximately 10 g of sample was mixed with 125 ml of potassium pyrophosphate ($K_4P_2O_7$) solution which acts as a deflocculant, preventing the clay minerals from adhering to one another in solution. The solution was analysed and produced graph results indicating the grain size distribution for particle sizes between $0.01\mu m$ and $2000\mu m$. The results from the two techniques, dry-sieving and laser granulometry, cannot be combined because it is difficult to merge data obtained from different analysis methods (Blott and Pye, 2001). Therefore the datasets must be examined separately but not independently of one another. The graph results for the individual layers as analysed by dry-sieving and laser granulometry are appended as supplementary data in Appendix A and B respectively.

2.3.4 GRADISTAT Calculations

The sieved size fractions were used to plot cumulative frequency distribution curves for each sample in order to determine the dominant grain size and the sorting of the sediments. Several statistical values can be calculated to examine the grain size distribution of sediments, namely the mean, mode, median, standard deviation, skewness and kurtosis. The *mean* value represents the average of all grain sizes present, *mode* the most frequently occurring particle size, *median* the midpoint of the grain distribution by weight, standard deviation determines the spread or *sorting* of the grain sizes about the average (Table 2.1), *skewness* describes the symmetry or preferential spread to one side of the average value (Table 2.1) and *kurtosis* the degree of concentration of the grains relative to the average value (Table 2.1) (Folk, 1980; Blott and Pye, 2001; Boggs, 2006; Nichols, 2009). Statistical analysis of the grain size data from the two techniques, dry sieving and laser granulometry, was completed using GRADISTAT (Blott, 2010), a computer program written for the rapid analysis of grain size statistics.

GRADISTAT calculated the statistics using the mathematical method of moments approach and then extracted values from the cumulative frequency curve using linear interpolation to determine the statistics using the graphical Folk and Ward (1957) approach; for the equations used and a full description of the GRADISTAT programme see Blott and Pye (2001). The Folk and Ward statistics are reported logarithmically, as a log-normal distribution of ϕ sizes and geometrically, as a log-normal distribution of metric sizes. Furthermore, each sample is given a descriptive term based on a modified Udden-Wentworth grade scale. Blott and Pye (2001) recommend reporting results from the Folk and Ward graphical method as this method more accurately describes the general characteristics of the bulk sample. Therefore all statistical values quoted in this thesis are calculated using the Folk and Ward approach and are reported geometrically in μm as this is the standard unit used for all data throughout this research study.

Table 2.1: Scales for sorting, skewness and kurtosis as calculated by GRADISTAT using the Folk and Ward (1957) graphical measures (Blott and Pye, 2001).

Sorting (σ_G)		Skewness (Sk_G)		Kurtosis (K_G)	
Very well sorted	<1.27	Very fine skewed	-0.3 to -1.0	Very platykurtic	<0.67
Well sorted	1.27–1.41	Fine skewed	-0.1 to -0.3	Platykurtic	0.67–0.90
Moderately well sorted	1.41–1.62	Symmetrical	-0.1 to +0.1	Mesokurtic	0.90–1.11
Moderately sorted	1.62–2.00	Coarse skewed	+0.1 to +0.3	Leptokurtic	1.11–1.50
Poorly sorted	2.00–4.00	Very coarse skewed	+0.3 to +1.0	Very leptokurtic	1.50–3.00
Very poorly sorted	4.00–16.00			Extremely leptokurtic	>3.00
Extremely poorly sorted	>16.00				

When calculating the statistics using the Folk and Ward method, errors become significant if > 5 % of the sample is undetermined and Blott and Pye (2001) recommend excluding the fraction remaining in the pan if it comprises > 1 % of the sample. Based on this recommendation and due to the fact that the majority of samples had > 1 % of the total sample remaining in the pan *i.e.* all grains smaller than 63 μm , the < 63 μm fraction was excluded from all statistical calculations for dry sieved samples. It would be preferable to analyse the excluded pan fraction separately using another method such as laser granulometry, however it is difficult to merge data from different methods. Therefore, all samples perceived to be fine-grained during the sieving process *i.e.* sediments with a majority of fine-grained particles that contained no grains larger than 2000 μm and which clumped while drying, were analysed using laser granulometry instead of the dry sieving method.

2.4 Geomorphological Investigation - Results

2.4.1 Stratigraphic Comparison of the Profiles across the Tributary Fan

A detailed stratigraphy of the profiles was recorded in the field (Figure 2.5) as described in section 2.3.2 and stratigraphic correlations were inferred (Figure 2.7) based on the sedimentary characteristics of each horizontal layer. The close spatial association of Profiles A and B lead to a fairly consistent correlation across the banks of the Nyl/Mogalakwena River and the presence of a doublet (two parallel, thin black horizons within a single layer) located in layers NVA4 and NVB9 provided confidence in the correlation. Alternatively, Profiles C and D which were originally believed to be separate profiles of a non-continuous section could not be correlated stratigraphically based solely on their sedimentary characteristics. Therefore, due to the sedimentological differences (in terms of colour, grain size, description and relative stratigraphy) and the lack of any definite correlation between layers, it can be assumed that the two profiles represent two separate depositional events.

The stratigraphy of the four profiles was similar to those described by McCarthy *et al.* (2011) with several meters of sediment exposed by the incision of the Rooisloot into the tributary fan. The incision has exposed layers of fine-grain, dark sediments interlayered with coarse-grained, brownish sediments, assumed to be floodplain and tributary fan deposits respectively. The fine-grain, dark sediments are considered to be organic-rich because of their black colour (which is due to the humic content) and a carbon content of over 5 % (determined at Lund University).

A detailed description of the sediments (Table 2.2) was recorded following the methodology of Retallack (2001) and several features were observed. First, the colour of the sedimentary layers in Profiles A and B corresponds loosely to the grain size of the layer; the dark, blackish coloured layers are generally composed of fine-grained sedimentary particles and are organic-rich while the brownish – orange coloured layers contain coarser-grained particles. However several brown layers were also fine-grained. The colour-grain size relationship does not hold for Profiles C and D where the black layers, while organic-rich, are coarse-grained. Furthermore, the dark, blackish layers (across all four profiles) display ped structures. Generally the ped structures in layers from Profiles C and D are better

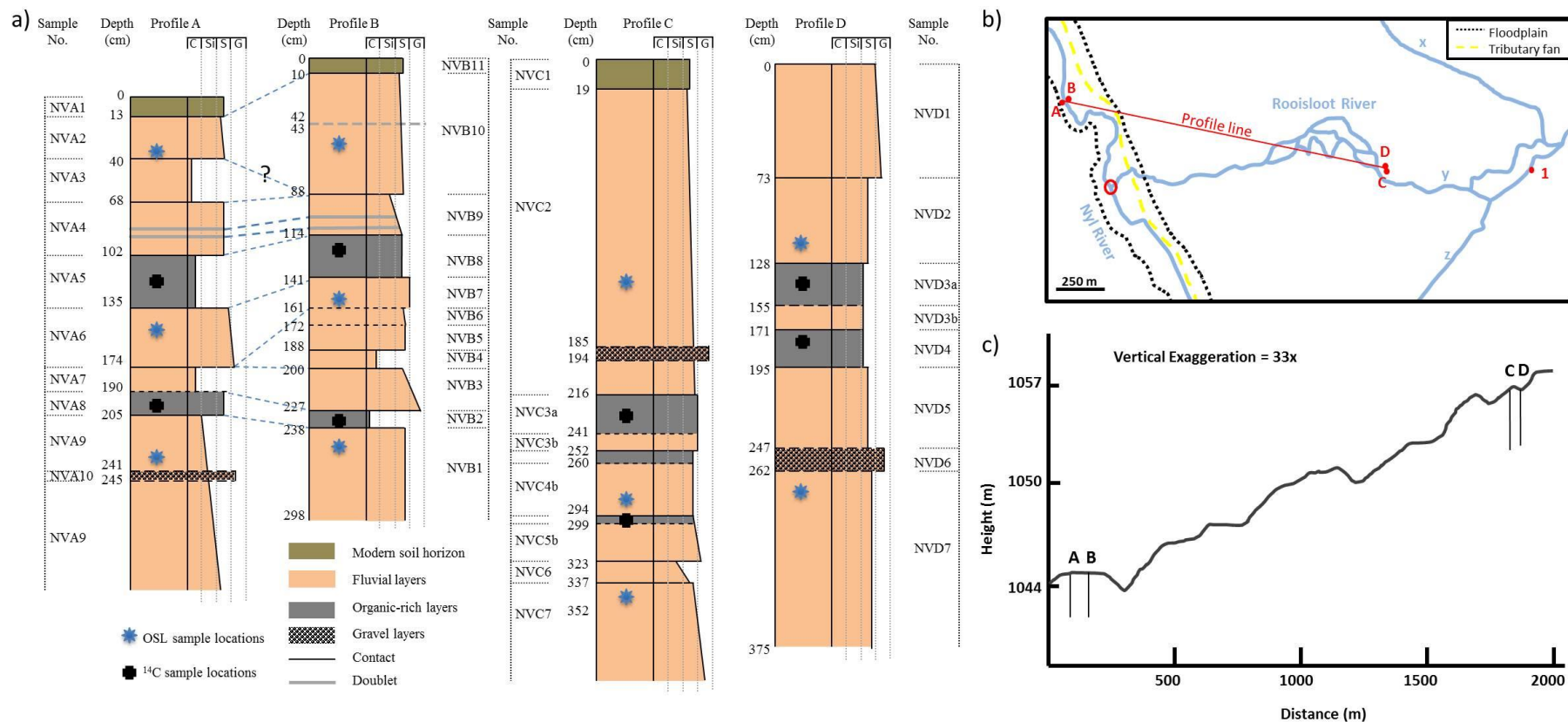


Figure 2.7: (a) Stratigraphic correlation between the Nyl/Mogalakwena River and Rooisloot profiles based on field descriptions. The doublet in layers NVA4 and NVB9 is depicted by thick grey solid lines. The four Profiles represent three depositional phases, one for Profile A-B, one for Profile C and one for Profile D. Depth from the surface is shown in cm. (b) Schematic representation of the Nyl River floodplain showing the profile line for the surface profile illustrated in (c). (c) Surface profile of the Rooisloot tributary fan showing the location of the sampled profiles in relation to one another; the vertical lines labelled A to D show the extent of the incised profiles.

Table 2.2(a): Detailed stratigraphy recorded in the field for Profile A along the banks of the Nyl/Mogalakwena River. Samples were collected for grain size (GS), optically stimulated luminescence dating (OSL) and radiocarbon dating (C14).

Sample	Grain size	Colour Reference	Colour	Contacts		Thickness (cm)	Reaction to HCl	Grain roundness	Descriptions	Samples collected
				Upper	Lower					
NVA1	medium sand	5YR2.5/1	brownish black	-	sharp	13	none	subrounded to rounded	black turf, organics and root traces	GS
NVA2	fine-medium sand	10R3/4	dark reddish brown	sharp	sharp	27	none	subangular to subrounded	orange-brown colour, unconsolidated, numerous roots	GS, OSL
NVA3	fine-medium silt	5YR3/3	moderate brown	sharp	sharp	28	none	rounded	Grey (orangey) brown, numerous roots, harder/more consolidated, has ped structure/clumps	GS
NVA4	fine sand	10YR4/6	dark yellowish orange	sharp	sharp	34	none	rounded	pale colour, fine root traces, contains dark black doublet (thin parallel lines within layer), planar bedding	GS
NVA5	coarse silt to fine sand	5YR3/2	grayish brown	sharp	sharp	33	none	subrounded to rounded	black colour, organic rich, easily weathered, approx. columnar peds, possibly a vertisol, remnant roots visible at the base of the layer	GS, C14
NVA6	coarse sand to gravel	10R4/3	grayish brown	sharp	sharp	39	none	subrounded	yellow brown colour, planar bedding	GS, OSL
NVA7	coarse silt	5YR3/3	moderate brown	sharp	gradational	24	none	subrounded	grey-brown colour, orange root oxidation (Fe-oxide)	GS
NVA8	fine sand	7.5YR3/2	dark brown	gradational	sharp	15	none	subangular to subrounded	black colour	GS, C14
NVA9	fine sand to silt	5YR3/3	moderate brown	sharp	-	36	none	well rounded	very wet sample (looks like wet building sand), orange root oxidation	GS, OSL
NVA10	gravel	-	-	sharp	sharp	4	none	-	possible lens or depositional event, layer is located within NVA9	GS

Table 2.2(b): Detailed stratigraphy recorded in the field for Profile B along the banks of the Nyl/Mogalakwena River. Samples were collected for grain size (GS), optically stimulated luminescence dating (OSL) and radiocarbon dating (C14).

Sample	Grain size	Colour Reference	Colour	Contacts		Thickness (cm)	Rxn to HCl	Grain roundness	Descriptions	Samples collected
				Upper	Lower					
NVB11	medium sand	5YR2.5/1	brownish black	-	sharp	10	none	subrounded to rounded	black turf, organics and root traces	GS
NVB10	fine to medium sand	10R3/4	dark reddish brown	sharp	sharp	78	none	subrounded	orange-brown colour, hosts pebble lag ~1cm (clasts 2mm - 3cm), clasts quartz and feldspar, homogenous layer	GS, OSL
NVB9	very fine sand to silt, Δ	10YR4/6	dark yellowish orange	sharp	sharp	26	none	subrounded to rounded	light orange-brown, termites, contains black doublet (corresponds to NVA4), planar bedding	GS
NVB8	fine to coarse silt	5YR3/2	grayish brown	sharp	sharp	27	none	subrounded to rounded	black colour, hard layer (well consolidated), peds and clumps (possibly a vertisol), bioturbated (termite nests), remnant roots at base of layer	GS, C14
NVB7	very coarse sand	10R4/3	grayish red	sharp	gradational	20	none	subrounded	brown colour, very wet sample, planar bedding	GS, OSL
NVB6	medium to coarse sand	5R4/2	weak red	gradational	gradational	11	none	subangular to subrounded	brown colour, very wet sample, same as NVA9 but coarser	GS
NVB5	coarse sand	10R6/2	pale red	gradational	sharp	16	none	subangular	light brown with pinkish hue	GS
NVB4	fine to coarse silt	10R6/2	pale red	sharp	sharp	12	none	subrounded	white-orange colour, clayish texture, lots of oxidised root traces	GS
NVB3	coarse sand to gravel	5YR3/3	moderate brown	sharp	sharp	27	none	subrounded	grey-brown colour, small pebbles, few root traces, little Fe oxide	GS
NVB2	medium silt	Grayish Black	grayish black	sharp	sharp	11	none	subangular to subrounded	black colour, organic rich, red oxide roots, bioturbation (spiders)	GS, C14
NVB1	coarse sand to gravel	7.5YR3/2	dark brown	sharp	-	60	none	subangular to subrounded	brown colour, root traces, orange oxidised roots	GS, OSL

Table 2.2(c): Detailed stratigraphy recorded in the field for Profile C located within the Rooisloot tributary fan. Samples were collected for grain size (GS), optically stimulated luminescence dating (OSL) and radiocarbon dating (C14).

Sample	Grain size	Colour Reference	Colour	Contacts		Thickness (cm)	Rxn to HCl	Grain roundness	Descriptions	Samples collected
				Upper	Lower					
NVC1	medium to coarse sand	5YR3/3	moderate brown	-	gradational	19	none	subangular	large amount of roots and dry grass, moderately sorted, pale brown colour	GS
NVC2	fine to medium sand	10YR5/8	yellowish brown	gradational	sharp	197	none	subrounded	light brown colour, linear clast layers @ 105cm & 190cm, clasts ~2-15mm, planar bedding	GS, OSL
NVC2 gravel	gravel	10YR4/6	dark yellowish orange	gradational	gradational	9	none	subrounded	clasts generally < 2cm	GS
NVC3(a)	very coarse sand & gravel	5YR3/3	moderate brown	sharp	gradational	25	none	subrounded	top 1cm has ped structure, black colour grades down into dark brown, grain size decreases slightly in NVC3(b), poorly sorted	GS, C14
NVC3(b)	very coarse sand	10YR5/8	yellowish brown	gradational	sharp	11	none	subrounded	grains smaller than NVC3(a), well sorted, dark brown colour	GS
NVC4(a)	medium sand grading down to gravel	5YR3/3	moderate brown	sharp	gradational	8	none	subrounded	consolidated, weak ped structure, black colour grades down into dark brown, numerous clods, fining upwards	GS, OSL
NVC4(b)	very coarse sand	10YR5/8	yellowish brown	gradational	sharp	34	none	subrounded	well sorted, dark brown colour very similar to NVC3(b)	GS
NVC5(a)	very coarse sand & gravel	5YR3/3	moderate brown	sharp	gradational	5	none	subrounded	poorly sorted, same as NVC3(a) but with larger clasts and more clods	GS, C14
NVC5(b)	very coarse sand	5YR4/6	strong brown	gradational	sharp	24	none	subrounded	looks the same as NVC3(b) & 4(b) except grains slightly bigger	GS
NVC6	medium sand to silt	10YR4/6	dark yellowish orange	sharp	gradational	14	none	subrounded	numerous clods	GS
NVC7	very coarse sand to gravel	5YR4/6	strong brown	gradational	-	>50	none	subangular to subrounded	basal unit, fluvial deposit, horizontal laminations, sudden dip of 45° @ 352cm (possible basement control), clasts < 1.5cm	GS, OSL

Table 2.2(d): Detailed stratigraphy recorded in the field for Profile D located within the Rooisloot tributary fan. Samples were collected for grain size (GS), optically stimulated luminescence dating (OSL) and radiocarbon dating (C14).

Sample	Grain size	Colour Reference	Colour	Contacts		Thickness (cm)	Rxn to HCl	Grain roundness	Descriptions	Samples collected
				Upper	Lower					
NVD1	very coarse sand to gravel	5YR4/6	strong brown	-	sharp	73	none	subangular	orange colour, weathered modern horizon	GS
NVD2	medium sand	10YR4/6	dark yellowish orange	sharp	sharp	55	none	subangular to subrounded	brown colour, some gravel clasts distributed thruout layer	GS, OSL
NVD3(a)	fine sand	5YR3/2	yellowish brown	sharp	gradational	27	none	subrounded	black colour grades down into light brown, some oxidised roots in 3(a), no gravel, ped structure throughout	GS, C14
NVD3(b)	fine sand	10YR5/8	grayish brown	gradational	sharp	16	none	subrounded	light brown colour, ped structure, no gravel	GS
NVD4	fine sand	5YR3/2	grayish brown	sharp	sharp	24	none	subrounded to rounded	black colour, ped sturcture	GS, C14
NVD5	fine to medium sand	5YR3/2	grayish brown	sharp	sharp	52	none	subangular	looks like wet river sand, some gravel	GS
NVD6	gravel layer	10R4/3	grayish red	sharp	sharp	15	none	subrounded	gravel layer, possibly a lens or representative of a depositional event	GS
NVD7	very coarse sand	10YR4/6	dark yellowish orange	sharp	-	>113	none	subangular	fining downwards, very little gravel, clods present, poor to moderate sorting	GS, OSL

defined than those from Profiles A and B. Second, each of the layers sampled showed no reaction to HCl in the field therefore it can be concluded that there is very little or no carbonate material present within the samples. This was confirmed during the preparation of the OSL samples as they did not react to HCl in the lab after being submerged for several days. Third, while the majority of the coarse-grained layers appear homogenous some of the layers showed evidence of planar- or cross bedding (see Table 2.2).

2.4.2 Statistical Analysis of Grain Size Data

Grain size data was plotted using cumulative frequency curves as a graphical representation of the grain size distribution obtained from dry sieving (Figure 2.8) and laser granulometry (Figure 2.9). The distribution of grain sizes obtained from laser granulometry shows two distinctly different types of curve, the first represented by the group of plots with a high percentage of silt sized grains (smaller than 63 μm) and the second by the smoother (yellow) curve with a large proportion of sand sized grains (63 – 2000 μm). Although the plot for NVA8 (yellow curve, Figure 2.9) is distinctly different from the other plots obtained using laser granulometry, it is similar to the plots obtained by dry-sieving. Plots of the individual grain size distributions for dry sieving and laser granulometry are included in Appendix A and B respectively.

The grain size data from both the dry sieving and laser granulometry techniques was analysed in GRADISTAT to produce statistical values for the mean, median, mode, standard deviation, skewness and kurtosis (Table 2.3). The majority of samples are poorly *sorted* irrespective of the depositional environment. In total 11 % of the samples are very poorly sorted, 74 % poorly sorted, 13 % moderately sorted and 2 % well sorted. The majority of the moderately sorted samples are located within Profile C and have mean particle sizes of very coarse sand to gravel.

The *mean* particle size is most commonly within the range of very coarse to medium sand with 73 % of all samples falling within this range. Seven samples (19% of total samples) collected from Profiles A and B have a mean particle size within the silt range of 3.9 μm to 63 μm . These seven samples correspond to the fine-grained samples analysed by laser granulometry. However, one sample analysed by laser

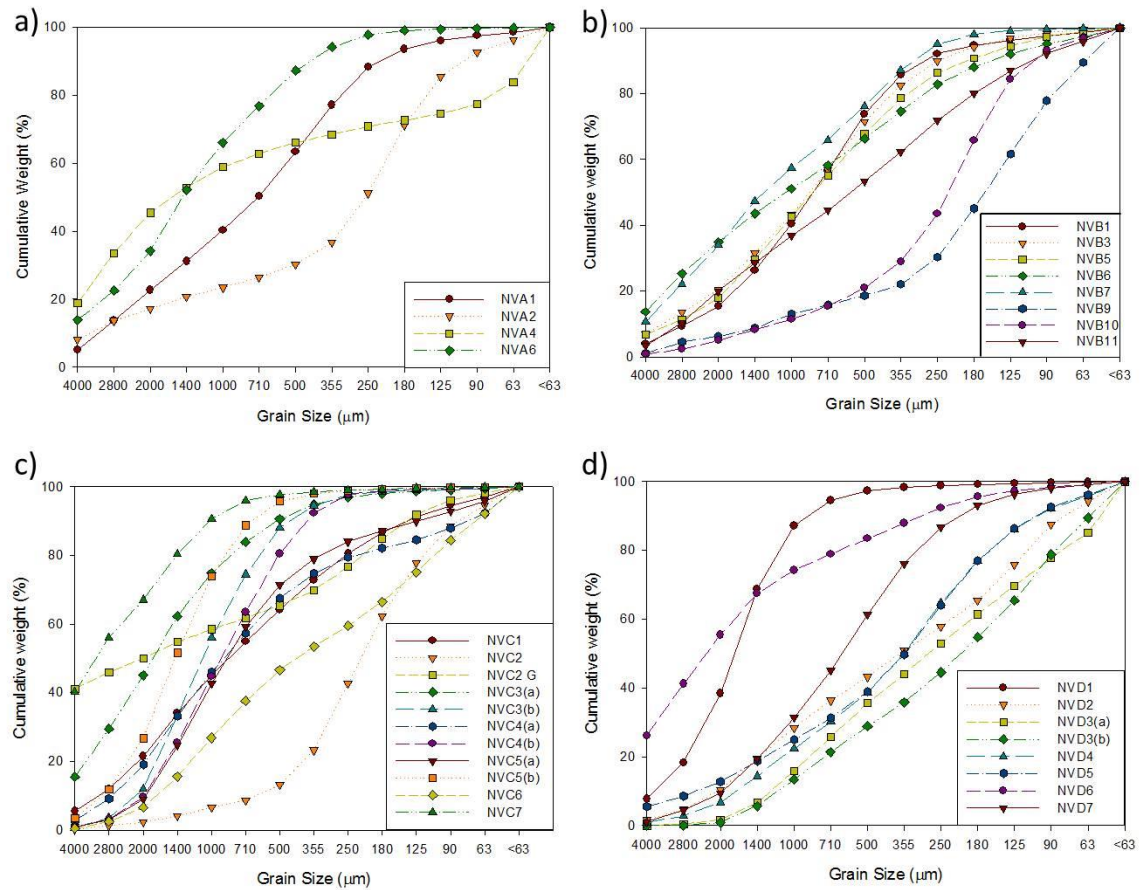


Figure 2.8: Cumulative frequency curves for each horizontal layer sampled and dry-sieved for (a) Profile A, (b) Profile B, (c) Profile C and (d) Profile D.

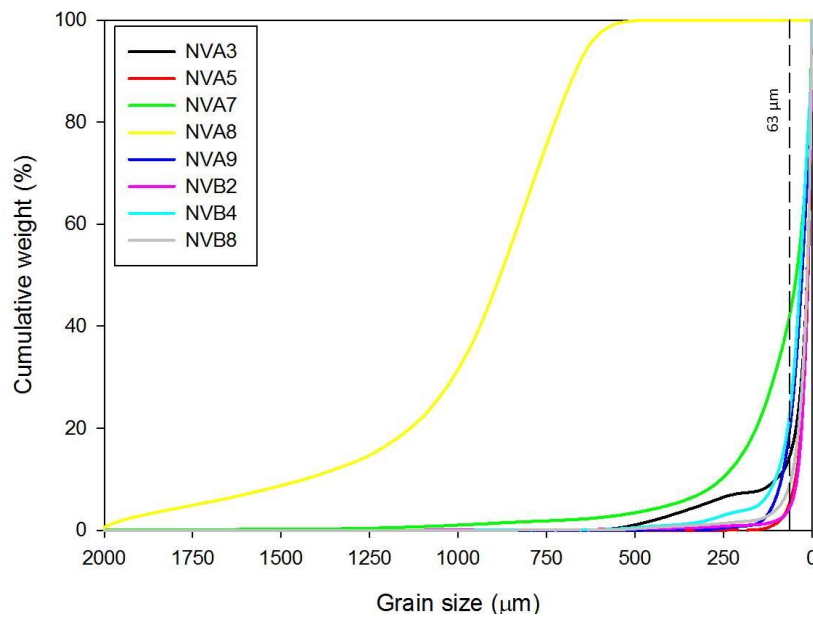


Figure 2.9: Cumulative frequency curves for each horizontal layer sampled and analysed using laser granulometry for Profile A and Profile B. According to the Udden-Wentworth Scale grains between 63 μm and 2000 μm are classified as sand and grains smaller than 63 μm as silt.

Table 2.3: GRADISTAT statistical data for the floodplain depositional environment (Profile A and B)

Sample	Geometric (μm)					Description					Deposit type
	Median (D_{50})	Mean (M_G)	Sorting (σ_G)	Skewness (Sk_G)	Kurtosis (K_G)	Mode	Mean (M)	Sorting (σ)	Skewness (Sk)	Kurtosis (K)	
NVA1	734	827	2.753	0.128	0.815	Bimodal	coarse sand	poorly	coarse skewed	platykurtic	fan
NVA2	269	447	3.644	0.502	0.95	Bimodal	medium sand	poorly	very coarse skewed	mesokurtic	fan
NVA3	14	13	5.822	-0.062	1.316	Polymodal	medium silt	very poorly	symmetrical	leptokurtic	floodplain
NVA4	2205	1366	3.813	-0.550	1.016	Bimodal	very coarse sand	poorly	very fine skewed	mesokurtic	fan
NVA5	11	10	3.267	-0.051	0.857	Bimodal	medium silt	poorly	symmetrical	platykurtic	floodplain
NVA6	1462	1442	2.411	-0.060	0.896	Bimodal	very coarse sand	poorly	symmetrical	platykurtic	fan
NVA7	44	36	5.574	-0.189	0.979	Polymodal	very coarse silt	very poorly	fine skewed	mesokurtic	floodplain
NVA8	882	911	1.341	0.252	1.172	Bimodal	coarse sand	well	course skewed	leptokurtic	fan
NVA9	28	21	3.887	-0.361	1.052	Bimodal	coarse silt	poorly	very fine skewed	mesokurtic	fan
NVB1	830	858	2.325	0.053	1.092	Unimodal	coarse sand	poorly	symmetrical	mesokurtic	fan
NVB2	12	10	3.742	-0.267	1.032	Bimodal	medium silt	poorly	fine skewed	mesokurtic	floodplain
NVB3	847	893	2.690	0.048	0.99	Bimodal	coarse sand	poorly	symmetrical	mesokurtic	fan
NVB4	33	25	4.312	-0.379	1.494	Bimodal	coarse silt	very poorly	very fine skewed	leptokurtic	floodplain
NVB5	828	812	2.831	-0.039	1.04	Trimodal	coarse sand	poorly	symmetrical	mesokurtic	fan
NVB6	1118	1035	3.418	-0.142	0.753	Bimodal	very coarse sand	poorly	fine skewed	platykurtic	fan
NVB7	1286	1197	2.674	-0.104	0.757	Bimodal	very coarse sand	poorly	fine skewed	platykurtic	fan
NVB8	13	12	3.532	-0.078	0.874	Trimodal	medium silt	poorly	symmetrical	platykurtic	floodplain
NVB9	181	245	3.009	0.454	1.318	Trimodal	fine sand	poorly	very coarse skewed	leptokurtic	fan
NVB10	232	279	2.418	0.370	1.238	Unimodal	medium sand	poorly	very coarse skewed	leptokurtic	fan
NVB11	621	635	3.329	0.004	0.782	Trimodal	coarse sand	poorly	symmetrical	platykurtic	fan

Table 2.3: GRADISTAT statistical data for the tributary fan depositional environment (Profile C and D)

Sample	Geometric (μm)					Description					Deposit type
	Median (D_{50})	Mean (M_G)	Sorting (σ_G)	Skewness (Sk_G)	Kurtosis (K_G)	Mode	Mean (M)	Sorting (σ)	Skewness (Sk)	Kurtosis (K)	
NVC1	889	805	3.093	-0.136	0.895	Unimodal	coarse sand	poorly	fine skewed	platykurtic	fan
NVC2	231	234	2.129	0.139	1.277	Unimodal	fine sand	poorly	coarse skewed	leptokurtic	fan
NVC2 Gravel	2168	1286	4.004	-0.509	0.576	Bimodal	very coarse sand	very poorly	very fine skewed	platykurtic	fan
NVC3(a)	1817	1730	2.278	-0.155	0.945	Bimodal	very coarse sand	poorly	fine skewed	mesokurtic	fan
NVC3(b)	1097	1049	1.832	-0.119	0.999	Unimodal	very coarse sand	moderately	fine skewed	mesokurtic	fan
NVC4(a)	994	870	2.937	-0.245	1.102	Bimodal	coarse sand	poorly	fine skewed	mesokurtic	fan
NVC4(b)	911	896	1.927	-0.034	0.943	Unimodal	coarse sand	moderately	symmetrical	mesokurtic	fan
NVC5(a)	898	792	2.448	-0.282	1.204	Bimodal	coarse sand	poorly	fine skewed	leptokurtic	fan
NVC5(b)	1435	1427	1.802	-0.020	1.067	Unimodal	very coarse sand	moderately	symmetrical	mesokurtic	fan
NVC6	512	441	3.152	-0.141	0.72	Bimodal	medium sand	poorly	fine skewed	platykurtic	fan
NVC7	3214	2697	1.893	-0.429	0.775	Bimodal	very fine gravel	moderately	very fine skewed	platykurtic	fan
NVD1	1748	1778	1.728	0.029	1.114	Unimodal	very coarse sand	moderately	symmetrical	leptokurtic	fan
NVD2	420	431	3.341	0.048	0.697	Trimodal	medium sand	poorly	symmetrical	platykurtic	fan
NVD3(a)	377	363	2.780	-0.044	0.769	Trimodal	medium sand	poorly	symmetrical	platykurtic	fan
NVD3(b)	248	286	2.800	0.192	0.719	Trimodal	medium sand	poorly	coarse skewed	platykurtic	fan
NVD4	378	430	2.782	0.160	0.871	Bimodal	medium sand	poorly	coarse skewed	platykurtic	fan
NVD5	373	462	3.224	0.274	0.943	Bimodal	medium sand	poorly	coarse skewed	mesokurtic	fan
NVD6	2295	1744	2.828	-0.431	0.934	Bimodal	very coarse sand	poorly	very fine skewed	mesokurtic	fan
NVD7	645	659	2.366	0.025	0.983	Unimodal	coarse sand	poorly	symmetrical	mesokurtic	fan

granulometry (NVA8, yellow curve on Figure 2.9) has a coarse-sand mean grain size similar to the samples which were dry-sieved. Furthermore, all samples with silt-sized mean particle size are located in Profiles A and B along the Nyl/Mogalakwena River bank.

In an asymmetrical population skewness is either fine (positive) or coarse (negative) indicating the dominant grain-size fraction to be fine-grained or coarse-grained respectively. The *skewness* values show 34 % of the total samples collected to be symmetrical, 42% to be fine (or positively) skewed, and 24 % coarse (or negatively) skewed. Of the eight samples analysed using laser granulometry, the seven samples that displayed silt-sized means are all symmetrical or finely skewed, whereas the single sample that had a coarse sand-sized mean was coarsely skewed. The samples that were dry sieved displayed symmetrical, fine and coarse skewness.

Kurtosis values for all samples collected show that 37 % of the grain size distributions are platykurtic (relatively flat), 42 % are mesokurtic and 21 % are leptokurtic (strongly peaked). There is no observable relationship between the kurtosis of the samples and the grain size analysis technique, *i.e.* both the dry sieved and the laser granulometry samples display all three kurtosis categories. Both skewness and kurtosis are a measure of how closely the grain size distribution is to a normal Gaussian distribution. Commonly single source sediments feature fairly normal distributions (symmetrical and mesokurtic) whilst multiple source sediments show pronounced skewness and kurtosis (Folk, 1980).

2.5 Discussion

The four profiles were selected for sampling based on their relative locations with respect to the Nyl/Mogalakwena (trunk) River, the Rooisloot (tributary channel) and the tributary fan deposited at the confluence of the two rivers. Therefore Profiles A and B were selected along the banks of the Nyl/Mogalakwena River, representative of a channel floodplain depositional environment while Profiles C and D were selected within the tributary fan where incision had occurred due to the Rooisloot, representative of a tributary fan depositional environment. Whilst the individual profiles are representative of a specific depositional environment, each profile

contains sedimentary layers deposited by fluvial processes, such as overbank and channel sediments. Furthermore, Profiles A and B contain floodplain deposits (typically overbank sediments) but Profiles C and D do not.

2.5.1 Characteristics of tributary fan and floodplain sediments

The cumulative frequency curves (see Figures 2.8 and 2.9) identified two distinctly different plot types in terms of the distribution of grain sizes and the mean grain size. The first type of plot displayed high proportions of silt-sized particles together with silt-sized mean grain sizes, whilst the second type displayed a high proportion of coarser grained particles and sand- to gravel-sized mean grain sizes. The fine grain size of the first plot type would be produced by suspended particles settling in a low energy environment, whereas the coarser grained particles of the second plot type would be deposited in a higher energy flow regime. Therefore, these two different plot types likely represent two different depositional environments, with the silt-sized distributions indicating floodplain deposits (overbank sediments deposited due to episodic ponding within the Nyl/Mogalakwena River) and the sand to gravel sized distributions indicating fan deposits (mainly channel sediments with a small amount of overbank sediments).

From the total sample collection, seven samples can be identified as floodplain deposits and 32 samples as fan deposits (see Table 2.3). The floodplain sediments have silt-sized mean grain sizes, are symmetrical or finely skewed and are poorly to very poorly sorted. All floodplain deposits are located within Profiles A and B along the banks of the Nyl/Mogalakwena River, specifically layers NVA3, NVA5, NVA7, NVA9, NVB2, NVB4 and NVB8. Originally it was assumed that only the black, organic-rich layers were floodplain deposits but this is not the case. Several of the floodplain deposits are brown in colour with minimal organic material. Similarly, some of the black layers (*e.g.* NVA8) display the characteristics of tributary fan sediments, specifically sand- to gravel-sized mean grain sizes, with poorly to moderately sorted and symmetrical, finely- or coarsely-skewed sediments.

Furthermore, the stratigraphic correlation does not always match with the classification of sediments as floodplain and tributary fan. For example, there is a relative stratigraphic correlation between layers NVA8 and NVB2, both of which are

black, organic-rich layers. However, NVA8 is well-sorted and coarsely skewed with a coarse-sand mean grain size whereas NVB2 is poorly sorted and finely skewed with a medium-silt mean grain size. Both layers were sampled for radiocarbon dating and their ages concur; therefore it is possible that one of the samples was contaminated during collection or analysis.

The classification of NVA9 as a floodplain deposit is also problematic based on the thickness of the layer. NVA9 is located at the base of Profile A, has a cumulative thickness of over 1 m and hosts a 4 cm thick gravel layer (see Figure 2.7). The layer displays a fining upward grain size and the sample was collected near the top of the layer, therefore it is probable that the sample collected is not truly representative of the entire 1 m thick layer. However, fining upward sequences may be deposited in tributary fans during retrogradation of the fan. Therefore it is possible that the NVA9 layer is topped by a floodplain deposit that was not identified in the field or that the layer represents a period when the tributary fan was retrograding and the finest grains were deposited in what was the distal region of the fan at that time.

2.5.2 Particle sorting versus mean grain size

Particle sorting is a function of the mean grain size and the type of deposition (Folk, 1980). The general relationship observed between sorting and mean grain size (Figure 2.10a) for the samples identified as tributary fan sediments is one of decreased sorting with increased grain size for Profiles A, C and D, and increased sorting with increased grain size for Profile B. However, the decrease or increase in sorting is minimal. Alternatively, for the samples identified as floodplain sediments, there is a larger increase in sorting with increase in grain size (Figure 2.10b).

Furthermore, the tributary fan samples displayed generally larger mean grain sizes. This difference is most likely due to transportation of material in the different depositional environments. Water flowing across a floodplain carries fine-grained particles almost exclusively in suspension which increases the possibility of hydraulic sorting, whereas tributary fan sediments are transported episodically during high-runoff events which offer limited time for sorting prior to deposition.

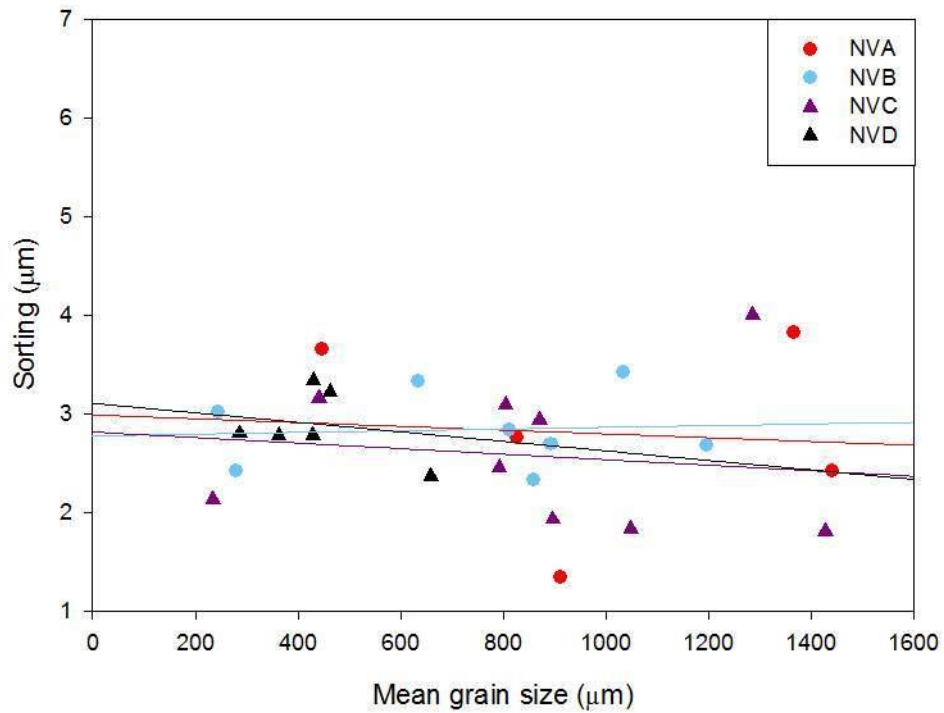


Figure 2.10a: Comparison between the mean grain size and sorting (standard deviation) within each Profile for the samples identified as tributary fan sediments.

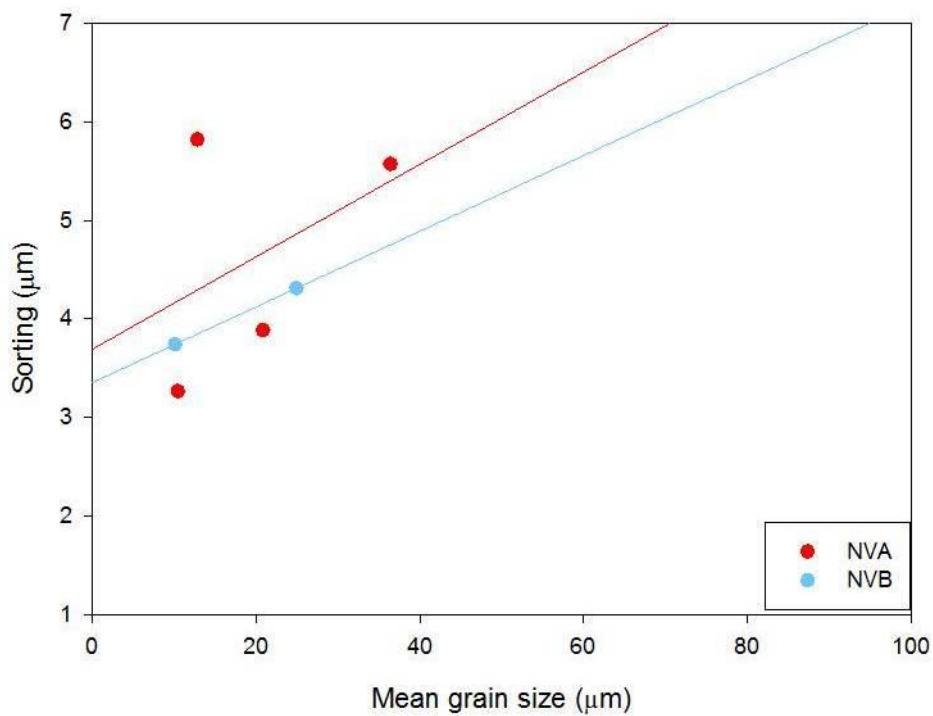


Figure 2.10b: Comparison between the mean grain size and sorting (standard deviation) within each Profile for the samples identified as floodplain sediments. Note the different x-axis.

2.5.3 Transport history of sediments

Extreme skewness and kurtosis values occur when two distributions are present within a sediment sample and are commonly ascribed to sediments being sorted in a high energy environment followed by transportation and deposition in a lower energy environment where the sorting process is less effective (Folk, 1980). Typical fluvial sediments have a positive (finely) skewed, leptokurtic distribution, and whilst the floodplain samples are positively skewed they do not display any dominant leptokurtic distributions. Furthermore, since neither the floodplain or tributary fan sediments display extreme skewness or kurtosis, it is unlikely that two separate distributions have been combined during transport and deposition. A single distribution is also supported by the grain roundness.

Grain roundness is a function of the transport history of the grain as abrasion chips off the edges and generally smooths the clast (Folk, 1980; Nichols, 2009). However, the roundness is also determined by the hardness of the grain, with soft minerals such as limestone being rounded far quicker than hard minerals such as quartz. Thus the roundness of the grain can be considered an indicator of the distance a sedimentary particle has travelled, conveying the relationship that the farther a grain has been transported the smoother and rounder it will appear. The floodplain sediments are generally subrounded to rounded, whilst the tributary fan sediments are more commonly subangular to subrounded. This relationship is intuitive as the floodplain sediments have been transported long distances downstream, whereas the tributary fan sediments are transported sporadically over shorter distances and thus undergo less abrasion and are therefore less rounded.

Given the low skewness and kurtosis values and the small number of rounded grains it would appear that the sediments deposited in the research area are from a local source location composed of varying materials. This is further supported by the fact that the upper reaches of the Nyl/Mogalakwena River and the Rooisloot have different sources, the Waterberg Group and the Transvaal Supergroup respectively. Furthermore, the extreme skewness and kurtosis values indicative of multiple source regions would most likely occur further downstream of the confluences of the major tributaries (Dorpsrivier, Rooisloot and Pholotsi) in the Nyl/Mogalakwena River.

2.5.4 Stratigraphic comparison

The grain-size analysis reflects a distinct difference in the sedimentary characteristics of the two depositional environments which must be considered in terms of the logged stratigraphic sections. The dark-coloured layers in Profiles A and B, assumed to be floodplain deposits in the field, proved to be fine-grained and organic-rich with the exception of NVA8. This supports their interpretation as being floodplain (or overbank) deposits. In contrast, the dark layers identified in Profiles C and D do not represent floodplain deposits as their sedimentological characteristics and statistical values are equivalent to those of the tributary fan sediments.

The most likely explanation for the presence of black, organic-rich layers in the tributary fan is the existence of soil-forming processes during periods when active sedimentation was not occurring on the fan. During these inactive periods soil profiles could form and the black layers may be representative of the A₁ soil horizon, typically the organic-rich, dark-coloured, topsoil layer. Furthermore, irrespective of their location all black layers displayed ped structures, but the peds observed at Profiles C and D were better defined than those observed at Profiles A and B. The formation of peds in the floodplain layers can be explained by extended dry periods when the floodplain was left devoid of water after the dark layers had been deposited. This would allow soil structures to be superimposed on the floodplain deposits before the tributary fan prograded over them burying them beneath new sediment. Regardless of the depositional environment where they formed, the dark layers proved important in the stratigraphic correlation of the deposit across the tributary fan.

The stratigraphic correlation produced from the grain size analysis and sediment descriptions supports the model of McCarthy *et al.* (2011) as shown in Figure 1.5 whereby the episodic progradation of the tributary fan has caused coarse-grained fan sediments to be deposited over fine-grained floodplain sediments creating an interlayered stratigraphy of fan and floodplain sediments. Although four stratigraphic profiles were logged, they are representative of three sedimentary sections. Profiles A and B, located on opposite banks of the Nyl/Mogalakwena River, were easily correlated based on the dark layers, the doublet located in layers NVA4 and NVB9 and the similar stratigraphy and sedimentary characteristics of the

layers. Profiles C and D were expected to correlate with one another, however the profiles are different in terms of their stratigraphy and sedimentary characteristics. Therefore Profile C and D are interpreted to represent different depositional periods of the Rooisloot. This is most likely due to an erosional event or channel avulsion within the Rooisloot, whereby the existing distributary was abandoned and a new distributary formed leading to erosion of the existing sediment and deposition of the younger sequence alongside the older sequence.

2.6 Summary

The Nyl/Mogalakwena River floodplain is located in Limpopo Province and is surrounded by the Waterberg to the west, the Springbok Flats to the south and the town of Maroteng to the east. The river flows northwest through a basin composed of rocks from the Pretoria Group, the Rooiberg felsites of the Bushveld Complex, the Waterberg Group and the sandstones and basalts of the Karoo Supergroup. The Nyl/Mogalakwena River is joined by numerous tributaries from the east, including the Rooisloot and less extensive tributaries from the west.

The Nyl/Mogalakwena River floodplain is an area of active sedimentation where the progradation of tributary fans across the Nyl/Mogalakwena River has resulted in the deposition of interfingered layers of floodplain and tributary fan sediments. The alluvial fan at the confluence of the Nyl/Mogalakwena River with the Rooisloot is a tributary-*junction fan* (or *tributary fan*) dominated by stream-flow processes. The sediments were analysed through a detailed stratigraphy and grain size analysis.

Four profiles were selected for a detailed stratigraphy, two representative of the Nyl/Mogalakwena River floodplain depositional environment and two representative of the tributary fan which has been incised by the Rooisloot. The first two profiles, located on opposite banks of the Nyl/Mogalakwena River correlate well across the river, but the latter two profiles within the tributary fan do not correlate based on sedimentary characteristics and relative stratigraphy alone, and appear to represent two separate depositional periods possibly due to erosion or channel avulsion of the Rooisloot.

Sediments were identified as belonging to one of two depositional environments, the Nyl/Mogalakwena River floodplain and the Rooisloot tributary fan. Floodplain sediments were poorly to very poorly sorted with mean grain sizes in the silt range (3.9 – 63 μm) and symmetrical to finely-skewed grain size distributions. Tributary fan sediments were generally poorly sorted, although some layers in Profile C displayed moderate sorting, with mean grain sizes in the sand range (63 – 2000 μm) and symmetrical, finely- or coarsely-skewed grain size distributions. Furthermore, the floodplain sediments displayed a higher degree of particle rounding than the tributary fan sediments, the former rounded to well-rounded and the latter subangular to subrounded.

There is a minimal decrease in sorting with increased grain size in the tributary fan sediments versus a significant increase in sorting with increased grain size in the floodplain sediments. This relationship is more pronounced in the floodplain sediments due to transport and deposition of the material, *i.e.* floodplain deposits are comprised of silt-sized grains transported downstream in suspension which should result in better sorting of the particles. In contrast tributary fan sediments are transported sporadically during high-runoff events and therefore result in very poorly sorted deposits. The subrounded to subangular appearance of the individual grains implies a short transport history and therefore distance, whilst the lack of extreme kurtosis and skewness values implies that the sediments are not mixtures of multiple populations. These two facts support a local source for the sediments, most likely the Waterberg Group from the Waterberg for the Nyl/Mogalakwena River and the Transvaal Supergroup from the Maribashoek and Buffelshoek Mountains for the Rooisloot.

Chapter 3:

Geochronology: Radiocarbon and Optically Stimulated Luminescence Dating

3.1 Introduction

Alluvial fans provide records of climate change (due to both natural and anthropogenic factors) and tectonic activity, thus by constraining accurate ages for alluvial fan sequences and the rate of sediment accumulation, the timing of the mechanisms that control fan formation can be determined (Harvey *et al.*, 2005; Pope and Wilkinson, 2005; Robinson *et al.*, 2005; Harvey, 2011). Numerous dating techniques are available for use in the field of geoscience depending on the material to be dated and the relevant timescale involved, including but not limited to luminescence dating (Aitken, 1985; Wintle, 2008; Wintle, 2010), U-series disequilibrium dating (Schwarcz, 1989), cosmogenic nuclide surface exposure dating (Harbor, 1999), radiocarbon dating (Libby, 1955; Hua, 2009), fission track dating (Jäger and Hunziker, 1979; Naeser and Naeser, 1988) and electron spin resonance dating (Hennig and Grün, 1983; Grün, 1989). Two techniques were selected for this research project based on the nature and suspected young age of the sediments being dated: radiocarbon (^{14}C) dating which dates associated organic matter, and optically stimulated luminescence (OSL) dating which dates the deposition of constituent mineral grains. Samples collected for radiocarbon dating were organic-rich, fine-grained sediments whilst the samples collected for OSL dating were coarse-grained, quartz- and feldspar-rich sediments.

The concepts relevant to OSL and ^{14}C dating will be introduced in this chapter and the suitability of the two methods to the dating of the Nyl/Mogalakwena River and Rooisloot sediments will be considered. OSL dating is covered in greater detail in this research project as it is a newer technique and has the potential to be a more reliable method of dating fluvial sediments than ^{14}C dating due to the fact that it uses constituent grains to determine the age of deposition of the sediment, as opposed to associated organic material.

3.2. Radiocarbon dating

Three isotopes of carbon exist in nature; the two stable isotopes are ^{12}C with a natural abundance of ~98.9 % and ^{13}C with ~1.1 %, while ^{14}C (radiocarbon) only occurs in minute amounts and is radioactive (Walker, 2005; Hua, 2009; Albarède, 2011). ^{14}C is produced in the atmosphere via the interaction of cosmic rays with atmospheric ^{14}N and then undergoes oxidation to produce $^{14}\text{CO}_2$ which is rapidly dispersed throughout the atmosphere, thereby allowing the transferal of ^{14}C into other carbon reservoirs, *i.e.* into the biosphere via photosynthesis or the ocean via air-sea exchange (Hua, 2009). The presence of ^{14}C in carbon reservoirs allows it to be continually taken up by living organisms such as plants and marine microorganisms, which results in a ^{14}C concentration in the organisms in equilibrium with the concentration in the atmosphere. However, when the organism dies it ceases to take up ^{14}C and the concentration begins to decrease at the rate of radioactive decay given by the half-life of ^{14}C , which is 5 730 years (Libby, 1955; Godwin, 1962). The rate of decay is independent of external environmental factors and thus the amount of time (t) that has elapsed since the formation of the organism is given by

$$t = \frac{T_{1/2}}{\ln 2} \ln \left(\frac{N(t)}{N_0} \right) \quad (3.1.)$$

where $T_{1/2}$ is the half-life of ^{14}C , N_0 is the original ^{14}C concentration and $N(t)$ is the remaining ^{14}C concentration at time t (Hua, 2009). Thus it is the disequilibrium of the ^{14}C concentration between the once-living organism and the atmosphere that allows the radiocarbon dating method to be used.

Considering that all living organisms were once in equilibrium with the atmospheric ^{14}C concentration, it is relatively common for samples to become contaminated by foreign material with a different ^{14}C signal. Therefore samples must be processed before dating and the contaminants removed. For example in a soil profile younger roots may penetrate downwards into the older sequence thereby producing an underestimation in the age if the roots are selected for analysis. Alternatively in a fluvial environment, reworked carbon in the form of bones, wood or charcoal can produce an overestimation in the calculated age for host sediments (Stanley and Hait, 2000; Hua, 2009).

3.2.1. Measurement of radiocarbon concentrations

The radiocarbon dating method measures the residual ^{14}C remaining in a sample relative to a modern standard, either through decay counting or accelerator mass spectrometry (AMS), the latter being the preferred method due to the smaller sample size required and faster and more efficient processing time (Walker, 2005; Hua, 2009). Decay counting measures the beta particles (~ 156 keV) emitted by the radioactive decay of the ^{14}C isotope, using either a gas proportional counter requiring pre-treated samples to be converted to CO_2 or a liquid scintillation counter using benzene synthesised from the sample. Alternatively, the AMS technique directly measures the ^{14}C isotopes relative to the stable ^{12}C and ^{13}C isotopes within the sample (Walker, 2005; Hua, 2009). The ratio of ^{14}C to ^{12}C and ^{13}C is then compared to the ratio of a known standard held by the American Bureau of Standards (Walker, 2005). All samples collected for radiocarbon dating in this research project were submitted to the Radiocarbon Dating Laboratory, Lund University, Sweden where they were analysed using the AMS technique. The ^{14}C dating report from Lund University is appended as supplementary data in Appendix F.

3.2.2. Reporting and calibrating ^{14}C ages

Reported radiocarbon ages are expressed in *years before present* (years BP) where present is defined conventionally as the year AD 1950 (Walker, 2005; Hua, 2009; Duller, 2011). However, due to the variability of the Earth's magnetic field and solar activity the atmospheric ^{14}C concentration has not been constant in the past (Hua, 2009; Reimer *et al.*, 2009) and so radiocarbon ages must be converted to calendar ages using a calibration curve constructed from precisely dated, independent materials (Hua, 2009). The current calibration curve (IntCal09) covers the past 50 000 calendar years (cal) BP and is based on tree-rings dated through dendrochronology and the independent dating of marine samples such as corals and foraminifera (Reimer *et al.*, 2009). The calibration of radiocarbon ages is completed using one of several computer programs available online.

3.2.3 Age limit of ^{14}C dating

^{14}C is an unstable isotope undergoing radioactive decay through beta-emission to form ^{14}N , with a half-life of 5730 years (Godwin, 1962; Walker, 2005). The half-life of ^{14}C determines the upper age limit obtainable through radiocarbon dating. The

limit of measurement is 9–10 half-lives, which therefore marks the upper age limit as ~ 50 000 years (Hua, 2009).

3.3 Luminescence dating

Luminescence dating involves measuring the emission of light from a natural material upon stimulation. The OSL dating technique was first presented by Huntley *et al.* (1985) and produces an estimated age for the last resetting event *i.e.* the last time the luminescence signal was reset by the exposure of the sediment to sunlight (Figure 3.1), rather than the age of formation of the sediment. Once the sediment is buried, natural minerals such as quartz and feldspar act as dosimeters, absorbing ambient radiation from the surrounding sediments and cosmic rays and storing electrons within defects in the crystal lattice structure known as *traps* (Figure 3.1, brown area) (Murray and Olley, 2002; Duller, 2004; Walker, 2005; Duller, 2008a; Rittenour, 2008). When these traps are stimulated by light the trapped radiation is liberated as energy, and the luminescence signal is reset through a process known as *bleaching*. After deposition, once the sediments have been removed from direct sunlight, the luminescence signal begins to accumulate again until the time of sampling (Figure 3.1, blue area); this second period between the bleaching event and the laboratory measurement event provides the age obtained by luminescence dating.

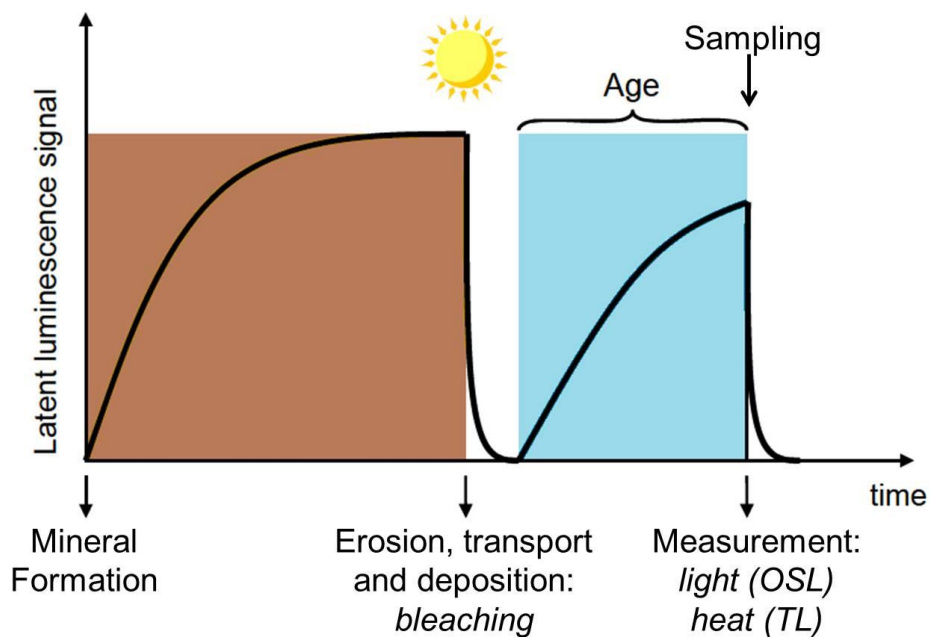


Figure 3.1: Schematic representation of the event dated by luminescence dating (after Vandenberghe, 2004).

During measurement the nature of the stimulation may be thermal, optical or infrared with the resultant luminescence signal termed *thermoluminescence* (TL), *optically stimulated luminescence* (OSL) or *infrared stimulated luminescence* (IRSL) respectively (Murray and Roberts, 1998; Stokes and Walling, 2003; Duller, 2004; Walker, 2005; Duller, 2008a). Each of these techniques produces ages for different types of events and is used on different materials. TL is most commonly used in archaeology to obtain ages for pottery by dating the last heating event. Alternatively OSL and IRSL date the depositional age of sediments. However, whilst OSL can be used for both quartz and feldspar, IRSL is suitable only for feldspar.

3.3.1 Optically Stimulated Luminescence

To produce the OSL signal the sample must be exposed to light, typically blue LEDs (Bøtter-Jensen *et al.*, 1999a, 1999b; Duller, 2008a). Measuring the brightness of the luminescence signal allows the total amount of radiation the sample was exposed to during burial to be calculated. In OSL dating the total dose as calculated from laboratory measurements is termed the *equivalent dose* (D_e), whilst the amount of energy absorbed through radioactive decay per year, known as the *dose rate* (D_r), can be measured directly in the field or calculated retrospectively in the laboratory (Wintle, 1991; Aitken, 1998; Duller, 2004; Walker, 2005; Duller, 2008a). These two quantities are employed to determine the age in ka of a sample by dividing the total radiation accumulated during burial by the amount of radiation delivered on a yearly basis is represented by the equation:

$$Age = \frac{D_e}{D_r} \quad (3.2)$$

where D_e is the equivalent dose in Gy and D_r the dose rate in Gy/ka (Wintle, 1991; Aitken, 1998; Wallinga, 2002; Stokes and Walling, 2003; Duller, 2004; Walker, 2005).

Due to the fact that the age of the sample is calculated using the D_e and the D_r , it is impossible to consider OSL dating without a thorough examination of these two values. Therefore the basic concepts behind the equivalent dose and dose rate will be reviewed in this chapter while the calculated D_e values for the Nyl/Mogalakwena River and Rooisloot samples are presented and discussed in Chapter 4, and the

measured dosimetry values of the Nyl/Mogalakwena River and Rooisloot samples are discussed in Chapter 5.

3.4 Basic concepts of OSL dating

3.4.1 The luminescence signal

The mechanism responsible for the luminescence process is best described by means of the energy level diagram for non-conducting ionic crystalline materials originally taken from Aitken (1998). This model (Figure 3.2) associates electrons with discrete energy bands, the lowest of these being the valence band and the highest the conduction band. Between these two bands is the ‘forbidden zone’, which ideally does not host any electrons. However, due to defects present in the ordered crystal structure, either as impurities or missing atoms, electrons can be associated with this middle zone. Thus natural radiation from the surrounding environment can interact with the crystal through ionisation, thereby raising an electron from the valence band to the conduction band (Figure 3.2(a)) and producing a *hole* or electron vacancy (Aitken, 1998). The electrons and holes move freely throughout the crystal, however should they become trapped in the defect sites, the energy will be stored in the crystal lattice temporarily (Figure 3.2(b)). In order to move the electrons out of the traps energy is required, with the amount of energy proportional to the depth of the trap below the conduction band; thus the energy stored in deeper traps is more stable than the energy stored in shallower traps and it is this stable energy that produces the signal used in luminescence dating. By stimulating the crystal with light or heat, the electrons can be released (Figure 3.2(c)), either to become trapped again or to recombine with the holes in which case they produce *luminescence centres*. The light emitted by this process is termed thermoluminescence (TL) or optically stimulated luminescence (OSL) depending on whether heat or light respectively was utilised to evict the electrons from the traps (Aitken, 1998).

The typical OSL signal produced decreases rapidly in the initial stages of the measurement, sometimes showing material-dependent properties, *i.e.* feldspar decreases at a slower rate than quartz (Duller, 2008a; Duller, 2003). Thus, it is important to understand the properties of the material to be dated.

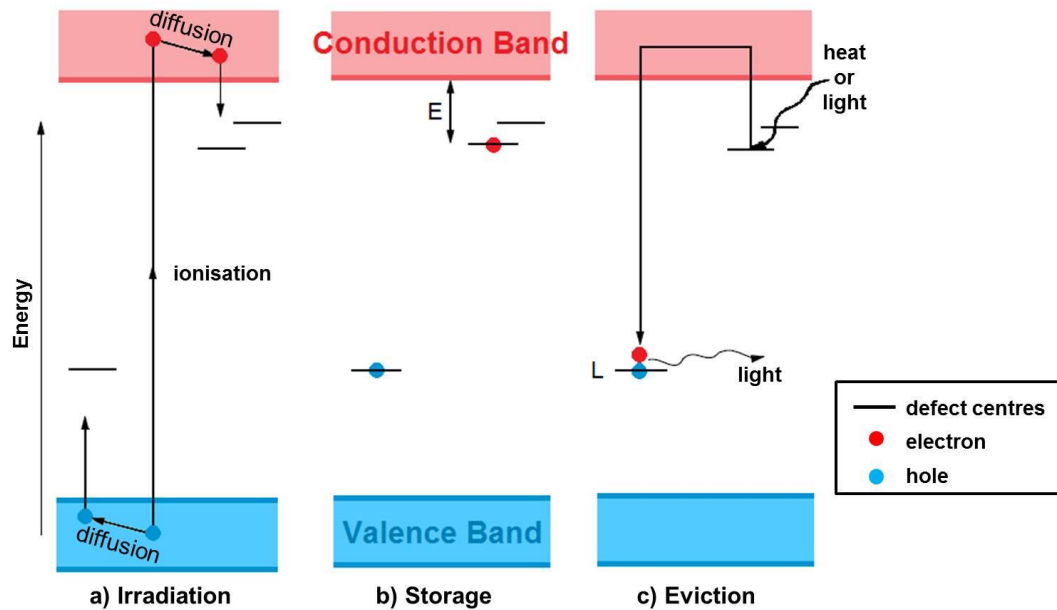


Figure 3.2: Energy-level diagram depicting the three stages of the luminescence process: (a) electrons are forced into the conduction band by ionising radiation; (b) electrons are trapped within defects in the crystal lattice; (c) stimulating the crystal with heat or light releases the trapped electrons which recombine at luminescence centres (L) and emit a luminescence signal (after Vandenberghe, 2004; Duller, 2008a; original in Aitken, 1998).

3.4.2 Minerals used for optical dating

Quartz and feldspar are the most extensively used minerals in the optical dating of sediments due to their natural abundance, however various other minerals have been found to emit an OSL signal, including zircon (Smith et al., 1986; Smith, 1988), apatite (Smith et al., 1986) and glass from volcanic ash deposits (Berger and Huntley, 1994; Berger and Neil, 1999). Zircon and apatite are limited in their application to OSL dating as their natural abundance is much lower than that of quartz and feldspar, whilst volcanic glass requires further study in order to better understand its properties (Vandenberghe, 2004).

The choice between feldspar and quartz depends on several factors, including the availability of the mineral in the sample, the age of the sediments being dated and the method of stimulation. Feldspar is useful in dating older deposits as quartz saturates at lower doses than feldspar (typically at 200 Gy), thereby limiting the age range to ~ 300 ka (Stokes and Walling, 2003; Vandenberghe, 2004; Duller, 2008a; Thomsen *et al.*, 2008). Furthermore, in some locations quartz may be totally absent (*e.g.* Hawaii) and in other locations the sensitivity of the quartz is so low that it has little

value as a natural dosimeter (Thomsen *et al.*, 2008). Possibly the most beneficial characteristic of feldspar is that it can be stimulated by infrared light whereas quartz cannot. This provides a way to target only feldspar grains for measurement and removes the issue of quartz contamination from the sample (Thomsen *et al.*, 2008). However, feldspar grains are subject to anomalous fading because electrons in the deeper traps are less stable than those found in quartz. Anomalous fading results in the strength of the luminescence signal decreasing over time and may be corrected for by applying a mathematical correction or by determining a signal that does not exhibit fading (Wintle, 1973; Spooner, 1994; Duller, 2008a; Thomsen *et al.*, 2008).

3.5 Measuring the equivalent dose (D_e)

In order to obtain the D_e value (the equivalent of the natural radiation dose), irradiated quartz is exposed to blue or green light and the amount of OSL observed; this signal is then used to estimate the natural radiation dose the sediment has acquired since the time of burial. The D_e is determined by comparing the natural OSL signal with a laboratory OSL signal produced from a known dose (Murray and Wintle, 2000). D_e measurements are undertaken on aliquots (stainless steel discs of 9 mm diameter onto which multiple grains of a single sample are mounted; see Figure 4.3a-c) using a Risø TL/OSL reader (see Section 4.4). The measured signal is then analysed using the standard Risø software package *Luminescence Analyst*.

3.5.1 The Single Aliquot Regenerative Dose (SAR) protocol

The standard technique used today to measure the luminescence signal has been refined over the last decade and the advent of the Single Aliquot Regenerative Dose (SAR) protocol has revolutionised OSL dating of sedimentary quartz grains. The SAR protocol, formalised by Murray and Wintle (2000), was based on the protocol suggested by Murray and Roberts (1998) where the natural OSL signal and the laboratory generated signal are both corrected for sensitivity prior to being compared with one another. Whilst Murray and Roberts (1998) used the 110° TL peak to monitor sensitivity changes caused due to the laboratory treatment of the aliquot, Murray and Wintle (2000) used additional OSL measurements for this purpose (Wintle and Murray, 2006).

The conventional SAR sequence (Table 3.1) outlined by Wintle and Murray (2006) details the series of steps necessary to measure the luminescence signal. The natural dose (D_N) is measured in step 1 and thereafter progressively larger doses are used to irradiate the sample producing the stimulation values for L_x . A fixed test dose (D_T) is given after each OSL measurement in order to correct for sensitivity changes in the quartz grains (Armitage *et al.*, 2000). The growth curve for the sample can then be plotted using the L_x/T_x values onto which the natural signal (L_N) can be interpolated. Step 7 was included in Wintle and Murray (2006) to ensure that no residual signal is carried over to the following dose measurement. The preheat (step 2) is carried out in order to empty the 110 °C TL trap prior to the measurement of the OSL signal. Alternatively whilst the cutheat (step 5) serves the same purpose as the preheat and can be any temperature between 160 °C and 300 °C, it is generally held at 160 °C in order to minimise sensitivity change (Armitage *et al.*, 2000).

Table 3.1: Generalised SAR sequence for quartz using blue LEDs for stimulation (Wintle and Murray, 2006)

Step	Treatment	Observed
1	Give dose, D_x	-
2	Preheat (160-300 °C for 10 s)	-
3	Stimulate for 40 s at 125 °C	L_x
4	Give test dose, D_T	-
5	Heat (160-300 °C)	-
6	Stimulate for 40 s at 125 °C	T_x
7	Stimulate for 40 s at 280 °C	-
8	Return to 1	

3.5.2 Sensitivity change of quartz during the SAR protocol

The most important assumption underlying the SAR protocol is the proportionality of the sensitivity measured from the test dose (D_T) to the sensitivity measured from the prior regeneration dose (Armitage *et al.*, 2000; Murray and Wintle, 2000; Jacobs *et al.*, 2003b; Wintle and Murray, 2006). Several studies have been published in support of this assumption. Murray and Wintle (2000) presented experimental data for heated quartz which showed the D_T sensitivity to be consistent, although slightly higher than, the sensitivity of the preceding measurement. Armitage *et al.* (2000) used sedimentary quartz from South Africa (Figure 3.3) to show that low preheat

temperatures (160–200 °C) result in an initial decrease of sensitivity and high preheat temperatures (220–300 °C) showed an increase. Jacobs *et al.* (2003b) presented similar findings based on quartz from two archaeological sites in South Africa and identified a 30% variation in sensitivity over 7 measurement cycles, which was similar to the 40% variation identified by Armitage *et al.* (2000). Jacobs *et al.* (2003b) concluded that the validity of the sensitivity correction could be confirmed by using the recycling ratio and since the samples conformed to the recycling ratio test there was no preheat dependence in the measured D_e values.

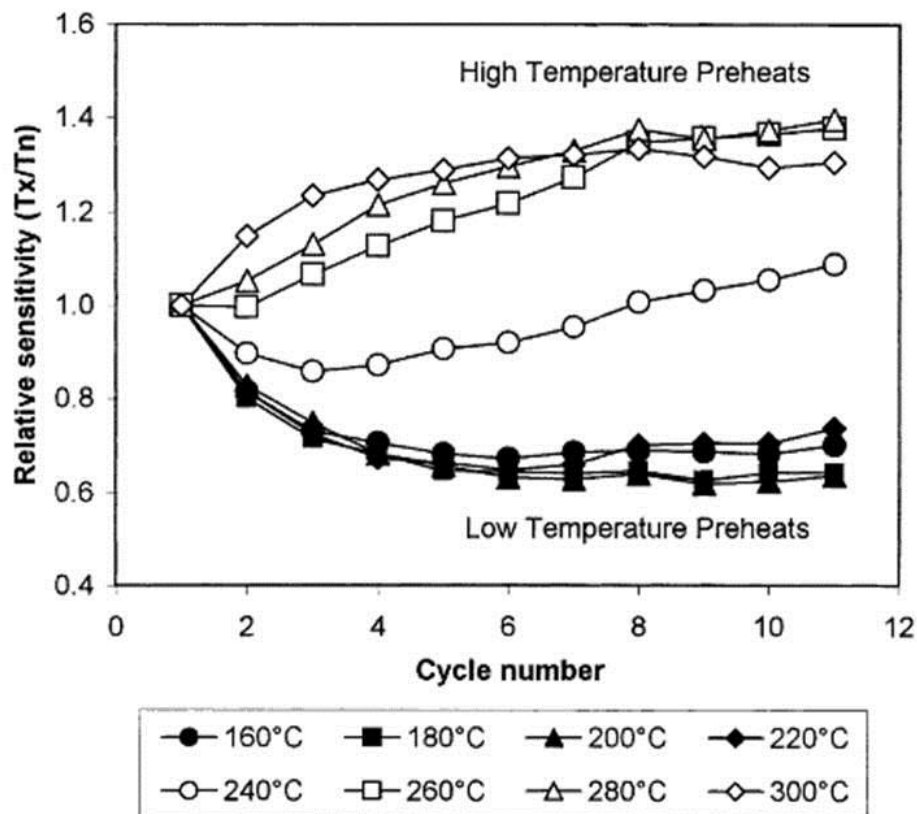


Figure 3.3: Graph showing the sensitivity change in a sample of South African quartz from Kosi Bay (Armitage *et al.*, 2000). Low preheat temperatures result in an initial decrease in sensitivity whilst high preheat temperatures result in an initial increase in sensitivity. The overall variation is 40%.

3.5.3 Preliminary tests for the SAR protocol

Several underlying assumptions exist for the SAR protocol, therefore it is necessary to ascertain whether individual samples meet these assumptions (Roberts *et al.*, 1999; Wintle and Murray, 2006). To this end there are several tests that can be carried out to determine whether the utilisation of the SAR protocol is appropriate for the sample.

Thermal transfer is defined as the transfer of charge from light-insensitive, thermally-stable traps to light-sensitive traps due to heating (Murray and Olley, 2002; Wintle and Murray, 2006). It is of greater significance in young samples than in older samples because the charge transfer resulting from the first preheat (prior to the measurement of the natural signal) may cause the sample to appear incompletely bleached when this is not the case (Murray and Olley, 2002; Wintle and Murray, 2006). Due to the variation of the D_e based on temperature the preheat temperature used in the SAR protocol is not a fixed value, and it is necessary to determine at what preheat temperature the D_e remains constant. The *preheat test* is designed to determine the preheat plateau (Figure 3.4), the temperature range that produces consistent D_e values, and to determine at which temperatures thermal transfer is significant (Wintle and Murray, 2006). The traps responsible for thermal transfer are within the 200 °C to 300 °C temperature range (Wintle and Murray, 2006) and the temperature range used in the preheat test is 160 °C to 300 °C for quartz based on the findings of Murray and Wintle (2000). This test requires running a standard SAR sequence on a set of aliquots while varying the preheat temperature, *i.e.* from a total of 24 aliquots, 3 are measured for each temperature between 160 °C and 300 °C at 20 °C intervals using a fixed cutheat of 160 °C. The preheat values are then plotted against the equivalent dose values and the preheat plateau identified; a preheat

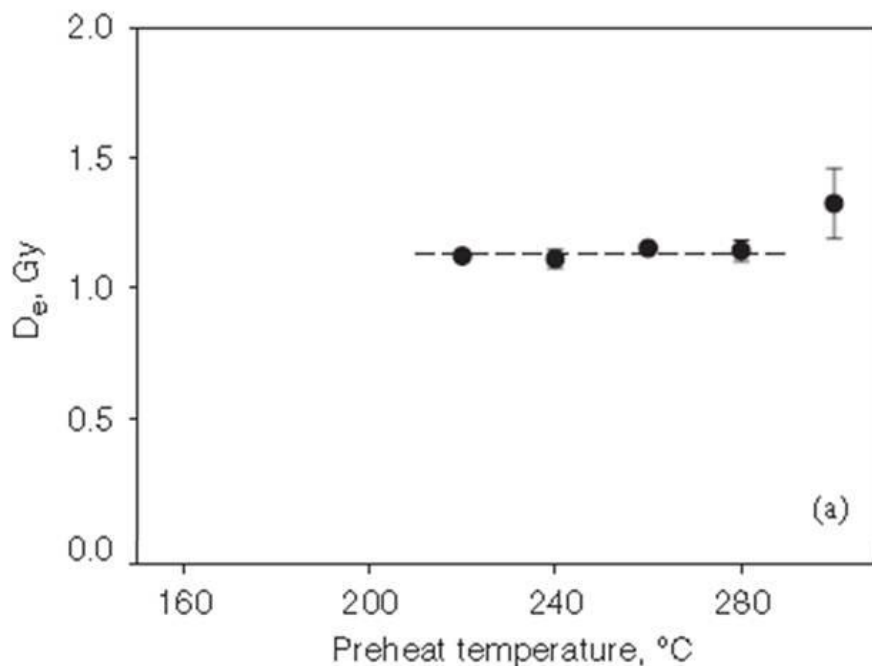


Figure 3.4: The preheat plateau (dashed line) identified from a preheat test (Wintle and Murray, 2006).

temperature can then be selected from the range where the D_e values are constant with respect to preheat temperature. In order to lessen the amount of time samples spend on the reader, the preheat test can be run concurrently with the dose recovery test.

The *dose recovery test* (DRT) aims to measure a known dose given before any thermal pre-treatment is applied to the grain (Wintle and Murray, 2006). This requires the sample be bleached using a similar process as experienced in nature in order to remove the natural signal prior to laboratory irradiation of a known dose, which is then treated as an unknown and obtained through the SAR protocol. This is achieved experimentally by illuminating the sample with blue LEDs in the Risø TL/OSL reader prior to irradiating the sample with a known dose and then running a complete SAR protocol on the sample. The given dose is then compared to the measured dose and if the SAR protocol is working correctly the ratio between the two doses should be consistent with unity (Wintle and Murray, 2006). The DRT provides a measure of the maximum precision with which a sample can be analysed when natural variations (such as sample inhomogeneity and a varying degree of bleaching) in the dose rate are excluded (Wintle and Murray, 2006). A sample that passes the DRT should also pass the recycling ratio test and recuperation test.

The final two routine tests are carried out using the data obtained from the construction of the dose-response curve. The *recycling ratio test* requires the re-measurement of a minimum of one point (Wintle and Murray, 2006), *i.e.* the response to a given dose is measured twice where all other given doses are measured once. Generally the smallest given dose is obtained first and the doses then increase to a given dose larger than the expected natural dose, with the repeated dose commonly chosen to be identical to the first given dose after the natural was measured. This is done due to the progressive nature of the sensitivity change in quartz grains and thereby allows the widest spread in the sensitivity change to be measured (Wintle and Murray, 2006). The ratio between the two sensitivity-corrected data points for the same dose must approximate unity with less than a 10 % error. If the recycling ratio is outside this range (0.90–1.10) the aliquot fails the test and no D_e value is obtained.

The ***recuperation test*** requires the measurement of the signal in response to a zero dose, since zero dose should result in zero signal (Wintle and Murray, 2006). However, this may not be the case as the transfer of charge from deeper traps due to previous irradiation, optical stimulation and preheating may produce a signal above zero. This signal was termed recuperation by Aitken and Smith (1988) and is expressed as a percentage of the natural signal or the equivalent dose, in either case Murray and Wintle (2000) recommend that recuperation should not exceed 5 %.

3.5.4 Single-grain techniques

The single grain technique requires that individual quartz grains are mounted onto a specially designed disc (an aliquot with a 10 x 10 grid of holes drilled into the surface; see Figure 4.3d) and stimulated with a green laser as opposed to the blue LEDs used in single aliquot (or multiple grain) stimulation. Duller (2008b) outlines the challenges faced when undertaking single-grain measurements; these include the possibility of “cross-talk” from stray beams of light *i.e.* when an adjacent grain is stimulated, the non-uniform irradiation of grains due to different types of beta sources, and the precision of the automated instrument. In response to the first issue, Duller (2012) ascertained that cross-talk has limited impact for standard single-grain measurements such as those undertaken in this research project. In response to the second and third issues Spooner and Allsop (2000) examined the two types of beta sources and determined that the older silver plaque sources (such as the sources in Risø 1 and 3, see section 4.4) produce a more uniform irradiation than the newer ceramic-substrate sources.

Single-grain techniques are a powerful tool when limited sample is available or when a large proportion of the grains display partial bleaching. It may also be prudent to use single-grain analyses when large aliquots are measured to ensure that the luminescence signal has not been averaged to the extent that the true variation within the D_e will not be observed.

3.6 Statistical analysis methods for determination of the true burial dose (D_b)

Regardless of the technique used, the measurement of single aliquot (multiple grain) or single-grain discs will produce numerous D_e values for a sample. Once the D_e

values for a sample have been measured they are subjected to statistical analysis in order to determine a representative D_e value for each sample, termed the true burial dose (D_b). The data can be represented in several ways, including histograms and probability density plots, however the preferred method in OSL dating is the radial plot (see Galbraith, 1988 and Galbraith *et al.*, 1999 for a detailed description). The combination of all three presentation methods provides an overview of the scatter within the dataset (that can be quantified by the overdispersion parameter) and plays a role in the choice of the statistical model which needs to be applied to the dataset in order to determine the D_b .

Overdispersion (σ_b) is defined as the relative standard deviation of the D_e measurements beyond that which is expected due to photon counting statistics and curve-fitting uncertainties (Galbraith and Roberts, 2006), *i.e.* it is the random variation within the dataset that cannot be explained by measurement uncertainties. The overdispersion value (calculated by the *Luminescence Analyst* program) can be estimated using one of the statistical methods, specifically the central age model described in Galbraith *et al.* (1999). Studies by Roberts *et al.* (2000), Olley *et al.* (2004b), Galbraith *et al.* (2005), Thomsen *et al.* (2005) and Jacobs *et al.* (2006b) have reported overdispersion values of up to 20 % for single aliquots of well-bleached quartz that have been heated prior to irradiation. Thus the value $\sigma_b = 20\%$ is used as a rough guide to selecting the statistical method to be applied to the dataset.

Several statistical methods have been devised to enable the determination of the true burial dose by isolating the representative population of grains. Such methods include the calculation of the mean of the lowest 5 % of D_e values (Olley *et al.*, 1998), fitting a Gaussian distribution to the leading edge of a D_e distribution histogram (Lepper *et al.*, 2000) and adapting the age models from the statistical models developed for fission track dating (Galbraith *et al.*, 1999). The age models adapted by Galbraith *et al.* (1999), specifically the central age model (CAM), the minimum age model (MAM), and the finite mixture model (FMM) were used in this research project. However, while statistical manipulation of the dataset is necessary to determine the true D_b for the sample, it is easy to fall into the trap of unthinkingly applying any or all of the available models. Thus it is important that statistical

modelling of the D_e data is performed with consideration of the depositional context of the sample, the stratigraphy and independent age controls (Galbraith *et al.*, 2005).

3.6.1 The common age model

The common age model represents an ideal sample where all the grains have received the same amount of bleaching and the D_e estimates are consistent with a common value (Figure 3.5a) (Galbraith *et al.*, 1999; Galbraith and Roberts, 2006). The observed spread in the data can be accounted for by measurement errors within the aliquot itself and there is no overdispersion to consider (Galbraith and Roberts, 2006). Such a sample likely does not exist in nature where heterogeneous bleaching and post-depositional mixing occur (Duller, 1994; Wallinga, 2002) and this model would be used almost exclusively on calibration quartz in experimental work.

3.6.2 The central age model (CAM)

For samples where the D_e estimates are not consistent with a common value and overdispersion is evident the central age model (CAM) may be most appropriate (Galbraith *et al.*, 1999, 2006). The model assumes a normal distribution for the D_e data with mean δ and standard deviation σ , where σ represents the overdispersion after the measurement errors within the aliquot have been accounted for (Galbraith *et al.*, 2006). The CAM (Figure 3.5b) determines a weighted mean; therefore D_e values with smaller errors hold a higher weight in the mean D_b value proportional to D_e values with larger errors. This model is generally acceptable when the overdispersion is below 20%.

The CAM is used for samples which have undergone homogeneous bleaching, *i.e.* the grains have been bleached to the same extent, and been deposited without any subsequent disturbance (Galbraith *et al.*, 2006; Duller, 1994). For examples of the application of CAM see Galbraith *et al.* (1999), Jacobs *et al.* (2003a, 2003b), Olley *et al.* (2004a) and Jacobs *et al.* (2008).

3.6.3 The minimum age model (MAM)

Sediments that have undergone incomplete or heterogeneous bleaching produce D_e distributions with a large amount of scatter and thus a large overdispersion (*i.e.* above 20%). In this case the minimum age model (MAM) may be appropriate to

determine the D_b specific to a population of well-bleached grains by using a truncated normal distribution (Figure 3.5c) (Galbraith *et al.*, 2006). The MAM fits a truncated normal distribution to the individual D_e data points and determines the proportion of grains that were fully bleached prior to deposition, the truncation point of the distribution, and the mean and overdispersion of the normal distribution fitted to the dataset (Galbraith and Laslett, 1993; Rodnight, 2006). The determination of these parameters requires complex equations, therefore a programme has been written for the statistical package “R” which allows the MAM to be calculated.

The MAM is used on sediments that have undergone partial bleaching prior to deposition and determines the D_b from the lowest D_e population. This applies to a number of depositional environments, typically young water-lain sediments, soils, archaeological deposits and deep-sea deposits (Olley *et al.*, 2004a, 2004b; Rodnight *et al.*, 2005; Galbraith *et al.*, 2006; Jacobs *et al.*, 2006a). However, Olley *et al.* (2004b) caution that the MAM applies only to sediments that have undergone partial bleaching and not necessarily to sediments where post-depositional mixing has introduced younger grains into the sample.

3.6.4 The finite mixture model (FMM)

The finite mixture model (FMM) is used when several discrete, well-bleached populations are present within the dataset and each population can be described by the central age model (Figure 3.5d) (Galbraith and Green, 1990; Galbraith *et al.*, 2006). As with the MAM, the FMM is run in the statistical program “R” with a user-defined value for the number of components (k) to be fit to the dataset. The programme calculates a D_b for each component in addition to the log likelihood and the Bayesian Information Criterion (BIC) used to assess the goodness of fit to the dataset. The dataset is repeatedly fit with an increasing number of components until the BIC reaches a minimum value representing the best fit, after which the BIC will continue to increase (Galbraith, 2005). The proportion of grains from each population is represented as a percentage to demonstrate the extent of heterogeneous bleaching.

The FMM has particular application to archaeological sites due to the mixing of grains from human activities (see Jacobs *et al.*, 2006b, 2008; David *et al.*, 2007).

However, it may also be relevant for fluvial sediments as shown by Rodnight *et al.* (2005). These depositional environments are capable of producing large overdispersion values and the FMM is only considered when the overdispersion value is greater than 20%.

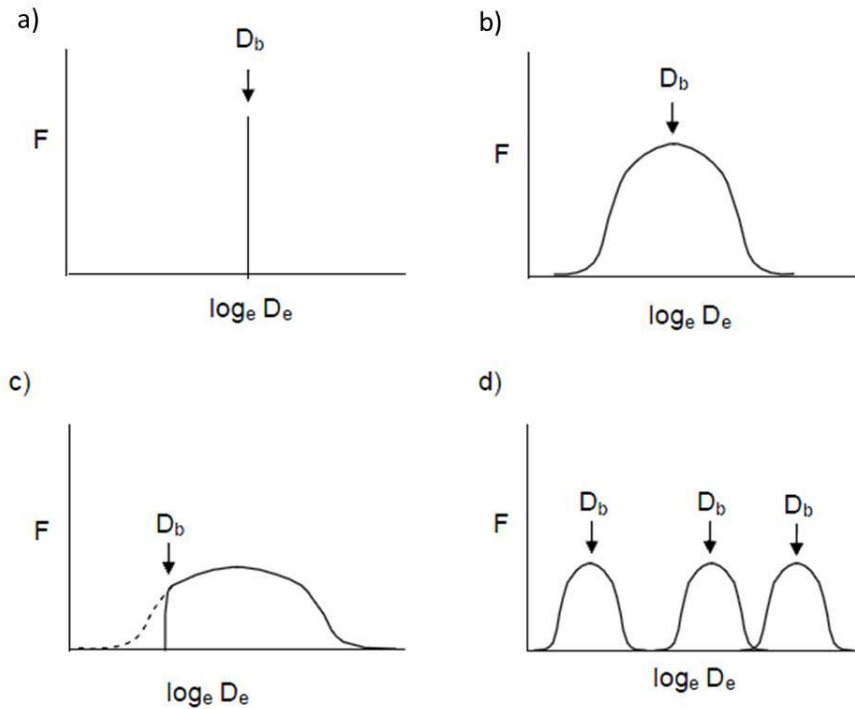


Figure 3.5: Schematic representation of the distribution of D_e values in the various age models: a) the common age model, b) the central age model, c) the minimum age model and d) the finite mixture model. The curve represents the D_e distribution, F is the frequency and D_b the burial dose value calculated by the model (Rodnight, 2006).

3.7 Calculating the environmental dose rate (D_r)

The environmental dose rate for each grain is produced by a combination of internal and external radiation, the former produced by alpha (α) and beta (β) radiation emitted by radioisotopes present within the grain and the latter by alpha (α), beta (β) and gamma (γ) radiation emitted by radioisotopes in the surrounding sediment in combination with a small dose of cosmic radiation (Aitken, 1985; Oczkowski *et al.*, 2000; Jacobs, 2004; Duller, 2008a; Guérin *et al.*, 2012).

3.7.1 Internal dose rate

The internal dose rate is produced by radiation emitted by radioisotopes present within individual grains of the sediment sample. Unlike feldspar grains which

contain high concentrations of potassium, quartz has very low potassium, uranium and thorium concentrations. Thus whilst a small amount of alpha activity may be produced within the individual grain it is largely held that the internal dose rate of quartz grains is negligible (Aitken, 1998). However, it is prudent to ascertain the internal dose rate via alpha-counting if the external dose rate is significantly low (Aitken, 1998). Jacobs (2004) measured an internal dose rate value of 0.029 ± 0.002 Gy/ka for samples from South Africa, which contributed $< 3\%$ to the total dose rate of the sample with the lowest environmental dose rate. This value corresponds to the range (0.01–0.05 Gy/ka) determined by Feathers and Migliorini (2001) for the attenuated internal alpha dose rate of East African quartz. Rodnight (2006) did not take into account the internal dose rate of fluvial sediments from South Africa based on the suggestion of Aitken (1985) that the internal dose rate is negligible and due to the small amount of sample obtained. This research project does not consider the internal dose rate for the reasons as stated by Rodnight (2006), and thus emphasis was placed on the external dose rate.

3.7.2 External dose rate

The environmental dose rate calculated for luminescence dating purposes is a result of the interaction of natural radioactivity with silt- and sand-sized grains (Figure 3.6). The radioisotopes responsible for the production of the external radiation are ^{40}K and ^{87}Rb and the decay chains of ^{232}Th , ^{238}U and ^{235}U , with roughly equal amounts from ^{40}K , ^{238}U and ^{232}Th and minor amounts from ^{87}Rb and ^{235}U (Aitken, 1985). Thus the external radiation source is a combination of α particles from the U and Th decay, β particles from U, Th, K and Rb decay and γ rays from U, Th and K decay with a small dose from cosmic radiation (Aitken, 1985; Rodnight, 2006). A relationship exists between soil, individual grains and the distance travelled by α particles ($\sim 1\text{--}5\ \mu\text{m}$), β particles ($\sim 2\ \text{mm}$) and γ rays ($\sim 30\ \text{cm}$) (Aitken, 1998; Duller, 2008a; Wintle, 2008), while cosmic rays are highly penetrating and dependent on latitude (increased dose rate towards the poles due to the Earth's magnetic field), altitude (increased dose rate at higher altitudes) and the depth of the sample (decreased dose rate with increased depth), referred to as the overburden (Prescott and Hutton, 1994; Aitken, 1998).

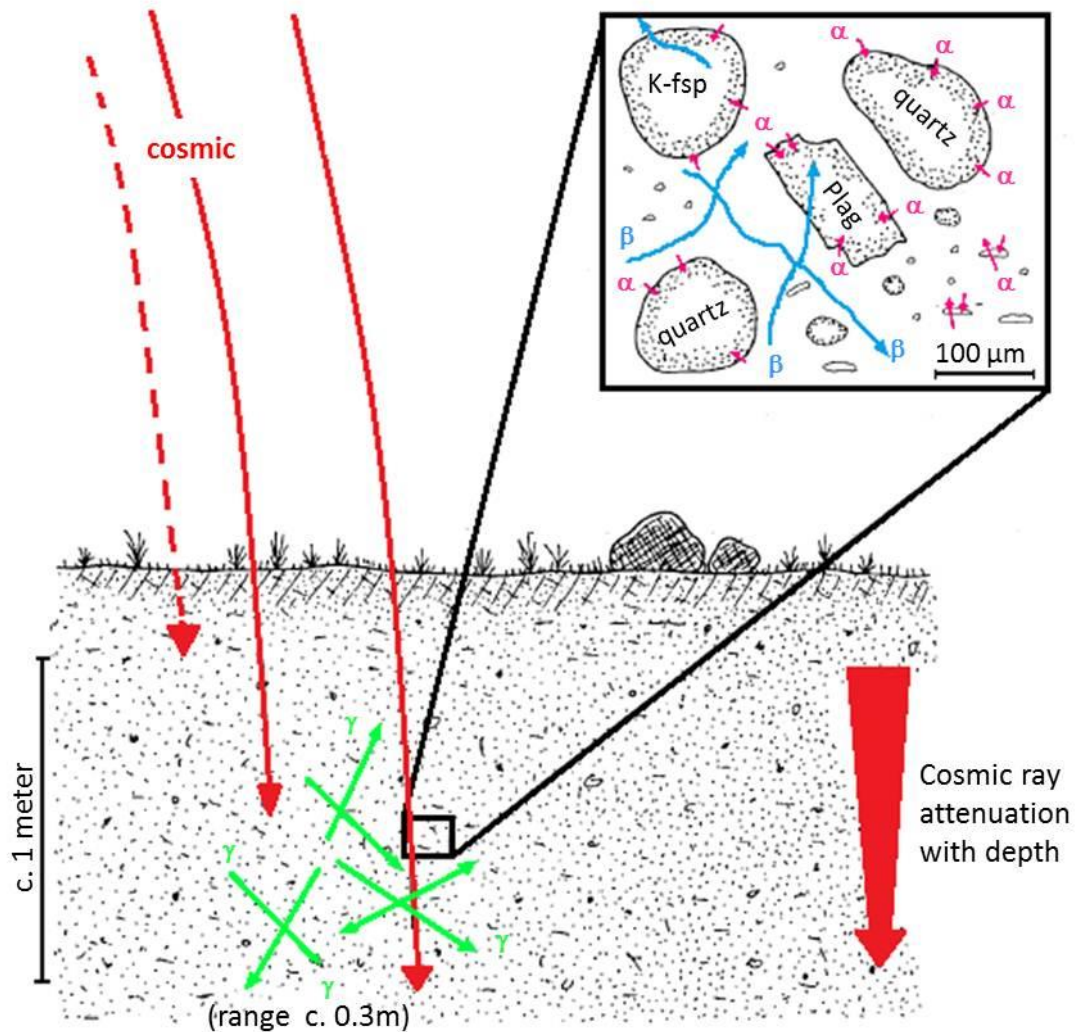


Figure 3.6: Natural radiation travelling through soil (after Aitken, 1998). Alpha particles (pink) travel up to 5 μm , beta particles (blue) travel up to 2 mm, gamma rays (green) travel up to 30 cm and cosmic rays (red) are dependent on the latitude, altitude and overburden.

3.7.2.1 Alpha particle contribution

A standard practice during the preparation of quartz samples for luminescence dating is the etching of grains in hydrofluoric (HF) acid in order to remove the alpha-irradiated skin (Wintle, 1997; Aitken, 1998; Oczkowski *et al.*, 2000; Brennan, 2006). This process removes the outer $\sim 10 \mu\text{m}$ of the grain, which equates to double the distance that alpha particles travel before they attenuate. Therefore the alpha particles do not reach the inner core of the grain and their influence is removed during sample preparation which allows the external alpha contribution to be excluded from the dose rate calculation (Aitken, 1998).

3.7.2.2 Beta particle and gamma ray contribution

The largest component of the external dose rate is composed of β and γ radiation produced by natural U, Th and K decay (Aitken, 1985; Ankjærgaard and Murray, 2007; Guérin *et al.*, 2012). Whilst decay chains exist for the parent isotopes ^{232}Th , ^{238}U and ^{235}U (Figure 3.7), ^{40}K decays directly into its stable daughter isotopes ^{40}Ar and ^{40}Ca through γ emission and β decay respectively (Aitken, 1985). Furthermore, the decay of ^{87}Rb to ^{87}Sr produces a very small contribution to the external dose rate due to the low energy β particles that are emitted (Warren, 1978). However, given the standard ratio of potassium to rubidium (200:1) and the negligible concentrations of potassium within quartz grains, the Rb contribution to the dose rate can be safely disregarded when working with quartz (Aitken, 1985; Warren, 1978).

3.7.2.3 Cosmic ray contribution

The contribution from cosmic rays to the environmental dose rate is usually fairly small and according to Aitken (1985) a standard value of 150 $\mu\text{Gy/a}$ is a valid assumption provided there are no special circumstances, such as weak sample radioactivity, high altitude or thick overburden. Alternatively, Prescott and Hutton (1994) present an equation, originally put forward by Barbouti and Rastin (1983), for the dose rate (D_0) delivered to a “standard rock”

$$D_0 = \frac{6072}{((x+11.6)^{1.68}+75)(x+212)} \exp(-5.50 \times 10^{-4}x) \quad (3.3)$$

where x is the depth in hg cm^{-2} and D_0 is in Gy/ka , which is valid from 1.5 hg cm^{-2} to 50 hg cm^{-2} . The dose rate must be corrected for the geomagnetic latitude (λ) of the sample site, using the equation:

$$\sin \lambda = 0.203 \cos \theta \cos(\phi - 291) + 0.979 \sin \theta \quad (3.4)$$

where θ is the geographic latitude and ϕ the geographic longitude, with positive values indicating north and east and negative values south and west. The dose rate must then be corrected for altitude using:

$$D = D_0 [F + J \exp \frac{h}{H}] \quad (3.5)$$

where D is the corrected cosmic dose rate, h is the altitude in km and F , J and H are read from the graph (Figure 3.8) using the calculated geomagnetic latitude value (Prescott and Hutton, 1994). The error on the cosmic dose rate is assumed to be 10 % of the total cosmic dose rate.

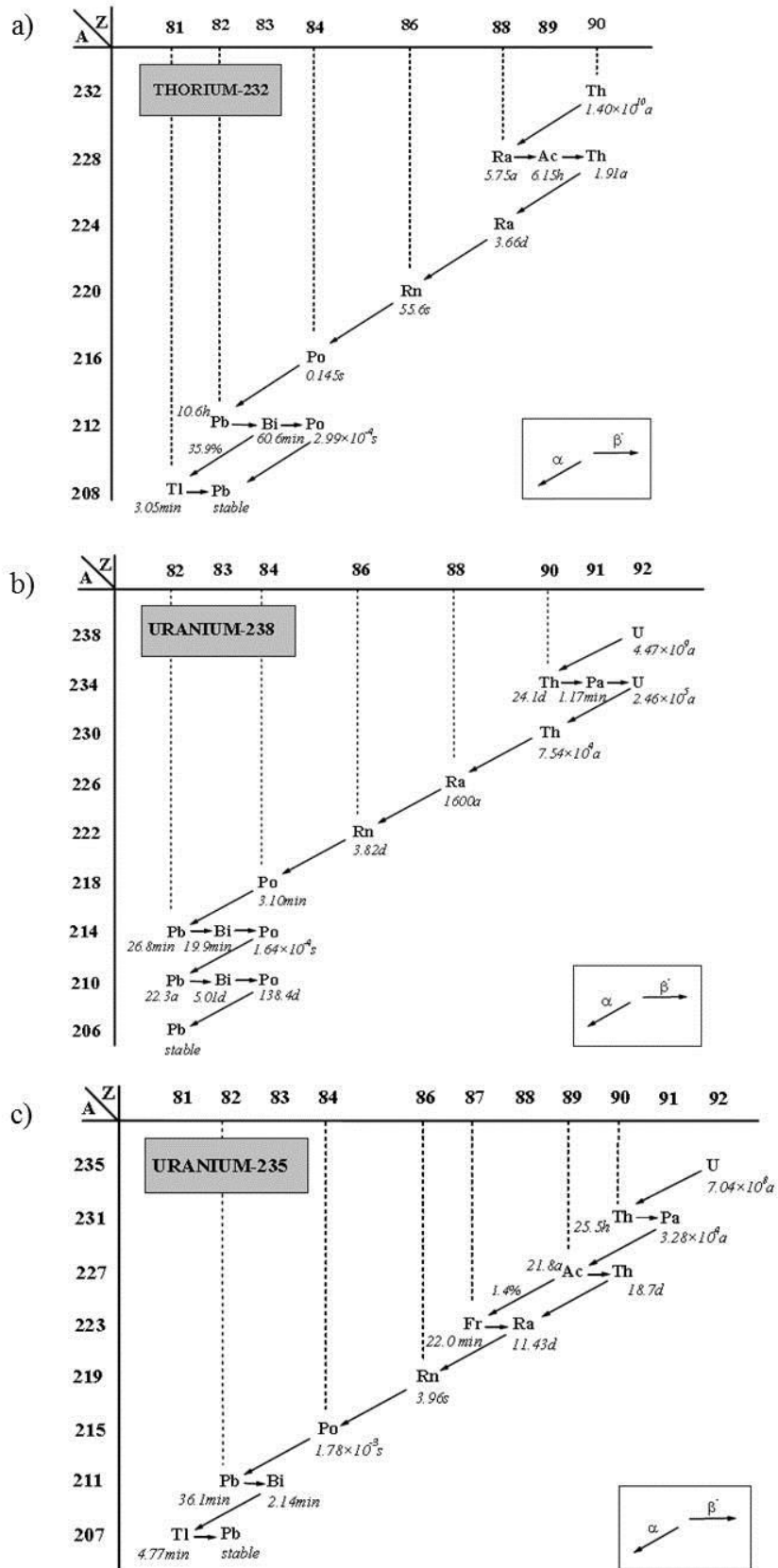


Figure 3.7: Decay chains for the parent isotopes (a) ^{232}Th , (b) ^{238}U and (c) ^{235}U . The half-life of each isotope is indicated, with alpha decay represented by diagonal arrows and beta decay by horizontal arrows (Aitken, 1985).

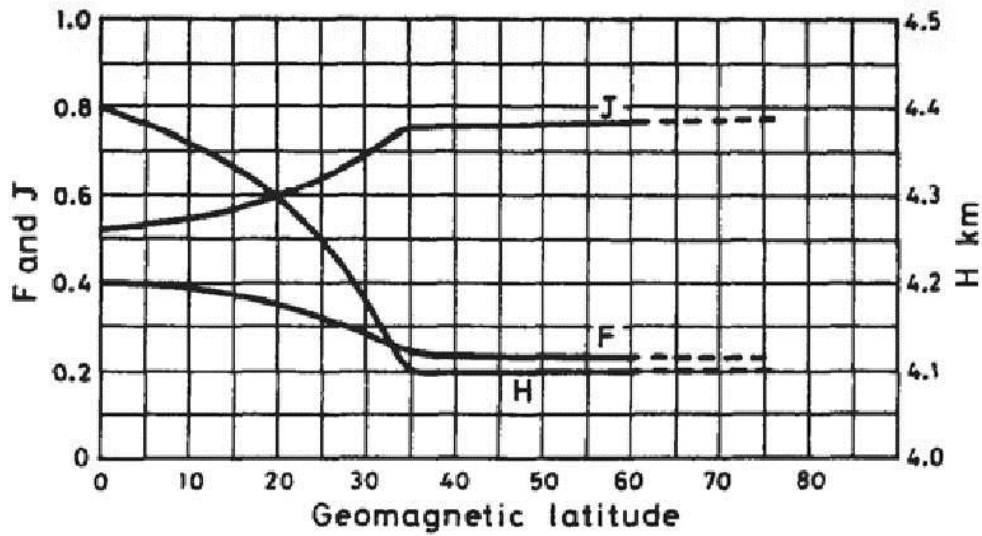


Figure 3.8: Parameters for determination of the cosmic dose rate as a function of altitude and geomagnetic latitude (Prescott and Hutton, 1994).

3.7.2.4 Water content corrections

Water is capable of absorbing beta and gamma radiation, thus water located within the pore spaces of sediments lowers the amount of radiation that is able to reach the grains and a correction is required to prevent an underestimation of the dose rate (Aitken, 1998). The corrections to the beta and gamma dose rates for water content are accomplished using the equations of Aitken and Xie (1990):

$$\beta_{\text{wet}} = \frac{\beta_{\text{dry}}}{(1+1.25WF)}, \text{ and} \quad (3.6)$$

$$\gamma_{\text{wet}} = \frac{\gamma_{\text{dry}}}{(1+1.14WF)} \quad (3.7)$$

respectively, where β_{wet} and γ_{wet} are the beta and gamma dose rates of wet soil, β_{dry} and γ_{dry} are the dry soil dose rates and W is the saturation water content for F , which is the average level of saturation in the sample over the burial period expressed as a fraction of W . The value 1.14 for the gamma correction and 1.25 for the beta correction was proposed by Zimmerman (1971) because they are the ratios of the coefficients of water to aluminium (which has absorption properties similar to that of soil) for gamma rays and beta particles of 1 MeV.

3.7.3 Disequilibrium in the decay chain

Luminescence dating utilises long-term radioactivity with respect to the age span of the sample (Aitken, 1985). Since the extent of OSL dating using feldspars is 10^6 years and the extent of quartz is less than that, and the half-lives of the parent

isotopes are in the order of 10^9 years, the natural abundance of the parent isotopes should remain effectively constant over the time span of interest (Rodnight, 2006). This remains true until the system undergoes disequilibrium, whereby an isotope is removed from or added to the system without its relevant parent or daughter isotope, thereby decreasing or increasing the amount of one isotope with respect to the other (Olley *et al.*, 1996). Thus if a parent isotope is removed, the amount of the daughter isotope will decrease exponentially with time until the system attains equilibrium once again; this applies to all successive members of the decay chain.

Several processes may result in disequilibrium of the decay chain, the most common being the diffusion of radon (Rn) gas through the pore spaces of the sediment (Aitken, 1985; Aitken, 1998). Radon is present midway through all three decay chains in gaseous form; however ^{220}Rn from the ^{232}Th series and ^{219}Rn from the ^{235}U series both have very short half-lives (55 s and 4 s respectively) thus they usually decay to non-gaseous daughter isotopes before they have the opportunity to diffuse out of the sample. Alternatively, ^{222}Rn from the ^{238}U series has a half-life of 3.82 days which allows it sufficient time to diffuse out of the sample, thereby lowering the activity of radon and all its daughter isotopes with respect to its parent isotope ^{226}Ra (Aitken, 1985; Prescott and Hutton, 1995; Olley *et al.*, 1996; Oczkowski, 2001). Disequilibrium may also be caused by water soluble isotopes which are susceptible to leaching by ground water; ^{238}U , ^{234}U and ^{226}Ra are particularly mobile with all three produced by the ^{238}U decay series (Olley *et al.*, 1996; Oczkowski, 2001; Duller, 2008a). Another cause is the incorporation of ^{234}U (to the exclusion of its daughter ^{230}Th) into calcite (CaCO_3) which is common in speleothems and results in the presence of U isotopes without any daughters and a gradual buildup over time throughout the rest of the series determined by the half-life of Th; this process provides the basis of the uranium-series disequilibrium dating method (Aitken, 1985; Walker, 2005).

Krbetschek *et al.* (1994) emphasise that any uncertainty when determining the upper members of the decay chains can produce large errors due to the fact that the entire chain is included. Given the short half-lives of the long-lived daughter products of ^{232}Th , the decay chain is expected to be in secular equilibrium in most natural materials. Alternatively, the daughters of the ^{238}U decay chain have sufficiently long

half-lives that any disequilibrium within the chain may persist for millennia and disequilibrium may be common within surficial environments (Olley *et al.*, 1996). Furthermore, secular disequilibrium is common in fluvial sediments where a slight depletion of ^{234}U commonly occurs due to leaching because of its high mobility. Olley *et al.* (1996) believe that disequilibrium of the U chain should be expected in surficial materials due to the relatively short time scale of weathering processes that occur at surface level.

Should the decay chain be in a state of disequilibrium it becomes impossible to determine the environmental dose rate based solely on the concentrations of the parent isotopes, and emission counting methods (which calculate the concentration of the parent radionuclides) become unsuitable for calculation of the dose rate. Thus it is necessary to consider techniques such as high-resolution gamma spectrometry (HRGS), inductively coupled plasma mass spectrometry (ICP-MS) or a combination of techniques. Olley *et al.* (1996) used HRGS to explore the degree of disequilibrium in the ^{232}Th and ^{238}U decay chains from modern fluvial sediments. They found that while the ^{232}Th chain was generally in secular equilibrium several individual samples had concentrations of ^{228}Ra in excess of ^{232}Th due to recent rapid radium redistribution. However the short half-life of ^{228}Ra (5.75 a) makes this of little concern. Conversely, significant disequilibrium in the ^{238}U chain was evident, but it was typically < 20 % and rarely exceeded 50 %. Krbetschek *et al.* (1994) utilised HRGS in conjunction with alpha spectrometry to investigate the uranium fraction ($^{234}\text{U}/^{238}\text{U}$) that occurs in various depositional environments and found that disequilibrium occurs in limnic sediments (associated with a body of fresh water) due to ^{234}U enrichment and in fluvial sediments due to ^{234}U depletion. Preusser and Degering (2006) used HRGS confirmed by ICP-MS to identify disequilibrium between ^{238}U and ^{226}Ra in sediments from the Niederweningen mammoth site in Switzerland indicating a strong differentiation during peat formation and/or an uptake of radionuclides after deposition. However, they concluded that the disequilibria produced only minor uncertainty in the dates whilst the major uncertainty was due to difficulties estimating the water content of the sediments over time. Using data acquired from HRGS and ICP-MS, Zander *et al.* (2007) used the ADELE software to model closed and open systems with linear U and Ra uptake on shallow marine and intertidal shell-rich sediments from Dubai, and concluded that

marine sediments with significant U disequilibrium can be effectively dated by OSL when an appropriate model of the influence of U-disequilibrium and a time-dependent dose rate is utilised.

Considering the frequency with which secular disequilibrium of the ^{238}U decay chain occurs, it is necessary to assess any possible disequilibrium in samples. Furthermore, the general consensus is that more than one method is required to be used in conjunction to obtain an accurate estimation.

3.8 Suitability of OSL and ^{14}C dating for the Nyl/Mogalakwena River and Rooisloot sediments

Based on the model proposed by McCarthy *et al.* (2011) regarding the nature of the Nyl/Mogalakwena River and Rooisloot sediments (see Figure 1.5), the interlayered sediments observed in the vertical profiles within the incised tributary fan were formed by the alternating deposition of prograding tributary fan sediments with floodplain sediments. The fine-grained floodplain sediments are well-suited to ^{14}C dating due to their generally organic-rich nature and the expected young ages which are well within the 45-50 ka dating limit (Walker, 2005; Hua, 2009; Reimer *et al.*, 2009). These reasons combined with the wide acceptance of the ^{14}C dating technique within the Quaternary research community lead to the selection of ^{14}C dating as an independent age control for the OSL ages. The coarse-grained fluvial deposits are suited to OSL dating due to the quartz- and feldspar-rich nature of the sediments and the expected young ages of the samples which are within the dating limit of ~ 150 ka.

Whilst the suitability of the OSL technique is not in question, the constituent material used to obtain the OSL dates in this research project must be considered. Given the nature of the Nyl/Mogalakwena River setting it was decided to use quartz grains as opposed to feldspar for several reasons. First, the sediment deposition probably occurred very recently (Late Holocene), thus the luminescence signal from the quartz grains should be well below saturation and therefore within the lower age bracket of quartz. Second, South African quartz grains in general have proved to be sufficiently sensitive to act as natural dosimeters (Armitage *et al.*, 2000) and the negligible amount of K in the quartz grains makes the determination of the internal

dose rate from the grains unnecessary (Aitken, 1998). Third, unlike feldspar, quartz does not suffer from the effects of anomalous fading and fourth, the issue of feldspar contamination and the additional luminescence signal upon stimulation can be monitored using the OSL-IR depletion ratio test (Duller, 2003).

3.8.1 Previous dating studies undertaken on the Nyl/Mogalakwena River floodplain

One other independent geochronological study has been undertaken on the Nyl/Mogalakwena River floodplain. This study by McCarthy *et al.* (2011) collected sediments for OSL dating from exposures along the Rooisloot, located upstream from the sites sampled for this research project (see Figure 2.3, site location labelled “1”). McCarthy *et al.* (2011) identified two units: the basal unit, a hematite-cemented sand gave a minimum age of 226 ka, and the overlying unit composed of coarse yellow sand gave ages ranging from 518 ± 22 years to 833 ± 37 years. The lower unit is likely located stratigraphically below the profile sections analysed in this research project whilst the upper unit may occur at the same stratigraphic level.

3.9 Summary

In order to produce a palaeo-environmental reconstruction it is necessary to obtain accurate information regarding the timing of certain events, the duration of relevant phases and the rate at which certain processes occur (Vandenberghe, 2004). To that end two separate dating techniques have been selected in order to produce a detailed geochronology of the Nyl/Mogalakwena River and Rooisloot sediments, specifically OSL and ^{14}C dating.

The OSL date is calculated using the total radiation dose absorbed by the sample during burial (equivalent dose (D_e)) and the amount of energy absorbed per year (dose rate (D_r)) due to radioactive decay in the surrounding sediments and cosmic radiation. OSL dates the time of burial of constituent mineral grains and is suitable for dating the quartz-rich, sand-sized tributary fan deposits.

The D_e comprises half of the age equation for OSL dating. Single aliquot techniques are the currently accepted method to measure the D_e , most commonly the Single Aliquot Regenerative Dose (SAR) protocol formalised by Murray and Wintle (2000). The SAR protocol corrects the natural OSL signal for sensitivity by

administering a test dose which deals with the sensitivity change issue arising in the quartz grains due to repeated beta dosing. A series of preliminary tests are run to determine the suitability of the quartz for the SAR protocol, specifically the preheat test, dose recovery test, recycling ratio test and recuperation test. After the luminescence signal is measured the resulting D_e values are analysed statistically to determine the representative average called the true burial dose (D_b). The D_b is used in conjunction with the D_r to calculate the OSL age.

Natural radioactivity is produced by α and β emissions from radioisotopes present within individual sediment grains, called internal radiation, α , β and γ emissions from radioisotopes in the surrounding sediment, called external radiation, and cosmic radiation. The internal dose rate for quartz grains is negligible and the contribution from the external alpha particles is removed during sample preparation. Therefore these two values can be excluded from the determination of the environmental dose rate. Thus the main contributors to the D_r are external beta and gamma radiation with a small component from cosmic radiation.

The ^{14}C -dating technique, chosen to act as the independent age control for the OSL dates, is based on the radioactive decay and half-life of the ^{14}C -isotope relative to the level of ^{14}C in the atmosphere. The ^{14}C dating technique dates associated organic material, such as charcoal; and is suitable for dating the organic-rich, fine-grained floodplain deposits. Given the expected recent deposition of the sediments (based on the OSL ages obtained by McCarthy *et al.* (2011)) the sediments are well within the age limits of both techniques, 45–50 ka for ^{14}C dating and ~ 150 ka for OSL dating.

Chapter 4:

Equivalent Dose (D_e) Determination

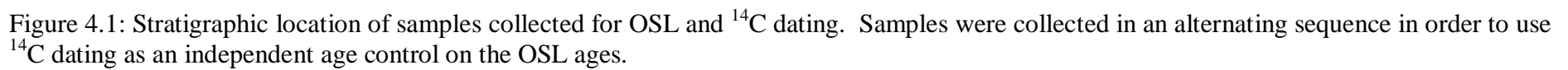
4.1 Introduction

In order to determine the depositional age of sediments using OSL dating, the equivalent dose (D_e) value and the environmental dose rate (D_r) are required. The D_e is defined as the laboratory dose equivalent to the amount of radiation the sediment received during burial *i.e.* the natural dose (Duller, 2008a). Thus a minimum of two measurements are required for the determination of the D_e , the natural dose and the known radiation dose given in the laboratory. To obtain these values, the luminescence signal of the sample is measured on a Risø TL/OSL reader using beta irradiation and optical stimulation.

4.2. Sampling strategy

The sampling sites were selected along the banks of the Nyl/Mogalakwena River and within the Rooisloot tributary fan (see Section 2.3 and Figure 2.4). Within each of the four vertical profiles, horizontal layers were identified and sampled for grain size, OSL and ^{14}C as per Table 2.2. Layers of quartz-rich sediments with sand-sized grains were selected for OSL dating, whereas organic-rich layers with clay- or silt sized grains were selected for ^{14}C dating. The interlayered nature of the sedimentary layers allowed the OSL samples to be constrained by ^{14}C samples, *i.e.* one ^{14}C sample was collected from between two OSL samples (Figure 4.1). In total eight ^{14}C samples and eleven OSL samples were collected. Duplicates of the OSL samples were collected in case repeat measurements were required.

OSL samples were collected in the field in 30 mm diameter stainless steel tubes. The ends of the tubes were stuffed with bubble wrap and secured with light-tight tape. After sampling, which required hammering the tubes horizontally into the selected layers, the tubes were then double-bagged in black plastic bags for transport in a sealed crate back to the Geoluminescence Laboratory at the University of the Witwatersrand. Ten OSL samples were shipped to Aberystwyth University for measurement and the duplicate samples remained at the University of the



Witwatersrand. In the end, three samples were measured at the University of the Witwatersrand (Table 4.1) when the original dates obtained at Aberystwyth University did not correlate with the remainder of the OSL ages in terms of the stratigraphic section (see Table 6.1).

Table 4.1: Samples measured at Aberystwyth University and the University of the Witwatersrand

Sample	Aberystwyth Univeristy	University of the Witwatersrand
NV-A2	No	Yes
NV-A6	Yes	No
NV-A9	Yes	No
NV-B10	Yes	No
NV-B7	Yes	No
NV-B1	Yes	No
NV-C2	Yes	Yes
NV-C4b	Yes	Yes
NV-C7	Yes	No
NV-D2	Yes	No
NV-D7	Yes	No

4.3 OSL Sample preparation

All thirteen samples for OSL analysis were opened and prepared under controlled red-light conditions. However, to remove any sample potentially exposed to light during sample collection, the outer portion of sediment in each tube (between 3 cm and 5 cm) was removed and used for dosimetry measurements and determination of the water content (Figure 4.2). A minimum of 200 g of unexposed sediment from the centre of each sample tube was placed into a labelled beaker for treatment following the standard procedure used at Aberystwyth University (described in sections 4.3.1 to 4.3.5). Samples did not have a large proportion of fine grains, thus the removal of fines through deflocculants and wet sieving was deemed unnecessary.

4.3.1. Removal of carbonates

The sample was covered with 1–2 cm of 10 % hydrochloric acid (HCl) in the beaker and stirred periodically to enable chemical reactions to occur. Samples showed very minor or no reaction to the addition of HCl, but following standard procedure a

second wash of HCl was added to each sample. Once any reactions had ceased, samples were rinsed in distilled water three times.

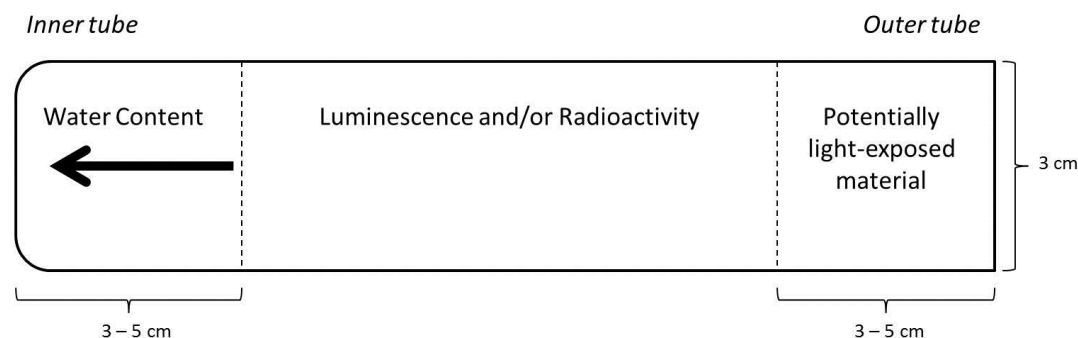


Figure 4.2: Schematic representation of a sample tube used to collect the OSL sample in the field and how the sample was split in the laboratory. The arrow indicates the orientation of the tube as it was inserted into the sediment.

4.3.2 Removal of organics

The removal of organic matter was completed using 20 % hydrogen peroxide (H_2O_2). As with HCl, the samples were stirred periodically and additional H_2O_2 was added until the reactions ceased. The reactions of the samples varied at this stage and the length of time taken varied between one and two months. Only weak to moderate reactions were observed, indicating that the organic content of the samples was indeed low, and once reactions had ceased the samples were rinsed three times with distilled water and dried at 50 °C in an oven.

4.3.3 Dry sieving

Each sample was dry sieved through a set of eight sieves (90, 125, 150, 180, 212, 250, 300 and 356 μm mesh size) for 45 min using an automatic shaker. The grain size fractions 180–212 μm and 212–250 μm were retained for further processing.

4.3.4 Extraction of quartz grains

The 180–212 μm and 212–250 μm fractions of multi-mineral sample underwent two stages in order to separate the quartz grains from all other minerals. In the first stage, sodium polytungstate (SPT) solution was diluted with distilled water to obtain a solution with a density of 2.62 g/cm^3 , and the quartz grains were separated from

feldspar grains and other lighter-density minerals ($\rho < 2.62 \text{ g/cm}^3$) via gravity settling. The sample was rinsed three times in distilled water and dried in an oven at 50°C overnight. A second batch of SPT was diluted to a density of 2.70 g/cm^3 and the process was repeated in order to remove any heavy minerals ($\rho > 2.70 \text{ g/cm}^3$). The sample was then rinsed three times in distilled water and dried overnight. The remaining sample represented the quartz-rich fraction ($2.62 \text{ g/cm}^3 < \rho < 2.70 \text{ g/cm}^3$) and was used in the second stage of quartz extraction.

The second stage in the extraction of quartz grains required a 45 min hydrofluoric acid (HF) etch which removed any feldspar contamination and the alpha-irradiated skin from the quartz grains. This was followed by a 40 min treatment in HCl to remove any fluoride precipitates. The grains were then rinsed in distilled water three times and dried in the oven overnight.

The remaining grains were re-sieved using sieve mesh sizes of 180, 212 and $250 \mu\text{m}$ with the $180\text{--}212 \mu\text{m}$ and $212\text{--}250 \mu\text{m}$ fractions once again being retained for the OSL analysis. All analyses were run on the $180\text{--}212 \mu\text{m}$ fraction with the $212\text{--}250 \mu\text{m}$ fraction stored in reserve in case the former fraction did not produce enough material for analyses.

4.3.5 Disc preparation

All samples of etched $180\text{--}212 \mu\text{m}$ quartz were analysed using single-aliquot measurement techniques and two samples were selected for single-grain analyses. Multiple grain aliquots (used for the single aliquot technique) were prepared on stainless steel discs of diameter 9.7 mm . The discs were covered with a mask of the chosen size (3 mm , 5 mm or 7 mm , termed small, medium and large respectively; Figure 4.3(a-c)) and sprayed with *Silkospray* silicon spray. The discs were then placed onto the prepared quartz grains which adhered to the silicon spray and tapped gently to remove any loose grains resulting in a disc with a single layer of grains adhered to the surface of the disc. Medium (5 mm) aliquots were used in the initial tests and small (3 mm) aliquots for all the subsequent OSL analyses due to the very bright signal emitted by the quartz grains. Duller (2008a,b) calculated that the average number of grains on a small aliquot can range from 10 to 1 000, whilst a

medium aliquot ranges from 100 to 1 500 grains and a large aliquot up to 10 000 grains depending on the exact size of the mask used.

Single-grain aliquots (Figure 4.3(d)) are composed of 1 mm thick, 9.7 mm diameter aluminium discs with a 10 x 10 grid of holes (diameter 300 μm and depth 300 μm) drilled into the surface. Quartz grains were poured onto the surface of the disc and gently brushed across to encourage grains to fall into each hole and to remove any loose grains from the surface. It is common for more than one grain to fall into a single hole when smaller grain sizes are used in OSL analyses, thus the 180–212 μm fraction is ideally suited to single-grain discs. Once the discs were prepared they were placed onto the carousel and loaded into the Risø reader to undergo luminescence measurements.

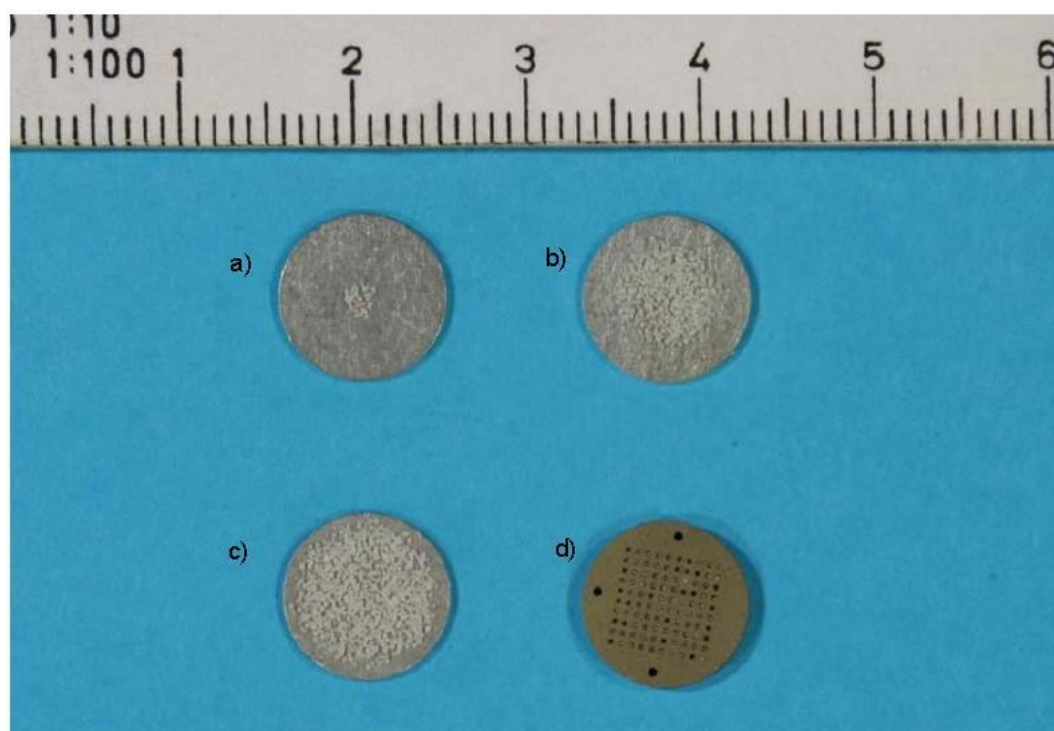


Figure 4.3: Examples of prepared aliquots: (a) small multiple-grain, (b) medium multiple-grain, (c) large multiple-grain and (d) single-grain aliquots (Rodnight, 2006). Multiple grain aliquots are used in single aliquot measurement techniques, such as the SAR protocol. The quartz OSL signal was bright enough that large multiple-grain aliquots were not necessary in this research project, preliminary tests were run on medium aliquots and all D_e measurements were done on small aliquots. Single-grain analyses were run on selected samples.

4.4 Instrumentation

Measurement of the luminescence signal utilising the SAR protocol requires a series of measurements to be made per aliquot. This is possible due to the automated Risø TL/OSL readers, the development and modifications of which are described in great detail by Bøtter-Jensen (1997) and Bøtter-Jensen *et al.* (1999a, 1999b, 2000, 2002). All single aliquot luminescence measurements were obtained on Risø 1 and the single grain measurements on Risø 3 at Aberystwyth University. Three samples (NVA2, NVC2 and NVC4b) were re-measured at the University of the Witwatersrand on Risø B because the author had already left Aberystwyth. The specifications of the readers used in this research project are included in Table 4.2.

Table 4.2: Specifications of the Risø readers used in this research project

	Aberystwyth Univeristy		University of the Witwatersrand
Reader	Risø 1	Risø 3	Risø B
System type	TL-DA-10	TL-DA-15	TL-DA-20
Carousel positions	24	48	48
Beta source type	$^{90}\text{Sr}/^{90}\text{Y}$	$^{90}\text{Sr}/^{90}\text{Y}$	$^{90}\text{Sr}/^{90}\text{Y}$
Irradiation mechanism	Shutter	Rotating	Rotating
Dose-rate (Gy/min)	2.45 ± 0.05	5.43 ± 0.10	8.32 ± 0.93
Dose-rate (Gy/sec)	0.04 ± 0.00	0.09 ± 0.00	0.14 ± 0.02

The Risø readers are controlled by “MiniSys” controllers described by Markey *et al.* (1997) with the laboratory irradiation delivered from mounted $^{90}\text{Sr}/^{90}\text{Y}$ beta sources. There were two types of irradiation sources used in this research project, the shutter source (Risø 1) and the rotating source (Risø 3 and Risø B). The shutter source has a shutter located between the source and the aliquot, so when a dose is delivered the shutter is withdrawn and radiation of the aliquot occurs, whilst the rotating source positions itself directly above the aliquot, delivers the dose and inverts 180° before it ceases irradiation *i.e.* it begins irradiation once it is pointing downwards and ceases when it is pointing upwards (Markey *et al.*, 1997; Jacobs, 2004). Markey *et al.* (1997) determined the precision with which the two source types delivered small doses (1–5 s) and identified constant offset values of 0.04 s for the shutter source and 0.11 s for the rotating source. They concluded that the offset value was more

relevant to short irradiation times than to long irradiation times and therefore the shutter system is more appropriate for use with younger samples due to the delivery of more accurate short irradiations. The length of time a sample is irradiated for depends on the dose rate of the beta source, thus the dose rate for each reader needs to be accurately calibrated prior to measurement of the luminescence signal.

4.4.1. Calibration of the beta sources

Three Risø readers were used to measure the D_e values in this research project, Risø 1 and 3 at Aberystwyth University and Risø B at the University of the Witwatersrand. Manual calibration of the mounted beta source in Risø 1 was undertaken prior to sample measurement during September 2011 using 180–212 μm gamma-irradiated calibration quartz provided by Risø, with a known dose of 4.81 ± 0.07 Gy. Medium aliquots (~ 5 mm) of calibration quartz were measured using the standard SAR procedure and the resulting D_e value used to determine the beta dose rate. Manual calibration of Risø 3 for single-grain measurements was carried out in January 2012 and Risø B in July 2012. The same batch of calibration quartz and the same procedure was used for the calibration of all three readers. The dose rate calculations for each of the reader calibrations are included in Appendix C.

4.5 Optical stimulation

A range of stimulation sources have been used in OSL measurements in the past. In the original OSL work Huntley *et al.* (1985) used a 514 nm argon ion laser, Galloway (1994) and Galloway *et al.* (1997) used 565 nm green LEDs, Poolton and Bailiff (1989) and Spooner *et al.* (1990) used infrared (IR) diodes, and Bøtter-Jensen *et al.* (1993) and Bøtter-Jensen and Duller (1992) used a broad blue/green band (420–550 nm) from filtered halogen lamps. The newer model readers feature an OSL unit which consists of a combination of blue and IR LEDs (Bøtter-Jensen *et al.*, 2003).

The use of blue LEDs, with a peak emission at 470 ± 20 nm, is discussed by Bøtter-Jensen *et al.* (1999a, 1999b) as an alternative to the blue/green broad band. Advantages of the blue LEDs include lower cost, smaller more compact size, negligible heat dissipation, the electronic control of power delivery and the switch on

and off times are 10 times quicker than a shutter. Hong and Galloway (2000) compared the use of blue versus green LEDs on sedimentary quartz and found that D_e values determined from measurements made with blue LEDs showed better precision. All the readers used in this research project used blue LEDs for optical stimulation and either an IR laser diode or IR LEDs to test the purity of the samples with respect to feldspar contamination.

4.5.1 Single aliquot stimulation

Single aliquot (multiple grain) stimulation was carried out by blue LEDs with a peak emission at 470 nm for the measurement of the quartz OSL signal. Due to the bright OSL signal produced by the Nyl/Mogalakwena River and Rooisloot quartz, the LEDs were run at 75 % power. Technical specifications for Risø 1 state the stimulation power is 83 mW/cm² at 100%, which corresponds to 62.25 mW/cm² at 75% power. Feldspar contamination in samples was monitored using stimulation by an infrared laser emitting at 890 nm at 100 % power (161 mW/cm²). The rate at which electrons are evicted from the traps depends on the optical stimulation power, therefore a higher stimulation power results in a more rapid decay of the OSL signal (Rodnight, 2006).

4.5.2 Single-grain stimulation

Stimulation for single-grain measurements is performed by a 10 mW Nd:YVO₄ solid state diode-pumped laser, with a peak emission at 532 nm, which is significantly different from the peak emission of 470 nm used in single aliquot stimulation. Duller and Bøtter-Jensen (1996) investigated the OSL signal from quartz stimulated at various wavelengths ranging from 425 nm to 575 nm and determined that a similar set of traps was being used to produce the different signals (Figure 4.4), which behaved almost identically. Furthermore, this finding supported the study by Ditlefsen and Huntley (1994), who used lasers ranging from 458 nm to 645 nm to stimulate a single trap. Therefore it can be concluded that the same traps in quartz are stimulated by both the blue diodes used for multiple-grain stimulation and the laser used in single-grain stimulation (Rodnight, 2006).

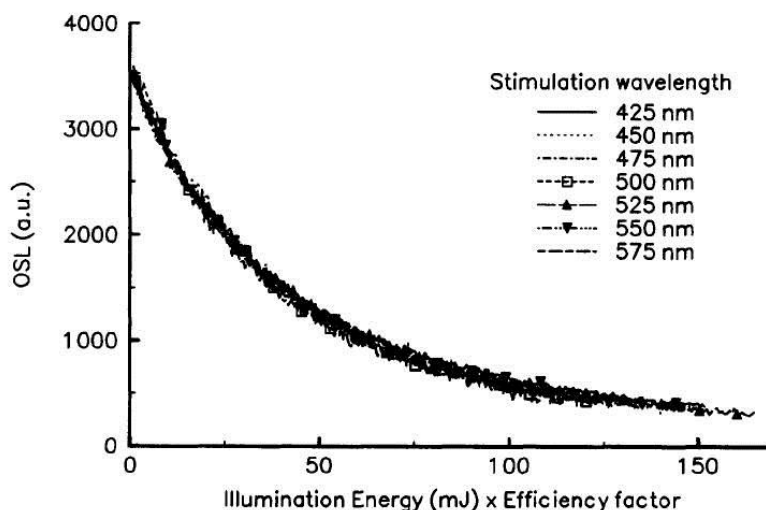


Figure 4.4: OSL decay curves for various stimulation wavelengths (Duller and Bøtter-Jensen, 1996).

4.5.3 Optical filters

To ensure that no scattered light from the stimulation source reaches the photomultiplier tube (PMT), various filters are used. The blue LED emission spectrum is centred on 470 nm (Figure 4.5a), therefore the most commonly used filter to block the LED signal is the Hoya U-340, centred on 340 nm because the light used to stimulate the sample must be at a different wavelength than the light emitted by the sample grains (Duller, 2008a). Detection of the luminescence signal occurs through three stacked U-340 filters fitted in front of the photomultiplier tube (Figure 4.5b), one of which is coated in metal oxide to reduce stray transmission in the red spectrum (Bøtter-Jensen *et al.*, 1999b). The green long-pass Schott GG-420 filter (Figure 4.5b) fitted in front of the individual blue LED clusters minimises the directly scattered blue light that is able to reach the photomultiplier cathode (Bøtter-Jensen *et al.*, 1999b).

4.6. Measurement of the luminescence signal

4.6.1 Preliminary tests for the SAR protocol

Several preliminary tests (see section 3.5.3) were completed on randomly selected samples (NVA6 and NVC4b) prior to the measurement of the D_e to determine the

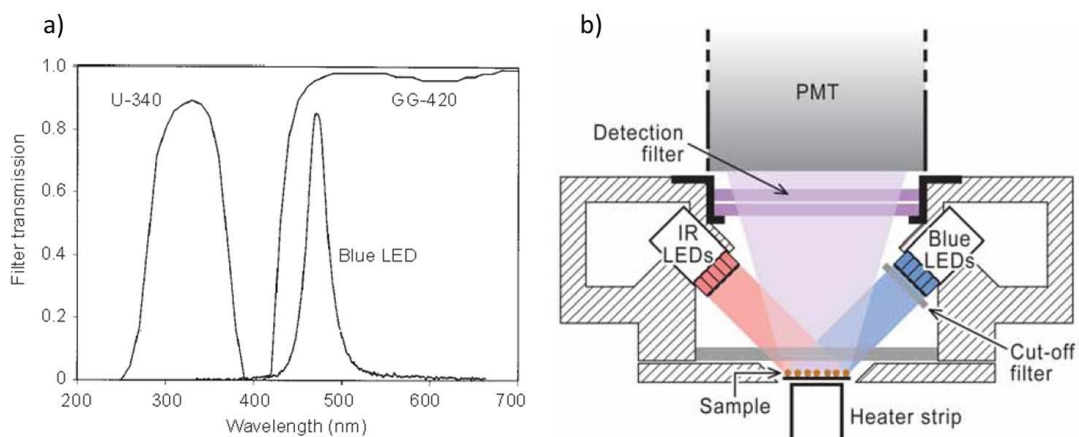


Figure 4.5: (a) Emission spectrum of the blue LEDs and the transmission curves for the Hoya U-340 detection filter and the Schott GG-420 green long-pass filter (Bøtter-Jensen *et al.*, 1999a,b). (b) The Hoya U-340 is the detection filter fitted below the photomultiplier tube (PMT) and the Schott GG-420 the cut-off filter fitted in front of the blue LED clusters (Duller, 2008).

suitability of the SAR protocol for the Nyl/Mogalakwena River and Rooisloot quartz.

4.6.1.1 The preheat and dose-recovery tests

The preheat test and dose-recovery test were combined and run on the same SAR sequence using 24 medium aliquots of quartz and the standard SAR protocol. Three aliquots were measured for each temperature at 20 °C intervals between 160 °C and 300 °C using a fixed cutheat of 160 °C. These values were plotted (Figure 4.6) and no preheat plateau was identified. However, three preheat temperatures plot at a similar D_e , specifically 160 °C, 200 °C and 220 °C. Thermal transfer is common at high preheat temperatures (200–300 °C; Wintle and Murray, 2006) and the outliers at 260 °C and 300 °C are an indicator that thermal transfer is occurring in this sample at temperatures above 240 °C. Therefore, the preheat temperatures which show the least amount of scatter, and are thus the most suitable temperatures are 160 °C, 200 °C and 220 °C. The preheat temperature of 180 °C was excluded because it is an outlier and it failed the dose-recovery test.

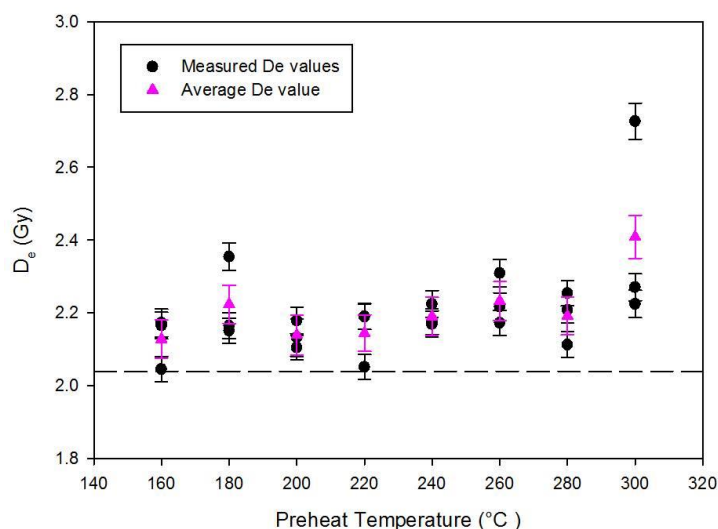


Figure 4.6: Plot of preheat temperature against D_e for sample NVA6. The dashed line represents the given dose of 2.04 Gy.

The dose recovery test required the sample to be bleached in order to remove the natural signal (done using two separate OSL stimulations of 100 s at 25 °C separated by a 420 s pause) prior to laboratory irradiation of a known dose of 2.04 Gy. The given dose was then treated as an unknown and obtained through the SAR protocol in order to determine the ratio between the given and measured dose. The ratio was consistent with unity for preheat temperatures at 160 °C (Figure 4.7), 200 °C and 220 °C, with ratio values of 1.04, 1.05 and 1.05 respectively. Since 160 °C and 220 °C were the only temperatures to recoup the exact given dose, and because the measured/given dose ratio was closer to unity for 160 °C than for 220 °C, the preheat temperature was selected as 160 °C even though it is the same as the cutheat temperature.

4.6.1.2 Sensitivity change in the Nyl/Mogalakwena River and Rooisloot quartz

The sensitivity change in the Nyl/Mogalakwena River and Rooisloot quartz was examined using the data acquired from the dose-recovery test. The average T_x/T_n was calculated for the three aliquots run at each preheat temperature and the data plotted against the cycle number (Figure 4.8). The low preheat temperatures show

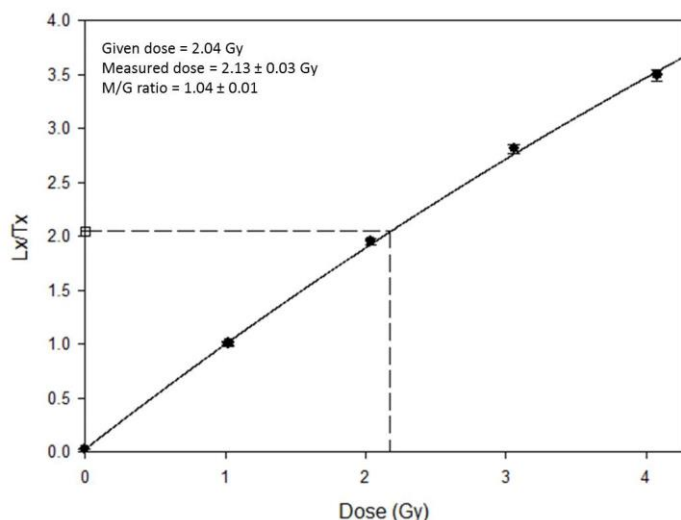


Figure 4.7: Dose-response curve plotted from the dose-recovery test for sample NVA6 with 160 °C preheat. The natural dose is illustrated by the open square.

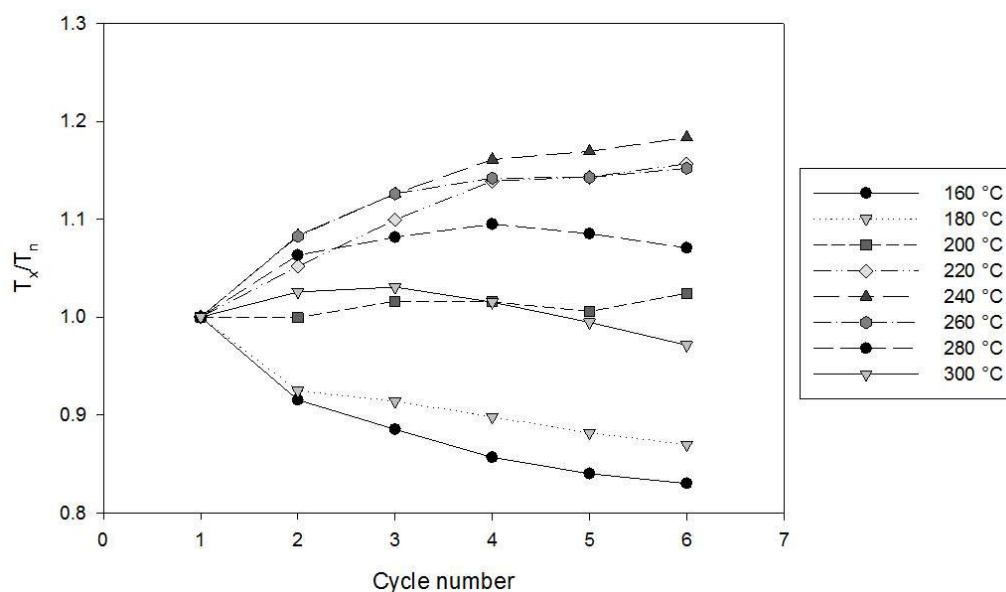


Figure 4.8: Plot of cycle number versus T_x/T_n showing the sensitivity change of the Nyl/Mogalakwena River quartz from sample NVA6 during the SAR sequence.

an initial decrease in sensitivity whilst the high preheat temperatures show an initial increase in sensitivity, similar to the South African quartz discussed by Armitage *et al.* (2000) (see section 3.5.2). Furthermore, the sensitivity change is less than 20% which is lower than the percentages quoted by Jacobs *et al.* (2003) and Armitage *et al.* (2000) for South African quartz. Therefore the sensitivity change within the Nyl/Mogalakwena River and Rooisloot quartz is within acceptable limits for the application of the SAR protocol.

4.6.1.3 Recycling ratio and recuperation ratio tests

The recycling ratio and recuperation were analysed using the dose-response curve plotted using Analyst for each aliquot. Every aliquot measured during the preliminary tests passed the recycling ratio test and therefore no aliquots were excluded from the D_e calculation for this reason. The recuperation was analysed for each aliquot and the L_x/T_x value was below 0.01 for every sample. Therefore the SAR protocol is applicable to the Nyl/Mogalakwena River and Rooisloot quartz.

4.6.2. Single aliquot measurements

All single aliquot measurements in this research project were made using the single aliquot regenerative dose (SAR) protocol (Table 4.3) with a preheat and cutheat of 160 °C for 10 s and a test dose of 1 Gy. The standard regenerative doses used to irradiate the samples were 0 Gy, 1 Gy, 2 Gy, 3 Gy and 4 Gy whilst recycling doses of 0 Gy and 1 Gy were used. The extent of feldspar contamination in the signal was determined using the OSL-IR depletion ratio test developed by Duller (2003) and outlined in detail by Jacobs *et al.* (2006a). This test includes an infra-red stimulation prior to the OSL stimulation in step 3 on an extra recycled point at the end of the SAR sequence, and provides an additional recycling ratio *i.e.* if the ratio approached unity the sample was not contaminated. All of the Nyl/Mogalakwena River and Rooisloot samples passed this recycling ratio test, but should an aliquot fail this test, the D_e value would be excluded from the dataset.

Table 4.3: The SAR sequence used on the Nyl/Mogalakwena River and Rooisloot quartz where L_x is the OSL signal measured from each regeneration dose and T_x is the OSL signal measured from each test dose

Step	Treatment	Observed
1	Give dose, D_x	-
2	Preheat (160°C for 10 s)	-
3	Stimulate OSL for 40 s at 125 °C	L_x
4	Give test dose, D_T	-
5	Cutheat (160°C for 10 s)	-
6	Stimulate OSL for 40 s at 125 °C	T_x
7	Return to 1 (0, 25, 50, 75, 100, 0, 25 Gy)	

Due to the very bright signal produced by the Nyl/Mogalakwena River and Rooisloot quartz the second illumination at the end of the standard SAR sequence (step 7 in Table 3.1) was omitted from the SAR sequence used in this research. This illumination at a higher temperature than the preceding test dose stimulation ensures that the deeper traps which produce the OSL signal have been completely emptied prior to the application of the dose in the following irradiation as suggested by Wintle and Murray (2006). However, it also increases the sensitivity of the quartz, and although of particular use with low-signal quartz, it was not necessary in this study.

4.6.3. Single-grain measurements

Single grain analyses were run on samples NVB10 and NVC2 on Risø 3 at Aberystwyth University due to the high overdispersion measured on the single aliquot samples (see Table 4.4). NVA2 (which has the highest overdispersion of all eleven samples) was not measured at Aberystwyth University and therefore was not available for single-grain measurements. The single grain analyses were carried out using an identical SAR protocol to that used for the single aliquot samples with a preheat and cutheat of 160 °C for 10 s and a test dose of 1 Gy. The standard regenerative doses used to irradiate the samples were 0 Gy, 1 Gy, 2 Gy, 3 Gy and 4 Gy whilst recycling doses of 0 Gy and 1 Gy were used. Sample NVC2 required the addition of two higher regenerative doses (10 Gy and 20 Gy) in order to better constrain the growth curve for the partially bleached grains.

4.7 Calculation of D_e values

4.7.1 Single aliquot D_e measurements

The construction of the SAR dose-response curve (Figure 4.7) is explained in detail by Preusser *et al.* (2008). The D_e is calculated by interpolation of the natural dose onto the dose-response curve, therefore each aliquot produces a single D_e value. Several cases exist whereby an aliquot will not produce a D_e value, such as when (i) no detectable OSL signal is present due to the lack of light-emitting grains on the aliquot, (ii) an exponential function cannot be fitted to the L_x/T_x points resulting in the absence of the growth curve due to low signal levels, (iii) failure of the recycling

ratio test due to non-functioning sensitivity correction, (iv) failure of the OSL-IR depletion ratio test due to feldspar contamination, and (v) the natural dose (L_N/T_N) does not intercept the dose-response curve, termed “Class 3” grains by Yoshida *et al.* (2000).

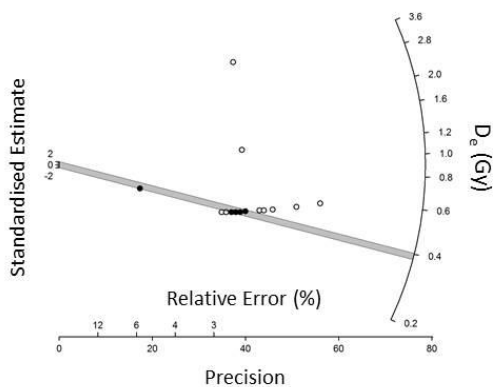
The only case for the rejection of aliquots from the D_e measurements for the Nyl/Mogalakwena River and Rooisloot quartz was (v) whereby the natural signal was far greater than the dose-response curve and therefore did not intersect the curve and could not produce a D_e value. However, this occurred on less than 1% of the aliquots measured and may be directly related to heterogeneous bleaching of the quartz grains in nature. Once the individual D_e values have been determined, the D_e distributions (Figure 4.9) are subjected to statistical analysis to determine the representative D_e value for each sample *i.e.* the true burial dose (D_b).

4.7.1.1 Calculation of D_b from single aliquot measurements

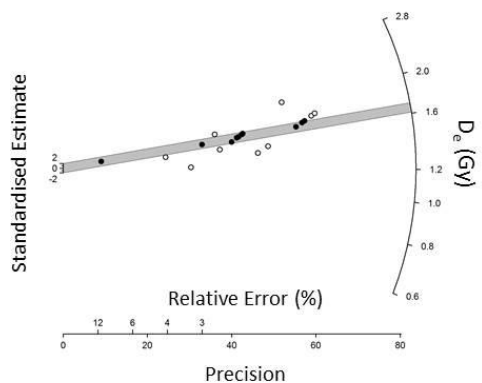
A common problem when determining the true D_b of fluvial sediments is the occurrence of partial bleaching, whereby the OSL signal in individual grains is not completely reset during the processes of erosion, transportation and deposition, thereby leaving a residual signal within the grain that will result in age overestimation (Duller, 1994; Wallinga, 2002; Rittenour, 2008). One of the simplest ways to identify whether a sample has undergone partial bleaching is to consider the overdispersion factor. When the overdispersion is greater than 20 % (see Section 3.6), the sample should be checked for partial bleaching which can be done visually by plotting the D_e values on a probability density (PD) or radial plot. Should partial bleaching be evident in the dataset, a different statistical model must be used to determine the D_b .

As discussed in Section 3.6 the true D_b is determined from the measured D_e dataset using one of several available statistical methods. Given that the majority of the Nyl/Mogalakwena River samples produced very low overdispersion values (Table 4.4), typically less than 11%, the most appropriate statistical method to use was the central age model (CAM). Therefore the CAM was used to determine eight of the

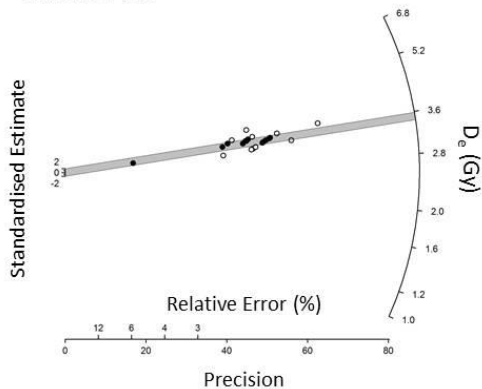
11/O/NV-A2



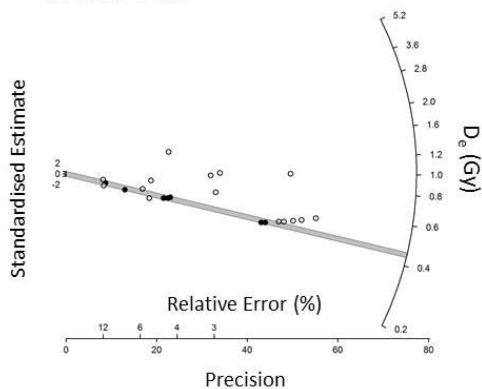
11/O/NV-A6



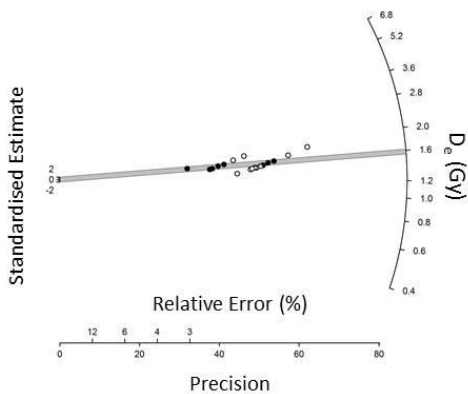
11/O/NV-A9



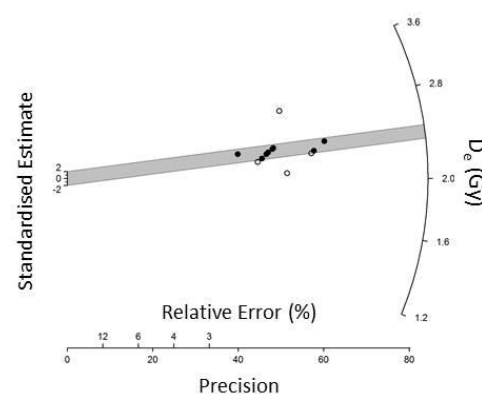
11/O/NV-B10



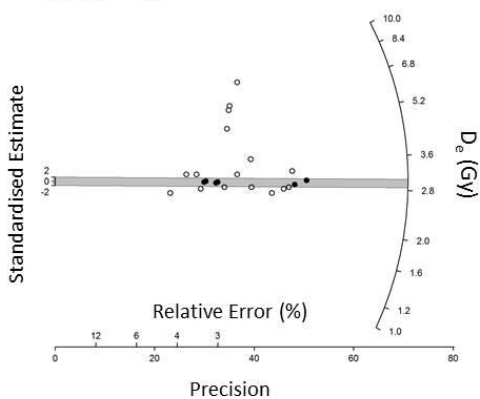
11/O/NV-B7



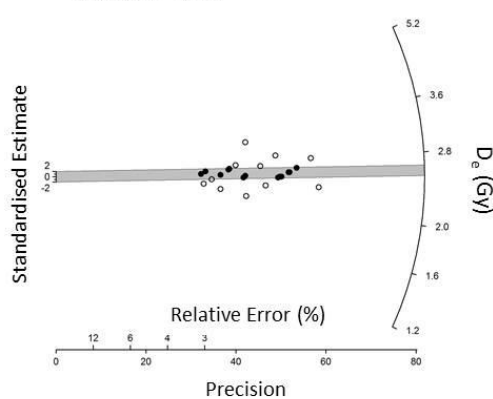
11/O/NV-B1



11/O/NV-C2



11/O/NV-C4b



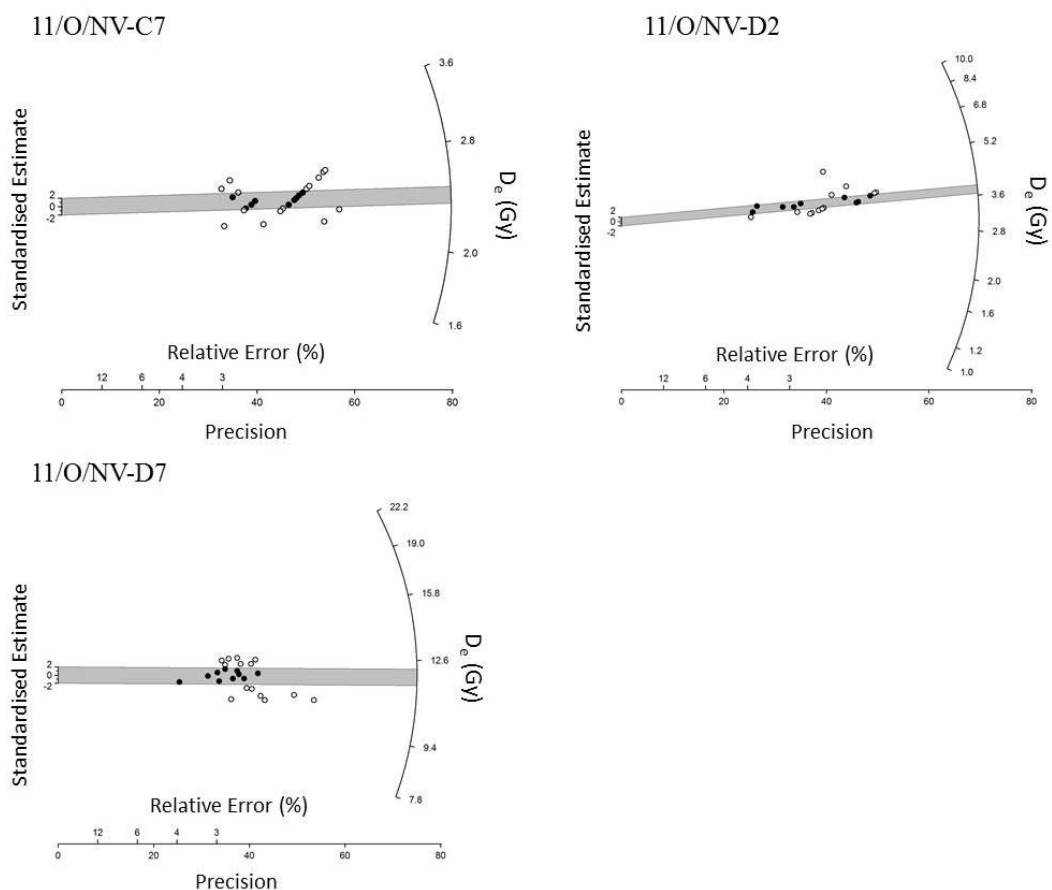


Figure 4.9a: Radial plots of single aliquot D_e values measured at Aberystwyth University (except NVA2 which was measured at the University of the Witwatersrand). The shaded region indicates the values consistent within 2σ of the D_b , *i.e.* the 95% confidence interval.

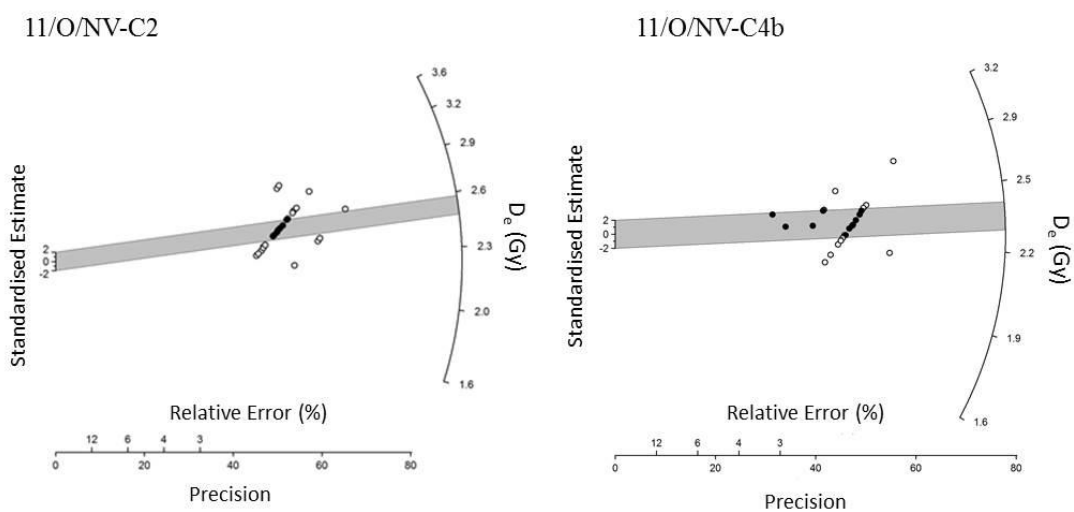


Figure 4.9b: Radial plots of the single aliquot D_e values re-measured at the University of the Witwatersrand. The shaded region indicates the values consistent within 2σ of the D_b , *i.e.* the 95% confidence interval.

Table 4.4: Overdispersion (σ_b) and true burial dose (D_b) data calculated from single aliquot measurements using the CAM and MAM; the samples with $\sigma_b < 20\%$ display identical D_b calculated by the CAM and MAM. D_b values in bold were used to calculate the final OSL ages.

Sample no	σ_b (%)	D_b (Gy) CAM	D_b (Gy) MAM
11/O/NV-A2	58 ± 2	0.47 ± 0.06	0.39 ± 0.01
11/O/NV-A6	9 ± 0	1.65 ± 0.03	1.64 ± 0.15
11/O/NV-A9	5 ± 0	3.51 ± 0.04	3.51 ± 0.26
11/O/NV-B10	40 ± 1	0.56 ± 0.05	0.45 ± 0.09
11/O/NV-B7	8 ± 0	1.57 ± 0.03	1.57 ± 0.12
11/O/NV-B1	8 ± 1	2.36 ± 0.06	2.36 ± 0.30
11/O/NV-C2	41 ± 1	2.98 ± 0.08	2.95 ± 0.23
11/O/NV-C4b	9 ± 0	2.58 ± 0.06	2.57 ± 0.23
11/O/NV-C7	8 ± 0	2.39 ± 0.04	2.39 ± 0.19
11/O/NV-D2	11 ± 0	3.75 ± 0.08	3.75 ± 0.40
11/O/NV-D7	8 ± 0	11.89 ± 0.21	11.89 ± 0.99
Repeat measurements			
11/O/NV-C2	8 ± 0	2.51 ± 0.04	-
11/O/NV-C4b	6 ± 0	2.37 ± 0.03	2.37 ± 0.08

eleven D_b values. Three burial doses, for samples NVA2, NVB10 and NVC2, were determined using the minimum age model (MAM) due to the large overdispersion values ($> 40\%$). Partial bleaching in these three samples is evidenced in the D_e distribution as a “tail” in the probability density plot (Figure 4.10a) and scatter in the radial plot (Figure 4.10b). The MAM was suitable for these three sediments because the lowest D_e population (*i.e.* the most bleached grains) were the target grains for the determination of the D_b . Two samples (NVC2 and NVC4b) were re-measured in November 2012 at the University of the Witwatersrand. Both samples displayed very low overdispersion values and the D_b was calculated using the CAM. The radial plots for each OSL sample are included in Figure 4.9 with the shaded region showing the 2σ error for the D_b determined by the CAM or MAM.

It is possible to overcome the problem of partial bleaching through measurement of small aliquots (< 100 grains) or single-grains, which should allow the unbleached grains within the population to be identified. Single-grain dating is important for

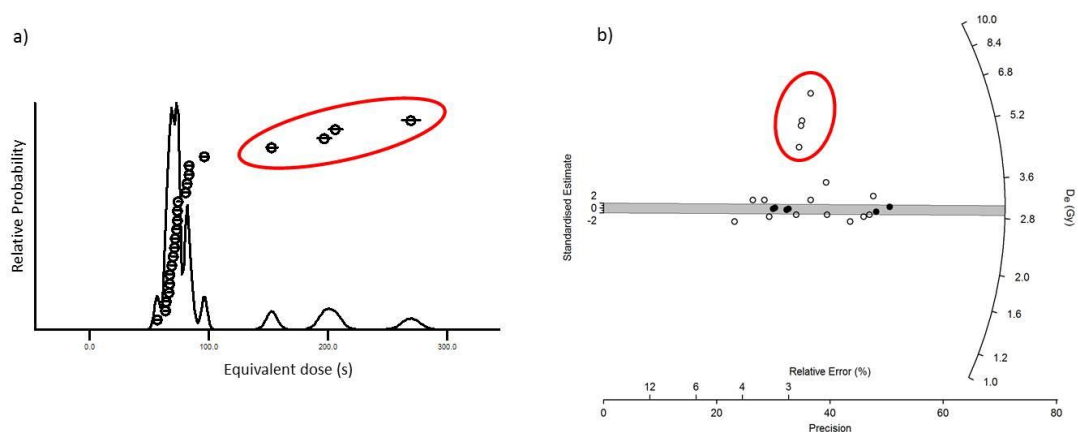


Figure 4.10: The a) probability density (PD) plot for sample NVC2, the red circle marks the “tail” typical of partially bleached fluvial sediments. b) The radial plot for the same sample, highlighting the outliers responsible for producing the high overdispersion value ($\sigma_b = 41\%$).

young samples as the residual signal contributes a large proportion of the measured D_e value, thereby resulting in a large age overestimate (Rittenour, 2008). For this reason, two of the three Nyl/Mogalakwena River samples which had overdispersion values above 40 % were analysed using single-grain OSL. The third sample was initially analysed at the University of the Witwatersrand and was therefore unavailable for OSL single-grain analysis at Aberystwyth University.

4.7.2 Single-grain D_e measurements

The single-grain measurements require a green laser to stimulate the quartz grains, this was done at 90% power. The luminescence signal emitted during the single-grain measurements was very bright due to the large proportion of grains which emitted an OSL signal. It is considered typical for 90-95% of the OSL signal to be emitted from 5-10% of the quartz grains (Duller *et al.*, 2000; Jacobs *et al.*, 2003; Duller, 2008b), however for the Nyl/Mogalakwena River and Rooisloot quartz (Figure 4.11) 95% of the OSL signal was emitted by 35% of the grains.

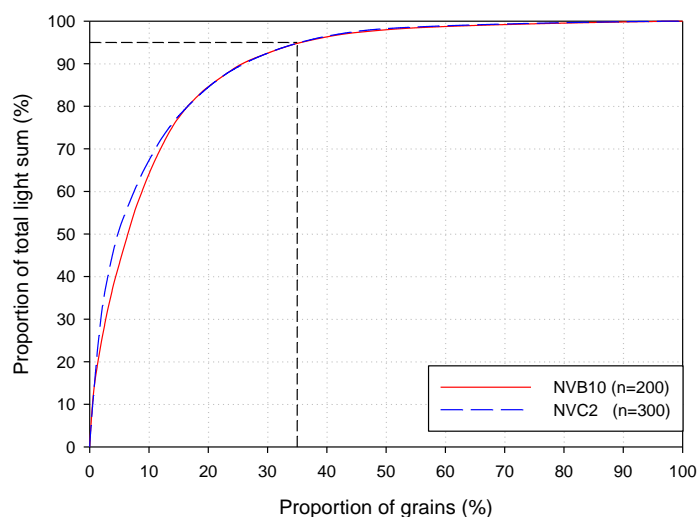


Figure 4.11: Proportion of single grains emitting light in sample NVB10 and NVC2.

4.7.2.1 Calculation of D_b from single-grain measurements

The single-grain samples displayed very high overdispersion (Table 4.5), confirming that at least two of the sampled sediment layers have undergone significant partial bleaching, which was to be expected in a fluvial environment. Although the two samples have similar overdispersion values, the radial plot (Figure 4.12) for sample NVB10 shows a single distinct outlier, whilst sample NVC2 displays a greater spread in D_e values indicating that the extent of partial bleaching is more severe in the latter sample. The D_b value for sample NVB10 calculated from the single aliquot data was very similar to that calculated from the single-grain data; *i.e.* 0.45 ± 0.09 and 0.39 ± 0.03 respectively to give a difference of 0.06 ± 0.09 Gy. Alternatively, sample NVC2 produced significantly different values, 2.95 ± 0.23 Gy for single aliquots and 2.42 ± 0.21 Gy for single-grain analysis, which gives a

Table 4.5: Overdispersion (σ_b) and true burial dose (D_b) data calculated from single-grain measurements by the CAM and MAM. D_b values in bold were used to calculate the final OSL ages.

Sample no	σ_b (%)	D_b (Gy) CAM	D_b (Gy) MAM
11/O/NV-B10	58 ± 1	0.42 ± 0.04	0.39 ± 0.03
11/O/NV-C2	56 ± 1	2.98 ± 0.27	2.42 ± 0.67

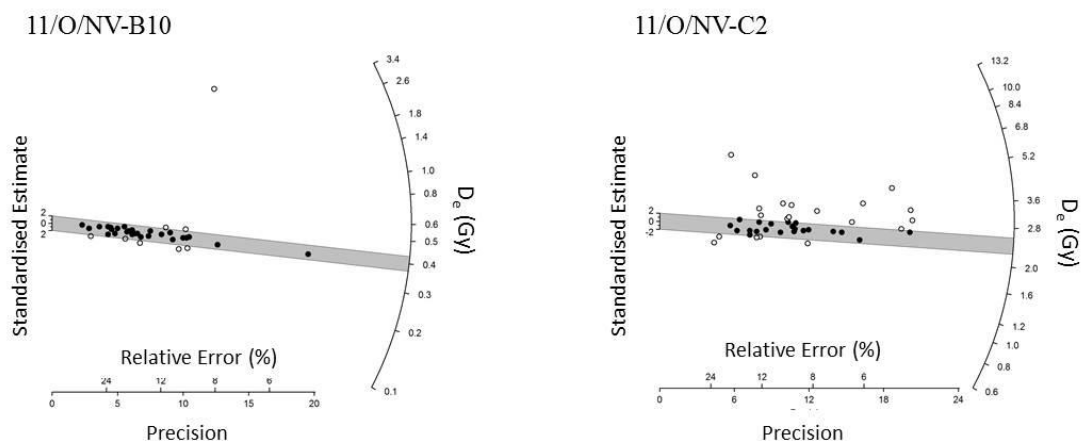


Figure 4.12: Radial plots of single grain D_e values. The shaded region indicates the values consistent within 2σ of the D_b , *i.e.* the 95% confidence interval.

difference of 0.53 ± 0.07 Gy. However, when the single aliquot analysis was repeated for NVC2, a D_b value of 2.51 ± 0.04 Gy was measured and this new value is in better agreement with the single grain measurement obtained for this sample. The difference in the D_b will result in significantly different ages for the NVC2 sedimentary layer whereas the similarity of the D_b values from the NVB10 layer will result in similar ages, most likely within error of one another.

4.8 Summary

The D_e comprises half of the age equation for OSL dating, thus it is imperative that the D_e value be determined accurately. The standard D_e measurement protocol is the Single Aliquot Regenerative Dose (SAR) protocol formalised by Murray and Wintle (2000), which corrects the natural OSL signal for sensitivity by administering a test dose. This protocol addresses the sensitivity change issue arising in the quartz grains due to repeated beta dosing.

A series of preliminary tests were run on the Nyl/Mogalakwena River and Rooisloot quartz to determine its suitability for the SAR protocol; the preheat test identified an ideal preheat temperature of 160°C and the dose recovery test successfully recovered the given dose of 2.04 Gy. A typical SAR protocol was run on thirteen samples using single aliquots and two samples using the single-grain technique, with each sample passing the recuperation ratio and recycling ratio tests.

Single aliquot D_e measurements were undertaken on thirteen samples from the Nyl/Mogalakwena River floodplain and the Rooisloot tributary fan, using a standard SAR protocol with a preheat temperature of 160 °C, a cutheat of 160 °C, a maximum dose of 4 Gy and a test dose of 1 Gy. D_e measurements were analysed using the CAM for samples displaying an overdispersion parameter below 20 % (ten of thirteen samples) and the MAM for samples in excess of 20 % (three of thirteen samples). The latter three samples showed evidence of significant partial bleaching, therefore two of the three were selected for single-grain analyses (NVA2 was measured at the University of the Witwatersrand and was not available for single-grain measurements at Aberystwyth University). The overdispersion of the single-grain dataset was higher than that of the corresponding single aliquot dataset for both samples. The D_b value calculated from the single-grain data for sample NVB10 was very similar to the single aliquot D_b , with a difference of 0.06 Gy between the two values. Conversely, sample NVC2 showed a significant difference of 0.53 Gy between the two D_b measurements which will significantly alter the calculated age of the NVC2 sedimentary layer. However, when the single aliquot analysis was repeated for sample NVC2, the calculated D_b showed a good correlation with the single-grain D_b value, and will therefore produce a similar age. The final D_b values used to calculate the OSL ages are presented in Table 4.6.

Table 4.6: Final D_e measurements (in bold) used to calculate OSL ages (Chapter 6)

Sample no	σ_b (%)	D_b (Gy) CAM	D_b (Gy) MAM
11/O/NV-A2	58 ± 2	0.47 ± 0.06	0.39 ± 0.01
11/O/NV-A6	9 ± 0	1.65 ± 0.03	1.64 ± 0.15
11/O/NV-A9	5 ± 0	3.51 ± 0.04	3.51 ± 0.26
11/O/NV-B10	40 ± 1	0.56 ± 0.05	0.45 ± 0.09
11/O/NV-B7	8 ± 0	1.57 ± 0.03	1.57 ± 0.12
11/O/NV-B1	8 ± 1	2.36 ± 0.06	2.36 ± 0.30
11/O/NV-C2	41 ± 1	2.98 ± 0.08	2.95 ± 0.23
11/O/NV-C4b	9 ± 0	2.58 ± 0.06	2.57 ± 0.23
11/O/NV-C7	8 ± 0	2.39 ± 0.04	2.39 ± 0.19
11/O/NV-D2	11 ± 0	3.75 ± 0.08	3.75 ± 0.40
11/O/NV-D7	8 ± 0	11.89 ± 0.21	11.89 ± 0.99
Duplicate Measurements			
11/O/NV-C2	8 ± 0	2.51 ± 0.04	-
11/O/NV-C4b	6 ± 0	2.37 ± 0.03	2.37 ± 0.08
Single-grain measurements			
11/O/NV-B10	58 ± 1	0.42 ± 0.04	0.39 ± 0.03
11/O/NV-C2	56 ± 1	2.98 ± 0.27	2.42 ± 0.67

Chapter 5:

The Environmental Dose Rate (D_r)

5.1 Introduction

The importance of the environmental dose rate in luminescence dating is often underestimated in comparison to the determination of the equivalent dose, even though these two values each form half of the age equation used in OSL dating (Guérin *et al.*, 2012). Consequently, few studies have focused on sedimentary grains and the dose rate they received over time, but some examples include Fain *et al.* (1999), Brennan (2003), Brennan (2006), Mayya *et al.* (2006) and Nathan and Mauz (2008). Several methods are available for determining the elemental concentrations of U, Th and K such as XRF, ICP-MS, neutron activation analysis (NAA) and atomic absorption spectrometry (AAS). However, in this research project, emission counting methods (TSAC, GM-beta counting and HRGS) were used to determine the environmental dose rate; this requires measurement of α and β particles and γ ray emissions which are then used to calculate the parent radionuclide concentration. Thirteen samples were ultimately measured to obtain OSL ages: dose rates were measured at Aberystwyth University using TSAC and GM-beta counting, and at the University of the Witwatersrand using HRGS.

5.2 Thick Source Alpha Counting (TSAC)

Thick source alpha counting (TSAC) is an emission counting method that measures the total alpha particles emitted from the decay of the ^{232}Th , ^{238}U and ^{235}U decay chains (Rodnight, 2006). It can be used to estimate the U and Th concentrations within a sample and requires a small amount of sample, usually between 1 g and 2 g. For a detailed discussion on TSAC and the pairs count see Appendix J in Aitken (1985). The TSAC for this research project was undertaken at Aberystwyth University using a Daybreak 582 alpha-counter.

5.2.1. Sample preparation

Each sample was dried and milled in a TEMA mill to obtain a homogenous powder and placed in a Perspex holder on a zinc sulphide (ZnS) screen held in place by a retaining ring (Figure 5.1). The powdered sample was spread evenly over the screen to a thickness of ~ 1 mm, which represents an “infinitely thick” layer of sample as the sample thickness is greater than the range of the alpha particles (R) emitted within the sample (Figure 5.2). Approximately $\frac{1}{4}$ of the alpha particles emitted by the nuclei reach the ZnS screen producing scintillations of light which emit photoelectrons from the photocathode of the photomultiplier (Aitken, 1985).

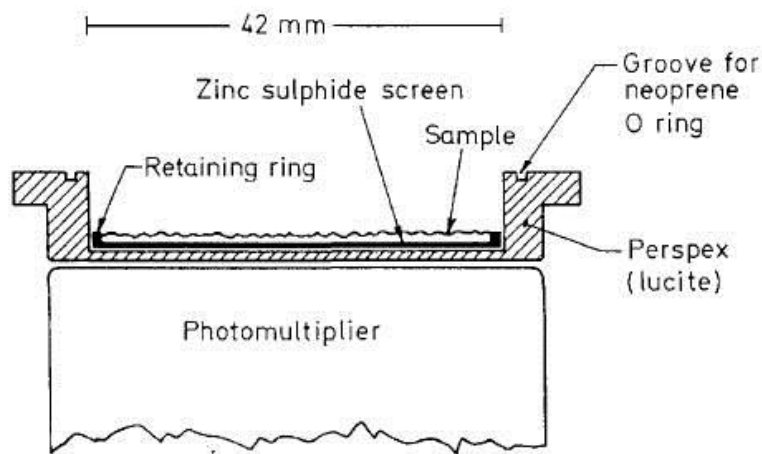


Figure 5.1: Sketch of the container used for TSAC (Aitken, 1985). The ZnS screen is placed into the Perspex container with a retaining ring and a neoprene O-ring. The homogenised sample is then spread directly onto the ZnS screen and the lid attached with screws.

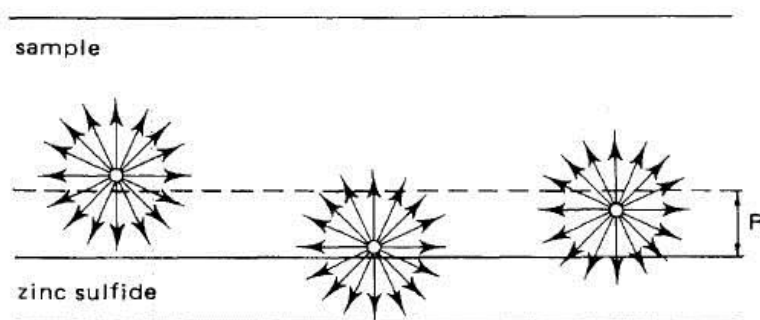


Figure 5.2: Idealised sketch of TSAC sample on a ZnS screen. Nearly half of the alpha particles from emitting nuclei close to the ZnS screen will produce scintillations. With increasing distance of the nuclei from the screen, the proportion of scintillations decreases until the nuclei is beyond the range (R) of the alpha particles and no scintillations are produced (Aitken, 1985).

Samples were measured in Perspex holders with counting areas of 15.45 cm^2 based on the geometry of the retaining rings available at the Aberystwyth Luminescence Research Laboratory (ALRL). Background counts were run on two ZnS screens placed face to face in the holder and covered with a glass screen to prevent counting Ra from the air. Each background count was done for a minimum of 24 hr. Each sample was counted twice: an “unsealed” alpha count was taken by placing wooden spacers between the pot and lid and counting for a minimum of 3,000 counts and a “sealed” alpha count was taken by removing the spacers, sealing the pot and counting for a minimum of 1,000 counts.

5.2.2 Pairs counting to determine the U and Th concentrations

The counts were used to determine the U and Th concentrations by the pairs counting method. Aitken (1985) outlines the process of pairs counting in an effort to determine the U and Th concentrations from the number of pairs counted compared to the total number of alpha particles detected. The pairs in question are a product of the ^{232}Th decay chain, when the successive alpha decays of ^{220}Rn ($t_{1/2} = 55.6 \text{ s}$) and ^{216}Po ($t_{1/2} = 0.145 \text{ s}$) occur in quick succession and are counted as a pairs count using a gate set to 0.38 s (Aitken, 1990). These pair counts account for $\sim 3 \%$ of the counts emitted by the Th decay chain and differ from other counts which usually display a time interval of 100 s between pulses (Aitken, 1985). Appendix D outlines the calculations used to derive the U and Th concentrations from the pairs counts recorded for sample NVA6, whilst Table 5.1 includes the U and Th concentrations calculated from TSAC for each sample collected.

5.2.3 Assessing radon escape using TSAC

Olley *et al.* (1996) assert that disequilibria in the uranium decay chain should be expected due to weathering processes that operate in surficial environments that include solution and precipitation reactions, gaseous diffusion of radon and alpha particle recoil. Therefore, it is not uncommon to find fluvial sediments with high porosity and permeability in a state of disequilibrium. The disequilibrium of the decay chains can be assessed by calculating the ratio between the sealed and unsealed alpha counts (Aitken, 1985), and if radon escape has not occurred then the sealed/unsealed ratio should approach unity, *i.e.* it should have a value of 1 ± 0.1 .

The measured sealed/unsealed ratios for each sample are included in Table 5.1 and are well within the accepted ratio, thereby confirming that the decay series are in equilibrium.

5.3. GM-Beta counting

Beta counting is a method that measures the total beta emission from U, Th and K in a homogenised sample (Bøtter-Jensen and Mejdahl, 1988). Beta counting at Aberystwyth University was carried out on a low level Risø GM-25-5 beta counter (Figure 5.3). The instrument, described by Bøtter-Jensen and Mejdahl (1988) is a gas flow counter (99 % argon, 1 % isobutene) that consists of a common guard counter and five individual Geiger-Mueller (GM) cylindrical detectors. External radiation in the form of cosmic rays is reduced by the guard counter, which detects and rejects coincident counts between it and the GM detectors, and by the 10 cm thick lead shield surrounding the instrument. Sample pots are placed on a lifting slide below the GM detectors to ensure accurate and reproducible positioning (Jacobs, 2004).

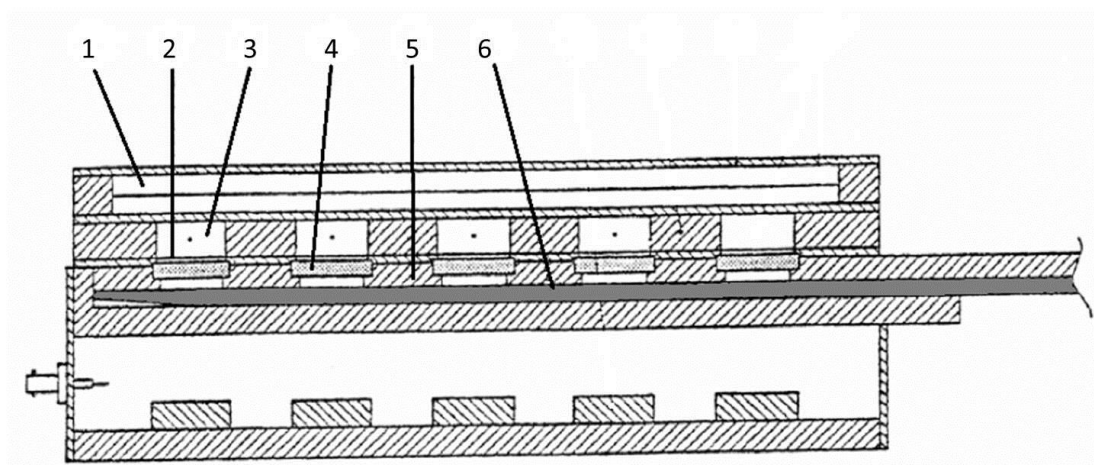


Figure 5.3: Schematic diagram of the GM-25-5 beta counter illustrating the (1) guard counter, (2) Mylar window, (3) sample counter, (4) sample, (5) sample slide and (6) lift slide (Jacobs, 2004; after Bøtter-Jensen and Mejdahl, 1988).

5.3.1. Sample preparation

As with TSAC, the sample was dried and milled in a TEMA mill in order to homogenise the sample. The sample was packed into a Perspex pot, with internal

dimensions of 21 mm diameter and 7 mm depth. The top was levelled and the pot covered with cling-film in order to prevent contamination of the instrument. Each sample was counted in sets of five pots, three pots of sample and two standards of known radioactivity, Shap granite ($D_{\beta\text{-Shap}}$) and magnesium oxide powder (D_{MgO}), with dose rates of 5.99 Gy/ka and 0.00 Gy/ka respectively, for a minimum of 24 h. The corrected counts (CC) for each position can then be determined from the raw counts by correcting for minor variations in the GM detector efficiency using values calculated from analyses of a ^{36}Cl standard by Helen Roberts (Rodnight, 2006).

5.3.2. Calculation of beta dose rate

Calculation of the beta dose rate ($D_{\beta\text{-sample}}$) for each sample was done by interpolation of the averaged corrected counts for the three sample pots between the two known standards, using the equation:

$$D_{\beta\text{-sample}} = D_{\beta\text{-Shap}} \left(\frac{CC_{\text{sample}} - CC_{\text{MgO}}}{CC_{\text{Shap}} - CC_{\text{MgO}}} \right) \quad (5.1.)$$

where D_{β} represents the beta dose rate and CC the corrected counts (Rodnight, 2006). Using the conversion factors of Adamiec and Aitken (1998), the concentrations of U and Th determined by TSAC were used to calculate the beta dose rate produced by U and Th. This value was then subtracted from the measured beta dose rate to obtain the beta dose rate produced by K, which was converted into a total K concentration using the conversion factors. Appendix D outlines the calculations used to derive the K-produced dose rate and K concentrations from the U and Th concentrations obtained by TSAC for sample NVA6, whilst Table 5.1 includes the K concentrations calculated from TSAC and GM-beta counting for each sample collected.

5.4 High Resolution Gamma Spectrometry (HRGS)

HRGS was used to determine the concentrations of individual radionuclides within the ^{238}U and ^{232}Th decay series, thereby determining whether the decay series was in secular equilibrium (Murray and Aitken, 1988; Oczkowski *et al.*, 2000; Ankjærgaard and Murray, 2007). The resolution of HRGS is much higher than that of FGS and allows photopeaks with a width of 1–2 keV to be identified. Therefore individual

isotopes with gamma energies separated by a few keV from each other can be measured (Aitken, 1985). All HRGS was carried out at the iThemba Laboratory in Johannesburg by Abie Kwelilanga with a high purity germanium crystal (HPGe) detector.

5.4.1 Sample preparation

Each sample was dried and packed into a Perspex Marinelli beaker, weighed and left to stand for 20 days to allow the radon levels to attain equilibrium. Since 20 days represents more than 5 half-lives of ^{222}Rn , the activity of ^{222}Rn will be within 97 % of equilibrium with its parent ^{226}Ra after this time (Ankjærgaard and Murray, 2007). Each sample was counted for 24 hours and the resultant concentrations were compared with IAEA reference materials counted in the same geometry and background normalised according to the sample mass.

5.4.2 Isotope concentrations

HRGS measures the peak intensities of known emission energies for different gamma emitting nuclides from each decay series (Murray and Aitken, 1988; Oczkowski, 2001), thus several peaks representing a single radionuclide can be measured in the U and Th decay series. The isotopes (and their energies) measured for the ^{238}U decay series were ^{226}Ra (~186 keV), ^{214}Pb (~241 keV, ~295 keV and ~352 keV) and ^{214}Bi (~609 keV, ~1120 keV, ~1764 keV and ~2204 keV), and for the ^{232}Th decay series were ^{228}Ac (~911 keV and 968 keV) and ^{208}Tl (~583 keV and ~2614 keV). No peaks were detected for the ^{235}U decay series; this was deemed acceptable due to the much lower atomic abundance of ^{235}U with respect to ^{238}U in nature (0.72 % and 99.28 % respectively; Aitken, 1985) and the very low concentration of uranium in the samples. ^{40}K displays a single, distinct peak at ~1460 keV which was measured to obtain the activity of ^{40}K .

The results from iThemba Laboratory were calculated using the weighted least squares method and returned as concentrations for natural U and ^{232}Th in ppm and as a percentage for ^{40}K . Errors on the U and Th concentrations were calculated as the standard deviation from the weighted mean concentration obtained from 8 and 4 peak determinations respectively, whilst the errors for the K concentrations were

calculated from the uncertainty on the area below the peak. The concentration values were converted to dose rates using the conversion factors of Adamiec and Aitken (1998), which produced a beta- and gamma dose rate for each element (U, Th and K). Appendix E outlines the calculations used to derive the environmental dose rate using HRGS for sample NVA6. Table 5.2 details the dose rate obtained for each sample collected using HRGS.

5.5 Equilibrium in the decay chain of the Nyl/Mogalakwena River and Rooisloot samples

The nature of fluvial sediments makes the escape of radon from the sample possible (see Sections 3.7.3 and 5.2.3). In an effort to determine whether radon escape has occurred, which would result in the disequilibrium of the decay chain and an underestimation of the deposition age of the sediments, certain values can be determined and compared.

The sealed/unsealed count ratio from TSAC was calculated, with a range of values from 0.95 ± 0.04 to 1.08 ± 0.04 (Table 5.1) which corresponds with the expected ratio for samples in equilibrium of 1.00 ± 0.10 , thereby confirming that the samples are in equilibrium. Alternatively, the HRGS technique identifies and measures isotopes above and below Rn in the decay chain, *i.e.* in the ^{238}U decay series ^{226}Ra is the parent of ^{222}Rn , whilst ^{214}Pb and ^{214}Bi represent its daughter products and in the ^{232}Th decay series, ^{228}Ac represents the parent isotope of ^{220}Rn with ^{208}Tl representing the daughter product. The measurement of these specific radioisotopes and the comparison of the concentrations allow the extent of equilibrium in the sample to be ascertained. For example, in sample NVA6, the U concentration determined from the ^{226}Ra peak was 1.3 ppm and the concentrations determined from the ^{214}Pb and ^{214}Bi peaks were 1.3 ppm, 1.1 ppm, 2.1 ppm, 1.2 ppm, 1.1 ppm, 1.3 ppm and 1.3 ppm; given the very good correlation between these values it can be assumed that the sample is in equilibrium with respect to the ^{238}U decay chain. A similar case was found for the ^{232}Th decay chain of sample NVA6.

Table 5.1: Site data and dosimetry obtained using TSAC and GM-beta counting

Sample	Latitude	Longitude	Altitude (m)	Depth (m)	WC (%) ¹	Cosmic dose-rate (Gy/ka) ²	Potassium (%) ³	Uranium (ppm) ⁴	Thorium (ppm) ⁴	S/US ratio	Infinite beta dose-rate (Gy/ka) ⁵	Gamma dose-rate (Gy/ka) ⁶	Environmental dose-rate (Gy/ka)
11/O/NV-A6	24°08'7.66"S	28°55'4.57"E	1046	1.51	0.81	0.176±0.018	2.66±0.11	1.19±0.20	2.65±0.64	1.01±0.04	1.82±0.09	0.82±0.05	2.81±0.10
11/O/NV-A9	24°08'7.66"S	28°55'4.57"E	1046	2.25	4.24	0.159±0.016	4.01±0.17	2.17±0.37	5.20±1.21	1.03±0.04	2.81±0.13	1.32±0.08	4.29±0.16
11/O/NV-B10	24° 08'7.29"S	28°55'5.69"E	1046	0.50	1.69	0.202±0.020	4.52±0.16	1.59±0.27	4.30±0.88	0.96±0.03	3.03±0.14	1.33±0.07	4.57±0.16
11/O/NV-B7	24° 08'7.29"S	28°55'5.69"E	1046	1.62	0.95	0.173±0.017	2.71±0.11	1.55±0.18	2.06±0.58	1.05±0.04	1.87±0.09	0.84±0.05	2.88±0.10
11/O/NV-B1	24° 08'7.29"S	28°55'5.69"E	1046	2.47	1.06	0.154±0.015	2.58±0.10	1.03±0.15	1.99±0.49	0.95±0.04	1.74±0.08	0.75±0.04	2.64±0.09
11/O/NV-C2	24° 08'17.4"S	28°56'04.7"E	1057	1.48	1.61	0.173±0.017	3.67±0.16	1.76±0.39	6.76±1.30	1.08±0.04	2.59±0.12	1.27±0.09	4.03±0.15
11/O/NV-C4b	24° 08'17.4"S	28°56'04.7"E	1057	2.87	1.88	0.167±0.017	3.15±0.12	1.35±0.23	3.44±0.75	1.00±0.04	2.15±0.10	0.97±0.06	3.29±0.12
11/O/NV-C7	24° 08'17.4"S	28°56'04.7"E	1057	3.49	0.70	0.136±0.014	1.94±0.09	1.53±0.19	2.28±0.61	0.95±0.03	1.41±0.07	0.68±0.04	2.22±0.08
11/O/NV-D2	24°08'16.8"S	28°56'04.5"E	1057	1.34	2.00	0.180±0.018	3.45±0.15	1.97±0.33	4.58±1.07	1.07±0.04	2.45±0.11	1.15±0.07	3.78±0.14
11/O/NV-D7	24°08'16.8"S	28°56'04.5"E	1057	2.76	1.30	0.149±0.015	2.95±0.12	1.21±0.22	3.21±0.72	1.01±0.04	2.01±0.09	0.90±0.05	3.06±0.11

¹Measured water content value.

²Cosmic dose rate calculated from Hutton & Prescott (1994) using conversion factors from Adamiec & Aitken (1998).

³K concentration calculated from beta-counting.

⁴U and Th concentration calculated from TSAC.

⁵Infinite matrix beta dose has been corrected for water content and attenuation.

⁶Gamma dose rate has been corrected for water content.

Table 5.2: Site data and dosimetry obtained using HRGS.

Sample no	Latitude	Longitude	Altitude (m)	Depth (m)	WC (%) ¹	Cosmic dose-rate (Gy/ka) ²	Potassium (%) ³	Uranium (ppm) ³	Thorium (ppm) ³	Infinite beta dose-rate (Gy/ka) ⁴	Gamma dose-rate (Gy/ka) ⁵	Environmental dose-rate (Gy/ka)
11/O/NV-A2	24°08'7.66"S	28°55'4.57"E	1046 m	0.37	2.63	0.205±0.021	4.62±0.08	1.51±0.07	2.81±0.39	3.06±0.11	1.28±0.05	4.55±0.12
11/O/NV-A6	24°08'7.66"S	28°55'4.57"E	1046 m	1.50	2.10	0.176±0.018	3.13±0.06	1.30±0.07	3.58±0.35	2.14±0.08	0.97±0.04	3.28±0.09
11/O/NV-A9	24°08'7.66"S	28°55'4.57"E	1046 m	2.33	3.10	0.157±0.016	3.98±0.07	1.52±0.07	4.14±0.37	2.69±0.10	1.20±0.04	4.05±0.11
11/O/NV-B10	24°08'7.29"S	28°55'5.69"E	1046 m	0.48	2.40	0.202±0.020	4.36±0.07	1.69±0.08	4.59±0.40	2.95±0.11	1.32±0.05	4.47±0.12
11/O/NV-B7	24°08'7.29"S	28°55'5.69"E	1046 m	1.61	1.40	0.173±0.017	3.61±0.06	0.98±0.06	2.03±0.32	2.36±0.09	0.97±0.04	3.51±0.10
11/O/NV-B1	24°08'7.29"S	28°55'5.69"E	1046 m	2.55	1.15	0.153±0.015	2.91±0.06	0.86±0.06	2.09±0.33	1.92±0.07	0.81±0.03	2.88±0.08
11/O/NV-C2	24° 08'17.4"S	28°56'04.7"E	1057m	1.48	2.62	0.177±0.018	4.01±0.07	2.69±0.08	5.33±0.41	2.87±0.11	1.38±0.05	4.43±0.12
11/O/NV-C4b	24° 08'17.4"S	28°56'04.7"E	1057m	2.87	1.10	0.147±0.015	3.06±0.06	0.98±0.06	1.87±0.27	2.02±0.08	0.85±0.03	3.01±0.08
11/O/NV-C7	24° 08'17.4"S	28°56'04.7"E	1057m	3.49	0.55	0.137±0.014	2.97±0.06	0.79±0.06	2.17±0.31	1.95±0.08	0.82±0.03	2.91±0.08

¹Measured water content value.

²Cosmic dose rate calculated from Hutton & Prescott (1994) using conversion factors from Adamiec & Aitken (1998).

³K, U and Th concentration calculated from HRGS.

⁴Infinite matrix beta dose has been corrected for water content and attenuation.

⁵Gamma dose rate has been corrected for water content.

5.6 Derivation of the environmental dose rate

This section will detail the process followed to calculate the environmental dose rate. A worked example for each method, the combination of TSAC and GM-beta counting and gamma spectroscopy, using sample NVA6 are included in Appendix D and Appendix E respectively. The concentrations of U (ppm), Th (ppm) and K (%) were calculated for each sample using a combination of TSAC and GM-beta counting at Aberystwyth University and HRGS at the University of the Witwatersrand.

5.6.1 Combining TSAC with GM-beta counting

By assuming an infinite matrix (where the rate of energy absorption within a volume greater than the ranges of the radiation equals the rate of energy emission) that is uniform in radioactivity and the absorption coefficient, the calculated emission values can be converted into a dose rate using the relevant conversion factors (Aitken, 1985; Guérin *et al.*, 2012). This was done automatically for each sample using the program LDB2005 written by Geoff Duller, with a manual calculation completed for sample NVA6 as a check on the accuracy of the database program. Furthermore, an Excel spread sheet was created and all dose rates were recalculated as a double check on the LDB2005 database.

Using the counting statistics obtained through TSAC, the Th concentration was determined using equation A1 (see Appendix A) and then converted to a count-rate using the expected count-rate values for a given parent material. The Th count-rate was then subtracted from the total count-rate to determine the U count-rate, which in turn was converted into the U concentration. The measured beta dose rate was then used in conjunction with the conversion factors from Adamiec and Aitken (1998) to determine the K concentration and the measured beta dose rate was corrected for attenuation and water content. The gamma dose rate from U, Th and K was calculated individually using the previously calculated concentrations and then summed to obtain the total gamma dose rate, which was then corrected for water content. The cosmic dose rate was calculated using the method described in Section 3.7.2.3. Finally the beta-, gamma- and cosmic dose rates were summed to obtain the total environmental dose rate. The alpha dose rate is omitted from the calculation

due to the reasons stated in Section 3.7.2.1. The values for the beta dose rates (corrected for attenuation and water content), the gamma dose rates (corrected for water content), and the total environmental dose rates are included in Table 5.1.

5.6.2 Attenuation of the beta dose rate

The total beta dose rate requires a correction for the attenuation of beta particles within the grain (Aitken, 1985; Bell, 1979; Mejdahl, 1979; Fain *et al.*, 1999; Brennan, 2003). The degree of attenuation is directly dependent on grain size and the energy of emission, which differs for U, Th and K. Mejdahl (1979) published value tables of the beta dose rate absorption and attenuation factors for spherical quartz grains between 5 μm and 1 mm, whilst Bell (1979) extended this work to include the effect of etching on the attenuation factors for 100 μm grains with 9 μm removed by the HF etching procedure. Brennan (2003) published updated values with adjustments of up to 3 % of the infinite matrix dose based on the work of Mejdahl (1979) and Bell (1979), whilst Fain *et al.* (1999) extended the work of Mejdahl (1979) to include various grain shapes using a Monte Carlo method. In this research project, the quartz grains of 180–212 μm were etched in HF to remove the outer 10 μm (see Chapter 3), and the correction values for attenuation of the beta dose rate and the effect of HF etching (Table 5.3) were based on the values of Mejdahl (1979) and Bell (1979).

Table 5.3: Correction factors for attenuation and the effects of HF etching on the beta dose rate for the grain size 180–212 μm (values from LDB2005)

Nuclide	Correction factor
K	0.931 ± 0.06
U	0.800 ± 0.07
Th	0.733 ± 0.08
Average	0.879 ± 0.04

5.6.3 Water content corrections

The average water contents measured for the two depositional environments, the floodplain (Profile A and B) and the tributary fan (Profile C and D), were 1.75 % and 1.5 % respectively for the samples processed at ALRL and 2.32 % and 1.42 % for the samples processed at the Geo-Luminescence Laboratory at the University of the

Witwatersrand. Thus a standard water content value of 10 ± 3 % was chosen to represent the water content over burial time in this research project due to the similarity of the sediments and the measured water contents. The beta- and gamma dose rates were corrected for water content as outlined in Section 3.7.2.4.

5.6.4 Determining the dose rate from HRGS

The HRGS analysis returned data as concentrations (ppm U, ppm Th, and % K), which were then multiplied by the conversion factors of Adamiec and Aitken (1998) to determine the beta and gamma dose rates for each element. The total beta and gamma dose rates were obtained by summing the individual elemental dose rates; the beta dose rate was then corrected for attenuation (Section 5.7.2) and water content (Section 3.7.2.4 and Section 5.7.3) and the gamma dose rate for water content. The cosmic dose rate and total beta and gamma dose rates were summed to determine the environmental dose rate; with the alpha dose rate omitted due to the reasons stated in Section 3.7.2.1. The values for the corrected beta- and gamma dose rates and the total environmental dose rates determined from HRGS are given in Table 5.2.

5.7 Comparison of data obtained from different methods of dose rate determination

Several studies have focused on the comparison of dose rates determined for luminescence dating (see Murray, 1981, 1982; Guibert and Schvoerer, 1991; Duller, 1992; Huntley *et al.*, 1993; Hossain *et al.*, 2002; Chen *et al.*, 2003; Jacobs, 2004). In this research project two techniques were used to examine the dosimetry of the Nyl/Mogalakwena River and Rooisloot samples, namely HRGS and a combination of TSAC with GM-beta counting. Duplicate samples were collected, which allowed individual samples to be analysed at two separate facilities where necessary, therefore each technique was run on a separate sample collected 30 cm apart from one another within the same stratigraphic unit. Thus, due to possible heterogeneity of the stratigraphic unit in the field, results obtained from the dosimetry analyses are expected to be similar though not identical.

A comparison of the environmental dose rate as measured by HRGS and the combination method of TSAC with GM-beta counting would produce a ratio of

unity if the two methods were in agreement with one another. The majority of the ratios (Table 5.4) are within 10% error and therefore the two methods are in a fairly good agreement. Similarly, a direct comparison of the two dose rates (Figure 5.4) shows that the measurement techniques are in reasonable agreement with one another. The slope of the regression line is 0.94 which indicates that the combination of TSAC and GM-beta counting tends to overestimate the environmental dose rate when compared with HRGS. However, the overall correlation between the two methods shows that the dosimetry results are reproducible.

Table 5.4: Final corrected environmental dose rates and ratios obtained from HRGS and a combination of TSAC with GM-beta counting (TSAC+B).

Sample	D _r (Gy/ka) HRGS	D _r (Gy/ka) TSAC+B	Ratio HRGS/A+B
11/O/NV-A2	4.55±0.12	-	-
11/O/NV-A6	3.28±0.09	2.81±0.10	1.17±0.05
11/O/NV-A9	4.05±0.11	4.29±0.16	0.95±0.04
11/O/NV-B10	4.47±0.12	4.57±0.16	0.98±0.04
11/O/NV-B7	3.51±0.10	2.88±0.10	1.22±0.05
11/O/NV-B1	2.88±0.08	2.64±0.09	1.09±0.05
11/O/NV-C2	4.43±0.12	4.03±0.15	1.10±0.05
11/O/NV-C4b	3.01±0.08	3.29±0.12	0.92±0.04
11/O/NV-C7	2.91±0.08	2.22±0.08	1.31±0.06
11/O/NV-D2	-	3.78±0.14	-
11/O/NV-D7	-	3.06±0.11	-
Mean (n=8)			1.09
Std dev			0.58

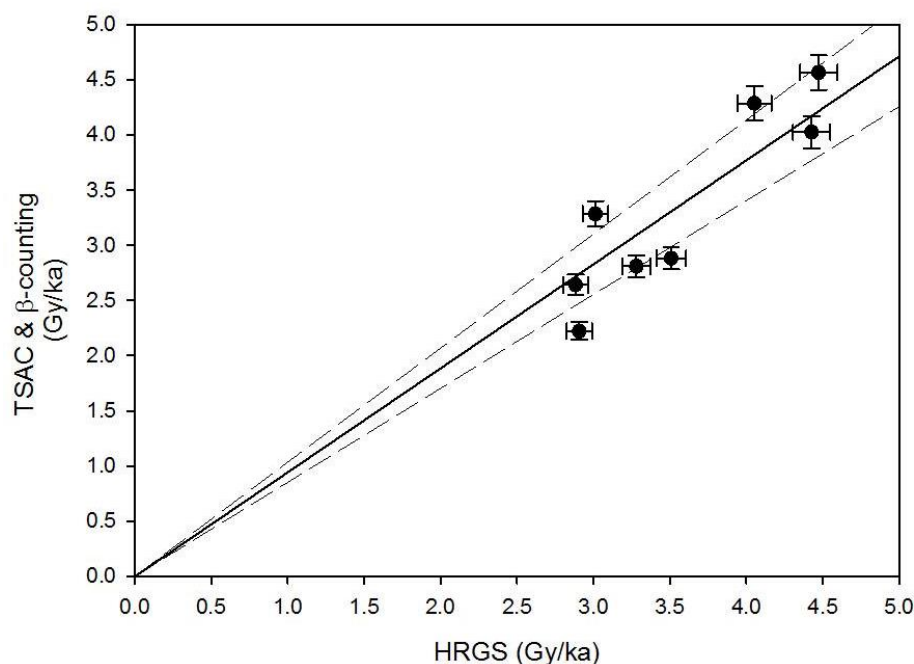


Figure 5.4: Direct comparison of derived environmental dose rates (D_r) obtained using HRGS and a combination of TSAC with GM-beta counting. The dose rates represent the final dose rate value used to calculate the age of the samples. The solid line represents the linear regression forced through the origin and the dashed lines represent the 95 % confidence interval.

5.8 Summary

Emission counting methods that utilise α and β particles and γ ray emissions to calculate the parent radionuclide concentration were used in this research project. The external beta and gamma dose rates were derived using a combination of TSAC with GM-beta counting at Aberystwyth University and HRGS at the University of the Witwatersrand. The beta dose rate was corrected for attenuation and water content and the gamma dose rate for water content. The cosmic dose rate was calculated using the methodology of Prescott and Hutton (1994) and corrected for the geomagnetic latitude, altitude and overburden of the sample site.

The final corrected environmental dose rates from both laboratory methods were compared. The results are in good agreement thereby confirming the reproducibility of the calculated dose rates. However the combination method of TSAC with GM-beta counting tends to overestimate the final environmental dose rate (*i.e.* D_r) when compared with HRGS. Both methods confirmed the secular equilibrium of the ^{238}U and ^{232}Th decay series.

Due to the good agreement of the two methods used to acquire the D_r values, there was no clear reason to select one set of values over the other for the calculation of the OSL ages. Therefore the measurements obtained from the combination TSAC and GM-beta counting were used with the D_e values measured at Aberystwyth University and the HRGS measurements were used in conjunction with the D_e measurements obtained from the University of the Witwatersrand (Table 5.5).

Table 5.5: Final D_r measurements (in bold) used to calculate OSL ages (Chapter 6)

Sample	D_r (Gy/ka) HRGS	D_r (Gy/ka) TSAC+B
11/O/NV-A2	4.55±0.12	-
11/O/NV-A6	3.28±0.09	2.81±0.10
11/O/NV-A9	4.05±0.11	4.29±0.16
11/O/NV-B10	4.47±0.12	4.57±0.16
11/O/NV-B7	3.51±0.10	2.88±0.10
11/O/NV-B1	2.88±0.08	2.64±0.09
11/O/NV-C2	4.43±0.12	4.03±0.15
11/O/NV-C4b	3.01±0.08	3.29±0.12
11/O/NV-C7	2.91±0.08	2.22±0.08
11/O/NV-D2	-	3.78±0.14
11/O/NV-D7	-	3.06±0.11
<i>Duplicate measurements</i>		
11/O/NV-C2	4.43±0.12	4.03±0.15
11/O/NV-C4b	3.01±0.08	3.29±0.12
<i>Single grain measurements</i>		
11/O/NV-B10	4.47±0.12	4.57±0.16
11/O/NV-C2	4.43±0.12	4.03±0.15

Chapter 6:

Age and Environmental Reconstruction of the Nyl/Mogalakwena River Floodplain

6.1 Introduction

The OSL and ^{14}C ages obtained during this research project and the palaeo-environment during the most recent phase of sedimentation on the Nyl/Mogalakwena River floodplain will be presented and discussed in this chapter.

6.2 Calculated OSL and ^{14}C ages

Thirteen OSL ages were calculated from across the four sampled profiles, six in the floodplain environment (Profiles A and B), five in the tributary fan environment (Profiles C and D) and two repeat measurements were made in Profile C. The OSL ages (Table 6.1) were constrained by way of eight ^{14}C ages (Table 6.2) by sampling the interlayered tributary fan and floodplain sediments respectively *i.e.* collecting one ^{14}C sample from between two OSL samples (see Figure 6.1). The OSL ages were calculated as described in Section 3.3.1 at the Aberystwyth Luminescence Research Laboratory and at the Geoluminescence Laboratory at the University of the Witwatersrand. The ^{14}C ages were determined using the AMS technique (Section 3.2.1) by the Radiocarbon Dating Laboratory at Lund University, Sweden.

6.3 Reliability of the OSL and ^{14}C ages

6.3.1 OSL ages

The OSL ages were calculated from the true burial dose (D_b) and the dose rate (D_r) as described in Section 3.3.1. The D_b was calculated using the central age model (CAM) for eight samples and the two duplicate samples because of the low overdispersion (OD) values and minor amount of scatter within the population of D_e values. Alternatively, the D_b for three samples (NVA2, NVB10 and NVC2) was calculated using the minimum age model (MAM) due to the high overdispersion value ($> 20\%$) and the large amount of scatter within the population of D_e values

Table 6.1: OSL ages calculated for the Nyl/Mogalakwena River and Rooisloot samples, where n is the number of D_e values used to determine the true burial dose (D_b), OD is the overdispersion parameter and D_r the dose rate. D_r values for NVA2 and the two repeat measurements were measured using HRGS, all other D_r values were measured using a combination of TSAC and GM-beta counting. Fifteen ages are reported because of repeat measurements, but the eleven ages reported in bold were used in the reconstruction.

Sample	Location	Environment	n	OD (%)	Statistical model	D_b (Gy)	D_r (Gy/ka)	Burial age (ka)
11/O/NV-A2	Profile A	Floodplain	24	58	MAM	0.39 ± 0.01	4.55 ± 0.12	0.086 ± 0.002
11/O/NV-A6	Profile A	Floodplain	24	9	CAM	1.65 ± 0.03	2.809 ± 0.099	0.586 ± 0.024
11/O/NV-A9	Profile A	Floodplain	24	5	CAM	3.51 ± 0.04	4.287 ± 0.156	0.819 ± 0.031
11/O/NV-B10	Profile B	Floodplain	23	40	MAM	0.45 ± 0.09	4.566 ± 0.157	0.099 ± 0.020
11/O/NV-B7	Profile B	Floodplain	24	8	CAM	1.57 ± 0.03	2.882 ± 0.101	0.544 ± 0.021
11/O/NV-B1	Profile B	Floodplain	12	8	CAM	2.36 ± 0.06	2.642 ± 0.092	0.894 ± 0.038
11/O/NV-C2	Profile C	Tributary Fan	23	41	MAM	2.95 ± 0.23	4.026 ± 0.147	0.732 ± 0.064
11/O/NV-C4b	Profile C	Tributary Fan	24	9	CAM	2.58 ± 0.06	3.285 ± 0.116	0.785 ± 0.033
11/O/NV-C7	Profile C	Tributary Fan	24	8	CAM	2.39 ± 0.04	2.222 ± 0.081	1.078 ± 0.043
11/O/NV-D2	Profile D	Tributary Fan	24	11	CAM	3.75 ± 0.08	3.778 ± 0.137	0.992 ± 0.042
11/O/NV-D7	Profile D	Tributary Fan	24	8	CAM	11.89 ± 0.21	3.060 ± 0.109	3.884 ± 0.155
<i>Repeat measurements</i>								
11/O/NV-C2	Profile C	Tributary Fan	24	8	CAM	2.52 ± 0.04	4.43 ± 0.12	0.569 ± 0.018
11/O/NV-C4b	Profile C	Tributary Fan	24	6	CAM	2.38 ± 0.03	3.01 ± 0.08	0.791 ± 0.023
<i>Single-grain measurements</i>								
11/O/NV-B10	Profile B	Floodplain	39	58	MAM	0.39 ± 0.03	4.566 ± 0.157	0.085 ± 0.007
11/O/NV-C2	Profile C	Tributary Fan	41	56	MAM	2.42 ± 0.67	4.026 ± 0.147	0.602 ± 0.167

Table 6.2: ^{14}C ages as determined by the Radiocarbon Dating Laboratory at Lund University, Sweden. Percentage modern carbon (pMC) denotes samples contaminated by modern carbon.

Stratigraphic unit	^{14}C age (years BP)
NVA5	105.8 ± 0.6 pMC
NVA8	955 ± 50
NVB8	475 ± 45
NVB2	905 ± 50
NVC3a	106.0 ± 0.6 pMC
NVC5a	645 ± 50
NVD3a	1365 ± 50
NVD4	765 ± 50

(see Section 4.7.1.1 and Figure 4.10). The observed scatter is indicative of partial bleaching or post-depositional mixing.

6.3.1.1 Partial bleaching in the Nyl/Mogalakwena River and Rooisloot samples

Partial bleaching, whereby the OSL signal in individual grains is not completely reset during the processes of erosion and transportation, is a common problem encountered in the OSL dating of fluvial sediments which results in a residual signal within the grain that causes overestimation of the D_b and therefore the calculated age (Aitken, 1994; Duller, 1994; Murray, 2000; Wallinga, 2002; Rittenour, 2008). The overestimation effect of partial bleaching can be prevented by measuring the D_e values using small aliquots (< 100 grains) or single-grains. This should allow the unbleached grains within the population to be identified and prevents the residual signal and thus the burial age from being averaged as is the case with larger aliquots (Wallinga, 2002; Hanson, 2006; Rittenour, 2008). For young samples, where the residual signal contributes a large proportion of the measured D_e value, thereby resulting in a large age overestimation, single-grain dating is of particular importance (Rittenour, 2008). Thus given the young ages of the Nyl/Mogalakwena River and Rooisloot sediments and the possibility of partial bleaching in samples NVA2, NVB10 and NVC2, single-grain measurements were completed on NVB10 and NVC2.

6.3.1.2 Comparison of D_e distributions and OSL ages

A comparison of the D_e distributions (see Figure 4.9 and Table 6.1) shows that while the single-grain measurements produced higher overdispersion values, the amount of scatter in the single-grain distribution for NVB10 significantly decreased from the single aliquot distribution and the two datasets produced similar D_b values, 0.39 ± 0.03 Gy and 0.45 ± 0.09 Gy respectively. Consequently, the calculated ages for NVB10 are in good agreement with one another displaying a difference of 14 years between the dates. The age obtained from the single-grain measurement should be the more accurate of the two dates as this method features the least amount of averaging of the luminescence signal.

Alternatively, for NVC2 while the single-grain distribution appears to display less scatter than the single aliquot distribution, the D_b values were significantly different, 2.42 ± 0.67 Gy and 2.95 ± 0.23 Gy respectively. This resulted in a difference of 130 years in the respective burial ages for NVC2, which is almost ten times the difference between the NVB10 burial ages. However, the large difference is most likely due to an error in the age calculated from the single aliquot measurements as it appears this age has been overestimated based on the stratigraphic relationship with sample NVC4b, *i.e.* NVC2 is 1.39 m above NVC4b with 53 years difference in the burial ages. Alternatively, considering the single-grain age, the difference in the burial ages becomes 183 years, thus in this instance the single-grain age appears to be more accurate which is to be expected due to the partial bleaching evident within the single aliquot D_e distribution.

In order to ascertain whether the single aliquot age obtained for NVC2 was indeed erroneous, repeat measurements were obtained for NVC2 and the underlying OSL sample in the same profile, NVC4b. The repeat NVC2 measurement produced a D_b of 2.52 ± 0.04 Gy, which is within error of the single grain D_b of 2.42 ± 0.67 Gy but not of the original single aliquot D_b of 0.732 ± 0.064 Gy. Due to the corresponding repeat and single grain measurements, the age for the NVC2 layer was calculated from the repeat D_b value. This gives an age of 569 ± 18 years as opposed to 732 ± 64 years for layer NVC2. Furthermore, the repeat age is within error of the single grain age of 602 ± 167 years.

Repeat measurements were also run on the sample from layer NVC4b and the revised value supports the original measured value. The new D_b value of 2.38 ± 0.03 Gy produced an age of 791 ± 23 years. When the revised OSL age is compared with the original age of 785 ± 33 years, both ages are within error of one another. Therefore, considering the revised ages, the OSL dates in Profile C are stratigraphically correct.

6.3.2 Radiocarbon ages

There were two issues surrounding the ^{14}C ages, specifically carbon contamination and inverted ages. The issue of carbon contamination is well documented specifically in fluvial sediments where old carbon in the form of bones, wood, or charcoal may be reworked by the river system resulting in overestimated ages (Warne and Stanley, 1995; Stanley *et al.*, 1999; Stanley and Hait, 2000; Rittenour, 2008; Fuchs and Lang, 2009; Hua, 2009). The ages for the NVA5 and NVC3a stratigraphic units have been contaminated by modern carbon (see reported ages, Table 6.2) rendering these ages unusable in the stratigraphic correlation.

The issue of inverted ages, where older ages are located stratigraphically above younger ages, appears to be characteristic of Holocene deltaic sediments according to Stanley and Hait (2000). They believe that this inversion is most likely due to the remobilisation of sediments during transportation down the river system, whereby old and young eroded material mixes as it is transferred from channels to adjacent alluvial plains; here it is stored temporarily until it is remobilised by channel migration and eventually redeposited. Age inversion was observed in the ^{14}C ages calculated for Profile D, specifically in layers NVD3a and NVD4. In the field, oxidised roots were noted in the NVD3a layer and both layers displayed ped structures. Therefore, the ^{14}C age inversion is most likely due to carbon contamination resulting from soil forming processes occurring on the tributary fan during periods when active progradation was suspended.

The issues of carbon contamination and age inversion highlighted above bring into question the validity of all the ^{14}C ages obtained for the Nyl/Mogalakwena River and Rooisloot sediments. Therefore, the ^{14}C ages and their relevance in the

reconstruction must be considered in terms of the calculated OSL ages and the relative stratigraphy.

6.3.3 Comparison of OSL and ^{14}C ages

Radiocarbon dating was chosen as an independent age control for this study due to: 1) the presence of organic-rich, fine-grained layers interlayered with the quartz-rich sandy layers used for OSL dating within the incised river cuts; 2) the wide acceptance of the technique within the Quaternary research community; and 3) the generally good correspondence between these two techniques. Ages from quartz OSL and independent age controls from various depositional settings were investigated by Murray and Olley (2002) and found to correlate well with one another (Figure 6.2), with no systematic offset for fluvial samples in comparison to other depositional environments. There were however inconsistencies between the OSL and radiocarbon methods which may reflect errors in the former due to partial bleaching and in the latter due to the repeated reworking of old carbon and extensive time intervals before the incorporation of organic material into the sediments (Fuchs and Lang, 2009; Rittenour, 2008). Furthermore, overestimation of ^{14}C ages is a common problem experienced when dating alluvial sediments and is particularly problematic for samples with an age of less than 500 years due to secular variations of ^{14}C production in the atmosphere (Jacobson *et al.*, 2003).

In their review papers on luminescence dating of fluvial deposits, Wallinga (2002), Stokes and Walling (2003) and Rittenour (2008) cite the lack of in situ organic material and the limited age range of the ^{14}C technique as reasons that radiocarbon dating may not be applicable to fluvial deposits even though it is the most widely used geochronological technique, whilst DeLong and Arnold (2007) concluded that the single grain OSL technique is particularly useful in fluvial sediments where ^{14}C ages are difficult to calibrate and in environments without reliable charcoal or with detrital-aged charcoal. Furthermore, they conclude that single grain OSL should be considered as a routine method for age-estimation in dryland alluvial-fan and axial-fluvial environments. Therefore, OSL dating (and particularly the single-grain technique) may be the most suitable geochronological tool for dating fluvial deposits while radiocarbon ages should instead be interpreted as a maximum limiting age for

the enclosing deposit due to the large errors which can be introduced by sampling carbon with an inherited age.

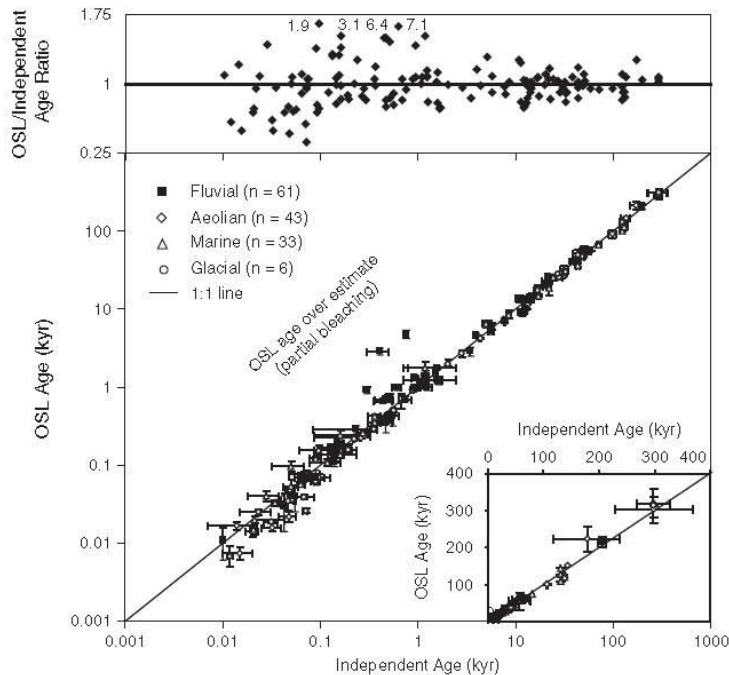


Figure 6.2: Graph showing the correlation between quartz OSL ages and those of independent age controls from various depositional settings (original by Murray and Olley, 2002; updated by Rittenour, 2008). No systematic offset is visible for fluvial samples in comparison to the other depositional environments.

6.3.3.1 Comparison of ages in Profiles A and B

The ages obtained for Profiles A and B corresponded well, with both OSL and ^{14}C ages generally displaying stratigraphic consistency (see Figure 6.1) *i.e.* ages increase with depth and no age inversion is evident. However, the ^{14}C ages for the lower of the sampled units (955 ± 50 years BP and 905 ± 50 years BP) are overestimated with respect to the underlying OSL ages (819 ± 31 years and 894 ± 38 years) although the 2σ error limits for the samples from Profile B do overlap. The ^{14}C age for the upper sampled unit in Profile A should have yielded an age similar to the 475 ± 45 years BP of the corresponding layer in Profile B had it not been contaminated by modern carbon in the form of roots.

6.3.3.2 Comparison of ages in Profiles C and D

The agreement of ages in Profiles C and D is very poor (see Figure 6.1). Profile D produced inverted ^{14}C ages and whilst the ^{14}C age for the upper unit (1365 ± 50 years BP) fits stratigraphically between the two OSL ages the ^{14}C age for the lower unit is

underestimated, due to contamination by younger carbon. Similarly, the ^{14}C age for the upper unit in Profile C was contaminated by modern carbon, and the ^{14}C age for the lower unit (645 ± 50 years BP) was underestimated with respect to the OSL age (791 ± 23 years) obtained from the overlying layer (NVC4b). Given the low overdispersion value of this sample it is unlikely that the OSL age has been overestimated due to an error in the calculation of the D_b . However it is possible that the D_r could be incorrect if the surrounding sediment was not completely homogenous. Sediment heterogeneity was observed during sampling; bioturbation was observed in Profiles A and B in the form of termite nests and in all four profiles in the form of root action. However, the revised OSL age for NVC4b was calculated using HRGS for the dosimetry and correlates with the original age obtained using TSAC and GM-beta counting. Therefore, it is more likely that the ^{14}C age is underestimated.

6.3.3.3 Age comparison across the sample area

When the OSL ages are considered in isolation they correspond well and show excellent stratigraphic consistency, both within the individual profiles and across the sample area. The similarity of the original single aliquot ages from the upper and middle sampled units from profile C (732 ± 64 years and 785 ± 33 years respectively; as discussed in Section 6.2.1) represents the only exception. However, the revised single aliquot ages calculated with HRGS correspond stratigraphically with the remainder of the OSL ages. The assertion of Wallinga (2002) that OSL dating of sand-sized quartz grains using the SAR protocol is the most suitable technique for the luminescence dating of fluvial sediments supports using the OSL ages for the reconstruction given the good agreement and consistency of the OSL ages and the discrepancy of these ages with the ^{14}C ages.

6.4 Environmental reconstruction of the Nyl/Mogalakwena River floodplain

The palaeo-environmental reconstruction was determined by combining the stratigraphy and geochronology for the sedimentary deposit located at the confluence of the Nyl/Mogalakwena River with the Rooisloot.

6.4.1 Stratigraphy

The stratigraphy of the four profiles was compared based on the data obtained from the site descriptions and grain size analysis (see Section 2.4.1 and Figure 2.6) and is supported by the calculated OSL and ^{14}C dates (see Figure 6.1). From the four profiles, three sedimentary packages were identified within the Rooisloot tributary fan. In order of deposition, the first package is represented by Profile D, the second by Profile C and the third across Profiles A and B.

The close spatial association of Profiles A and B produced a consistent stratigraphic correlation across the banks of the Nyl/Mogalakwena River, with the “doublet” in layers NVA4 and NVB9 providing visual confirmation, and the OSL ages in agreement both within the section and across the river, as discussed in Section 6.2.1. The ^{14}C dates overestimate the age of the organic-rich layers; however they are similar to the OSL ages (*i.e.* both OSL and ^{14}C dates indicate deposition occurred during the late Holocene).

Alternatively, Profiles C and D which were originally believed to be separate faces of a non-continuous section are instead separate depositional events, due to the difference in the stratigraphy and the large differences between the calculated ages. Furthermore, based on the OSL ages, it appears that an unconformity is located within the sequence in Profile D which is not reflected in Profile C. Radiocarbon ages for Profile D are inverted and so the exact location of the unconformity cannot be determined. Furthermore, it is likely that the dates for layers NVD3a (1365 ± 50 years BP) and NVD4 (765 ± 50 years BP) are both incorrect due to carbon contamination in the form of roots and reworking of sediments due to soil forming processes. Thus the relationship between Profile C and D is most likely due to incision within the tributary fan whereby the lower sequence observed in Profile D was deposited, followed by an erosional event and the subsequent deposition of the upper sequence of Profile D and the sequence observed in Profile C (see Figure 6.6). This theory is supported by the modern tributary fan environment, where numerous distributaries from the Rooisloot have produced incised channels within the tributary fan.

6.4.2 Depositional environment

The deposits of interfingering sedimentary layers (see Figure 1.5) are believed to be produced by alternating depositional cycles whereby sediments were deposited on the Nyl/Mogalakwena River floodplain and within the tributary fan at the river confluence. A series of depositional sequences can be identified in the sedimentary deposit at Profiles A and B (Figure 6.3a). A composite stratigraphic log of the two profiles shows distinct periods of progradation (labelled U_A , U_B , U_C , U_D and U_E on Figure 6.3a) of the tributary fan into the Nyl/Mogalakwena River which deposited thick, coarse-grained sedimentary layers. Interspersed among these depositional sequences are periods of non-deposition (labelled U_{AV} , U_{BV} , U_{CV} and U_{DV} , Figure 6.3a) when active sedimentation ceased and shallow lakes (vleis) developed. During these periods of non-deposition within the tributary fan (*i.e.* periods when the tributary fan was neither prograding nor aggrading) deposition of thin, fine-grained, generally organic-rich sedimentary layers (the floodplain sediments described in Section 2.5.1.) occurred on the Nyl/Mogalakwena River floodplain.

The encroachment of the floodplain into the distal reaches of the tributary fan would result from fluctuating water levels within the Nyl/Mogalakwena River, due to changing climatic factors such as rainfall and temperature or ponding due to a blockage in the trunk river flow as a result of the prograding tributary fan. Figure 6.3b depicts the basic depositional model in terms of varying water levels within the Nyl/Mogalakwena River. First, the tributary fan progrades into the trunk river and deposits the U_A depositional sequence. Then active sedimentation in the tributary fan ceases and the water level in the trunk river rises (due to downstream aggradation produced by the fan) causing a lake to develop. When the river overtops its banks the floodplain extends into the lowest reaches of the tributary fan and floodplain sediments are deposited (U_{AV} non-deposition period). Once again active sedimentation occurs and the fan begins to prograde into the trunk river (U_B depositional sequence) and tributary fan sediments are deposited over the previous floodplain sediments. When the next non-deposition period occurs the floodplain once again encroaches into the lowest reaches of the tributary fan and deposits floodplain sediments (U_{BV}) over the tributary fan sediments. This repeat process has

raised the fan surface by ~ 30 m and redirected the course of the Nyl/Mogalakwena River towards the Waterberg according to McCarthy *et al.* (2011).

Sedimentation in the tributary fan was not continuous and the episodic nature may be due to short-term climate fluctuations or migration of the distributary channels within the tributary fan. Historical photographs of the Nyl/Mogalakwena River floodplain obtained from Google Earth (Figure 6.4) show fluctuating water levels within the Nyl/Mogalakwena River which directly affected the extent of the lakes. The photographs were taken during the June-July period, when very little rain falls in the interior of South Africa. However, the photograph taken in 2004 shows a pronounced dry season with much lower water levels, particularly for the lake immediately upstream from the sample profiles (labelled V1, Figure 6.4). The contrast between the dry and wet season, the latter experienced in 2009, where water levels in the lake are considerably higher, is apparent. The variability of the water level within the Nyl/Mogalakwena River is also apparent in Figure 2.4, where the active progradation of the Rooisloot tributary fan is currently occurring. The extent of the river in 2004 is much reduced from that in 2008 and 2012.

Furthermore, during dry periods high runoff events such as flash floods are more likely to occur due to the lack of hillslope vegetation. Large bodies of water moving rapidly down the Rooisloot would produce thick, coarse-grained, poorly sorted deposits in the distal regions of the tributary fan, which would in turn result in progradation of the fan system. The stratigraphic units identified in the sampled profiles which were interpreted as tributary fan deposits were all thick layers (generally > 1 m), whilst the units interpreted as floodplain deposits were thinner layers (generally < 30 cm). Alternatively, the successions along the Rooisloot upstream from the sampled profiles displayed less complex layering with far greater layer thickness as seen in McCarthy *et al.* (2011) where two units were identified, namely the basal hematite-cemented, sand unit and the overlying coarse, yellow sand unit which was generally homogenous and ~ 12 m thick. The greater thickness and homogeneity of the layers upstream is most likely due to their position on the tributary fan, *i.e.* they are not located in the distal region of the fan and therefore do

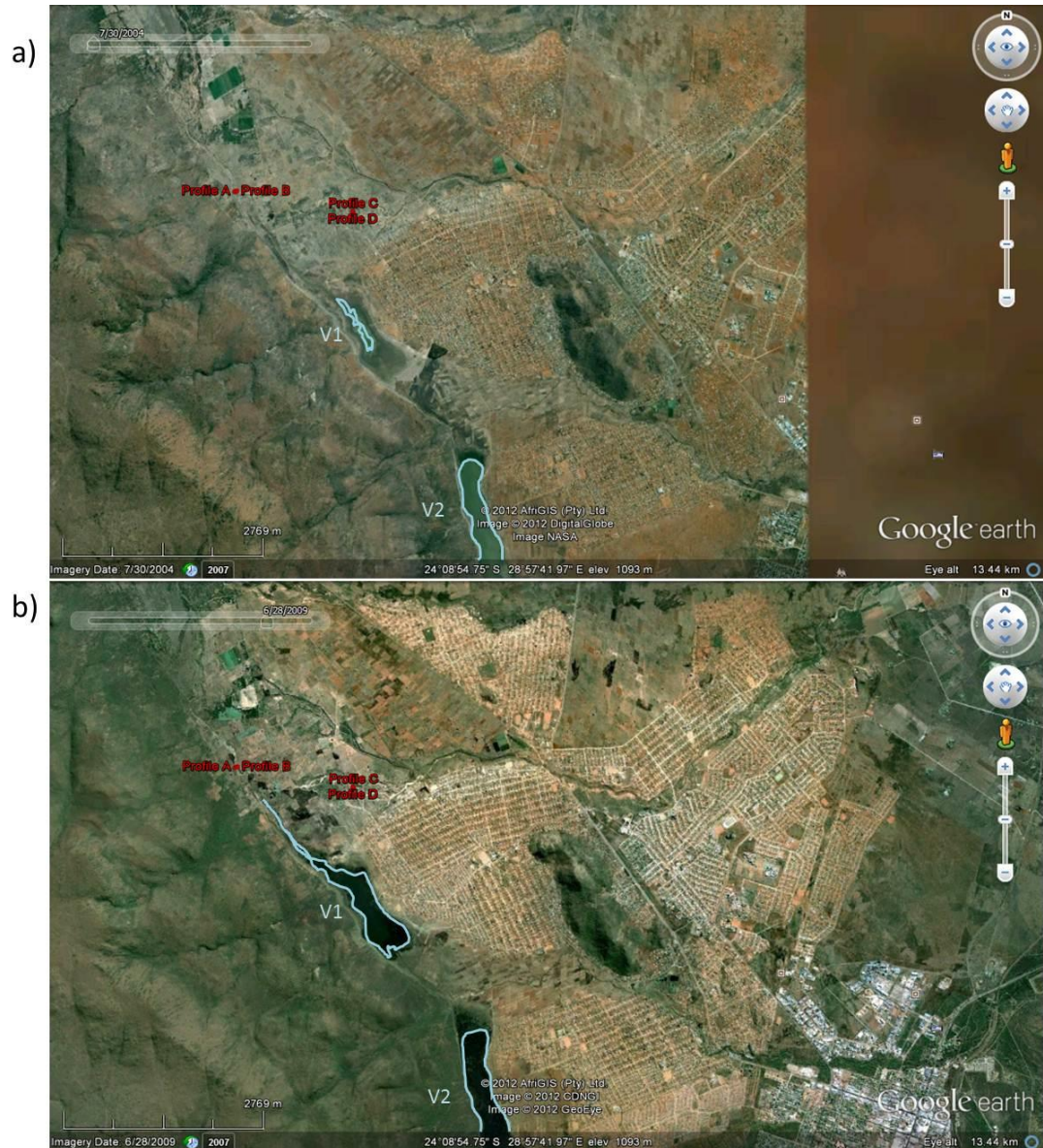


Figure 6.4: Historical images of the Nyl/Mogalakwena River floodplain taken in a) July 2004 during a dry season and b) June 2009 during a wet season. The water level of the lakes (V1 and V2) upstream (south) of the sample profiles are highlighted.

not possess a record of switching distributary channels or of interfingering floodplain deposits, hence their less complex layering.

In order to produce these alternating sequences the environment must have been controlled by short-term climate fluctuations with alternating periods of low and high water availability responsible for the alternating layers of floodplain and tributary sediments.

6.4.3 Sedimentation and established climatic events during the Holocene

Regardless of any systematic errors, both the OSL and ^{14}C ages place the tributary sedimentation along the Rooisloot within the Holocene epoch. Furthermore the deposition of these sediments occurred during the late Holocene when the climate was characterised by an overall cooling trend which began ~ 4300 years ago (Figure 6.5) based on data from the NorthGRIP ice core (Anderson *et al.*, 2007). Previously identified climatic events within this time frame include the Holocene climatic optimum between ~ 7 – 3 ka, the Medieval Warm Period from 900 – 1300 AD and the Little Ice Age from 1300 – 1800 AD (Anderson *et al.*, 2007; Walker, 2005; Holmgren *et al.*, 1999; Lowe and Walker, 1997).

The Medieval Warm Period (MWP) and Little Ice Age (LIA) have both been observed within South African proxy records (see Section 1.1), although the LIA has been more widely reported and appears to have had a greater effect on local South African climates (Tyson *et al.*, 2000). Maximum cooling during the LIA occurred at ~ 1700 AD based on the oxygen isotope records of speleothems from the Cold Air Cave and ocean corals off the southwestern coast of Madagascar (Holmgren *et al.*, 1999; Tyson *et al.*, 2000). Further evidence from the Cold Air Cave speleothems suggests that the period from 1200 to 1300 AD was unusually warm (Tyson *et al.*, 2000). This is supported by archaeological investigations in northern South Africa which reveal that severe droughts occurred during this period (Huffman, 2009). The lower units of Profile D (see Figure 6.1) were deposited at the end of the Holocene climatic optimum and the channel incision within the Rooisloot occurred prior to the onset of the MWP with the subsequent deposition of the upper units of Profile D and the lower units of Profile C occurring during the MWP.

6.4.3.1 Timing of the floodplain deposits

The fine-grained, organic-rich layers identified as floodplain deposits were deposited during periods when active sedimentation on the tributary fan ceased and the water level in the Nyl/Mogalakwena River increased. These events have been dated at 905 years BP (~ 1045 AD) and 475 years BP (~ 1475 AD) based on ^{14}C dates and ~ 600–700 years ago (1312–1412 AD) and ~ 100–150 years ago (1862–1912 AD) by the stratigraphic relationships between the OSL and ^{14}C dates (Figure 6.6). Therefore

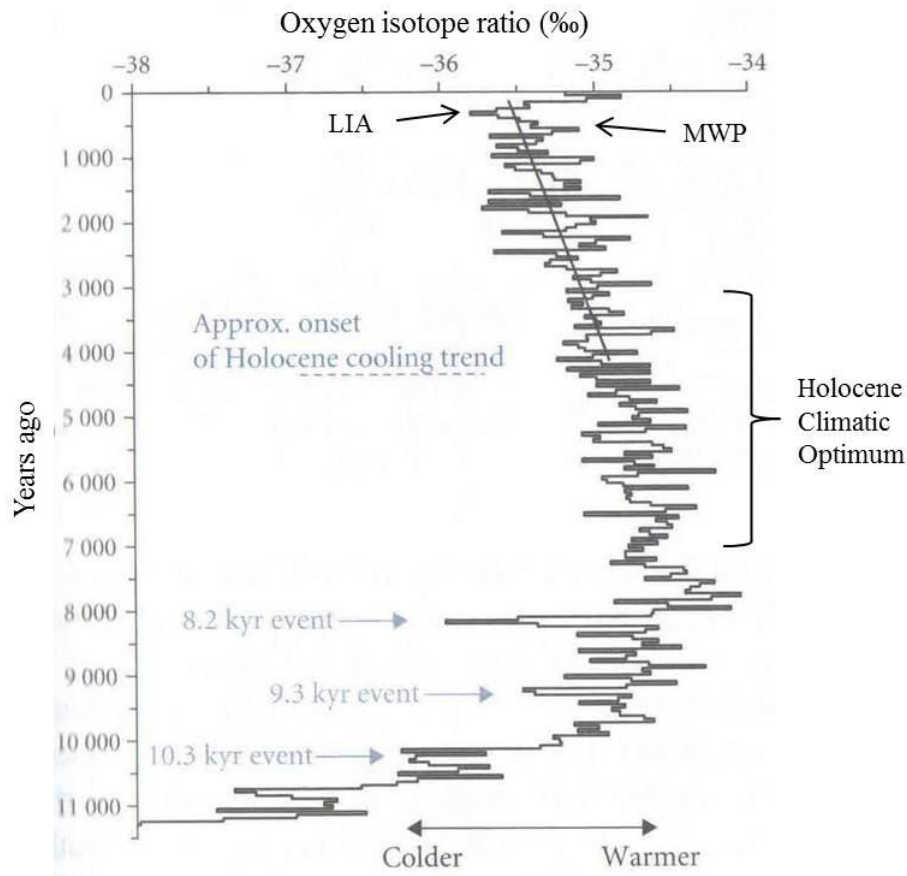


Figure 6.5: Graph depicting changes in air temperature determined from $\delta^{18}\text{O}$ variability from the NORTHGRIP ice core spanning the Holocene Epoch. Abrupt early Holocene cooling events are labelled, as are the Little Ice Age (LIA), Medieval Warm Period (MWP) and Holocene Climatic Optimum and the onset of the long-term cooling trend (illustrated by the solid line) is approximated by the dashed line (after Anderson *et al.*, 2007).

the oldest non-deposition event (U_{AV}) occurred during the MWP, the second non-deposition event (U_{BV}) at the boundary between the MWP and the LIA, the third non-deposition (U_{CV}) during the LIA and the fourth non-deposition event (U_{DV}) after the LIA had ended.

The ^{14}C date used for U_{AV} is overestimated with respect to the OSL ages of the underlying depositional sequence (U_A). Thus the age of the U_{AV} event is probably closer to 750 – 800 years, which would put this near the end of the MWP during the unusually warm period identified by Holmgren *et al.* (1999). Similarly the radiocarbon age for U_{CV} (which falls within the limits of the LIA) is overestimated. Therefore this age should be treated as a maximum possible age for this non-deposition event. If the U_{CV} age is overestimated by the same amount as the U_{AV} ^{14}C

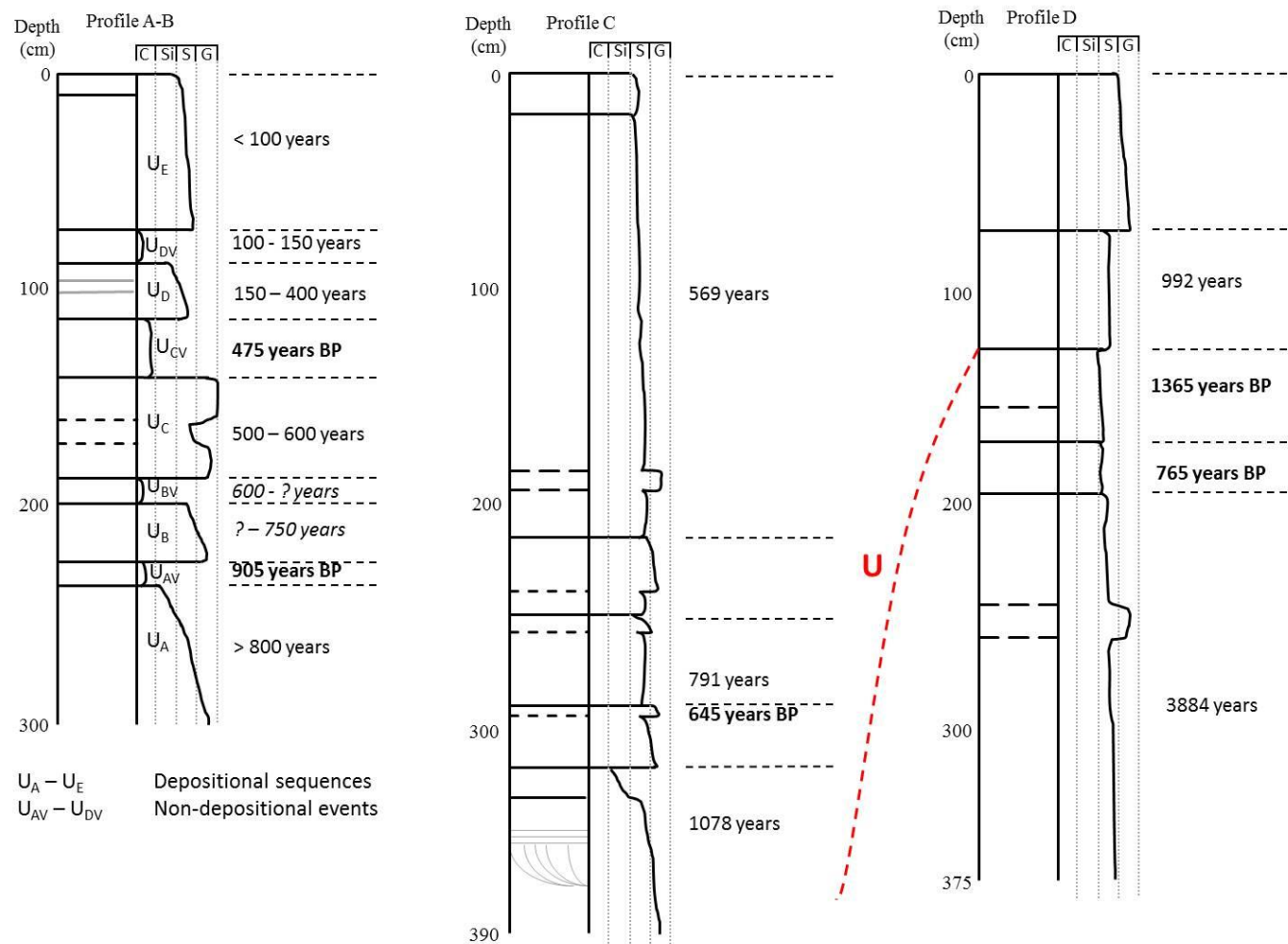


Figure 6.6: Approximate ages of the depositional sequences and non-deposition events identified in Profile A-B and the periods of aggradation in Profile C and Profile D. The dotted, red line represents the proposed unconformity between the deposition at Profiles C and D.

age, the former would be closer to 320 – 370 years which is nearer to the end of, but still within, the LIA. In contrast, the age for the U_{BV} non-deposition event was determined by the stratigraphic relationship of the dated layers and could occur at any time between 600 and 750 years ago, around the boundary between the MWP and LIA. The final non-deposition event (U_{DV}) occurred at ~ 100–150 years ago. These non-deposition events have occurred at times when water availability would have increased due to increased rainfall or blockage of and ponding in the Nyl/Mogalakwena River.

6.4.3.2 Periods of aggradation

Two periods of major aggradation in the tributary fan environment (Figure 6.6) occurred during the periods 800–1000 years ago (1000–1200 AD) and 500–700 years ago (1300–1500 AD). Aggradation between 800 and 1000 years can be observed in all four profiles, the U_A depositional sequence in Profile A-B, the lower depositional sequence in Profile C and the upper depositional sequence in Profile D. Aggradation between 500 and ~ 700 years can be observed in the U_C depositional sequence in Profile A-B and the upper sequence of Profile C. The corresponding aggradational periods prove that aggradation in the floodplain (Profile A and B) was matched by aggradation on the tributary fan (Profile C and D) in order to maintain the overall slope of the tributary fan. A third period of aggradation occurred ~ 150–400 years ago (1612–1862 AD).

The period of aggradation at 800–1000 years ago falls within the MWP and the periods at 500–700 years ago and ~ 150–400 years ago within the LIA. The LIA represents an arid period with overall low rainfall and little vegetation during which regional thunderstorms would produce short, intense runoff events which would result in deposition of thick successions in the distal region of the tributary fan. Similarly during the MWP the higher temperatures and drier conditions would result in less hillslope vegetation and intense runoff events would produce similar successions to those deposited during the LIA. Tyson *et al.* (2000) assert that the MWP was not as influential in South Africa as the LIA, as the latter imposed a general signal on patterns of local variability where the former did not. Furthermore, Holmgren *et al.* (1999) characterise the MWP as generally warmer but highly

variable, where the overall warm period was punctuated by short, cool periods based on the stalagmite records from the Cold Air Cave in Makapansgat Valley. However, archaeological work by Huffman (2009) in northern South Africa identified severe droughts during the period 1200-1300 AD which is in agreement with the unusually warm period identified by Holmgren *et al.* (1999) and Tyson *et al.* (2000). Therefore it is feasible that a semi-arid climate occurred during the MWP and the LIA, although the former was characterised by high temperatures and the latter by low temperatures.

Given the correlation between periods of aggradation in the tributary fan and the MWP and LIA, it is likely that the aggradation and progradation of the tributary fan is controlled by climate fluctuations. Alternatively, the periods of non-deposition are controlled by sedimentation in, and the amount of accommodation space available within the Nyl/Mogalakwena River. During periods of low water availability (such as those experienced under semi-arid conditions) hillslope vegetation decreases and intense runoff events deposit thick, coarse-grained successions which prograde into the Nyl/Mogalakwena River (identified as fan deposits in Chapter 2). Eventually these prograding tributary fans block the axial flow in the Nyl/Mogalakwena River and shallow lakes form within the river. The water level in the lakes rises until the river overtops its banks and thin, fine-grained sedimentary layers (identified as floodplain deposits in Chapter 2) are deposited across the floodplain, overlying the previous tributary fan deposit. The floodplain deposit will eventually be overlain by the next cycle of tributary fan sediments deposited in the Nyl/Mogalakwena River. This repeated process has resulted in the complex stratigraphy visible in the sedimentary deposit at the confluence of the Nyl/Mogalakwena River and the Rooisloot.

Aggradation within the tributary fan has been fairly rapid, with a mean aggradation rate of 0.29 cm/year over the last ~ 900 years (based on the age and depth of the lowest OSL sample in the Profile B stratigraphy). This corresponds to ~ 3 m of sedimentation over the last 900 years (as seen in the stratigraphy of Profile A and B), which implies that the entire 30 m thick sedimentary succession on the Nyl/Mogalakwena River floodplain could have been deposited within 9000 years if

the rate of aggradation was constant and sedimentation was continuous. However, tributary sedimentation on the Nyl/Mogalakwena River floodplain began prior to 200 ka as shown by McCarthy *et al.* (2011) who identified and dated two units further upstream in the Rooisloot (see Figure 2.3; site location labelled “1”). The upper unit was unconsolidated, yellowish, coarse sand which appeared to be a homogenous layer ~ 12 m thick and provided OSL ages ranging between 518 ± 22 years and 833 ± 37 years, which correlates with the two major periods of aggradation identified in this study (500-700 years ago and 800-1000 years ago). The underlying unit was coarse sand, cemented and stained red by hematite which produced a minimum age of 226 ka because the sample was in saturation. Therefore, it can be concluded that either the current rate of sedimentation is significantly higher than it was in the distant past or that the accumulated sediment is periodically eroded and flushed from the system due to headward erosion or the formation of local unconformities.

Periodic flushing of the system may be attributed to headward erosion within the Nyl/Mogalakwena River as increased tributary sediment delivery steepens the gradient sufficiently to create a knickpoint, which then migrates upstream. The knickpoint erodes the accumulated sediment and removes it from the system (McCarthy *et al.*, 2011). Alternatively, repeated channel avulsion within the tributary fan would result in periodic aggradation and erosion of sediment, which would produce a complex stratigraphy marked by local unconformities.

6.5 Summary

Thirteen OSL dates and eight ^{14}C dates were determined from the interlayered floodplain and tributary fan sediments located at the confluence of the Nyl/Mogalakwena River with its tributary the Rooisloot. The OSL dates ranged from 90 years to 3800 years, whilst the ^{14}C dates ranged from 1365 years BP to present. The OSL and ^{14}C dates in places are inconsistent with each other, due in part to partial bleaching and systematic errors for the former and overestimation and stratigraphic inversion for the latter. However, the OSL dates show excellent agreement and stratigraphic consistency across the study area. Thus in this research

project the OSL dating technique has proven to be a more reliable technique for the dating of fluvial sediments than ^{14}C dating.

Tributary sedimentation began on the Nyl/Mogalakwena River floodplain prior to 200 ka based on the OSL date obtained by McCarthy *et al.* (2011) in an independent research study. However the sampled profiles in this research project only extend through the late Holocene from ~ 3800 years to present. During this time period deposition appears to have been controlled by short-term climate fluctuations. Thick, coarse-grained, sandy-gravelly layers were deposited during semi-arid periods, when low rainfall and sparse vegetation caused regional thunderstorms to produce short, intense runoff events which resulted in deposition in the distal portion of the tributary fan. Eventually the tributary fans prograded across the Nyl/Mogalakwena River and blocked the axial flow of the river, causing shallow lakes to form. Once the water level in the lakes rose sufficiently, the river overtopped its banks and fine-grained (sometimes organic-rich) units were deposited on the floodplain and in the distal reaches of the tributary fan. The sandy, tributary fan layers are thicker than their floodplain counterparts and resulted in aggradation of the land surface and progradation of the Rooisloot tributary fan into the Nyl/Mogalakwena River. The correlation between the LIA and WMP and the periods of fan progradation imply that tributary fan sedimentation is controlled by short-term climate fluctuations.

The average rate of aggradation of the land surface is high with ~ 3 m of sediment being deposited over the last 900 years. Were this rate of aggradation constant and sedimentation continual, the entire 30 m sedimentary deposit could have been deposited in 9 000 years. However, since tributary sedimentation has been occurring since prior to 220 000 years ago this implies that either the recent sedimentation rate is higher than it was in the distant past or the sediment is periodically eroded from the system due to headward erosion or the formation of local unconformities.

Chapter 7:

Conclusions

In this research project a detailed stratigraphy was compiled and OSL and ^{14}C dating techniques were used to determine an accurate chronology for sedimentary deposits located at the confluence of the Nyl/Mogalakwena River with its tributary the Rooisloot in Limpopo Province, South Africa. A palaeo-environmental reconstruction of the area at the confluence showed that deposition of the interlayered floodplain and tributary fan sediments occurred in accordance with the depositional model published by McCarthy *et al.* (2011).

7.1 Summary of findings

The palaeo-environmental record for the northern hemisphere is more extensive than that for the southern hemisphere, thus Quaternary reconstructions within the southern hemisphere are necessary to extend the record and our understanding of climatic variations during the recent past. The Nyl/Mogalakwena River floodplain in Limpopo Province represents one of the few basins in the interior of South Africa that is undergoing active sedimentation. This research project analysed the stratigraphy in the Rooisloot tributary fan and determined a detailed geochronology in an effort to assess the validity of the depositional model for the floodplain as published by McCarthy *et al.* (2011).

The geochronology relied on OSL and ^{14}C dates obtained from the coarse-grained, quartz-rich sediments and fine-grained, organic-rich sediments respectively. The OSL dates were obtained using the standard Single Aliquot Regenerative Dose (SAR) protocol on 24 small aliquots of sand-sized quartz grains for each sample. Minimal partial bleaching was evident but for samples with an overdispersion value greater than 20 % the minimum age model (MAM) was used to determine the D_b value and a single-grain sequence was run as a check. The single-grain measurements produced more accurate results for sample NVC2, which had been overestimated by the single aliquot measurements, the former providing a date of 602 ± 167 years, 130 years younger than the latter. A repeat single aliquot

measurement for NVC2 produced an age of 569 ± 18 years, which is in clear agreement with the single-grain age. Alternatively, the single-grain and single aliquot measurements for NVB10 produced similar dates within 2σ of one another and a difference of 14 years.

The ^{14}C dates proved to be problematic in some cases displaying overestimation of the age and stratigraphic inversion. These issues are most likely due to contamination by older or younger carbon, with two samples (NVA5 and NVC3a) displaying contamination by modern carbon. Overall, the OSL and ^{14}C dates were inconsistent when compared, with the OSL dates ranging between 90 years and 3884 years and the ^{14}C dates from 1365 years BP to present. However when considered in isolation, the OSL dates displayed excellent agreement and stratigraphic consistency across the sample area, proving (in this research project) that OSL dating was the preferable technique for determining the ages of the fluvial sediments.

The geochronology was combined with the stratigraphy in order to infer the palaeo-environmental conditions and led to the identification of three sedimentary packages within the four sampled profiles. Although tributary sedimentation began prior to 220 ka based on the OSL date obtained by McCarthy *et al.* (2011) in an independent research study, the sequences analysed in this research project only extend through the late Holocene from ~ 3900 years to present. During this time period deposition appears to have been controlled by short-term climate fluctuations. Progradation of the alluvial fan into the Nyl/Mogalakwena River and aggradation of the deposit occurred during arid or semi-arid periods when regional thunderstorms produced short, intense runoff events which resulted in deposition in the distal portion of the alluvial fan. This is observed in the sedimentary sequence as thick successions of yellowish – brownish, coarse-grain sandy layers. The floodplain deposits are thin, laterally extensive, fine-grained, generally (but not necessarily) organic-rich layers deposited when the water level in the Nyl/Mogalakwena River rose, which increased the extent of the shallow lakes (vleis) and caused the Nyl/Mogalakwena River to overtop its banks resulting in floodplain deposition overlying the tributary fan deposits. The floodplain deposits correlate to periods of high water availability due to increased rainfall or ponding within the Nyl/Mogalakwena River. These

alternating periods produced the interlayered sediments as observed in the incised river cuts at the confluence of the Nyl/Mogalakwena River with the Rooisloot. The correlation between the LIA and WMP and the periods of fan progradation imply that tributary fan sedimentation may be controlled by short-term climate fluctuations.

In conclusion, the use of the OSL dating technique on fluvial deposits in South Africa provides an accurate determination of the burial age of the deposit and appears to be preferable to ^{14}C dating of these sediments. The climate of the Nyl/Mogalakwena River area over the last 3.8 ka appears to have been controlled by short-term climate fluctuations which resulted in the deposition of interlayered floodplain and tributary fan sediments at the confluence of the Nyl/Mogalakwena River with the Rooisloot. Furthermore, the rapid rate of sedimentation over the last 900 years in relation to the thickness of the sedimentary deposit and the time span of tributary sedimentation implies that the Nyl/Mogalakwena River floodplain system undergoes extreme periods of erosion which enables the removal of a large volume of sediment from the system.

7.2 Future research direction

Whilst the geochronology is considered to be of a sufficiently high-resolution for this research project, based on the OSL dates obtained by McCarthy *et al.* (2011) tributary sedimentation began prior to 200 ka. This implies that the sedimentary deposit at the confluence of the Nyl/Mogalakwena River with the Rooisloot contains a palaeo-environmental signal extending back into the Pleistocene epoch. The profiles selected for analysis in this research project only extended back ~ 3800 years into the late Holocene. Therefore the true extent of the palaeo-environmental signal remains to be analysed and requires further, more extensive regional sampling and analysis of the sedimentary deposit. This would require the completion of a thorough sedimentological study to better understand the depositional relationships within the region, a detailed mineralogical study to ascertain the source material and further geochronology work to extend the age range of the record and determine more accurate sedimentation rates. This extended record would allow the sedimentary deposits on the Nyl/Mogalakwena River floodplain to be correlated with other lower resolution proxy records from the immediate area, such as the pollen

record from the Wonderkrater spring mound (McCarthy *et al.*, 2010; Scott *et al.*, 2003; Scott and Thackeray, 1987) and the rainfall and climate records from the Tswaing Crater lake (Kristen *et al.*, 2007; Scott, 1999; Partridge *et al.*, 1997) in an effort to better constrain the local conditions during the Quaternary.

References

Adamiec, G. and Aitken, M.J. (1998). Dose-rate conversion factors: update. *Ancient TL*, **16**, 37-49.

Aitken, M. J. (1985). *Thermoluminescence dating*, Academic Press.

Aitken, M.J. (1990). Pairs precision required in alpha counting. *Ancient TL*, **8**, 12-14.

Aitken, M. J. (1994). Optical dating: a non-specialist review. *Quaternary Science Reviews*, **13**, 503-508.

Aitken, M. J. (1998). *An Introduction to Optical Dating: The Dating of Quaternary Sediments by the Use of Photon-Stimulated Luminescence*, Oxford University Press.

Aitken, M.J. and Smith, B.W. (1988). Optical dating: recuperation after bleaching. *Quaternary Science Reviews*, **7**, 387-393.

Aitken, M.J. and Xie, J. (1990). Moisture correction for annual gamma dose. *Ancient TL*, **8**, 6-9.

Albarède, F. (2011). *Geochemistry: An Introduction*. Cambridge University Press, Cambridge, pp. 342.

Anderson, D.E., Goudie, A.S. and Parker, A.G. (2007). *Global Environments Through the Quaternary: Exploring Environmental Change*. Oxford University Press, Oxford, pp. 392.

Ankjærgaard, C. and Murray, A.S. (2007). Total beta and gamma dose rates in trapped charge dating based on beta counting. *Radiation Measurements*, **42**(3), 352-359.

Armitage, S. J., Duller, G. A. T. and Wintle, A. G. (2000). Quartz from southern Africa: sensitivity changes as a result of thermal pretreatment. *Radiation Measurements*, **32**, 571-577.

Baker, P. A., Seltzer, G. O., Fritz, S. C., Dunbar, R. B., Grove, M. J., Tapia, P. M., Cross, S. L., Rowe, H. D. and Broda, J. P. (2001). The history of South American tropical precipitation for the past 25,000 years. *Science*, **291**, 640-643.

Barboudi, A.I. and Rastin, B.C. (1983). A study of the absolute intensity of muons at sea level and under various thicknesses of absorber. *Journal of Physics G: Nuclear and Particle Physics*, **9**, 1577-1595.

Bar-Matthews, M., Marean, C. W., Jacobs, Z., Karkanas, P., Fisher, E. C., Herries, A. I. R., Brown, K., Williams, H. M., Bernatchez, J., Ayalon, A. and Nilssen, P. J. (2010). A high resolution and continuous isotopic speleothem record of paleoclimate

- and paleoenvironment from 90 to 53 ka from Pinnacle Point on the south coast of South Africa. *Quaternary Science Reviews*, **29**, 2131-2145.
- Bell, W.T. (1979). Attenuation factors for the absorbed radiation dose in quartz grains for thermoluminescence dating. *Ancient TL*, **8**, 2-13.
- Berger G.W. and Huntley D.J. (1994). Tests for optically stimulated luminescence from tephra glass. *Quaternary Geochronology (Quaternary Science Reviews)*, **13**, 509-511.
- Berger G.W. and Neil P.A. (1999). *Photon-stimulated-luminescence (PSL) dating tests of glass-rich volcanic ash*. Book of Abstracts LED99: 138.
- Blair, T. C. and McPherson, J. G. (1994). Alluvial fan processes and forms. In: Abrahams, A. D. and Parsons, A. J. (eds.) *Geomorphology of Desert Environments*. Chapman and Hall, London, 354-402.
- Blott, S.J. (2010). GRADISTAT, Version 8.0.
- Blott, S.J. and Pye, K. (2001). Gradistat: A grain size distribution and statistics package for the analysis of unconsolidated sediments. *Earth Surface Processes and Landforms*, **26**, 1237-1248.
- Boggs, S. (2006). *Principles of Sedimentology and Stratigraphy* (4th edition). Pearson Prentice Hall, New Jersey, 59.
- Botha, G.A. (1996). *The geology and palaeopedology of Late Quaternary colluvial sediments in northern Kwazulu/Natal*. Memoir 83 of the Geological Survey of South Africa, Council for Geoscience, pp. 165.
- Bøtter-Jensen, L. (1997). Luminescence techniques: instrumentation and methods. *Radiation Measurements*, **27**, 749-768.
- Bøtter-Jensen, L., Anderson, C.E., Duller, G.A.T. and Murray, A.S. (2003). Developments in radiation, stimulation and observation facilities in luminescence measurements. *Radiation Measurements*, **37**, 535-541.
- Bøtter-Jensen, L., Bulur, E., Duller, G.A.T. and Murray, A.S. (2000). Advances in luminescence instrument systems. *Radiation Measurements*, **32**, 523-528.
- Bøtter-Jensen, L., Bulur, E., Murray, A. S., and Poolton, N.R.J. (2002). Enhancements in luminescence measurement techniques. *Radiation Protection Dosimetry*, **101**, 119-124.
- Bøtter-Jensen, L. and Duller, G.A.T. (1992). A new system for measuring OSL from quartz samples. *Nuclear Tracks and Radiation Measurements*, **20**, 549-553.

- Bøtter-Jensen, L., Duller, G.A.T., Murray, A.S. and Banerjee, D. (1999a). Blue light emitting diodes for optical stimulation of quartz in retrospective dosimetry and dating. *Radiation Protection Dosimetry*, **84**, 335-340.
- Bøtter-Jensen, L., Junger, H. and Mejdahl, V. (1993). Recent developments in OSL techniques for dating quartz and feldspars. *Radiation Protection Dosimetry*, **47**, 643-648.
- Bøtter-Jensen, L. and Mejdahl, V. (1988). Assessment of beta dose-rate using a GM multicounter system. *Nuclear Tracks and Radiation Measurements*, **14**, 187-191.
- Bøtter-Jensen, L., Mejdahl, V. and Murray, A.S. (1999b). New light on OSL. *Quaternary Geochronology*, **18**, 303-309.
- Brennan, B.J. (2003). Beta doses to spherical grains. *Radiation Measurements*, **37**, 299-303.
- Brennan, B.J. (2006). Variation of the alpha dose rate to grains in heterogeneous sediments. *Radiation Measurements*, **41**, 1026-1031.
- Brook, G.A., Cowart, J.B., Brandt, S.A. and Scott, L. (1997). Quaternary climatic change in southern and eastern Africa during the last 300 ka: the evidence from caves in Somalia and the Transvaal region of South Africa. *Zeitschrift für Geomorphologie, Supplementband*, **108**, 15-48.
- Chase, B. (2009). Evaluating the use of dune sediments as a proxy for palaeo-aridity: A southern African case study. *Earth-Science Reviews*, **93**, 31-45.
- Chen, Y.W., Chen, Y.G., Murray, A.S., Liu, T.K. and Lai, T.C. (2003). Luminescence dating of neotectonic activity on the southwestern coastal plain, Taiwan. *Quaternary Science Reviews*, **22**(10-13), 1223-1229.
- Cohen, A. and Tyson, P.D. (1995). Sea-surface temperatures during the Holocene on the south coast of Africa: implications for terrestrial climate and rainfall, *Holocene*, **5**, 304-312.
- Crossley, R., Davison-Hirschman, S., Owen, R.B. and Shaw, P. (1983). Lake level fluctuations during the last 2000 years in Malawi. In: Vogel, J.C., (ed), *Late Cainozoic palaeoclimates of the Southern Hemisphere*, Rotterdam: Balkema, 305-16.
- David, B., Roberts, R. G., Magee, J., Mialanes, J., Turney, C., Bird, M., White, C., Fifield, L. K. & Tibby, J. (2007). Sediment mixing at Nonda Rock: investigations of stratigraphic integrity at an early archaeological site in northern Australia and implications for the human colonisation of the continent. *Journal of Quaternary Science*, **22**, 449-479.

- DeChant, L. J., Pease, P. P. and Tchakerian, V. P. (1999). Modelling alluvial fan morphology. *Earth Surface Processes and Landforms*, **24**, 641-652.
- DeLong, S.B. and Arnold, L.J. (2007). Dating alluvial deposits with optically stimulated luminescence, AMS ^{14}C and cosmogenic techniques, western Transverse Ranges, California, USA. *Quaternary Geochronology*, **2**, 129-136.
- Ditlefsen and Huntley (1994). Optical excitation of trapped charges in quartz, potassium feldspars and mixed silicates: the dependence on photon energy. *Radiation Measurements*, **23**, 675-682.
- Dunwiddie, P.W. and LaMarche, V. (1980). A climatologically-responsive tree-ring record from Widdringtonia cedarbergensis, Cape Province, South Africa. *Nature*, **286**, 796-97.
- Duller, G.A.T. (1992). *Luminescence chronology of raised marine terraces, south-west North Island, New Zealand*. Unpublished PhD thesis, University of Wales, Aberystwyth, pp. 147.
- Duller, G.A.T. (1994). Luminescence dating of poorly bleached sediments from Scotland. *Quaternary Science Reviews* **13**, 521-524.
- Duller, G.A.T. (2003). Distinguishing quartz and feldspar in single grain luminescence measurements. *Radiation Measurements*, **37**, 161-165.
- Duller, G.A.T. (2004). Luminescence dating of Quaternary sediments: recent advances. *Journal of Quaternary Science*, **19**, 183-192.
- Duller, G.A.T. (2008a). *Luminescence Dating: guidelines on using luminescence dating in archaeology*, English Heritage, Swindon.
- Duller, G.A.T. (2008b). Single-grain optical dating of Quaternary sediments: why aliquot size matters in luminescence dating. *Boreas*, **37**, 589-612.
- Duller, G.A.T. (2011). What date is it? Should there be an agreed datum for luminescence ages? *Ancient TL*, **29**, 1-4.
- Duller, G.A.T. (2012). Cross-talk during single grain optically stimulated luminescence measurements of quartz and feldspar. *Radiation Measurements*, **47**, 219-224.
- Duller, G.A.T. and Bøtter-Jensen, L. (1996). Comparison of optically stimulated luminescence signals from quartz using different stimulation wavelengths. *Radiation Measurements*, **26**, 603-609.

- Duller, G.A.T., Bøtter-Jensen, L. and Murray, A. S. (2000). Optical dating of single sand-sized grains of quartz: sources of variability. *Radiation Measurements*, **32**, 453-457.
- Espizua, L.E., Bigazzi, G., Junes, P.J., Hadler, J.C. and Osorio, A.M. (2002). Fission-track dating of a tephra layer related to Poti-Malal and Seguro drifts in the Río Grande basin, Mendoza, Argentina, *Journal of Quaternary Science*, **17**, 781-788.
- Fain, J., Soumana, S., Montret, M., Miallier, D., Pilleyre, T. and Sanzelle, S. (1999). Luminescence and ESR dating: beta-dose attenuation for various grain shapes calculated by a Monte-Carlo method. *Quaternary Geochronology*, **18**, 231-234.
- Feathers, J.K and Migliorini, E. (2001). Luminescence dating at Katanda – a reassessment. *Quaternary Science Reviews*, **20**, 961-966.
- Folk, R. L. (1980). *Petrology of sedimentary rocks*, Hemphill Pub. Co.
- Folk, R. L. and Ward, W. C. (1957). Brazos River Bar: A study in the significance of grain size parameters. *Journal of Sedimentary Petrology*, **27**, 3-26.
- Frost, P.G.H. (1987). *The regional landscape: Nylsvley in perspective*. South African National Scientific Programmes Report No. 133. Foundation for Research and Development, Council for Scientific and Industrial Research, Pretoria.
- Fuchs, M. and Lang, A. (2009). Luminescence dating of hillslope deposits—A review. *Geomorphology*, **109**, 17-26.
- Galbraith R.F. (1988). Graphical display of estimates having differing standard errors. *Technometrics*, **30**, 271-281.
- Galbraith, R. F. (2005). *Statistics for fission track analysis*, Chapman & Hall/CRC Press, Boca Raton.
- Galbraith, R. F. and Green, P. F. (1990). Estimating the component ages in a finite mixture. International Journal of Radiation Applications and Instrumentation. Part D. *Nuclear Tracks and Radiation Measurements*, **17**, 197-206.
- Galbraith, R. F. & Laslett, G. M. (1993). Statistical models for mixed fission track ages. *Nuclear Tracks and Radiation Measurements*, **21**, 459-470.
- Galbraith, R. F. & Roberts, D. L. (2006). *Statistical aspects of OSL equivalent dose and error calculation*. Unpublished book chapter.
- Galbraith, R. F., Roberts, R. G., Laslett, G. M., Yoshida, H. & Olley, J. M. (1999). Optical dating of single and multiple grains of quartz from Jinmium rock shelter, northern Australia: Part I, experimental design and statistical models. *Archaeometry*, **41**, 339-364.

- Galbraith, R. F., Roberts, R. G. & Yoshida, H. (2005). Error variation in OSL palaeodose estimates from single aliquots of quartz: a factorial experiment. *Radiation Measurements*, **39**, 289-307.
- Galloway, R.B. (1994). On the stimulation of luminescence with green light emitting diodes. *Radiation Measurements*, **23**, 547-550.
- Galloway, R.B., Hong, D.G. and Napier, H.J. (1997). A substantially improved green light emitting diode system for luminescence stimulation. *Measurement Science and Technology*, **8**, 267-271.
- Godwin, H. (1962). Half-life of radiocarbon. *Nature*, **195**, 984.
- Grün, R. (1989). Electron spin resonance (ESR) dating. *Quaternary International*, **1**, 65-109.
- Guérin, G., Mercier, N., Nathan, R., Adamiec, G. and Lefrais, Y. (2012). On the use of the infinite matrix assumption and associated concepts: A critical review. *Radiation Measurements*, in press.
- Guibert, P. and Schvoerer, M. (1991). TL dating: low background gamma spectrometry as a tool for the determination of the annual dose. *Nuclear Tracks and Radiation Measurements*, **18**, 231-238.
- Hanson, P. R. (2006). *Dating ephemeral stream and alluvial fan deposits on the central Great Plains: Comparing multiple-grain OSL, single-grain OSL, and radiocarbon ages*. United States Geological Survey Open File Report 2006-1351, p. 14. Available at: http://pubs.usgs.gov/of/2006/1351/pdf/of06-1351_508.pdf
- Hansen, J.E. and Sato, M. (2011). Paleoclimate implications for human-made climate change. In: Berger, A., Mesinger, F. and Šijači, D. (eds.). *Climate Change at the Eve of the Second Decade of the Century: Inferences from Paleoclimate and Regional Aspects: Proceedings of Milutin Milankovitch 130th Anniversary Symposium*.
- Harbor, J. (ed.). (1999). Cosmogenic isotopes in geomorphology. *Geomorphology* (Special Issue), **27**, 1-172.
- Harvey, A. M., Mather, A.E. and Stokes, M. (2005). Alluvial fans: geomorphology, sedimentology, dynamics - introduction. A review of alluvial fan research. In: Harvey, A. M., Mather, A.E. and Stokes, M. *Alluvial Fans: Geomorphology, Sedimentology, Dynamics*. London, Geological Society, Special Publications. **251**, 1-7.
- Harvey, A.M. (2011). Chapter 14: Dryland alluvial fans. In: Thomas, D.S.G. (ed). *Arid Zone Geomorphology: Process, form and change in Drylands* (3rd edition). Wiley-Blackwell, New York, 333-371.

- Hennig, G.J. and Grün, R. (1983). ESR dating in Quaternary geology. *Quaternary Science Reviews*, **2**, 157-238.
- Higgins, S.I. and Rogers, K.H. (1993). *The Nyl River floodplain: situation report and preliminary statement of impacts of the proposed Olifantsspruit dam*, Report no. 3/93, Centre for Water in the Environment, University of the Witwatersrand, Johannesburg.
- Higgins, S.I., Coetzee, M.A.S., Marneweck, G.C. and Rogers, K.H. (1996). The Nyl River floodplain, South Africa, as a functional unit of the landscape: a review of current information. *African Journal of Ecology*, **34**, 131-145.
- Holmgren, K., Karlén, W., Lauritzen, S. E., Lee-Thorp, J. A., Partridge, T. C., Piketh, S., Repinski, P., Stevenson, C., Svanered, O. and Tyson, P. D. (1999). A 3000-year high-resolution stalagmite based record of palaeoclimate for northeastern South Africa. *The Holocene*, **9**, 295-309.
- Holmgren, K., Lee-Thorp, J. A., Cooper, G. R. J., Lundblad, K., Partridge, T. C., Scott, L., Sithaldeen, R., Siep Talma, A. and Tyson, P. D. (2003). Persistent millennial-scale climatic variability over the past 25,000 years in Southern Africa. *Quaternary Science Reviews*, **22**, 2311-2326.
- Hong, D. G. and Galloway, R. B. (2000). Comparison of equivalent dose values determined by luminescence stimulation using blue and green light. *Nuclear Instruments and Methods in Physics Research Section B: Beam Interactions with Materials and Atoms*, **160**, 59-64.
- Hossain, S.M., DeCorte, F., Vandenberghe, D., Van den Haute, P. (2002). A comparison of methods for the annual radiation dose determination in the luminescence dating of loess sediment. *Nuclear Instruments and Methods in Physics Research A*, **490**, 598-613.
- Hua, Q. (2009). Radiocarbon: A chronological tool for the recent past. *Quaternary Geochronology*, **4**, 378-390.
- Huffman, T. N. (2009). A cultural proxy for drought: ritual burning in the Iron Age of Southern Africa. *Journal of Archaeological Science*, **36**, 991-1005.
- Huntley, D. J., Godfrey-Smith, D. I. and Thewalt, M. L. W. (1985). Optical dating of sediments. *Nature*, **313**, 105-107.
- Huntley, D.J., Hutton, J.T. and Prescott, J.R. (1993). The stranded beach-dune sequence of south-east South Australia: a test of thermoluminescence dating, 0-800ka. *Quaternary Science Reviews*, **12**, 1-20.

- Jacobs, Z. (2004). *Development of luminescence techniques for dating Middle Stone Age sites in South Africa*. Unpublished PhD thesis, University of Wales, Aberystwyth.
- Jacobs, Z., Duller, G.A.T. and Wintle, A.G. (2003a). Optical dating of dune sands from Blombos Cave, South Africa: II – single grain data, *Journal of Human Evolution*, **44**, 613-625.
- Jacobs, Z., Duller, G.A.T. and Wintle, A.G. (2006a). Interpretation of single grain D_e distributions and calculation of D_e . *Radiation Measurements*, **41**, 264-277.
- Jacobs, Z., Duller, G. A. T., Wintle, A. G. & Henshilwood, C. S. (2006b). Extending the chronology of deposits at Blombos Cave, South Africa, back to 140 ka using optical dating of single and multiple grains of quartz. *Journal of Human Evolution*, **51**, 255-273.
- Jacobs, Z., Wintle, A. G., Duller, G. A. T., Roberts, R. G. & Wadley, L. (2008). New ages for the post-Howiesons Poort, late and final Middle Stone Age at Sibudu, South Africa. *Journal of Archaeological Science*, **35**, 1790-1807.
- Jacobs, Z., Wintle, A.G. and Duller, G.A.T. (2003b). Optical dating of dune sand from Blombos Cave, South Africa: I – multiple grain data. *Journal of Human Evolution*, **44**, 599-612.
- Jäger, E. and J. C. Hunziker (1979). *Lectures in isotope geology*, Springer-Verlag, New York.
- Johnson, R.F. (1988). *A history of climate and marine productivity from sediment off the west coast of southern Africa*. Final Report, National Programme for Weather, Climate and Atmosphere Research. FRD, Pretoria, 6 pp.
- King, L.C. (1962). *The Morphology of the Earth*. Oliver and Boyd, White Plains, N.Y., 726pp.
- Krbetschek, M.R., Rieser, U., Zöller, L. and Heinicke, J. (1994). Radioactive disequilibria in palaeodosimetric dating of sediments. *Radiation Measurements*, **23**, 485-489.
- Kristen, I., Fuhrmann, A., Thorpe, J., Röhl, U., Wilkes, H. and Oberhänsli, H. (2007). Hydrological changes in southern Africa over the last 200 ka as recorded in lake sediments from the Tswaing impact crater. *South African Journal of Geology*, **110**, 311-2326.
- Lepper, K., Larsen, N. A. and McKeever, S. W. S. (2000). Equivalent dose distribution analysis of Holocene eolian and fluvial quartz sands from Central Oklahoma. *Radiation Measurements*, **32**, 603-608.

- Libby, W.F. (1955). *Radiocarbon Dating* (2nd edition). University of Chicago Press, Chicago.
- Lowe, J.J. and Walker, M.J.C. (1997). *Reconstructing Quaternary Environments* (2nd edition). Longman, Hong Kong.
- Markey, B. G., Bøtter-Jensen, L. and Duller, G. A. T. (1997). A new flexible system for measuring thermally and optically stimulated luminescence. *Radiation Measurements*, **27**, 83-89.
- Mayya, Y.S., Morthekai, P., Murari, P., Singhvi, A.K. (2006). Towards quantifying beta microdosimetric effects in single-grain quartz dose distribution. *Radiation Measurements*, **41**, 1032-1039.
- McCarthy, T.S., Ellery, W.N., Blackwell, L., Marren, P., de Klerk, B., Tooth, S., Brandt, D. and Woodborne, S. (2010). The character, origin and palaeoenvironmental significance of the Wonderkrater spring mound, South Africa. *Journal of African Earth Sciences*, **58**, 115-126.
- McCarthy, T.S., Tooth, S., Jacobs, Z., Rowberry, M.D., Thompson, M., Brandt, D., Hancox, P.J., Marren, P.H., Woodborne, S. and Ellery, W.N. (2011). The origin and development of the Nyl River floodplain wetland, Limpopo Province, South Africa: trunk-tributary interactions in a dryland setting. *South African Geographical Journal*, **93**, 172-190.
- Mejdahl, V. (1979). Thermoluminescence dating: dose attenuation in quartz grains. *Archaeometry*, **21**, 61-72.
- Moreno, C. and Romero-Segura, M. J. (1997). The development of small-scale sandy alluvial fans at the base of a modern coastal cliff: process, observations and implications. *Geomorphology*, **18**, 101-118.
- Morgan, C.S. (1996). *The application of digital terrain models and a geographic information system in the modelling of flooding in the Nyl River Flood plain*. Unpublished MSc Thesis, University of the Witwatersrand, South Africa, pp. 159.
- Murray, A.S. (1981). *Environmental radioactivity studies relevant to thermoluminescence dating*. Unpublished DPhil thesis, University of Oxford, pp. 404.
- Murray, A.S. (1982). Stability of radioisotopic concentrations and their dependence on grain size. *PACT*, **6**, 216-233.
- Murray, A. S. (2000). Single aliquot protocols in luminescence dating. Luminescence and its applications I. *Luminescence Society of India*, **C 1/2000**, 103-117.

- Murray, A. S. and Aitken, M. J. (1988). Analysis of low-level naturally occurring radioactivity in small samples for use in thermoluminescence dating using high-resolution gamma spectrometry. *International Journal of Applied Radiation Isotopes* **39**, 145-158.
- Murray, A. S. and Olley, J. M. (2002). Precision and accuracy in the optically stimulated luminescence dating of sedimentary quartz: a review. *Geochronometria*, **21**, 1-16.
- Murray, A.S. and Roberts, R.G. (1998). Measurement of the equivalent dose in quartz using a regenerative-dose single-aliquot protocol. *Radiation Measurements*, **29**, 503-515.
- Murray, A.S. and Wintle, A.G. (2000). Luminescence dating of quartz using an improved single-aliquot regenerative-dose protocol. *Radiation Measurements*, **32**, 57-73.
- Naeser, C.W. and Naeser, N.D. (1988). Fission-track dating of Quaternary events. *Geological Society of America, Special Paper*, **227**, 1-11.
- Nathan, R.P. and Mauz, B. (2008). On the dose-rate estimate of carbonate-rich sediments for trapped charge dating. *Radiation Measurements*, **43**, 14-25.
- Nichols, G. (2009). *Sedimentology and Stratigraphy*, Wiley-Blackwell, Oxford, UK.
- Oczkowski, H.L. (2001). Gamma spectrum analysis for environmental nuclides. *Geochronometria*, **20**, 39-44.
- Oczkowski, H.L., Przegietka, K.R., Lankauf, K.R. and Szmańda, J.B. (2000). Gamma Spectrometry in Thermoluminescence Dating. *Geochronometria - Journal on Methods and Applications of Absolute Chronology*, **18**, 57-62.
- Oguchi, T., Saito, K., Kadomura, H. and Grossman, M. (2001). Fluvial geomorphology and paleohydrology in Japan. *Geomorphology*, **39**, 3-19.
- Olley, J. M., Caitcheon, G. and Murray, A. S. (1998). The distribution of apparent dose as determined by Optically Stimulated Luminescence in small aliquots of fluvial quartz: Implications for dating young sediments. *Quaternary Geochronology*, **17**, 1033-1040.
- Olley, J. M., De Deckker, P., Roberts, R. G., Fifield, L. K., Yoshida, H. and Hancock, G. J. (2004a). Optical dating of deep-sea sediments using single grains of quartz: a comparison with radiocarbon. *Sedimentary Geology*, **169**, 175-189.
- Olley, J.M., Murray, A. and Roberts, R.G. (1996). The effects of disequilibrium in the Uranium and Thorium decay chains on burial dose rates in fluvial sediments. *Quaternary Science Reviews (Quaternary Geochronology)*, **15**, 751-760.

- Olley, J. M., Pietsch, T. and Roberts, R. G. (2004b). Optical dating of Holocene sediments from a variety of geomorphic settings using single grains of quartz. *Geomorphology*, **60**, 337-358.
- Partridge, T.C. and Maud, R.R. (1987). Geomorphic evolution of southern Africa since the Mesozoic. *South African Journal of Geology*, **90**, 179-208.
- Partridge, T. C., Demenocal, P. B., Lorentz, S. A., Paiker, M. J. and Vogel, J. C. (1997). Orbital forcing of climate over South Africa: A 200,000-year rainfall record from the Pretoria saltpan. *Quaternary Science Reviews*, **16**, 1125-1133.
- Petit, J. R., Jouzel, J., Raynaud, D., Barkov, N. I., Barnola, J. M., Basile, I., Bender, M., Chappellaz, J., Davis, M., Delaygue, G., Delmotte, M., Kotlyakov, V. M., Legrand, M., Lipenkov, V. Y., Lorius, C., Pepin, L., Ritz, C., Saltzman, E. and Stievenard, M. (1999). Climate and atmospheric history of the past 420,000 years from the Vostok ice core, Antarctica. *Nature*, **399**, 429-436.
- Poolton, N.R.J. and Bailiff, I.K. (1989). The use of LEDs as an excitation source for photoluminescence dating of sediments. *Ancient TL*, **7**, 18-20.
- Pope, R.J.J. and Wilkinson, K.N. (2005). Reconciling the roles of climate and tectonics in Late Quaternary fan development on the Sparta piedmont, Greece. In: Harvey, A. M., Mather, A.E. and Stokes, M. *Alluvial Fans: Geomorphology, Sedimentology, Dynamics*. London, Geological Society, Special Publications, **251**, 133-152.
- Porszasz, K. (1971). *Provisional report of Nyl River valley subterranean water supply project*, Technical Report no. GH 3407, Department of Water Affairs, Pretoria.
- Porszasz, K. (1973). *Nyl River valley: an investigation of the groundwater potential*, Technical report no. GH 2984, Department of Environmental Affairs, Pretoria.
- Porszasz, K. (1978). *Groundwater in the upper Nyl River Basin at Nylstroom*, Technical Report no. GH 3053, Department of Water Affairs, Pretoria.
- Powers, M.C. (1953). A new roundness scale for sedimentary particles. *Journal of Sedimentary Petrology*, **23**, 117-119.
- Prell, W. L., Hutson, W. H. and Williams, D. F. (1979). The Subtropical Convergence and late Quaternary circulation in the southern Indian Ocean. *Marine Micropaleontology*, **4**, 225-234.
- Prescott, J.R. and Hutton, J.T. (1994). Cosmic ray contributions to dose rates for luminescence and ESR dating: large depths and long-term time variations. *Radiation Measurements*, **23**, 497-500.

- Prescott, J.R. and Hutton, J.T. (1995). Environmental dose rates and radioactive disequilibrium from some Australian luminescence dating sites. *Quaternary Science Reviews*, **14**, 439-448.
- Preusser, F., Degering, D., Fuchs, M., Hilgers, A., Kadereit, A., Klasen, N., Krbetschek, M. R., Richter, D. and Spencer, J. Q. G. (2008). Luminescence dating: basics, methods and applications. *Quaternary Science Journal*, **57**, 95-149.
- Preusser, F. and Degering, D. (2006). Luminescence dating of the Niederweningen mammoth site, Switzerland. *Quaternary International*, **164-165**, 106-112.
- Reimer, P.J., Baillie, M.G.L., Bard, E., Bayliss, A., Beck, J.W., Blackwell, P.G., Ramsey, C.B., Buck, C.E., Burr, G.S., Edwards, R.L., Friedrich, M., Grootes, P.M., Guilderson, T.P., Hajdas, I., Heaton, T.J., Hogg, A.G., Hughen, K.A., Kaiser, K.F., Kromer, B., McCormac, F.G., Manning, S.W., Reimer, R.W., Richards, D.A., Southon, J.R., Talamo, S., Turney, C.S.M., van der Plicht, J. and Weyhenmeyer, C.E. (2009). IntCal09 and Marine09 Radiocarbon Age Calibration Curves, 0–50,000 Years cal BP. *Radiocarbon*, **51**, 1111-1150.
- Retallack, G.J. (2001). *Soils of the past: an introduction to palaeopedology* (2nd edition). Blackwell Science, Oxford.
- Rittenour, T. M. (2008). Luminescence dating of fluvial deposits: applications to geomorphic, palaeoseismic and archaeological research. *Boreas*, **37**, 613-635.
- Roberts, R.G., Galbraith, R.F., Olley, J.M., Yoshida, H. and Laslett, G.M. (1999). Optical dating of single and multiple grains of quartz from Jinmium rock shelter, northern Australia: Part II, results and implications. *Archaeometry*, **41**, 365-395.
- Roberts, R. G., Galbraith, R. F., Yoshida, H., Laslett, G. M. and Olley, J. M. (2000). Distinguishing dose populations in sediment mixtures: a test of single-grain optical dating procedures using mixtures of laboratory-dosed quartz. *Radiation Measurements*, **32**, 459-465.
- Robinson, R.A.J., Spencer, J.Q.G., Strecker, M.R., Richter, A. and Alonso, R.N. (2005). Luminescence dating of alluvial fans in intermontane basins of NW Argentina. In: Harvey, A. M., Mather, A.E. and Stokes, M. *Alluvial Fans: Geomorphology, Sedimentology, Dynamics*. London, Geological Society, Special Publications, **251**, 153-168.
- Rodnight, H. (2006). *Developing a luminescence chronology for late Quaternary fluvial change in South African floodplain wetlands*. PhD, University of Wales, Aberystwyth.
- Rodnight, H., Duller, G.A.T., Tooth, S. and Wintle, A.G. (2005). Optical dating of a scroll-bar sequence on the Klip River, South Africa, to derive the lateral migration rate of a meander bend. *The Holocene*, **15**, 802-811.

- Rowberry, M. D., McCarthy, T. S., Thompson, M., Nomnganga, A. and Moyo, L. (2011). The spatial and temporal characterisation of flooding within the floodplain wetland of the Nyl River, Limpopo Province, South Africa. *Water SA*, **37**, 445-451.
- Sand Forum International. (2009). World Atlas of Sands: Collection of Sands Worldwide. *Shape of sand grains*. [www] <http://www.sand-atlas.com/en/shape-of-sand-grains/> (3 October 2010).
- Schwarcz, H.P. (1989). Uranium series dating of Quaternary deposits. *Quaternary International*, **1**, 7-18.
- Scott, L. (1999). Vegetation history and climate in the Savanna biome South Africa since 190,000 ka: a comparison of pollen data from the Tswaing Crater (the Pretoria Saltpan) and Wonderkrater. *Quaternary International*, **57–58**, 215-223.
- Scott, L., Holmgren, K., Talma, A. S., Woodborne, S. and Vogel, J. C. (2003). Age interpretation of the Wonderkrater spring sediments and vegetation change in the Savanna Biome, Limpopo province, South Africa. *South African Journal of Science*, **99**, 484-488.
- Scott, L. and Thackeray, J.F. (1987). Multivariate analysis of Late Pleistocene and Holocene pollen spectra from Wonderkrater, Transvaal, S. Africa. *South African Journal of Science*, **83**, 93-98.
- Smith B.W. (1988). Zircon from sediments: a combined OSL and TL auto-regenerative dating technique. *Quaternary Science Reviews*, **7**, 401-406.
- Smith B.W., Aitken M.J., Rhodes E.J., Robinson P.D. and Geldard D.M. (1986). Optical dating: methodological aspects. *Radiation Protection Dosimetry* **17**, 229-233.
- South African Geological Survey. (1978). *1:250 000 Geological Series Map 2428 Nylstroom*. Government Printer, Pretoria.
- Spooner, N.A. (1994). The anomalous fading of infrared-stimulated luminescence from feldspars. *Radiation Measurements*, **23**, 625-632.
- Spooner, N.A., Aitken, M.J., Smith, B.W., Franks, M. and McElroy, C. (1990). Archaeological dating by Infrared-stimulated luminescence using a diode array. *Radiation Protection Dosimetry*, **34**, 83-86.
- Spooner, N. A. and Allsop, A. (2000). The spatial variation of dose-rate from $^{90}\text{Sr}/^{90}\text{Y}$ beta sources for use in luminescence dating. *Radiation Measurements*, **32**, 49-55.

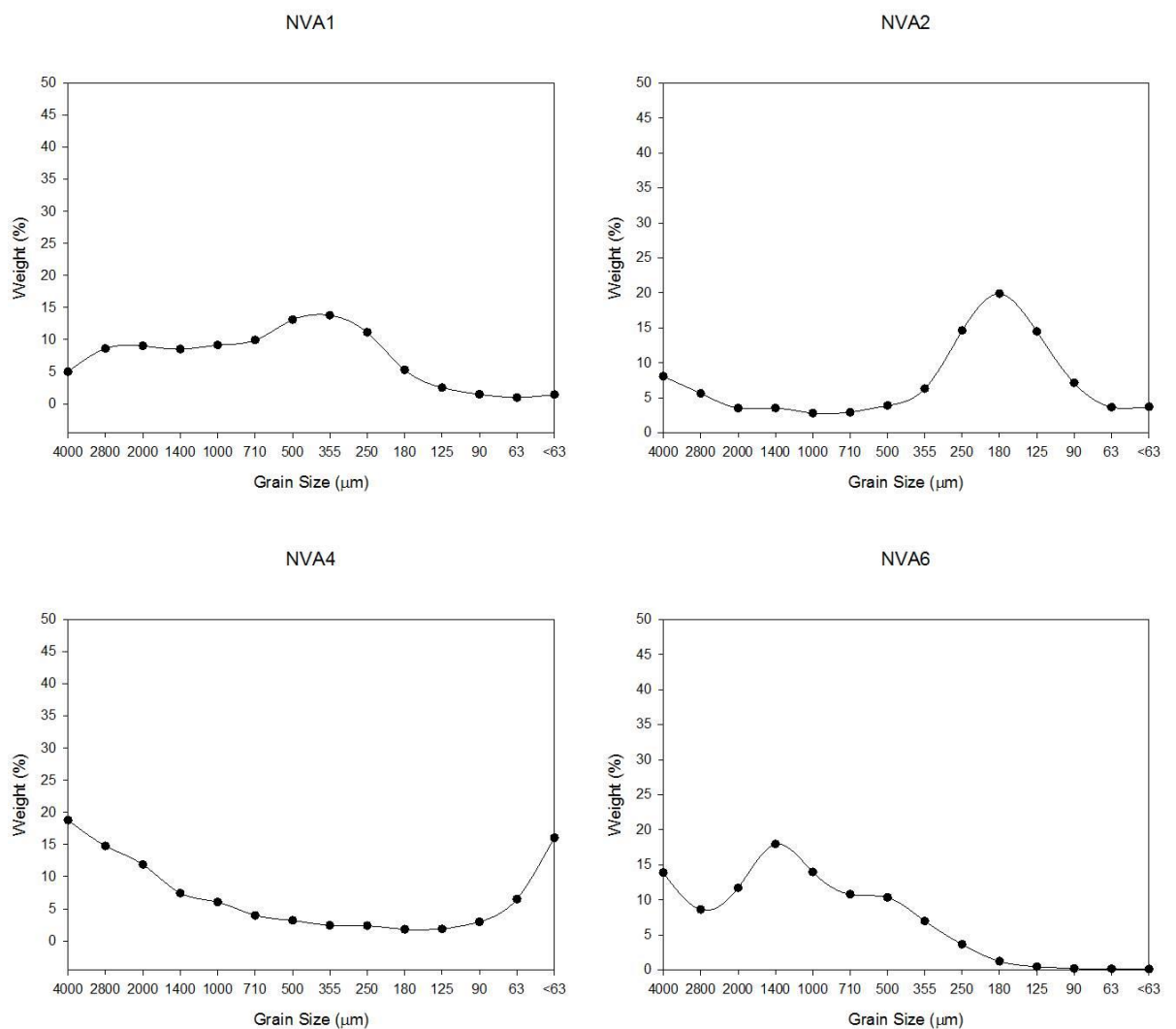
- Stanley, D. J., Chen, Z. and Song, J. (1999). Inundation, Sea-Level Rise and Transition from Neolithic to Bronze Age Cultures, Yangtze Delta, China. *Geoarchaeology*, **14**, 15-26.
- Stanley, D. J. and Hait, A. K. (2000). Deltas, radiocarbon dating, and measurements of sediment storage and subsidence. *Geology*, **28**, 295-298.
- Stokes, S. and Walling, D.E. (2003). Radiogenic and Isotopic Methods for the Direct Dating of Fluvial Sediments. In: Kondolf, G.M. and Piégay, H. (eds). *Tools in Fluvial Geomorphology*. John Wiley and Sons Ltd, England, pg. 233-267.
- Talma, A.S. and Vogel, J.C. (1992). Late Quaternary paleotemperatures derived from a speleothem from Cango Caves, Cape Province, South Africa. *Quaternary Research*, **37**, 203-13.
- Thackeray, J.F. (1996). Ring width variation in a specimen of South African *Podocarpus*, circa 1350–1937 AD. *Palaeoecology of Africa*, **24**, 233-40.
- Thomsen, K. J., Murray, A. S. and Bøtter-Jensen, L. (2005). Sources of variability in OSL dose measurements using single grains of quartz. *Radiation Measurements*, **39**, 47-61.
- Thomsen, K. J., Murray, A. S., Jain, M. and Bøtter-Jensen, L. (2008). Laboratory fading rates of various luminescence signals from feldspar-rich sediment extracts. *Radiation Measurements*, **43**, 1474-1486.
- Tooth, S., McCarthy, T.S., Hancox, P.J., Brandt, D., Buckley, K., Nortje, E. and McQuade, S. (2002). The Geomorphology of the Nyl River and floodplain in the semi-arid Northern Province, South Africa. *South African Geographical Journal*, **84**, 226-237.
- Tyson, P. D., Karlen, W., Holmgren, K. and Heiss, G. A. (2000). The Little Ice Age and medieval warming in South Africa. *South African Journal of Science*, **96**, 121-126.
- Vandenberghe, D. (2004). *Investigation of the Optically Stimulated Luminescence dating method for application to young geological sediments*. Unpublished PhD Thesis, Universiteit Gent, Belgium, pp. 358.
- Walker, M. (2005). Radiometric Dating 1: Radiocarbon Dating. In: Walker, M. *Quaternary Dating Methods*. John Wiley and Sons Ltd, England, pg. 17-55.
- Wallinga, J. (2002). Optically stimulated luminescence dating of fluvial deposits: a review. *Boreas*, **31**, 303-322.
- Warne, A. G. and Stanley, D. J. (1995). Sea-level Change as Critical Factor in Development of Basin Margin Sequences: New Evidence from Late Quaternary Record. *Journal of Coastal Research*, **Special Issue 17**, 231-240.

- Warren, S.E. (1978). Thermoluminescence dating of pottery: an assessment of the dose-rate from rubidium. *Archeometry*, **20**, 71-72.
- Williams, M.A.J., Dunkerley, D.L., De Deckker, P., Kershaw, A.P. and Stokes, T. (1993). *Quaternary Environments*. Edward Arnold, Auckland.
- Wintle, A.G. (1973). Anomalous fading of thermoluminescence in mineral samples. *Nature*, **245**, 143-144.
- Wintle, A.G. (1991). Luminescence Dating. In: Smart, P.L. and Frances, P.D. (eds.). *Quaternary dating methods – a user's guide*. Technical Guide 4, Quaternary Research Association, p. 108-127.
- Wintle, A.G. (1997). Luminescence dating: laboratory procedures and protocols. *Radiation Measurements*, **27**, 769-817.
- Wintle, A.G. (2008). Luminescence dating: where it has been and where it is going. *Boreas*, **37** (4), 471-482.
- Wintle, A.G. (2010). Future directions of luminescence dating of quartz. *Geochronometria*, **37**, 1-7.
- Wintle, A. G., Botha, G. A., Li, S. H. and Vogel, J. C. (1995). A chronological framework for colluviation during the last 110kyr in Kwazulu/Natal. *South African Journal of Science*, **91**, 134-139.
- Wintle, A.G. and Murray, A.S. (2006). A review of optically stimulated luminescence characteristics and their relevance in single-aliquot regeneration dating protocols. *Radiation Measurements*, **41**, 369-391.
- Wooller, M.J., Swain, D.L., Ficken, K.J., Agnew, A.D.Q., Street-Perrott, F.A. and Eglinton, G. (2003). Late Quaternary vegetation changes around Lake Rutundu, Mount Kenya, East Africa: evidence from grass cuticles, pollen and stable carbon isotopes, *Journal of Quaternary Science*, **18**, 3-15.
- Yoshida, H., Roberts, R. G., Olley, J. M., Laslett, G. M. and Galbraith, R. F. (2000). Extending the age range of optical dating using single 'supergrains' of quartz. *Radiation Measurements*, **32**, 439-446.
- Zander, A., Degering, D., Preusser, F., Kasper, U.H. and Brückner, H. (2007). Optically stimulated luminescence dating of sublittoral and intertidal sediments from Dubai, UAE: Radioactive disequilibria in the uranium decay series. *Quaternary Geochronology*, **2**, 123-128.
- Zimmerman, D.W. (1971). Thermoluminescent dating using fine grains from pottery. *Archaeometry*, **13**, 29-52.

Appendix A:

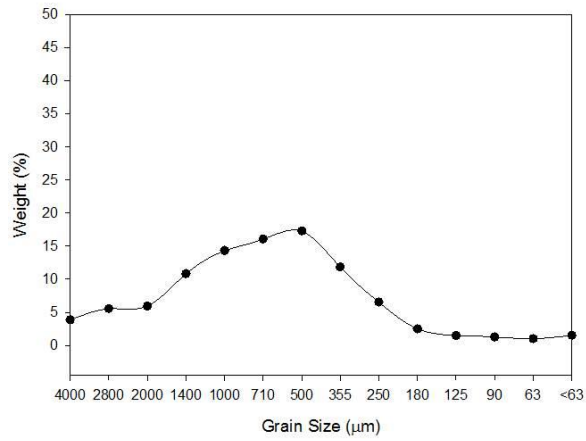
Grain Size Distributions

The measured grain size distributions for each horizontal layer in each vertical profile are presented. The fraction of sample remaining in the pan after sieving is denoted by $< 63 \mu\text{m}$. Cumulative frequency distributions for each Profile were compiled and included in Figure 2.8.

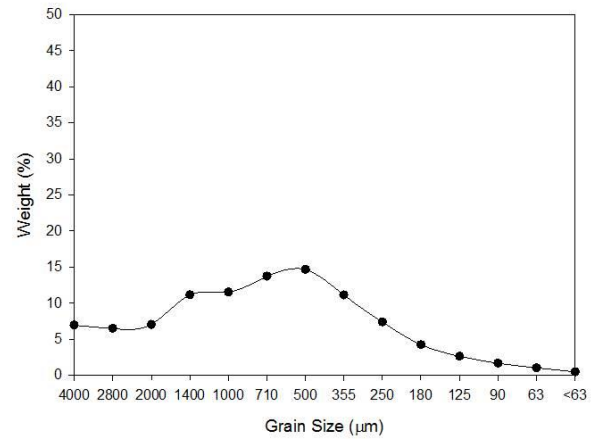


Appendix A: Grain Size Distributions

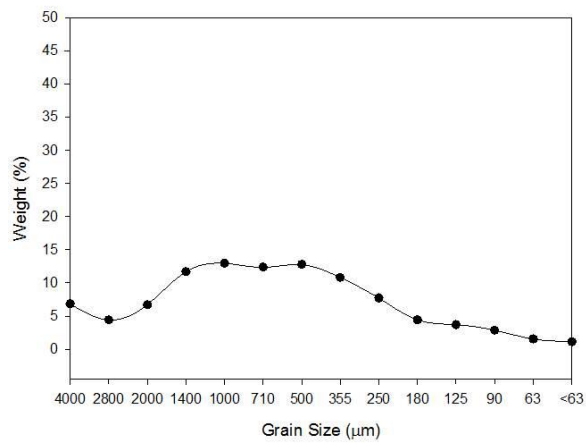
NVB1



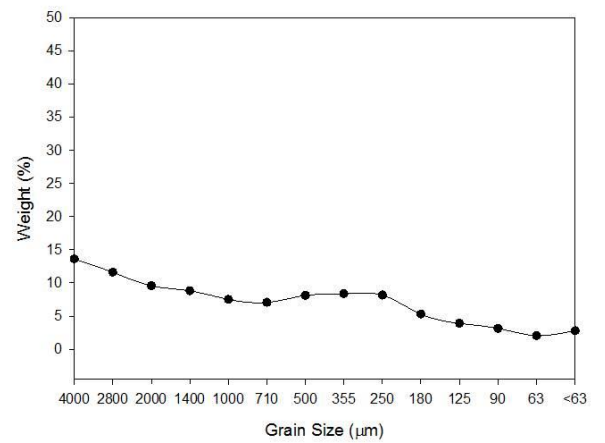
NVB3



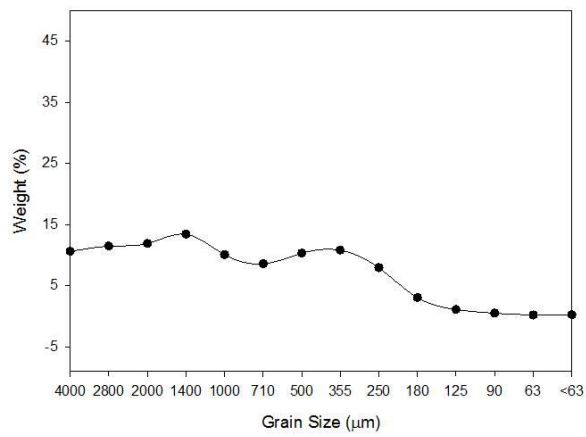
NVB5



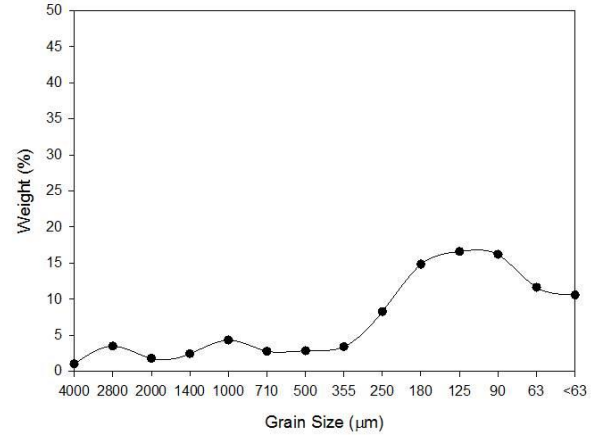
NVB6



NVB7

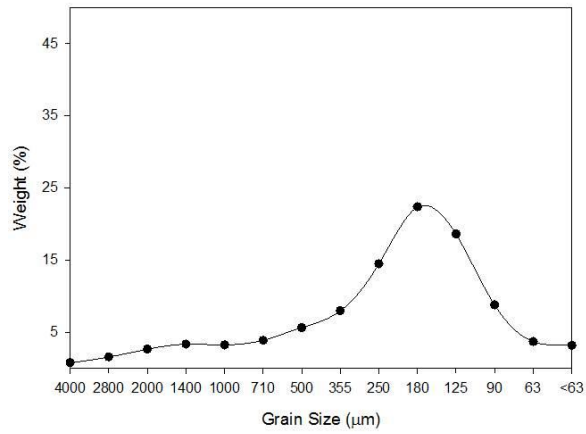


NVB9

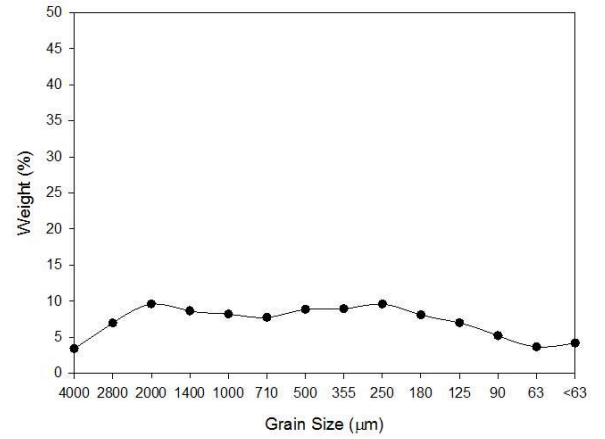


Appendix A: Grain Size Distributions

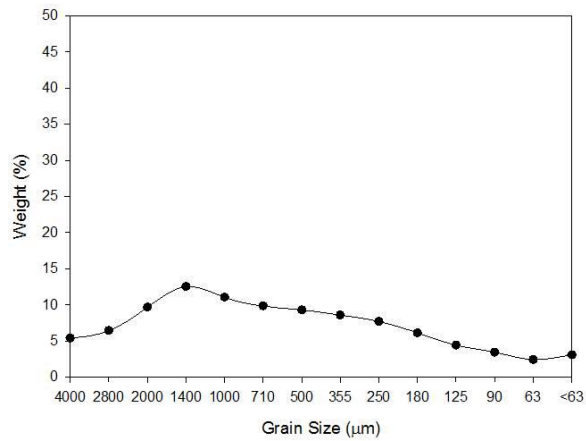
NVB10



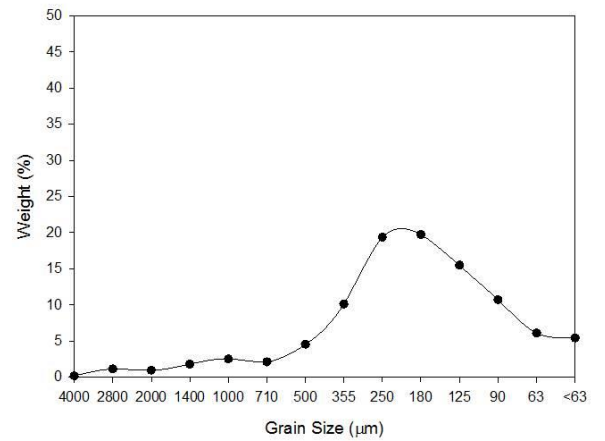
NVB11



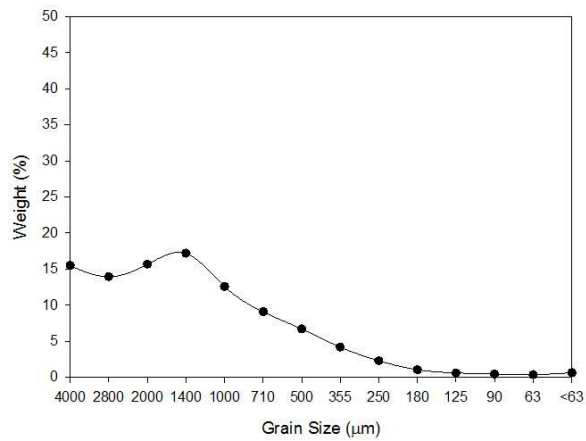
NVC1



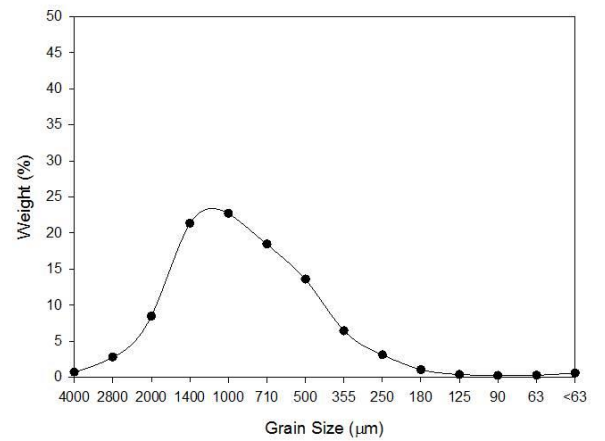
NVC2



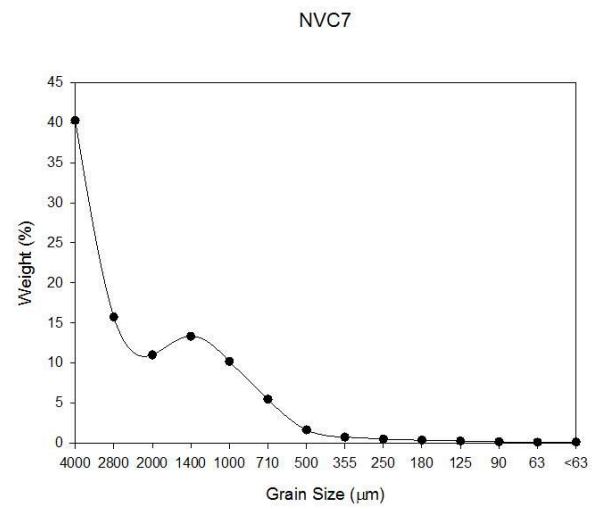
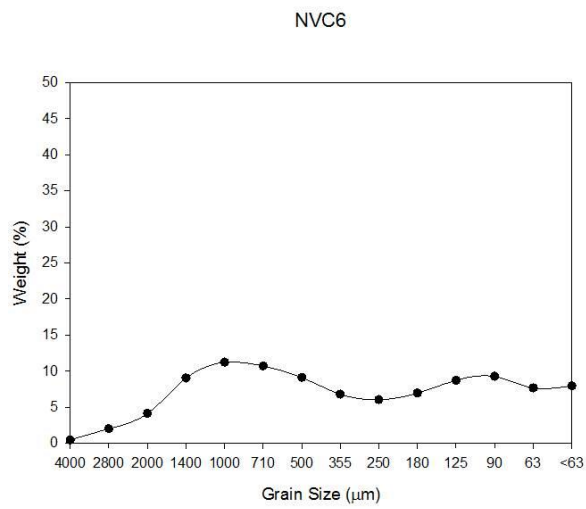
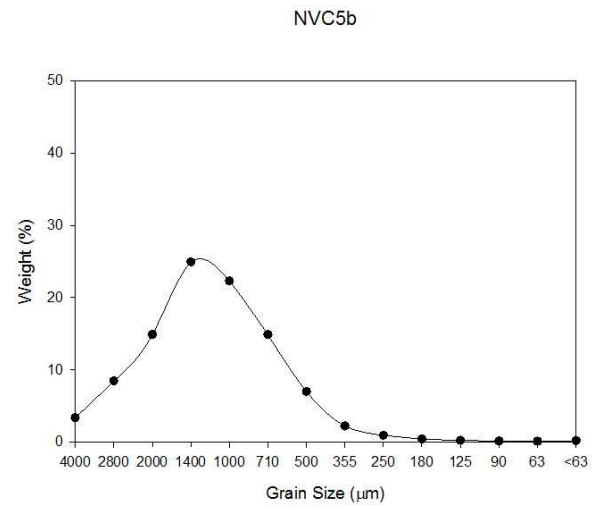
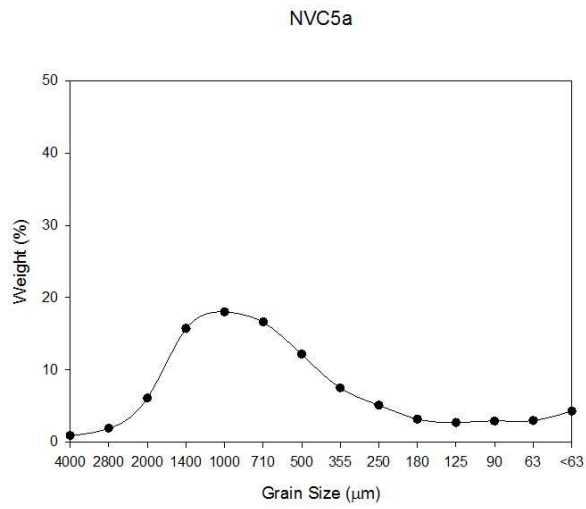
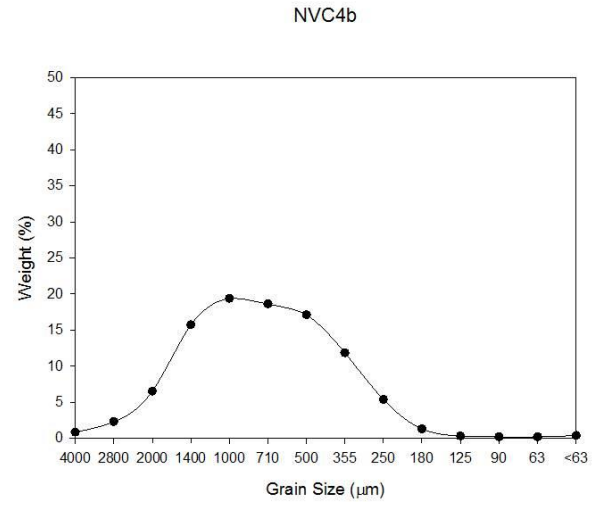
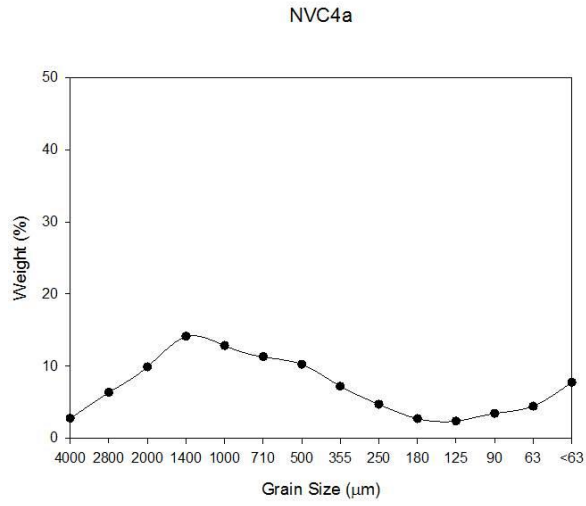
NVC3a



NVC3b

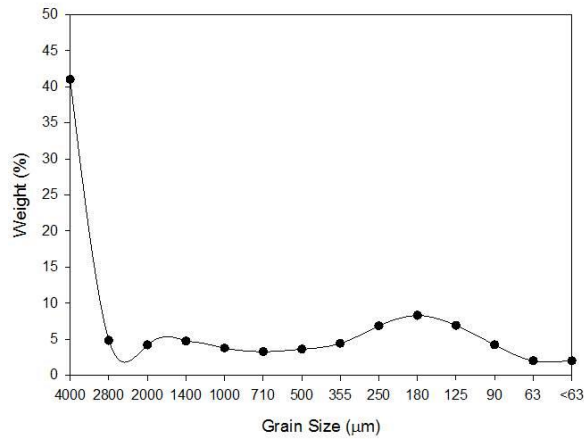


Appendix A: Grain Size Distributions

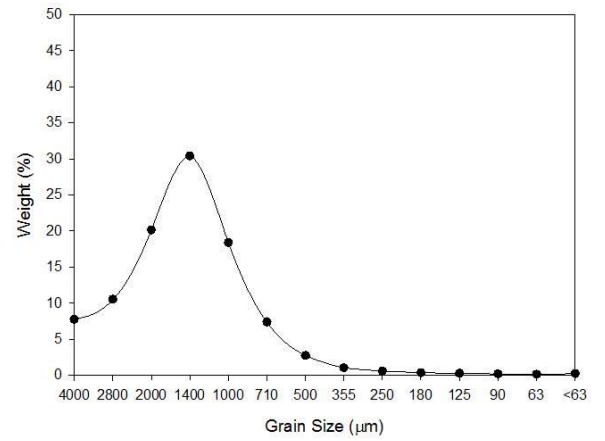


Appendix A: Grain Size Distributions

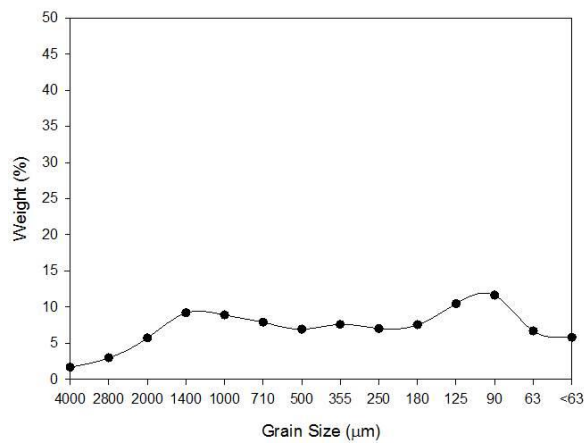
NVC2 Gravel



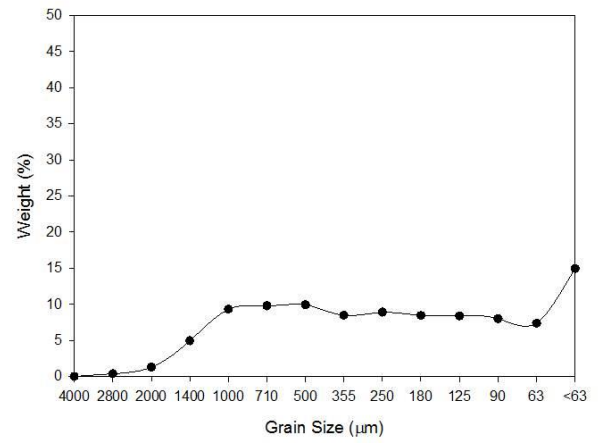
NVD1



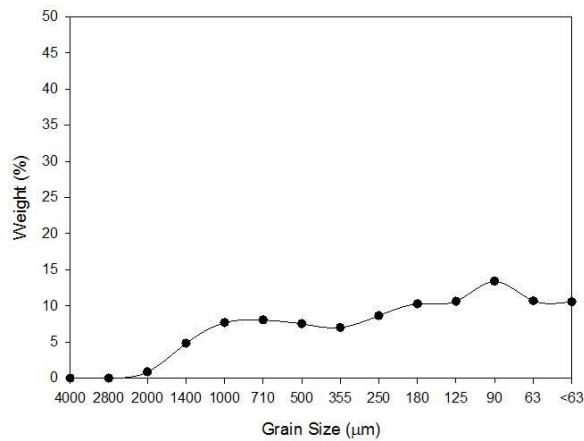
NVD2



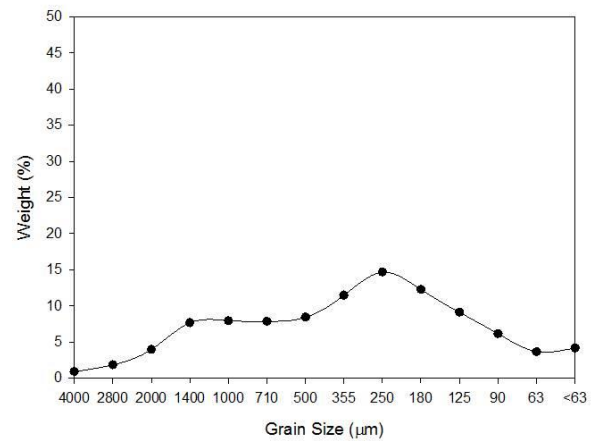
NVD3a



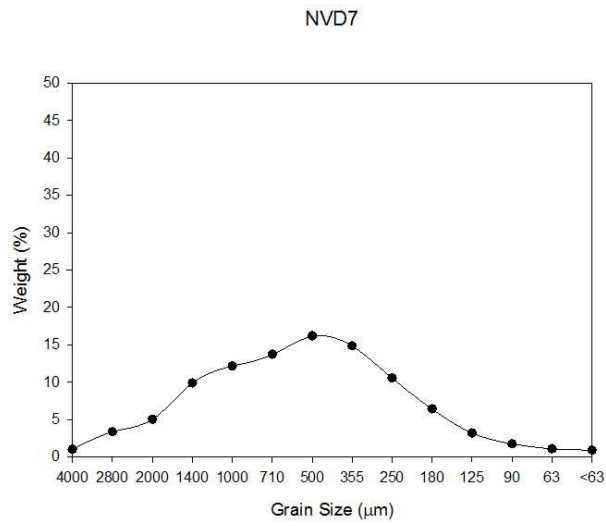
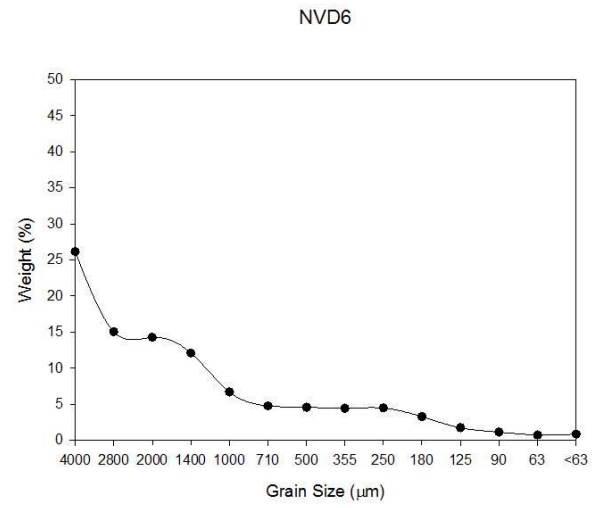
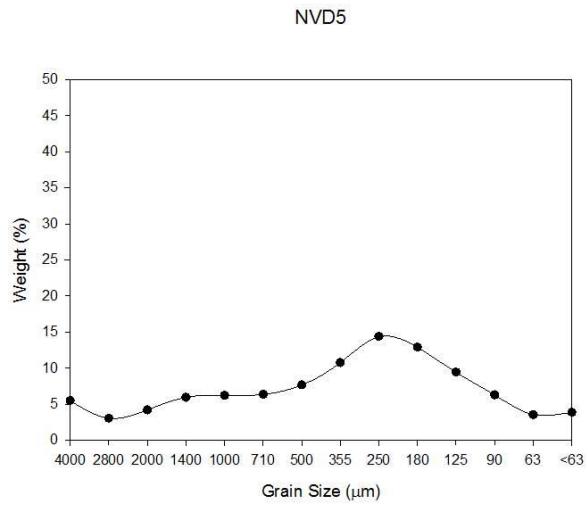
NVD3b



NVD4



Appendix A: Grain Size Distributions

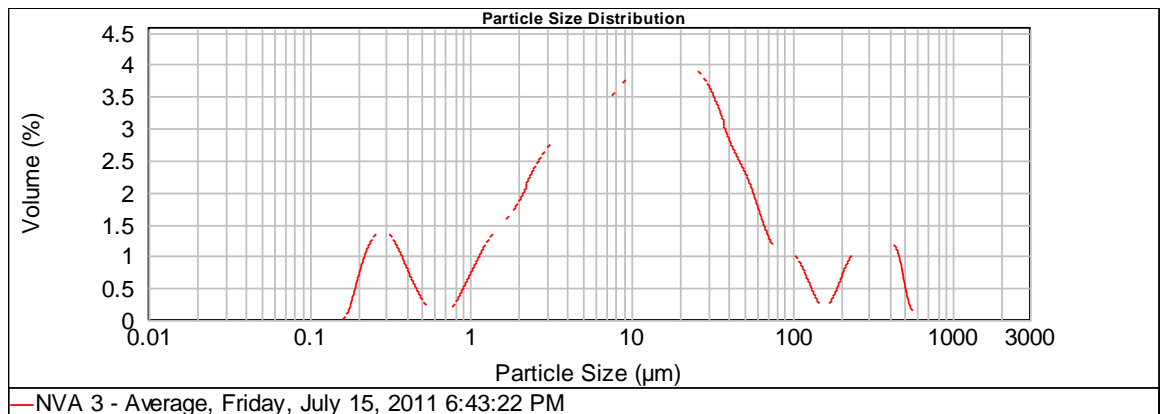


Appendix B:

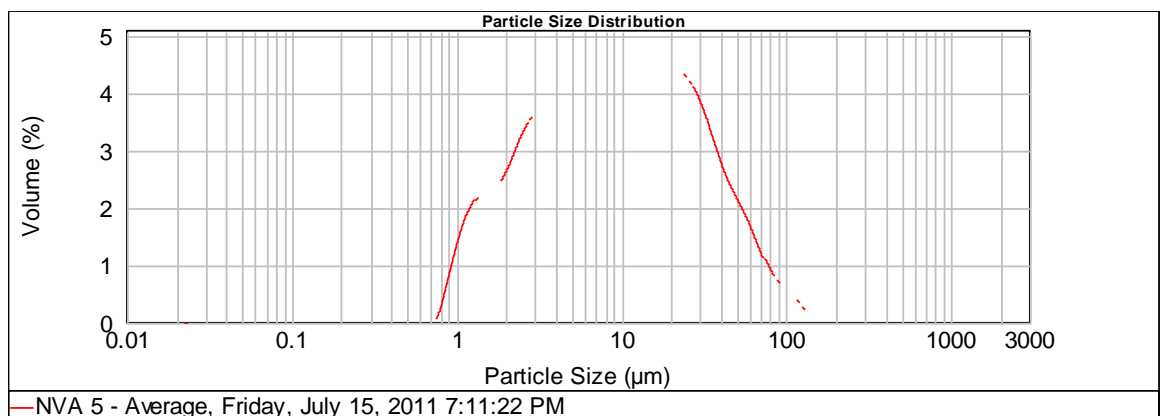
Laser Granulometer Graph Results for Clay-Rich Samples

The original data received from the Department of Chemical Engineering at the University of the Witwatersrand for the grain size analysis undertaken on the laser granulometer are presented.

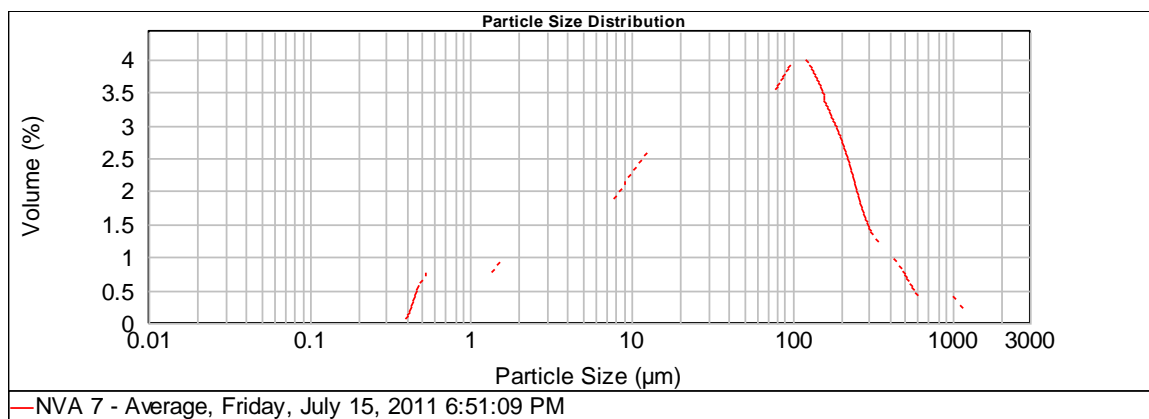
Sample number: NVA3



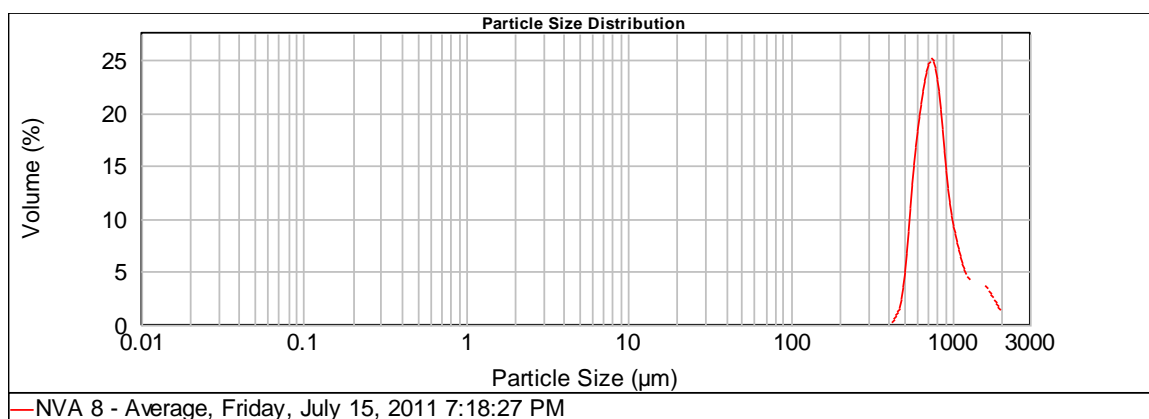
Sample number: NVA5



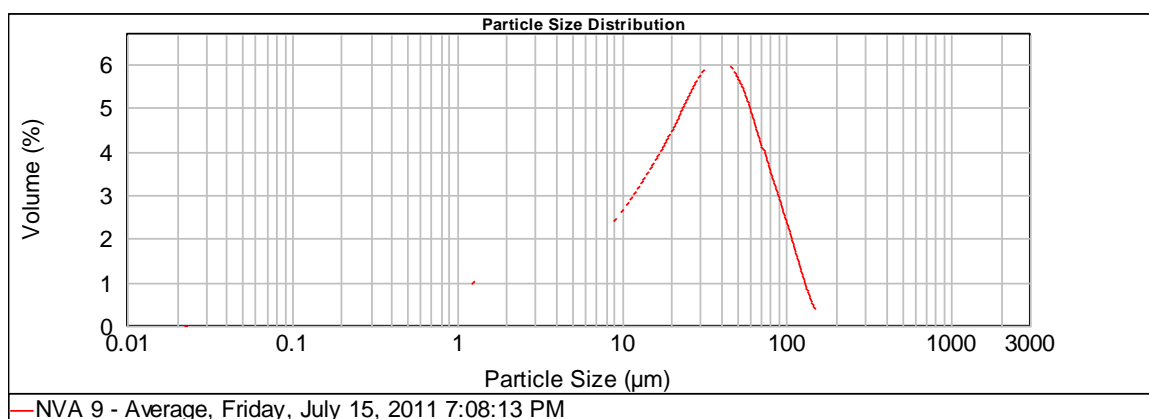
Sample number: NVA7



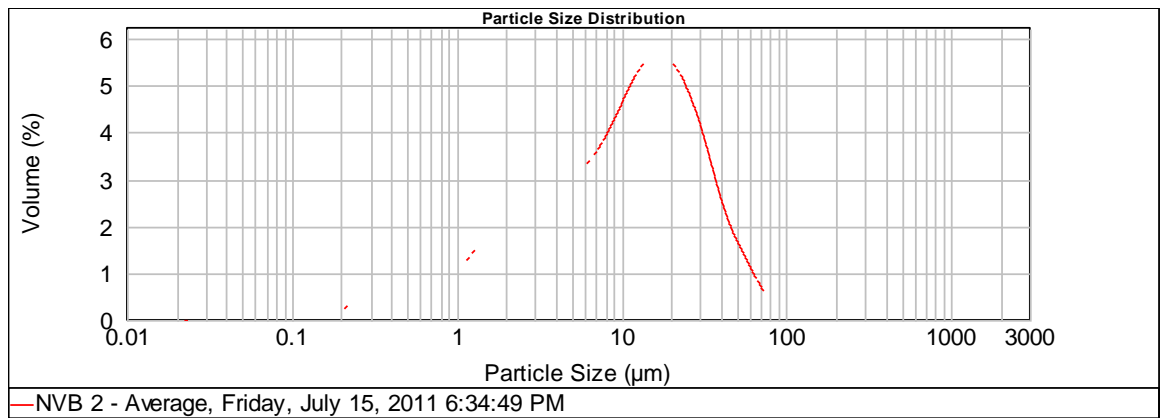
Sample number: NVA8



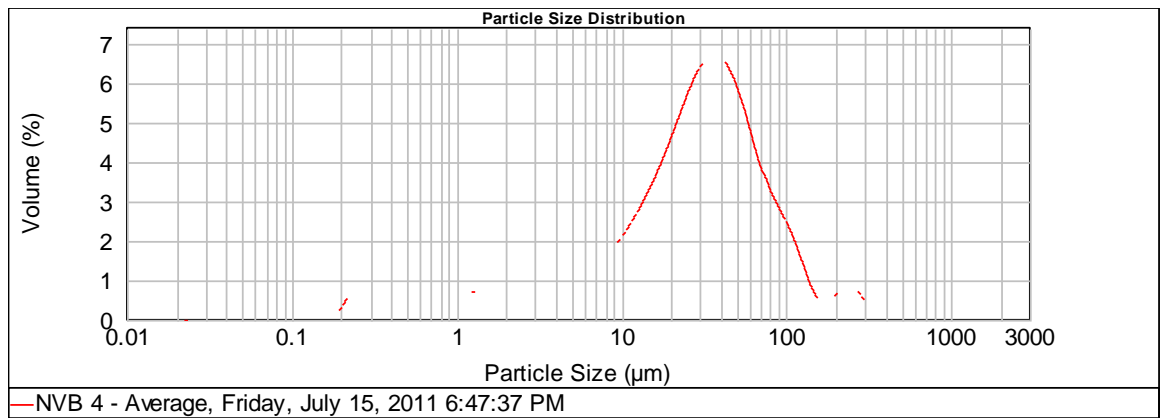
Sample number: NVA9



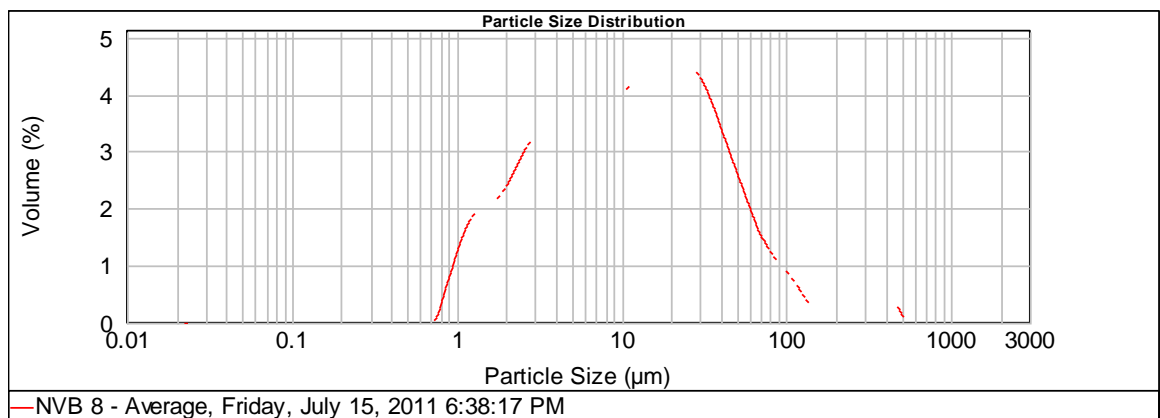
Sample number: NVB2



Sample number: NVB4



Sample number: NVB8



Appendix C:

Calibration of Beta Sources and Calculation of Dose Rate

Calibration of the beta sources was carried out on Risø 1 and Risø 3 at Aberystwyth University and on Risø B at the University of the Witwatersrand prior to D_e measurements.

C.1. Manual Calculation of the dose rate for Risø 1, Aberystwyth University

Calibration was undertaken using 180 - 212 μ m “calibration quartz” supplied by Risø. The quartz had been irradiated previously by a gamma source with a known dose of 4.81 ± 0.07 Gy. For calibration three medium (± 5 mm) aliquots of calibration quartz were measured using the standard SAR procedure and the resulting D_e value used to determine the beta dose rate using the formula

$$Dose\ rate = \frac{Dose}{Equivalent\ dose} \quad (B.1)$$

where the dose rate is in Gy/s, the dose in Gy and the equivalent dose in sec. The dose rate was then multiplied by 60 to obtain the dose rate in Gy/min.

Known dose from “calibration quartz” (Gy)	4.81 ± 0.07
Equivalent dose calculated using the Central Age Model (CAM) (s)	117.78 ± 1.56
Dose rate (Gy/s) ($4.81/117.78$)	0.0408 ± 0.0008
Error on dose rate (Gy/s) ($0.041 \times \sqrt{(0.07/4.81)^2 + (1.56/117.78)^2}$)	
Dose rate (Gy/min) (0.0408×60)	2.448 ± 0.048
Error on dose rate (Gy/s) (0.0008×60)	

Errors were combined using equation (12) for the division of independent variables from Hogan (2006).

C.2. Manual Calculation of the dose-rate for Risø B, University of the Witwatersrand

Manual calibration of Risø B was completed during July 2012 using the same method described above for Risø 1.

Known dose from “calibration quartz” (Gy)	4.81 ± 0.00
Equivalent dose calculated using the Central Age Model (CAM) (s)	34.72 ± 0.54
Dose rate (Gy/s) (4.81/34.72)	0.139 ± 0.02
Error on dose rate (Gy/s) $(0.138 \times \sqrt{(0.00/4.81)^2 + (0.54/34.72)^2})$	
Dose rate (Gy/min) (0.139 x 60)	8.312 ± 0.932
Error on dose rate (Gy/s) (0.02 x 60)	

C.3. Calibration of the Risø 3 single-grain reader, Aberystwyth University

Single-grain data was measured on Risø 3. A manual calibration was completed in January 2012 using the same batch of calibration quartz used to calibrate Risø 1. The grains were mounted on single-grain discs and analysed using the SAR protocol. The dose-rate was calculated as follows:

Known dose from “calibration quartz” (Gy)	4.81 ± 0.07
Equivalent dose calculated using the Central Age Model (CAM) (s)	53.13 ± 0.62
Dose rate (Gy/s) (4.81/53.13)	0.0905 ± 0.0017
Error on dose rate (Gy/s) $(0.041 \times \sqrt{(0.07/4.81)^2 + (0.62/53.13)^2})$	
Dose rate (Gy/min) (0.0905 x 60)	5.437 ± 0.101
Error on dose rate (Gy/s) (0.0017 x 60)	

Appendix D:

Calculating the Environmental Dose Rate from Thick Source Alpha Counting and GM-Beta Counting

Samples for this research project were analysed at the Aberystwyth Luminescence Research Laboratory (ALRL) at Aberystwyth University, Wales and the Luminescence Laboratory at the University of the Witwatersrand, South Africa. At ALRL the environmental dose rate was determined using TSAC in conjunction with GM-beta counting. The alpha pairs-count was used to determine the Th and U concentrations (ppm), which were then combined with the infinite matrix beta dose rate obtained through beta counting to determine the K concentration (%); the concentrations were multiplied by the Adamiec and Aitken (1998) conversion factors for the dose rate (Gy/ka) for a given amount of parent material to determine the gamma dose rate and finally the alpha-, beta-, gamma- and cosmic dose rates are combined to give the total environmental dose rate.

The ALRL at Aberystwyth University calculates the environmental dose rate of a sample using the LDB2005 database. To confirm that the database calculations were correct, the calculation for sample 11/O/NV-A6 was completed manually. The final dose rate and error, together with the worked values throughout the calculation were identical to those produced by LDB2005, which confirms that the automated values are correct. The following worked example is based upon the calculation from Appendix A of Rodnight (2006).

D.1. Alpha counting

Table D.1 details the TSAC results for sample 11/O/NV-A6, collected between 07/10/2011 and 20/10/2011 and using an active counting area of 15.45 cm².

Appendix D: Calculating the Environmental Dose Rate from Thick Source
Alpha Counting and GM-Beta Counting

Table D.1: TSAC results for 11/O/NV-A6

	Count time (ks)	Total counts (cnts)	Pairs counts (cnts)	Count-rate (cnts/ks)	Background subtracted count-rate (cnts/ks)
Background	96.18	6	-	0.062	-
Unsealed	851.4	3139	38	3.687	3.625
Sealed	271.5	1008	20	3.713	3.651

Sealed/Unsealed ratio ($3.651 \text{ cnts/ks} / 3.625 \text{ cnts/ks}$) 1.007 ± 0.038

Background counts expected on sealed measurement (cnts) ($0.062 \text{ cnts/ks} \times 271.5 \text{ ks}$) 16.83

Error on sealed count-rate (cnts/ks) ($\sqrt{(16.83 + 1008)/271.5}$) 0.118

Aitken (1990) outlines the use of the pairs count to determine the U and Th concentrations.

Observed pairs counts 20

Count time (ks) 271.5

Observed pairs count-rate (pairs/ks) ($20/271.5$) 0.0736

Dead time per ks (with coincidence time of $0.4 - 0.002 \text{ s} = 0.38 \text{ s}$) 0.00038

Gate open (ks) (0.00038×3.712) 0.0014

Random coincidence pairs count-rate (pairs/ks) (0.0014×3.712) 0.0052

True pairs count-rate (pairs/ks) ($0.0736 - 0.0052$) 0.0684

True pairs count-rate per area (pairs/ks/cm²) ($0.0684/15.45$) 0.0044

The relationship between Th concentration (in ppm) and the true pairs count-rate is given by equation (A1) taken from Huntley and Wintle (1981) as

$$\text{Th} = p/0.0022a; \quad (\text{A1})$$

where p is the true pairs count-rate per area and a is the proportion of pairs measured in the $0.02 - 0.40 \text{ s}$ coincidence window. For the purpose of this calculation the value of a is 0.77 as given in the Daybreak model 583 User's Manual. Thus the Th concentration can be calculated as follows:

Th concentration (ppm) ($0.0044/(0.0022 \times 0.77)$)

2.649 ± 0.638

Th (ppm) error ($((2.649 \times \sqrt{(0.0736 \times 271.5)}) / (0.0684 \times 271.5))$)

Using the expected count-rate (cnts/ks) for a given parent material (Table D.2) the U concentration can be determined from the Th concentration and the pairs counts.

Table D.2: The expected count-rate (cnts/ks) for 1 ppm of parent material (Adamiec & Aitken, 1998)

	Values for 42 mm diameter detector screen from Adamiec and Aitken (1998)	Values for a 15.45 cm ² detector screen (used in Aberystwyth)
Thorium	0.483	0.539
Natural Uranium	1.67	1.862

Th count-rate (cnts/ks) (2.649×0.539)

1.428 ± 0.344

Th count-rate error (cnts/ks) (0.638×0.539)

U count-rate (cnts/ks) ($3.651 - 1.428$)

2.223 ± 0.364

U count-rate error (cnts/ks) ($\sqrt{(0.0118^2 + 0.344^2)}$)

U concentration (ppm) ($2.223/1.862$)

1.194 ± 0.195

U concentration error (ppm) ($0.364/1.862$)

D.2. GM-beta counting

The operation of the GM-beta counter and the determination of the measured beta dose was discussed in section 5.3.2.

Measured beta dose rate (Gy/ka)

2.328 ± 0.076

Measured beta dose rate error (Gy/ka)

The TSAC and GM-beta counting can be combined to produce an estimate of the K concentration using the standard values shown in Table D.3 taken from Adamiec and Aitken (1998).

Table D.3: Dose rate (Gy/ks) for a given amount of parent material

	Alpha	Beta	Gamma
Thorium (1 ppm)	2.78	0.146	0.133
Natural Uranium (1 ppm)	0.732	0.0273	0.0476
Potassium (1 %)		0.782	0.243

Thus using the U and Th concentrations as calculated from the TSAC results it is possible to calculate the K concentration.

Beta dose rate from U (Gy/ka) (1.194×0.146)	0.174 ± 0.028
Beta dose rate from U error (Gy/ka) ($0.174 \times 0.195/1.194$)	
Beta dose rate from Th (Gy/ka) (2.649×0.0273)	0.072 ± 0.017
Beta dose rate from Th error (Gy/ka) ($0.072 \times 0.638/2.649$)	
Beta dose rate from U and Th (Gy/ka) ($0.174 + 0.072$)	0.246 ± 0.033
Beta dose rate from U and Th error (Gy/ka) ($\sqrt{(0.028^2 + 0.017^2)}$)	
Beta dose rate from K (Gy/ka) ($2.328 - 0.246$)	2.082 ± 0.083
Beta dose rate from K error (Gy/ka) ($\sqrt{(0.076^2 + 0.033^2)}$)	
K concentration (%) ($2.082/0.782$)	2.662 ± 0.106
K concentration error (%) ($2.662 \times 0.083/2.082$)	

D.3. Total dose rate

D.3.1. Beta dose rate

Measured total beta dose rate (Gy/ka)	2.328 ± 0.076
Measured total beta dose rate error (Gy/ka)	

The attenuated beta dose rate can be calculated using the beta attenuation factor for the relevant grain size, in this case 0.879 ± 0.004 for the 180 – 212 μm fraction.

Thus:

Total beta dose rate (Gy/ka) (2.328×0.879)	2.046 ± 0.067
Total beta dose rate error (Gy/ka) ($2.046 \times \sqrt{((0.004/0.879)^2 + (0.076/2.328)^2)}$)	

Finally the beta dose rate is corrected for water content (see discussion in section 5.10.3). The water content for 11/O/NV-A6 was $10 \pm 3 \%$.

Total beta dose rate (Gy/ka) ($2.046/(1 + (1.25 \times 0.1))$)	1.818 ± 0.085
Total beta dose rate error (Gy/ka) ($1.818 \times \sqrt{((0.0375/1.125)^2 + (0.068/2.046)^2)}$ *)	

D.3.2. Gamma dose rate

The U, Th and K concentrations are combined with the standard values from Table A.3. to determine the gamma dose rate contributed by each element:

Gamma dose rate from U (Gy/ka) (1.194×0.113)	0.135 ± 0.022
Gamma dose rate from U error (Gy/ka) $(0.135 \times 0.196/1.194)$	

Gamma dose rate from Th (Gy/ka) (2.649×0.0476)	0.126 ± 0.030
Gamma dose rate from Th error (Gy/ka) $(0.126 \times 0.638/2.649)$	

Gamma dose rate from K (Gy/ka) (2.662×0.243)	0.647 ± 0.026
Gamma dose rate from K error (Gy/ka) $(0.646 \times 0.106/2.662)$	

and the total gamma dose rate is then calculated by combining the calculated gamma dose rates:

Total gamma dose rate (Gy/ka) $(0.135 + 0.126 + 0.647)$	0.908 ± 0.045
Total gamma dose rate error (Gy/ka) $(\sqrt{0.022^2 + 0.030^2 + 0.026^2})$	

which is then corrected for water content, as with the beta dose rate:

Total gamma dose rate (Gy/ka) $(0.908 / 1 + (1.14 \times 0.1))$	0.815 ± 0.048
Total gamma dose rate error (Gy/ka) $(0.815 \times \sqrt{(0.0342/1.114)^2 + (0.045/0.908)^2})^*$	

*The error calculations above include the terms $(0.0375/1.125)$ and $(0.0342/1.114)$ derived from the propagation of the error on the water content through the equation.

D.3.3. Cosmic dose rate

The cosmic dose rate is calculated using equation (2) from Prescott and Hutton (1994) as detailed in section 5.3.3, with the overburden of sample 11/O/NV-A6 equal to 1.51 m.

Total cosmic dose rate (Gy/ka)	0.175 ± 0.017
Total cosmic dose rate error (Gy/ka)	

D.3.4. Total environmental dose rate

The total environmental dose rate is determined by adding together the alpha-, beta-, gamma- and cosmic dose rates; the environmental dose rate for sample 11/O/NV-A6 is calculated as:

Total dose rate (Gy/ka) $(0.000 + 1.818 + 0.815 + 0.175)$

2.808 ± 0.099

Total dose rate error (Gy/ka) $(\sqrt{0.000^2 + 0.085^2 + 0.048^2 + 0.017^2})$

Appendix E:

Calculating the Environmental Dose Rate from High-Resolution Gamma Spectroscopy

Samples for this research project were analysed at two luminescence laboratories, the Aberystwyth Luminescence Research Laboratory (ALRL) at Aberystwyth University, Wales and the Luminescence Laboratory at the University of the Witwatersrand, South Africa. The dates produced at the University of the Witwatersrand utilised data collected from high-resolution gamma spectroscopy to calculate the environmental dose rate. The data from HRGS was reported as concentrations of natural U, Th and K; the concentrations were multiplied by the conversion factors of Adamiec and Aitken (1998) to determine the dose rates contributed by each element. The individual beta and gamma dose rates were then combined to determine total beta- and gamma dose rates, which were then corrected for attenuation and water content and water content respectively. This Appendix includes a worked example for sample 11/O/NV-A6 using the data from the HRGS.

E.1. Using High-Resolution Gamma Spectrometry Data to Determine the Environmental Dose Rate

The results from the iThemba Laboratory were reported as concentrations for each sample, with the results for 11/O/NV-A6 shown in Table F1. Using the conversion factors (Table F2) from Adamiec and Aitken (1998) each of the concentrations was converted to a beta- and gamma dose rate, which were then summed to determine a total beta- and gamma dose rate for the sample.

Table E.1.: HRGS results for sample NVA2

Natural U (ppm)	Th (ppm)	K (%)
1.30 ± 0.07	3.58 ± 0.35	3.13 ± 0.06

Table E.2.: Conversion factors (Adamiec and Aitken, 1998)

	Natural U	Th	K
Dose rate (Gy/ka) per ppm			
Beta, full series	0.146	0.0273	-
Gamma, full series	0.113	0.0476	-
Dose rate (Gy/ka) for 1% natural K			
Beta	-	-	0.782
Gamma	-	-	0.243

E.1.1. Total Beta Dose Rate

The concentration for each element (Table F.1) was multiplied by the relevant conversion factor (Table F.2) to determine the beta dose rate contributed by each element.

Beta dose rate from U (Gy/ka) (1.30×0.146) 0.190 ± 0.008

Beta dose rate from U error (Gy/ka) ($0.175 \times 0.07/1.30$)

Beta dose rate from Th (Gy/ka) (3.58×0.0273) 0.098 ± 0.010

Beta dose rate from Th error (Gy/ka) ($0.085 \times 0.35/3.58$)

Beta dose rate from K (Gy/ka) (3.13×0.782) 2.448 ± 0.047

Beta dose rate from K error (Gy/ka) ($2.448 \times 0.06/3.13$)

The individual beta dose rates were summed to determine the total beta dose rate for the sample.

Total beta dose rate (Gy/ka) ($0.190+0.098+2.448$) **2.736 ± 0.049**

Total beta dose rate error (Gy/ka) ($\sqrt{(0.008^2 + 0.010^2 + 0.047^2)}$)

The attenuated beta dose rate was then calculated using the beta attenuation factor for the relevant grain size, in this case 0.879 ± 0.004 for the 180 – 212 μm fraction. Thus:

Total beta dose rate (Gy/ka) (2.736×0.879) 2.404 ± 0.044

Total beta dose rate error (Gy/ka) ($2.379 \times \sqrt{((0.004/0.879)^2 + (0.049/2.736)^2)}$)

Finally, the beta dose rate was corrected for water content (see discussion in section 5.10.3). The standard value applied for the water content was $10 \pm 3 \%$.

Appendix E: Calculating the Environmental Dose Rate from High-Resolution Gamma Spectroscopy

Total beta dose rate (Gy/ka) $(2.380 / (1 + (1.25 \times 0.1)))$ **2.137 ± 0.081**

Total beta dose rate error (Gy/ka) $(2.115 \times \sqrt{((0.0375/1.125)^2 + (0.044/2.404)^2})^2}$ *

E.1.2. Total Gamma Dose Rate

The total gamma dose rate was calculated using the same method as the beta dose rate. The reported concentrations (Table F.1) were multiplied by the relevant conversion factor (Table F2).

Gamma dose rate from U (Gy/ka) (1.30×0.113) 0.147 ± 0.008

Gamma dose rate from U error (Gy/ka) $(0.147 \times 0.07/1.30)$

Gamma dose rate from Th (Gy/ka) (3.58×0.0476) 0.170 ± 0.017

Gamma dose rate from Th error (Gy/ka) $(0.170 \times 0.35/3.58)$

Gamma dose rate from K (Gy/ka) (3.13×0.243) 0.761 ± 0.015

Gamma dose rate from K error (Gy/ka) $(0.761 \times 0.06/3.13)$

The total gamma dose rate was calculated by combining the calculated gamma dose rates for each element.

Total gamma dose rate (Gy/ka) $(0.147 + 0.170 + 0.761)$ **1.078 ± 0.024**

Total gamma dose rate error (Gy/ka) $(\sqrt{0.008^2 + 0.017^2 + 0.015^2})$

The total gamma dose rate was then corrected for water content, as with the beta dose rate:

Total gamma dose rate (Gy/ka) $(1.078 / 1 + (1.14 \times 0.1))$ **0.968 ± 0.036**

Total gamma dose rate error (Gy/ka) $(0.968 \times \sqrt{(0.0342/1.114)^2 + (0.024/1.078)^2})^2$ *

*The error calculations above include the terms (0.0375/1.125) and (0.0342/1.114) derived from the propagation of the error on the water content through the equation.

E.1.3. Cosmic Dose Rate

The cosmic dose rate was calculated using equation (2) from Prescott and Hutton (1994) as detailed in section 5.3.3, with the overburden of sample 11/O/NV-A6 equal to 1.50 m.

Appendix E: Calculating the Environmental Dose Rate from High-Resolution Gamma Spectroscopy

Total cosmic dose rate (Gy/ka)	0.176 ± 0.018
Total cosmic dose rate error (Gy/ka)	

E.1.4. Total Environmental Dose Rate

The total environmental dose rate was determined by adding together the alpha-, beta-, gamma- and cosmic dose rates; the environmental dose rate for sample 11/O/NV-A6 was calculated as:

Total dose rate (Gy/ka) $(0.000 + 2.137 + 0.968 + 0.176)$	3.281 ± 0.090
Total dose rate error (Gy/ka) $(\sqrt{0.000^2 + 0.081^2 + 0.036^2 + 0.018^2})$	

Appendix F:

Radiocarbon Dating Report



LUND
UNIVERSITY

*GeoBiosphere Science Centre
Radiocarbon Dating Laboratory
Associate professor Mats Rundgren*

Lund 2011-11-18

Mary Evans
University of Witwatersrand
School of Geosciences
Private Bag 3
WITS, 2050
South Africa

Dear Mary Evans,

Please find enclosed the dating certificate and calibrations for the samples from Nyl River. Two samples (LuS 9833 and LuS 9837) show a ^{14}C activity that is close to that of modern material (pMC = percent modern carbon; at present the atmospheric level is ca 105 pMC). This means that they fall within the period of the so-called 'bomb pulse', which peaked in the 1960s. Calibrating these results with the southern hemisphere calibration dataset (SH1.14c) only gives ages around 1957-1958. However, this dataset does not continue up to 2010. If it had done so, a second possible age interval very close to present would also have been shown on the diagram. Therefore, we have also calibrated these results with a northern hemisphere dataset (Levin.14c), where this second possibility appears (ca 2003-2006). Please note that this calibration dataset also does not continue up to 2011, although it continues longer than the SH one. Therefore, the calibrated interval represents only about half of the total age distribution. Moreover, the indicated interval is likely to be offset a few years from the SH. The bottom line is that the carbon in the two samples, in addition to ca 1957-1958, also could derive from the last few years.

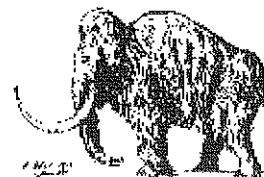
Best regards,


Mats Rundgren



LUNDS
UNIVERSITET

Institutionen för geo- och ekosystemvetenskaper
Laboratoriet för ^{14}C -datering
Sölvegatan 12, Geocentrum II
223 62 LUND
Tel. 046/2227885 Fax 046/2224830
e-mail: goran.skog@c14lab.lu.se



Department of Earth and Ecosystem Sciences
Radiocarbon Dating Laboratory
Sölvegatan 12, Geocentrum II
S-223 62 LUND
Sweden

Mary Evans

University of Witwatersrand, School of Geosciences

Private Bag X3, WITS, 2050, South Africa

D a t i n g C e r t i f i c a t e

Sample designation	Lab no	Radiocarbon age BP	$\delta\text{C}13$ ‰	Weight (mg C)	Pretreatment
Nyl River NVA5	LuS 9833	105.8 \pm 0.6 pMC		4,1	HCl, NaOH
Nyl River NVA8	LuS 9834	955 \pm 50		3,8	HCl, NaOH
Nyl River NVB2	LuS 9835	905 \pm 50		1,7	HCl, NaOH
Nyl River NVB8	LuS 9836	475 \pm 45		3,1	HCl, NaOH
Nyl River NVC3	LuS 9837	106.0 \pm 0.6 pMC		3,1	HCl, NaOH
Nyl River NVC5	LuS 9838	645 \pm 50		1,7	HCl, NaOH
Nyl River NVD 3(a)	LuS 9839	1365 \pm 50		1,7	HCl, NaOH
Nyl River NVD4	LuS 9840	765 \pm 50		1,9	HCl, NaOH

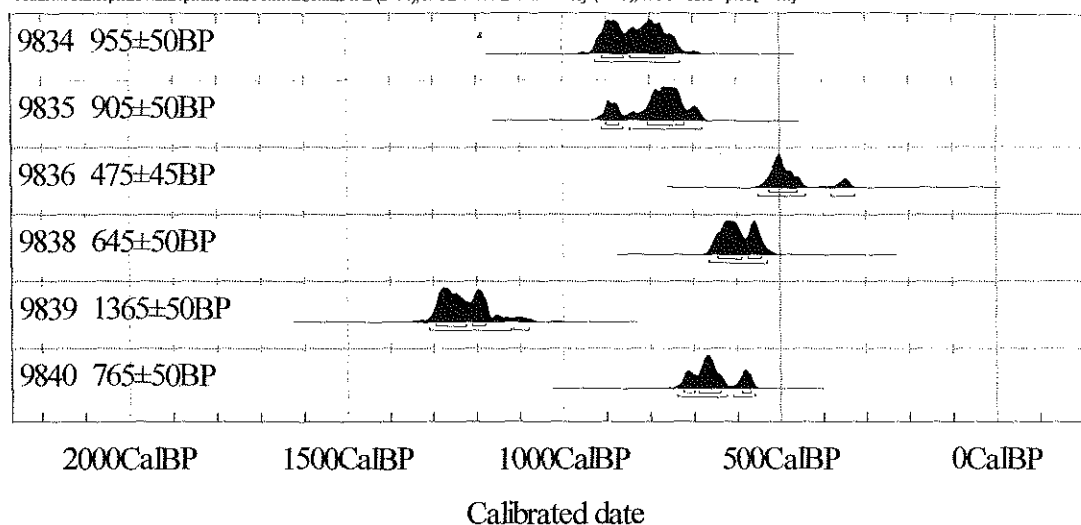
The calculations of the radiocarbon ages are based on the "Libby half life" of 5568 yrs. The results are given in years before 1950 (radiocarbon age BP). The uncertainty in the age determination is given as \pm one standard deviation. All radiocarbon ages are corrected for isotopic fractionation using the measured $^{13}\text{C}/^{12}\text{C}$ -ratio. The radiocarbon ages must be translated to calibrated radiocarbon years using either the IntCal09 dataset (for terrestrial samples) or the Marine09 dataset (for marine samples). For further information see Radiocarbon Vol 51, nr 4, 2009.

Lund 2011-11-17

Göran Skog

Mats Rundgren

Southern Hemisphere Atmospheric data from McCormac et al (2004); OxCal v3.10 Bronk Ramsey (2005); cub r:5 sd:12 prob[chron]



INFORM : References - Southern Hemisphere Atmospheric data from McCormac et al (2004); OxCal v3.10 Bronk Ramsey (2005); cub r:5 sd:12 prob[chron]

9834 : 955±50BP

68.2% probability

910BP (25.9%) 860BP

845BP (42.3%) 765BP

95.4% probability

925BP (95.4%) 730BP

9835 : 905±50BP

68.2% probability

900BP (10.6%) 870BP

805BP (57.6%) 720BP

95.4% probability

910BP (15.7%) 860BP

845BP (79.7%) 680BP

9836 : 475±45BP

68.2% probability

525BP (68.2%) 460BP

95.4% probability

550BP (83.5%) 440BP

380BP (11.9%) 325BP

9838 : 645±50BP

68.2% probability

645BP (47.0%) 590BP

575BP (21.2%) 545BP

95.4% probability

665BP (95.4%) 530BP

9839 : 1365±50BP

68.2% probability

1295BP (46.9%) 1225BP

1210BP (21.3%) 1180BP

95.4% probability

1310BP (92.4%) 1120BP

1115BP (3.0%) 1080BP

9840 : 765±50BP

68.2% probability

725BP (12.9%) 700BP

690BP (43.9%) 640BP

590BP (11.4%) 570BP

95.4% probability

740BP (75.0%) 625BP

610BP (20.4%) 560BP

Calibration of 1.058000 ± 0.006000 with SH1.14c dataset**Smoothing: 1.000000**

Q Hua and M Barbetti,
"Review of Tropospheric Bomb ^{14}C Data for Carbon Cycle Modeling
and Age Calibration Purposes", (2004) Radiocarbon 46: 1273-1298.

#

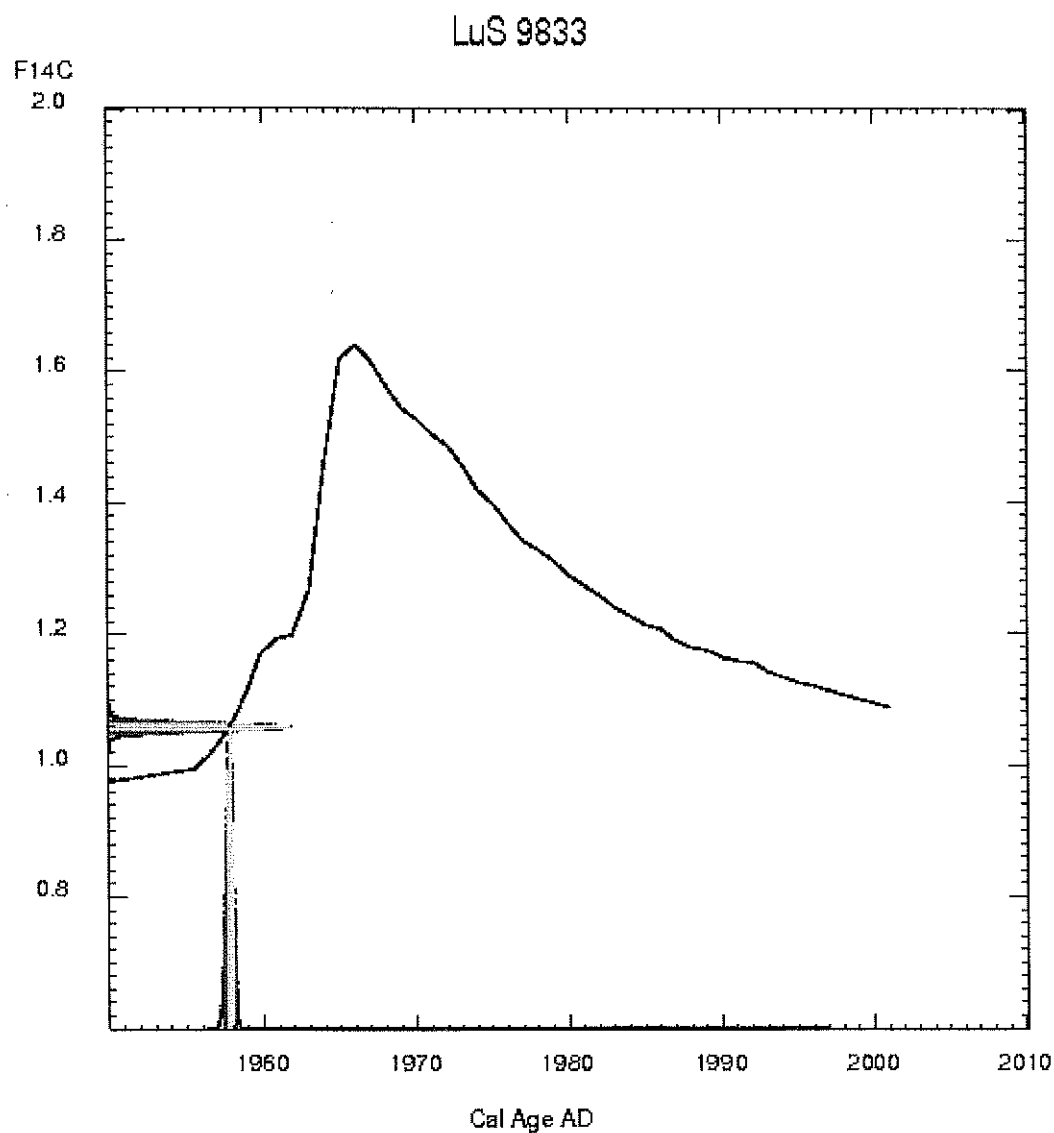
OneSigma

[1957.56(Jul) - 1958.02(Jan)]1.000000

TwoSigma

[1957.30(Apr) - 1958.20(Mar)]1.000000

Note: 300 years of INTCAL04 data have been prepended to this data set



Calibration of 1.058000 ± 0.006000 with Levin.14c dataset

Smoothing: 1.000000

```
# I. Levin and B. Kromer,
# "The tropospheric  $^{14}\text{CO}_2$  level in mid latitudes of the Northern Hemisphere"
# (2004) Radiocarbon 46(3):1261-1272.
# I. Levin, S. Hammer, et al
# "Radiocarbon observations in atmospheric  $\text{CO}_2$ : Determining fossil fuel  $\text{CO}_2$ 
# over Europe using Jungfraujoch observations as background" (2008)
# Science of the Total Environment 391:211-216.
```

OneSigma

[1952.86(Nov) - 1953.36(May)]0.293821

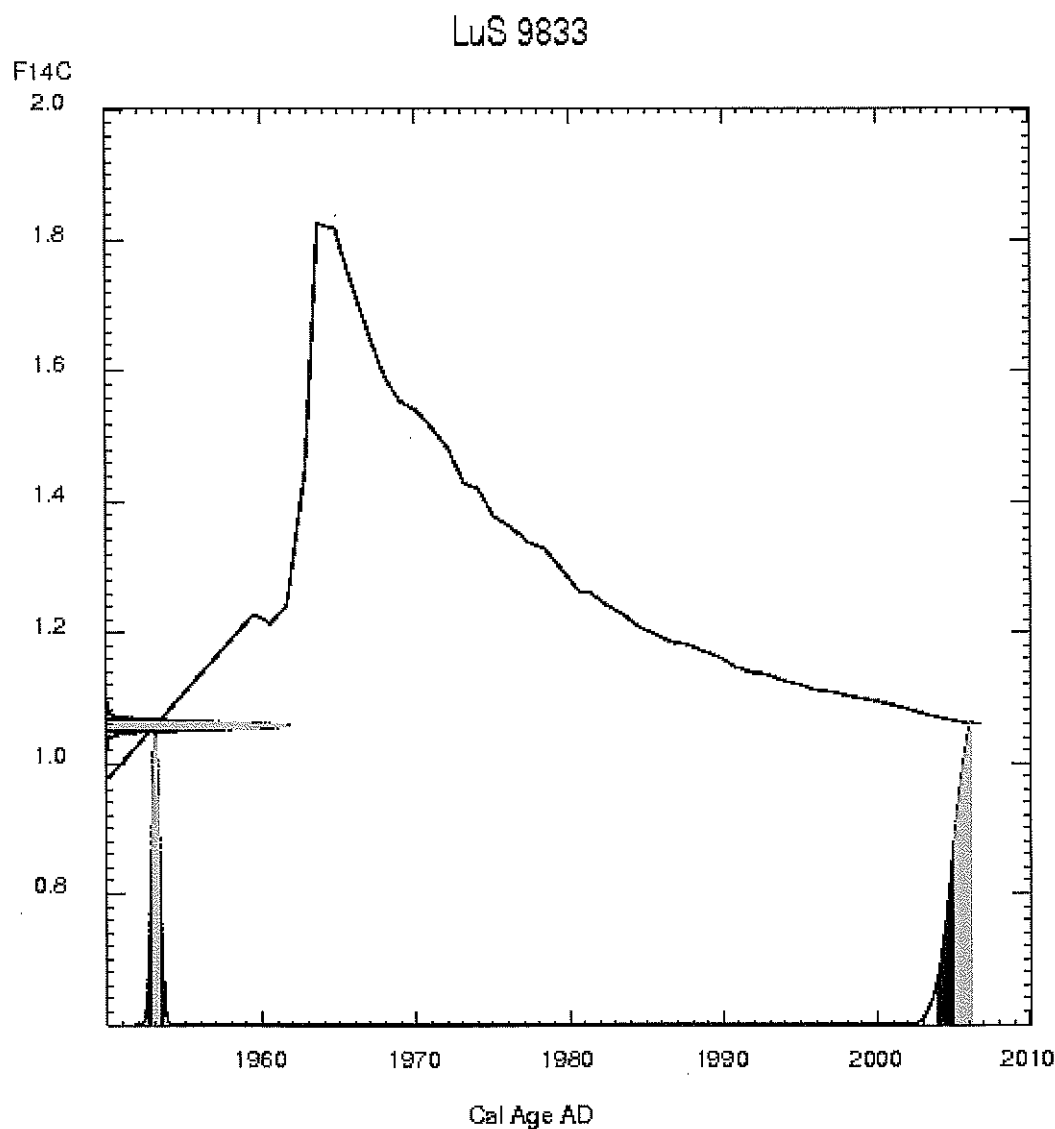
[2005.06(Jan) - 2006.24(Mar)]0.706179

TwoSigma

[1952.62(Aug) - 1953.62(Aug)]0.298030

[2003.90(Nov) - 2006.24(Mar)]0.701970

Note: 300 years of INTCAL04 data have been prepended to this data set



Calibration of 1.060000 ± 0.006000 with SH1.14c dataset**Smoothing: 1.000000**

Q Hua and M Barbetti,
"Review of Tropospheric Bomb ^{14}C Data for Carbon Cycle Modeling
and Age Calibration Purposes", (2004) Radiocarbon 46: 1273-1298.

#

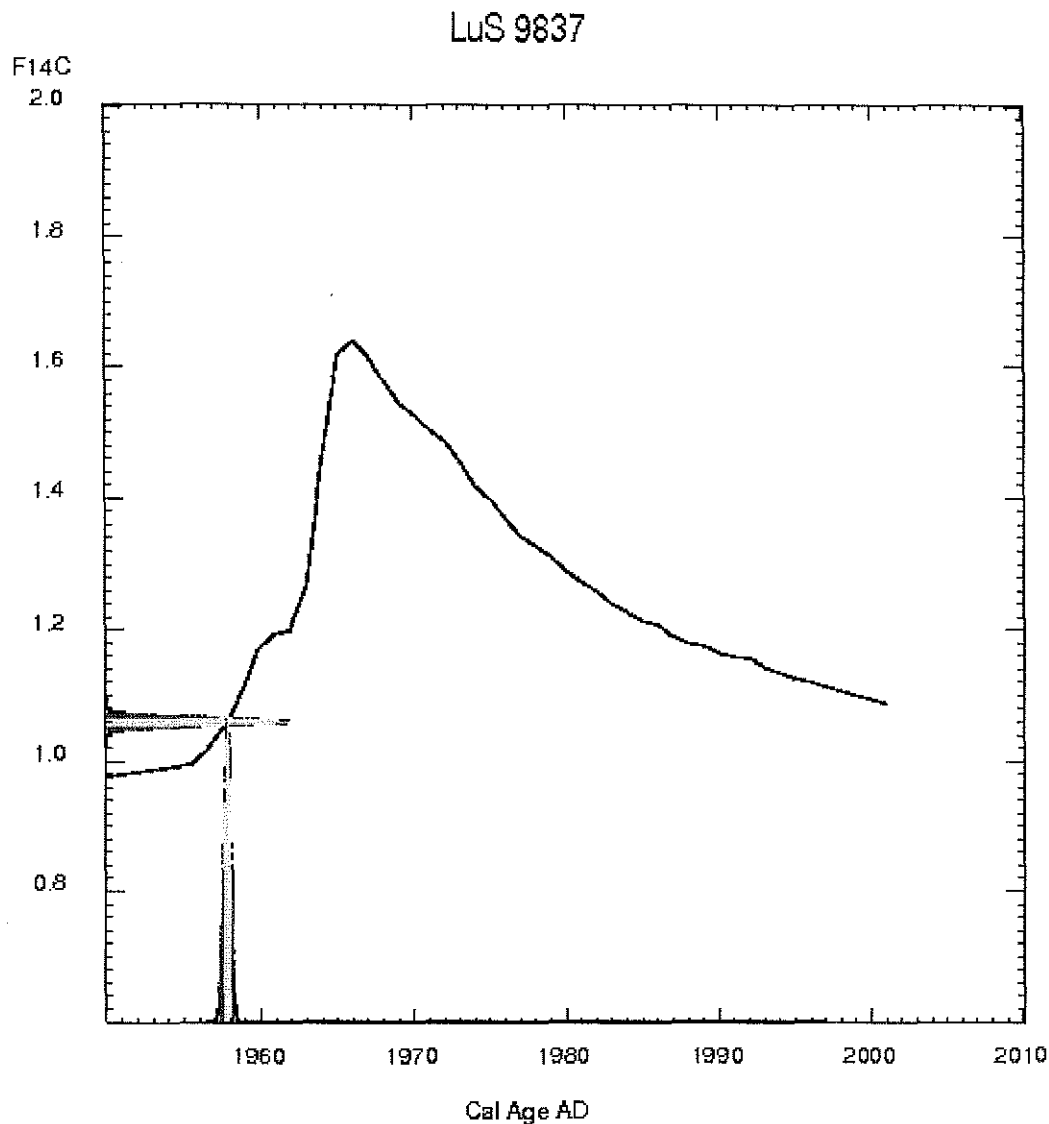
OneSigma

[1957.61(Aug) - 1958.06(Jan)]1.000000

TwoSigma

[1957.36(May) - 1958.25(Apr)]1.000000

Note: 300 years of INTCAL04 data have been prepended to this data set



Calibration of 1.060000 ± 0.006000 with Levin.14c dataset

Smoothing: 1.000000

```
# I. Levin and B. Kromer,
# "The tropospheric  $^{14}\text{CO}_2$  level in mid latitudes of the Northern Hemisphere"
# (2004) Radiocarbon 46(3):1261-1272.
# I. Levin, S. Hammer, et al
# "Radiocarbon observations in atmospheric  $\text{CO}_2$ : Determining fossil fuel  $\text{CO}_2$ 
# over Europe using Jungfraujoch observations as background" (2008)
# Science of the Total Environment 391:211-216.
```

OneSigma

[1952.96(Dec) - 1953.40(May)]0.222413
[2004.82(Oct) - 2006.24(Mar)]0.777587

TwoSigma

[1952.71(Sep) - 1953.67(Sep)]0.246019
[2003.62(Aug) - 2006.24(Mar)]0.753981

Note: 300 years of INTCAL04 data have been prepended to this data set

